Universität Hamburg
DER FORSCHUNG | DER LEHRE | DER BILDUNG

FAKULTÄT
FÜR MATHEMATIK, INFORMATIK
UND NATURWISSENSCHAFTEN

Material realistic modelling of the electron-lattice effects in transition metal dichalcogenide structures

Dissertation

zur Erlangung des Doktorgrades
an der Fakultät für Mathematik, Informatik und Naturwissenschaften
Fachbereich Physik
der Universität Hamburg

vorgelegt von
Michael Winter

Hamburg
2026

Gutachter der Dissertation:	Prof. Dr. Tim Oliver Wehling Prof. Dr. Gabriel Bester
Zusammensetzung der Prüfungskomission:	Prof. Dr. Michael Potthoff Prof. Dr. Gabriel Bester Prof. Dr. Tim Oliver Wehling Prof. Dr. Martin Christian Eckstein Prof. Dr. Nils Huse
Vorsitzender der Prüfungskommission:	Prof. Dr. Michael Potthoff
Datum der Disputation:	27.05.2026
Vorsitzender des Fach-Promotionsausschusses PHYSIK:	Prof. Dr. Johannes Haller
Leiter des Fachbereichs PHYSIK:	Prof. Dr. Markus Drescher
Dekan der Fakultät MIN:	Prof. Dr.-Ing. Norbert Ritter

Abstract

This dissertation investigates a broad range of phenomena arising from the interplay between electronic and lattice degrees of freedom in condensed matter systems. Central to this work is the role of electronic dispersion, phononic dispersion, and electron–phonon coupling across different energy and length scales and how their mutual feedback governs emergent material properties.

We first demonstrate how modifications in the electronic sector can influence lattice dynamics through coupling to phonons. In particular, we examine the proposed formation of stable monopolarons in metallic MoS_2. Employing a combination of Eliashberg theory, Fan–Migdal spectral functions, and the cumulant expansion formalism, we show that electron–phonon interactions in this system do not lead to static lattice distortions, thereby ruling out the formation of stable monopolarons.

The dissertation then turns to the construction and analysis of downfolded quantum lattice models for transition metal dichalcogenide bilayers. We demonstrate that physically meaningful effective models can be formulated in which interlayer phonon modes are excluded *a priori*. Within this framework, we systematically investigate phonon-mediated superconductivity, extracting relevant physical parameters and identifying general trends across a wide range of bilayer material combinations.

As a further extension to bilayer systems, we study twisted bilayers of WSe_2. We propose a methodology for construction of tight-binding models in large moiré supercells based on *ab initio* calculations of aligned bilayers. The functional form and spatial dependence of the hopping matrix elements are analysed in detail, providing a scalable approach to modelling electronic structure in twisted systems.

Finally, we investigate adsorbate-induced lattice dynamics by analysing vibrational modes in a silicon adsorbate on silicon-rich SiC. Using density functional perturbation theory, we track the evolution of oscillatory modes and identify infrared-active vibrations in order to guide later experiments of phonon-pumping.

Overall, this work advances the theoretical understanding of electron–phonon interactions across a diverse set of materials and modelling approaches. By combining first-principles calculations with effective low-energy models, it establishes robust frameworks for disentangling electronic and lattice effects, clarifies the limitations of polaronic lattice instabilities in metallic systems, and provides transferable methodologies for studying superconductivity, moiré physics, and vibrational properties in complex condensed matter systems.

Kurzzusammenfassung (German abstract)

Diese Dissertation untersucht eine Vielzahl von Phänomenen, die aus dem Zusammenspiel zwischen elektronischen und Gitterfreiheitsgraden in kondensierten Materiesystemen entstehen. Im Mittelpunkt dieser Arbeit steht die Rolle der elektronischen Dispersion, der phononischen Dispersion und der Elektron-Phonon-Kopplung über verschiedene Energie- und Längenskalen hinweg und wie ihre gegenseitige Rückkopplung die entstehenden Materialeigenschaften bestimmt.

Zunächst zeigen wir, wie Veränderungen auf Elektronenebene durch Kopplung an Phononen die Gitterdynamik beeinflussen können. Insbesondere untersuchen wir die vorgeschlagene Bildung stabiler Monopolaronen in metallischem MoS_2. Unter Verwendung einer Kombination aus Eliashberg-Theorie, Fan-Migdal-Spektralfunktionen und dem Formalismus der Kumulantenentwicklung zeigen wir, dass Elektron-Phonon-Wechselwirkungen zu den gegebenen experimentell bestimmten Parametern im System nicht zu statischen Gitterverzerrungen führen, wodurch die Bildung stabiler Monopolaronen ausgeschlossen wird.

Die Dissertation wendet sich dann der Konstruktion und Analyse von heruntergefalteten Quanten-Gittermodellen für Übergangsmetall-Dichalkogenid-Bilagen zu. Wir zeigen, dass physikalische, effektive Modelle formuliert werden können, in denen Interlagen-Phononenmoden *a priori* ausgeschlossen sind. Innerhalb dieses Rahmens untersuchen wir systematisch die phonongetriebene Supraleitung, extrahieren relevante physikalische Parameter und identifizieren allgemeine Trends über einen breiten Bereich von Bilagen-Materialkombinationen hinweg.

Als weitere Erweiterung von Bilagenystemen untersuchen wir verdrehtes WSe_2. Wir schlagen eine Methodik zur Konstruktion von Enge-Bindungen-Modellen für große Moiré-Superzellen vor, die auf Erste-Prinzipien-Berechnungen ausgerichteter Bilagen basiert. Die funktionale Form und die räumliche Abhängigkeit der Hüpfmatrixelemente werden detailliert analysiert, wodurch ein skalierbarer Ansatz zur Modellierung der elektronischen Struktur in verdrehten Systemen bereitgestellt wird.

Schließlich untersuchen wir die durch Adsorbate induzierte Gitterdynamik, indem wir die Schwingungsmoden in einem Siliziumadsorbaten auf siliziumreichem SiC analysieren. Mit Hilfe der Dichtefunktional-Störungstheorie verfolgen wir die Entwicklung der Schwingungsmoden und identifizieren infrarotaktive Schwingungen.

Insgesamt fördert diese Arbeit das theoretische Verständnis der Elektron-Phonon-Wechselwirkungen über eine Vielzahl von Materialien und Modellierungsansätzen hinweg. Durch die Kombination von Ersten-Prinzipien-Berechnungen mit effektiven Niederenergiemodellen schafft sie robuste Rahmenbedingungen für das Aufdröseln von elektronischen und gitterdynamischen Effekten, verdeutlicht die Grenzen der polaronischen Gitterinstabilitäten in metallischen Systemen und liefert übertragbare Methoden zur Untersuchung der Supraleitung, der Moiré-Physik und der Schwingungseigenschaften in komplexen kondensierten Materiesystemen.

Etzadla amal ganz gschwind gsacht

In dera Arbat gehds drum, wia si die Elektron und des Gidder im Feschdkörber gegenseitig in de Quere kemma. Also wia des mit die Elektron, die Phonon und dem ganzen Zamghudl af allemeglichn Längn- und Energieskaln laffd und was am End fir a Effegd bei rumkimmt.

Zerschd hamma uns ogschaut, wia Ändrungn bei die Elektron über Phonona is Gidder mit verbiegn kenna. Ganz schbeziell des Gschmarri mit de angeblich stabiln Monopolarona im medallischn MoS_2. Mit Eliashberg, Fan-Migdal und dera Kumulanterei hamma zeichd: Da verzerrt si nix dauerhafd. Des Gidder bleibt brav, also koa stabile Monopolarone, feddich. Erschd wemma a baar mehra Elektron nei bumbn wirds was mit am Polaron.

Dann gehds weider mit effegdive Giddermodelle fir Dobbllagn vo Übergangsmedall-Dichalkogenidn. Da zeign mir, dass ma saubere Modelle baun ko, wo gwisse Zwischenschicht-Phonona glei von vornherein draußn bleim. In dem Rahmn hamma uns dann des mit dera Subraleiderei über Phonon a bisserl exblizider vorgnommn, wichtige Zahln rausgzogn und gschaut, wia si des über ganz vül verschiedene Madrial-Kombinationa so ausdreibt.

Als nächsts san verdrehte Dobbllagn vo WSe_2 dru. Da schlogn mir a Vorgehnsweis vor, wia ma aus Rechnungen erschder Brinzibien von schee ausgerichtete Lagn Enge-Bindungs-Modelle fir riesiche Moiré-Zelln zammstrickt. Mir ham uns genau ogschaut, wia die Hüpfer ausschauen und wia se räumlich variiern – des is dann aa praktisch, wenns System größer wird.

Zum Schluss gehds no um Gidderdynamik, wenn si wos aufsetzt: Mir undersuchn Schwingungsmodn vo am Silizium-Adsorbat af siliziumreichm SiC. Mit Dichdefungtional-Störungsrechnung verfolgn mir, wia si die Schwingunga verhaldn, und findn aa raus, welche im Infrarot mitmacha.

Unterm Strich bringt die Arbat a gscheids Bild davon, wia Elektron und Gidder zamwirgn – und des fir ganz unterschiedliche Madrialien und Rechnansätz. Durchs Zamspuin vo ab-initio-Rechnerei und effegdive Niedrichenergie-Modelle werd klar, wo polaronischer Schmarrn im Metall sei End hat, und ma gricht brauchbare Werkzeig fir Subraleidung, Moiré-Physik und Gitterschwingunga in komblizierde Feschdkörber.

Danksagung

Bevor es nun wirklich an den Inhalt meiner Dissertationsschrift geht, möchte ich mir hier etwas Zeit und Platz nehmen, um nicht nur die verganenen vier Jahre sondern auch etwas darüber hinaus revue passieren zu lassen. Im Laufe meiner späten schulischen und akademischen Laufbahn hatte ich immer wieder die Freude und das Vergnügen mit Personen arbeiten zu können, die an meine Fähigkeiten und mein Wachstumspotential geglaubt haben. Für dieses häufiger auch durchaus nötige Quäntchen Vertrauen und indirekter Motivation bin ich zu tiefem Dank verpflichtet.

Für die Möglichkeit in Hamburg meinen Weg weiter gehen zu können möchte ich zunächst Prof. Dr. Philipp Hansmann und Dr. Xavier Blase danken, die mich zum Ende meines Masterstudiums ermutigt haben den Schritt zu machen eine Promotion zu starten. Für die Zeit in Hamburg selbst möchte ich mich bei Prof. Dr. Tim Wehling herzlich bedanken, der besonders an Tiefpunkten bereit war auch längere Gespräche zu führen und wiederholt den Kurs in der Forschungsarbeit zu unterstützen und zu korrigieren. Neben der inhaltlichen Betreuung sollte hier aber auch einmal deutlich gesagt werden, dass ich den Umgang nach meiner Knieverletzung und die mir entgegen gebrachte Flexibilität in der Endphase meiner Arbeit sehr zu schätzen weiß.

Im Bereich der wissenschaftlichen Zusammenarbeit möchte ich Dr. Niklas Witt zunächst hervorstellen, der mit seiner ruhigen Art und seinem gefühlt allumfassenden Wissen immer für schnelle Diskussionen und Hilfestellungen bereit war. Die Zusammenarbeit mit Dr. Wouter Jolie, Prof. Dr. Isabella Gierz und Maria Federl aus dem Experiment waren für mich besonders lehrreich, weil sie nach einem starken Fokus hinein in die Numerik und Analytik eine wundervolle Gelegenheit geboten haben auch wieder anders über Physik nachzudenken. Weiterhin möchte ich mich bei meinen Kolleginnen Laura Pätzold und Clara Pfister aus der Phonon-Gang für all die Stunden des Brütens über Code und Ergebnissen sowie die vielen inhaltlich abdriftenden Gespräche bedanken.

Auf einer ganz persönlichen und privaten Ebene möchte ich mich bei meinen Eltern bedanken; vor allem bei meiner Mutter, die meinen Weg in den richtigen Momenten immer unterstützt hat. Ein nicht weniger tiefgreifendes Dankeschön möchte ich an meine besten Freunde Benny und Kili richten, weil die Stunden beim Sport und Versacken in den unterschiedlichsten Bars immer wieder eine willkommene Abwechslung und Erfrischung zum Unialltag waren. Über all die Jahre ist unsere Freundschaft ein wichtiger Bestandteil geblieben und ich freue mich schon jetzt auf die nächste Gelegenheit die Krüge einmal mehr zu heben. In diesem Sinne:

It's dangerous to go alone! Take this.

An unnamed old man in The Legend of Zelda

Motivation

But why?

Werner Herzog in "Encounters at the End of the World" musing about a penguin going astray from its colony and heading towards the inner parts of Antarctica. The penguin's motivation remains elusive.

. . . we will approach this rather challenging question directly and head-on. The interplay between electronic and lattice degrees of freedom is a unifying and overarching theme in condensed matter physics. A wide range of emergent phases in solids arise from the feedback between these two sectors. Effects such as superconductivity, charge density waves, polaron formation and moiré flat bands cannot be understood by treating electrons or phonons as detached from one another.

It is our committed goal to study this specific interaction. Due to its complexity we will need to set out for material-realistic modelling beyond idealised toy models. While simplified models provide conceptual insight, a deeper quantitative understanding of real materials requires parameters derived from first principles. Upon involving multiple scales of energy and length, bridging from first principles to effective low-energy models remains challenging.

In the class of 2D materials we identify transition metal dichalcogenides as a versatile platform. They combine reduced dimensionality, tunable screening and rich lattice dynamics with structural properties such as moiré lattice formation and various stacking configurations in thin layered systems. Layer number, stacking, twisting and external perturbations offer unprecedented control over electronic correlations and electron–phonon coupling.

Central to our approaches and fuel to our motor are these questions:

> Are polaronic lattice instabilities viable in metallic TMDCs under realistic conditions?
>
> How can phonon degrees of freedom be consistently incorporated in or excluded from effective qunatum-lattice models for bilayer systems?
>
> How does stacking and twisting modify electronic structure and interaction effects across large moiré supercells?
>
> How can adsorbates be used to engineer and probe lattice dynamics in a controlled manner?

All these deep reaching questions will however not be addressable without a suitable framework development. It will connect density functional theory, many-body perturbation theory and quantum-lattice models. Thus, scalable modelling strategies that remain computationally feasible while retaining essential physics have to be set up and tested. To do so clear criteria for when electron–phonon coupling leads to genuine lattice instabilities and when it does not are established and effective modelling approaches for bilayer and twisted TMDCs are defined.

As a final extend to our efforts, the investigation of electron–lattice effects beyond pristine crystals to adsorbate-induced vibrational dynamics is studied.

Contents

Conventions

Throughout the text of this thesis scalars are written in italic s, vectors in bold italic $\boldsymbol{v}$ and matrices in bold $\mathbf{M}$ fonts. Furthermore, Hartree atomic units are used in general and only in selected instances it is deviated from this: $\hbar = m_\mathrm{e} = \mathrm{e} = {}^{4\pi}/_{\varepsilon_0} = 1$.

At this point it is also noteworthy that we choose to use the colour palette proposed by M. Okabe and K. Ito. It established foundational principles for colour universal design. The set of colours unambiguous for colour-blinds and non-colour-blinds.

I Model Hamiltonians from *first principles* and beyond

『ただ知りたい』という、それこそが科学の原動力だ。
That "just wanting to know" is the driving force behind all of science.

Senku Ishigami in Dr. Stone

Solid-state physics in contrast to high-energy physics does not have to deal with the question of "What is the theory of everything?". The answer to this question is very well known and can be condensed into solving the Hamiltonian of interacting electrons and nuclei. One possible representation is

$$\hat{H} = -\sum_i \frac{\hbar^2 \nabla_i^2}{2m_\mathrm{e}} + \frac{1}{2}\sum_{i\neq j} \frac{\mathrm{e}^2}{|\boldsymbol{r}_i - \boldsymbol{r}_j|} - \sum_I \frac{\hbar^2 \nabla_I^2}{2M_I} + \frac{1}{2}\sum_{I\neq J} \frac{Z_I Z_J \mathrm{e}^2}{|\boldsymbol{R}_I - \boldsymbol{R}_J|} - \sum_{i,I} \frac{Z_I \mathrm{e}^2}{|\boldsymbol{r}_i - \boldsymbol{R}_I|}\,, \tag{I.1}$$

where N electrons and M nuclei are considered [1–3]. Their positions are given by $\boldsymbol{r}_i$ and $\boldsymbol{R}_I$ respectively, the kinetics are encoded in ∇_i^2 and ∇_I^2, nucleus masses are M_I, and nucleus charges are Z_I. In order from left to right the terms in equation I.1 describe the kinetics of the electrons, the pair-wise Coulomb repulsion of electrons, the kinetics of the nuclei, the pair-wise Coulomb repulsion of the nuclei and the Coulomb attraction between electrons and nuclei.

At this point the question "Since we know how to describe the problem, all that is left to do for us, is solving it, is it not?" might arise. It is here, where we have to realise that throughout the history of physics—be it in the description of classical objects or quantum objects—we know rather well how to deal with one or two objects. For instance the Keppler problem or the hydrogen atom are very well studied and understood. The classical three-body problem or the helium atom however lack analytic solutions and we typically resort to approximations and numerical approaches. Hence, it becomes clear that dealing with $N + M$ objects in a quantum mechanical description needs more than the apparently simple step of writing the problem down.

In order to make progress, the model is approximated by including different ideas stemming from a wide variety of view points. No matter the approach and initial direction, the problem has to be made more simple. Like many things it is often not obvious where a certain path will end and most certainly the path itself is unclear. However, the path has to be taken in order to understand the fruitfulness of an approach. This way insights are generated, which can be used to speculate about a next step to take.

Applying a bottom-up approach, we could neglect all interactions in the system and deal with non-interacting electrons and nuclei. This way every object can be treated individually and the solution is simple. Thus, interesting things start happening upon inclusion of interactions

between electrons and nuclei. While we do know that strong Coulomb interactions between nuclei are in general possible, they are typically levelled out against each other in solids when the nuclei are in close vicinity to their equilibrium positions. To this vicinity the nuclei are confined by the potential energy surface. In contrast to this, the physics of the electrons is a lot more complex due to the interplay between their kinetic energy and Coulomb interactions.

Here, we take the path of quantum lattice models. It is our goal to make them material-realistic by derivation from *first principle* calculations. We reduce complexity by choosing a minimal electronic basis via so called *downfolding* of the full *ab initio* description. While doing so, we have to carefully choose the submanifold in a way such that the relevant physics is still being captured. We end up with a model of electronic orbitals and atomic displacements. Each of which are localised in space. Last but not least, we derive the interaction of the localised orbitals with the displacements.

In second quantisation—using creation and annihilation operators for electrons $\hat{c}^{(\dagger)}$ and phonons $\hat{b}^{(\dagger)}$ as quantisation of ion oscillations—a possible form to write down a general model is

$$\begin{aligned}\hat{H} = &\sum_{\boldsymbol{k}n\sigma} \varepsilon_{\boldsymbol{k}n\sigma} \hat{c}^\dagger_{\boldsymbol{k}n\sigma} \hat{c}_{\boldsymbol{k}n\sigma} + \sum_{\boldsymbol{q}\nu} \omega_{\boldsymbol{q}\nu} \left(\hat{b}^\dagger_{\boldsymbol{q}\nu} \hat{b}_{\boldsymbol{q}\nu} + \frac{1}{2} \right) \\ &+ \frac{1}{\sqrt{N}} \sum_{\substack{\boldsymbol{q}\nu \\ \boldsymbol{k}mn\sigma}} g_{\boldsymbol{q}\nu\boldsymbol{k}mn} \hat{c}^\dagger_{\boldsymbol{k}+\boldsymbol{q}m\sigma} \hat{c}_{\boldsymbol{k}n\sigma} \left(\hat{b}^\dagger_{-\boldsymbol{q}\nu} + \hat{b}_{\boldsymbol{q}\nu} \right) \\ &+ \frac{1}{2N} \sum_{\substack{\boldsymbol{q}\boldsymbol{k}mn\sigma \\ \boldsymbol{k}'m'n'\sigma'}} U_{\boldsymbol{q}\boldsymbol{k}mn\boldsymbol{k}'m'n'} \hat{c}^\dagger_{\boldsymbol{k}+\boldsymbol{q}m\sigma} \hat{c}^\dagger_{\boldsymbol{k}'n'\sigma'} \hat{c}_{\boldsymbol{k}'+\boldsymbol{q}m'\sigma'} \hat{c}_{\boldsymbol{k}n\sigma} \,,\end{aligned} \tag{I.2}$$

where details on the individual terms will be discussed further into this chapter.

Often, this is the way quantum-lattice models will be written down in practice by using a general Hamiltonian. We will develop the structure and contents of the individual terms within this chapter. First, we will address the construction of the leading purely electronic term and how it can be derived from density functional theory in section I.2 and how shortcomings may be resolved by applying many-body perturbation theory section I.3. We then extend the theory towards a description of lattice degrees of freedom in section I.4 and the quantisation of vibrations into phonons. Finally, in section I.5 we will discuss the coupling of electrons and phonons in a localised Wannier basis. A rigorous many-body treatment in section I.6 of the interaction opens the possibility to discuss how changes in the electron sector influence the phonon sector, concluding the model construction.

We then turn our attention to the derivation of critical temperatures in phonon-driven superconductivity. Section I.7 lays out Eliashberg theory as well as correction approaches. In sections I.8 and I.10 we turn away from the idea of phonons mediating electron-electron interaction to the concept of trapping electrons in a local lattice deformation originating in the electron-phonon interaction. A closure to the chapter will be given by a discussion of the material class of transition metal dichalcogenides.

I.1 Adiabatic approximations

The adiabatic approximation of a detailed condensed matter Hamiltonian such as equation I.1 decouples electronic and nucleic degrees of freedom. It is often referred to as Born-Oppenheimer approximation after M. Born and R. Oppenheimer [3, 4].

Within equation I.1, the only parameter setting one term apart from the rest is the inverse nucleus mass. Recasting the Hamiltonian according to [3], we write

$$\hat{H} = \hat{T}_\mathrm{N} + \hat{T}_\mathrm{e} + \hat{U}\,, \tag{I.3}$$

where $\hat{T}$ are kinetic energies of the nuclei and electrons respectively and $\hat{U}$ gathers all potential interaction terms. Treating the kinetic energy as perturbation, we formally write $E_i(\boldsymbol{R})$ for the eigenenergies and $\Psi_i(\boldsymbol{r};\boldsymbol{R})$ for the electrons dependent on the set of nuclear positions $\boldsymbol{R}$ as a parameter rather than a variable, where we drop the indices to $\boldsymbol{r}_i$ and $\boldsymbol{R}_J$ to indicate the respectively full-set of positions. Solutions of the coupled systems can be rewritten via

$$\Psi_\jmath(\boldsymbol{r},\boldsymbol{R}) = \sum_i \chi_{\jmath i}(\boldsymbol{R})\Psi_i(\boldsymbol{r};\boldsymbol{R})\,, \tag{I.4}$$

where we use $\jmath$ as label for states of the coupled system. With this linear combination of electronic wave functions by functions of the nuclear coordinates $\chi_{\jmath i}(\boldsymbol{R})$, we determine

$$\left[\hat{T}_N + E_i(\boldsymbol{r}) - E_\jmath\right]\chi_{\jmath i}(\boldsymbol{R}) = -\sum_j C_{ij}\chi_{\jmath j}(\boldsymbol{R})\,, \tag{I.5}$$

where the matrix elements $C_{ij} = A_{ij} + B_{ij}$ are

$$\begin{aligned} A_{ij}(\boldsymbol{R}) &= \sum_I \frac{m_\mathrm{e}}{M_I}\left\langle\Psi_i(\boldsymbol{r};\boldsymbol{R})\,|\,\boldsymbol{\nabla}_I\,|\,\Psi_j(\boldsymbol{r};\boldsymbol{R})\right\rangle\boldsymbol{\nabla}_I \quad \text{and} \\ B_{ij}(\boldsymbol{R}) &= \sum_I \frac{m_\mathrm{e}}{2M_I}\left\langle\Psi_i(\boldsymbol{r};\boldsymbol{R})\,\middle|\,\nabla_I^2\,\middle|\,\Psi_j(\boldsymbol{r};\boldsymbol{R})\right\rangle\,. \end{aligned} \tag{I.6}$$

Now, assuming that the electrons will not change their states, the off-diagonal terms in $\mathbf{C}$ are neglected [4]. The diagonal terms of $A_{ii} = 0$ and B_{ii} can be grouped with the eigenenergies $E(\boldsymbol{R})$ to a modified nucleic potential function $U_i(\boldsymbol{R})$. In the Born-Oppenheimer approximation, the equation

$$\left[-\sum_J \frac{m_\mathrm{e}}{2M_J}\nabla_J^2 + U_i(\boldsymbol{R}) - E_{ni}\right]\chi_{ni}(\boldsymbol{R}) = 0 \tag{I.7}$$

describes the nucleic motion, where n labels its states. This formulation allows for solving the problem of nuclear motion.

Neglecting off-diagonal terms removes any coupling of different electronic states by nuclear kinetics. All other kinds of electron-phonon couplings will be preserved. In addition to this, work presented in this thesis focuses on the ground state of electrons $E_{i=0}$.

I.2 Density functional theory and Wannier construction

First introduced in 1964 by P. Hohenberg and W. Kohn, density functional theory (DFT) pathed a way from a semi-classical "density only" theory of L. Thomas and E. Fermi into a theory of first principles. DFT is based on two theorems dubbed after their inventors [3, 5].

Those theorems come with the upside of applicability to all systems of interacting particles in an external potential. Specifically, a stationary many-body system with energy composed of electron kinetic energy, electron-nuclei interaction and electron-electron interaction from which a quantum Hamiltonian and a many-body wave-functio can be derived.

Theorem 1: The ground state particle density $n_0(\boldsymbol{r})$ determines the external potential $V_{\text{ext}}(\boldsymbol{r})$ of the system uniquely up to a constant.
This immediately leads to the full determination of the system Hamiltonian and hence the many-body wave function for all states. Wherefore all properties of the system are completely known, if the ground state particle density is known.

Theorem 2: no matter what the external potential is, a universal functional depending on the ground state particle density can be defined for the energy $E[n]$. For any V_{ext} the exact ground-state energy of the system is the global minimum of the functional and the minimising density is the exact ground-state density $n_0(\boldsymbol{r})$.
We gain the insight, that the functional $E[n]$ is sufficient for the determination of the exact ground-state energy and density.

Within the approach of P. Hohenberg and W. Kohn, the total energy functional is given as the sum of kinetic energy $T[n]$, electron-electron interaction energy $E_{\text{int}}[n]$, external energy originating generally in an ionic potential and nucleic interaction energy $E_{\text{n-int}}$:

$$\begin{aligned} E^{\text{HK}}[n] &= T[n] + E_{\text{int}}[n] + \int \mathrm{d}^3 r\, V_{\text{ext}}(\boldsymbol{r}) n(\boldsymbol{r}) + E_{\text{n-int}} \\ &= F^{\text{HK}}[n] + \int \mathrm{d}^3 r\, V_{\text{ext}}(\boldsymbol{r}) n(\boldsymbol{r}) + E_{\text{n-int}} \end{aligned} \tag{I.8}$$

The functional F^{HK} in this case is universal for all electronic systems and does not depend on the external potential. If this functional were to be known, a minimisation of the total energy functional in the particle density would lead to the exact ground-state wave function and density.

These findings complete a circular relation between the external potential, the set of many-body wave functions, the ground-state energy and the ground state density. E. Schrödinger's equation introduces a connection from the external potential to the many-body wave functions via the Hamiltonian, within the many-body wave functions one can find the ground-state wave function and from this the ground-state particle density. P. Hohenberg and W. Kohn closed this circle between the ground-state particle density and the external potential.

One closed-form approximation to the functional $F^{\text{HK}}[n]$ was introduced early on by L. Thomas and E. Fermi [6–8], which neglects effects of exchange [9]. The Coulomb interaction is taken as Hartree potential and the kinetic energy is extracted from a non-interacting homogeneous

electron gas, leading to

$$U[n(\boldsymbol{r})] = \frac{1}{2}\int \mathrm{d}^3r\,\mathrm{d}^3r'\,\frac{n(\boldsymbol{r})n(\boldsymbol{r'})}{|\boldsymbol{r}-\boldsymbol{r'}|} \quad \text{and}$$
$$T[n(\boldsymbol{r})] = \frac{3}{10m}\left(2\pi^2\right)^{\frac{2}{3}}\int \mathrm{d}^3r\, n^{\frac{5}{3}}(\boldsymbol{r})\,. \tag{I.9}$$

It is, however, crucial to include effect of exchange and correlation in calculations in order to reach material realistic predictions of physical quantities.

I.2.1 Kohn-Sham DFT

Nowadays most implementations of DFT* use a derived version of the original idea by P. Hohenberg and W. Kohn. The mapping to an auxiliary system as introduced by W. Kohn and L.J. Sham made a wider breakthrough of DFT possible [13]. The auxiliary system chosen here is assumed to be an effective non-interacting system. Casting everything except for the kinetic energy into a potential V_{eff}, the Schrödinger-type equation of the Kohn-Sham system is

$$\hat{H}^{\mathrm{KS}}\varphi_i = \left(\sum_{i=1}^{N_\mathrm{e}}\frac{\hat{\boldsymbol{p}}_i^2}{2} + V_{\mathrm{eff}}(\hat{\boldsymbol{r}}_i)\right)\varphi_i = \varepsilon_i\varphi_i\,. \tag{I.10}$$

The potential V_{eff} has to be determined in a way such that the ground-state electron-density in the auxiliary non-interacting system and the fully-interacting system are identical. The KS wave functions φ_i and the resulting electron density via summation over all orbitals and occupation of energy states $f(\varepsilon_i)$ is given as $n(\boldsymbol{r}) = \sum_i f(\varepsilon_i)|\varphi_i(\boldsymbol{r})|^2$. This allows for the calculation of the kinetic energy and Hartree energy according to equation I.9. In analogy to the Hohenberg-Kohn functional in equation I.8, we write:

$$F^{\mathrm{KS}}[n(\boldsymbol{r})] = T[n(\boldsymbol{r})] + \int \mathrm{d}^3r\, V_{\mathrm{ext}}(\boldsymbol{r})n(\boldsymbol{r}) + U[n(\boldsymbol{r})] + E_{\mathrm{n-int}} + E_{\mathrm{xc}}[n(\boldsymbol{r})] \tag{I.11}$$

This leaves us with the exchange-correlation term as last unknown part of the functional. All many-body effects of exchange and correlation are gathered within this term. Due to its construction it is equivalent to the energy difference of the original fully-interacting many-body system and of the fictitious independent-particle system. If the exchange-correlation functional were known (or were to be found), solving the Kohn-Sham equations would lead to the exact ground-state energy and ground-state density of the many-body problem.

Via variational calculus of E^{KS}, the effective potential in equation I.10 can be expressed as sum of the external potential, Hartree potential and exchange-correlation potential:

$$V_{\mathrm{eff}}(\boldsymbol{r}) = V_{\mathrm{ext}}(\boldsymbol{r}) + \int \mathrm{d}^3r'\,\frac{n(\boldsymbol{r'})}{|\boldsymbol{r}-\boldsymbol{r'}|} + \frac{\delta E_{\mathrm{xc}}[n(\boldsymbol{r})]}{\delta n(\boldsymbol{r})} = V_{\mathrm{ext}}(\boldsymbol{r}) + V^{\mathrm{Har}}(\boldsymbol{r}) + V_{\mathrm{xc}}(\boldsymbol{r}) \tag{I.12}$$

With this formulation, a self-consistency circle just like for the Hohenberg-Kohn formulation is established.

*The code package of Quantum ESPRESSO used for work in this thesis does use Kohn-Sham DFT [10–12].

It should be noted that the Kohn-Sham energy eigenvalues ε_i are not intrinsically meaningful in a physics context. The only exception being the highest occupied eigenvalue of a finite system [14]. However, from the mathematical meaning [15] a connection to the exchange-correlation potential and thus the band gap discontinuity due to the response potential can be inferred [16, 17].

I.2.2 Tight-binding and downfolding

When applying Kohn-Sham DFT to periodic systems, the resulting electron density and electron wave functions are lattice periodic and thus delocalised in real space. We want to change this paradigm now and take a look at the tight-binding (TB) method [18–21]. Just like before, it is an effectively non-interacting description of the electronic structure. It is set apart by the fact that a tight-binding model has a simple representation in the basis of localised states, which due to their often very finite extension are interchangeably called orbitals.

For an orbital μ at lattice site $\boldsymbol{R}$ and an orbital ν at lattice site $\boldsymbol{R'}$, we write in Dirac notation for the matrix elements of the Hamiltonian

$$t_{\mu\nu}(\boldsymbol{R}-\boldsymbol{R'}) = \left\langle \boldsymbol{R}\mu \middle| \hat{H} \middle| \boldsymbol{R'}\nu \right\rangle . \tag{I.13}$$

This kind of description is usable for any kind of non-interacting system. Yet, for systems with rather freely moving electrons often is inconvenient. We would like to have matrix elements $t_{\mu\nu}$ rapidly decreasing with increasing distance $\boldsymbol{R}-\boldsymbol{R'}$, which is a sign that the corresponding electrons are **tightly bound**.

In our context, we deal with periodic systems, which gives us access to translational symmetry and thus Fourier transformability of the Hamiltonian. Upon subsequent diagonalisation, the $\boldsymbol{k}$-dependent eigenvalues (bands) can be obtained as $\varepsilon_n(\boldsymbol{k})$ with n indexing the bands.

One possible way to connect periodic Bloch functions from Kohn-Sham DFT to a tight-binding model is the construction of so called Wannier functions, which are localised and orthogonal orbitals [22]. While atomic orbitals for atoms at different positions would not form an orthogonal basis, Wannier orbitals do satisfy this condition. With this, the eigenvalue problem for determination of electronic bands becomes a inherently simpler.

There is no unique choice for Wannier functions and different approaches may lead to differently rapid decays of hopping amplitudes or different levels of relatedness to known physical objects. It is possible to choose orthogonalised atomic orbitals with clear physical interpretation yet long-range hopping [23] or maximally localised Wannier functions with short-range models and the disadvantage of possibly loosing intuition about the involved orbitals [24, 25].

When setting up a TB model, here we want to take the route of constructing the Wannier functions from Bloch functions $|\boldsymbol{k}n\rangle$ via

$$|\boldsymbol{R}\mu\rangle = \frac{1}{\sqrt{N}} \sum_{\boldsymbol{k}n} U^*_{\boldsymbol{k}\mu n} \mathrm{e}^{\mathrm{i}\boldsymbol{k}\boldsymbol{R}} |\boldsymbol{k}n\rangle , \tag{I.14}$$

where $U^*_{\boldsymbol{k}\mu n}$ is an unitary matrix mixing bands at every $\boldsymbol{k}$-point. it can be chosen freely and different choices lead to different sets of Wannier functions [25].

We will be using the Wannier90 code [26, 27] in order to construct Wannier functions from DFT calculations here. Wannier90 offers a built-in routine to choose a subset of bands of

interest as well as a disentanglement procedure for isolation of these bands [28], if they are embedded within a larger manifold. The procedure of choosing only a submanifold of bands from the full *ab initio* band structure is called **downfolding**.

During this process, effective hopping amplitudes for the description of the bands are obtained, which are considered partially screened. The constructed model often reduces the number of degrees of freedom significantly. Hence, methods of downfolding offer means to reduce complexity by adding complexity in the partially screened parameters, which might gain a more complex dependency on the quantum numbers involved or even frequency dependence [29].

It is of utmost importance that the subspace is chosen such that all relevant dependencies on quantum numbers are included. Otherwise, the connection to a material-realistic model may be sacrificed.

I.3 GW self-energy correction

Section I.11 will give a deeper dive into the material family of transition metal dichalcogenide materials. In chapters II to IV, we will extensively study the subset of semiconducting TMDCs. The approach of the so far presented KS-DFT comes with the well-established short-coming of the band gap problem for GGA functionals. The usage of energy correction as calculated from the GW-approximation in many-body perturbation theory is a reliable method to correct the band gaps [30–33]. It is based on the set of five equations introduced by Hedin [30], which reduce to four within the GW approximation:

$$\begin{aligned} G(1,2) &= \mathcal{G}(1,2) + \mathcal{G}(1,3) \star \Sigma(3,4) \star G(4,2)\,, \\ \chi_0(1,2) &= -\mathrm{i}\hbar G(1,2)G(2,1)\,, \\ W(1,2) &= v(1,2) + v(1,3) \star \chi_0(3,4) \star W(4,2) \quad \text{and} \\ \Sigma(1,2) &= \mathrm{i}\hbar G(1,2)W(1^+,2)\,, \end{aligned} \tag{I.15}$$

where G is a one-particle Green's function, $\mathcal{G}$ is the non-interacting version of the former, Σ denotes the self-energy, χ_0 is the susceptibility of interacting electrons without vertex corrections, v is the bare electronic potential and W its screened version. The integer arguments should be interpreted as $(\boldsymbol{r}_1, t_1) \equiv 1$, where at some instances a superscript "+" indicates infinitesimal shifts in the time argument to ensure causality. $\star$ is short-hand notation for convolution of adjacently identical integer arguments.

At this point, the set of equations looks rather condensed and may lead to the assumption that the calculation of the electronic self-energy is straight forward. Unfortunately, this is not the case and a set of well-defined approximations has to be used in order to make real-life calculations possible. We will determine GW corrections of semiconducting TMDCs using the yambo code [34].

After Fourier transformation of the above expression for the electron self-energy, the two temmporal variables t_1 and t_2 will be combined into one frequency dependence. It is possible to separate contributions of exchange and correlation in a non-local, non-Hermitian self-energy:

$$\Sigma(\boldsymbol{r}, \boldsymbol{r'}, \omega) = \Sigma_\mathrm{x}(\boldsymbol{r}, \boldsymbol{r'}) + \Sigma_\mathrm{c}(\boldsymbol{r}, \boldsymbol{r'}, \omega) \tag{I.16}$$

The exchange term does not depend on energy in any way, i.e. it is static, and the correlation term captures all effects of screening.

Using the GW approximation and Kohn-Sham states obtained from DFT, we can write the matrix elements as

$$\langle \boldsymbol{k}m \,|\, \Sigma_{\mathrm{c}}(\omega) \,|\, \boldsymbol{k}n \rangle = \sum_{\ell \boldsymbol{q}} \int \frac{\mathrm{d}\nu}{2\pi \mathrm{i}} I_{\ell \boldsymbol{q}}^{mn\boldsymbol{k}}(\nu) \left[\frac{f(\varepsilon_{\boldsymbol{k}-\boldsymbol{q}\ell})\theta(\nu)}{\omega - \nu - \varepsilon_{\boldsymbol{k}-\boldsymbol{q}\ell} - \mathrm{i}\eta} + \frac{(1 - f(\varepsilon_{\boldsymbol{k}-\boldsymbol{q}\ell}))\theta(-\nu)}{\omega - \nu - \varepsilon_{\boldsymbol{k}-\boldsymbol{q}\ell} + \mathrm{i}\eta} \right], \tag{I.17}$$

where θ is the Heaviside function and an integrand matrix is introduced. It is closely related to the spectral function and in yambo is defined as

$$I_{\ell \boldsymbol{q}}^{mn\boldsymbol{k}}(\nu) = -\frac{1}{N_k \Omega} \sum_{\boldsymbol{G}\boldsymbol{G}'} W^{\delta}_{\boldsymbol{G}\boldsymbol{G}'}(\boldsymbol{q}, \nu) \rho_{\boldsymbol{k}mn}(\boldsymbol{q}, \boldsymbol{G}) \rho^{*}_{\boldsymbol{k}\ell m}(\boldsymbol{q}, \boldsymbol{G}') \,, \tag{I.18}$$

where $\rho_{\boldsymbol{k}mn}(\boldsymbol{q}, \boldsymbol{G}) = \langle \boldsymbol{k}n \,|\, \exp(\mathrm{i}(\boldsymbol{q} + \boldsymbol{G})\boldsymbol{r}) \,|\, \boldsymbol{k} - \boldsymbol{q}m \rangle$ and W^{δ} is a Dirac-peak-like part of the screened interaction:

$$\begin{aligned} W^{\delta}_{\boldsymbol{G}\boldsymbol{G}'}(\boldsymbol{q}, \omega) &= \frac{1}{2} \operatorname{Im}[W_{\boldsymbol{G}\boldsymbol{G}'}(\boldsymbol{q}, \omega) + W_{\boldsymbol{G}'\boldsymbol{G}}(\boldsymbol{q}, \omega)] - \frac{\mathrm{i}}{2} \operatorname{Re}[W_{\boldsymbol{G}\boldsymbol{G}'}(\boldsymbol{q}, \omega) - W_{\boldsymbol{G}'\boldsymbol{G}}(\boldsymbol{q}, \omega)] \\ \text{and} \quad W_{\boldsymbol{G}\boldsymbol{G}'}(\boldsymbol{q}, \omega) &= \epsilon^{-1}_{\boldsymbol{G}\boldsymbol{G}'}(\boldsymbol{q}, \omega) \frac{4\pi}{|\boldsymbol{q} + \boldsymbol{G}||\boldsymbol{q} + \boldsymbol{G}'|} \end{aligned} \tag{I.19}$$

As a final point, the newly introduced dielectric function ϵ has to be determined. We will use the plasmon pole approximation as already implemented in yambo. Basis of the approximation is the assumption that spectral weight of the dielectric function is concentrated around a plasmon excitation pole. The validity and importance of this approximation has been proven for materials including a wide range of semiconducting materials [35, 36]. In practice, the self-energy is determined on a G_0W_0 level, i.e. no full self-consistency in the Green's function and screened interaction is reached. This often serves as a compromise between accuracy and computational costs just as much as the interesting fact that often on this level, the energy gap calculated is closer to the experimental values than a fully self-consistent one.

I.4 Phonons and density functional perturbation theory

From the discussion presented in section I.1, it can be easily seen that the ground-state energy $E_0(\boldsymbol{R})$ is that of interacting electrons moving in an array of fixed nuclei. Using the force theorem by R. Feynman [37], the force conjugate to the position of a nucleus, can be written as

$$\boldsymbol{F}_I = -\frac{\partial E(\boldsymbol{R})}{\partial \boldsymbol{R}_I} = -\int \mathrm{d}^3 r \, n(\boldsymbol{r}) \frac{\partial V_{\mathrm{ext}}(\boldsymbol{r})}{\partial \boldsymbol{R}_I} - \frac{\partial E_{\mathrm{n-int}}}{\partial \boldsymbol{R}_I} \,, \tag{I.20}$$

which contains only contributions dependent on the position of nuclei. Specifically, the external Coulomb potential induced by the array of nuclei and the nucleic interaction among each other. A second differentiation of the forces yields the force constant matrix $\mathbf{C}$ [38, 39]:

$$C_{IJ}(\boldsymbol{R}) = \frac{\partial^2 E(\boldsymbol{R})}{\partial \boldsymbol{R}_I \partial \boldsymbol{R}_J} = \int \mathrm{d}^3 r \, \frac{\partial n(\boldsymbol{r})}{\partial \boldsymbol{R}_J} \frac{\partial V_{\mathrm{ext}}(\boldsymbol{r})}{\partial \boldsymbol{R}_I} + \int \mathrm{d}^3 r \, n(\boldsymbol{r}) \frac{\partial^2 V_{\mathrm{ext}}(\boldsymbol{r})}{\partial \boldsymbol{R}_I \partial \boldsymbol{R}_J} + \frac{\partial^2 E_{\mathrm{n-int}}}{\partial \boldsymbol{R}_I \partial \boldsymbol{R}_J} \tag{I.21}$$

Via Fourier transform and scaling by the corresponding nucleus masses, the dynamical matrix $\mathbf{D}$ can be obtained as

$$D_{\varkappa\lambda}(\boldsymbol{q}) = \frac{1}{\sqrt{M_\varkappa M_\lambda}} C_{\varkappa\lambda}(\boldsymbol{q}) \quad \longrightarrow \quad \big(\mathbf{D}(\boldsymbol{q}) - \omega^2_{\boldsymbol{q}\nu}\big) \boldsymbol{e}_{\boldsymbol{q}\nu} = 0 \,, \tag{I.22}$$

where $\varkappa$ and λ is a combined index of unit cell atoms and spatial displacement direction, the phonon frequencies in branch ν as $\omega_{\boldsymbol{q}\nu}$ and the corresponding polarisation vector as $e_{\boldsymbol{q}\nu}$ are formally by the given eigenvalue equation.

The latter of which provide a connection between phononic eigendisplacements $u_{\boldsymbol{q}\nu}$ and real displacement of the atoms $u_{\boldsymbol{R}\alpha}$:

$$\begin{aligned} u_{\boldsymbol{R}\alpha} &= \sum_{\boldsymbol{q}} u_{\boldsymbol{q}\alpha} \mathrm{e}^{-\mathrm{i}\boldsymbol{q}\boldsymbol{R}} \quad \text{and} \quad u_{\boldsymbol{q}\alpha} = \frac{1}{N} \sum_{\boldsymbol{R}} u_{\boldsymbol{R}\alpha} \mathrm{e}^{\mathrm{i}\boldsymbol{q}\boldsymbol{R}} \\ u_{\boldsymbol{q}\nu} &= \sum_{\alpha} \sqrt{N M_\alpha} e^*_{\boldsymbol{q}\nu,\alpha} u_{\boldsymbol{q}\alpha} \quad \text{and} \quad u_{\boldsymbol{q}\alpha} = \frac{1}{\sqrt{N M_\alpha}} \sum_{\nu} e_{\boldsymbol{q}\nu,\alpha} u_{\boldsymbol{q}\nu} \end{aligned} \tag{I.23}$$

After introducing a conjugate momentum $p_{\boldsymbol{q}\nu}$ and quantising these expression in terms of phonon creation and annihilation operators, the virial theorem [40] implies that

$$\begin{aligned} \hat{H}_{\mathrm{ph}} &= \frac{1}{2} \sum_{\boldsymbol{q}\nu} \left[\hat{p}^\dagger_{\boldsymbol{q}\nu} \hat{p}_{\boldsymbol{q}\nu} + \omega^2 \hat{u}^\dagger_{\boldsymbol{q}\nu} \hat{u}_{\boldsymbol{q}\nu} \right] = \sum_{\boldsymbol{q}\nu} \omega_{\boldsymbol{q}\nu} \left[\hat{b}^\dagger_{\boldsymbol{q}\nu} \hat{b}_{\boldsymbol{q}\nu} + \frac{1}{2} \right] \\ \text{with} \quad \hat{u}_{\boldsymbol{q}\nu} &= \frac{1}{\sqrt{2\omega_{\boldsymbol{q}\nu}}} \left[\hat{b}^\dagger_{-\boldsymbol{q}\nu} + \hat{b}_{\boldsymbol{q}\nu} \right] \quad \text{and} \quad \hat{p}_{\boldsymbol{q}\nu} = \mathrm{i} \sqrt{\frac{\omega_{\boldsymbol{q}\nu}}{2}} \left[\hat{b}^\dagger_{-\boldsymbol{q}\nu} - \hat{b}_{\boldsymbol{q}\nu} \right]. \end{aligned} \tag{I.24}$$

The set of equations defining the polarisation vectors, the phonon frequencies and real-space nucleic displacement forms the basis for oscillatory movement of atoms as discussed in chapter V.

A standard approach for the calculation of vibronic quantities in real materials nowadays is the well-established density functional perturbation theory [38, 39], which is an approach combining DFT with linear response theory. It offers a way to determine the first term in equation I.21 via calculation of the derivative of the electron density as linear response term with respect to changes in the potential:

$$\Delta n(\boldsymbol{r}) = 2 \sum_{\boldsymbol{k}\boldsymbol{q}mn} \frac{f(\varepsilon_{\boldsymbol{k}+\boldsymbol{q}m}) - f(\varepsilon_{\boldsymbol{k}n})}{\varepsilon_{\boldsymbol{k}+\boldsymbol{q}m} - \varepsilon_{\boldsymbol{k}n}} \underbrace{\langle \boldsymbol{k}n \,|\, \boldsymbol{r} \rangle}_{\psi^*_{n\boldsymbol{k}}(\boldsymbol{r})} \underbrace{\langle \boldsymbol{r} \,|\, \boldsymbol{k}+\boldsymbol{q}m \rangle}_{\psi_{m\boldsymbol{k}+\boldsymbol{q}}(\boldsymbol{r})} \langle \boldsymbol{k}+\boldsymbol{q}m \,|\, \Delta V_{\mathrm{eff}} \,|\, \boldsymbol{k}n \rangle \tag{I.25}$$

The effective potential is identical to equation I.12 and its change

$$\Delta V_{\mathrm{eff}}(\boldsymbol{r}) = \Delta V_{\mathrm{ext}} + \int \mathrm{d}^3 r' \, \frac{\Delta n(\boldsymbol{r}')}{|\boldsymbol{r} - \boldsymbol{r}'|} + \left. \frac{\delta E_{\mathrm{xc}}[n]}{\delta n} \right|_{n(\boldsymbol{r})} \Delta n(\boldsymbol{r}) \tag{I.26}$$

as a result of nucleic displacement contains Δn, offering a self-consistency condition. However, in every encounter of equation I.26 a costly summation over empty conduction states has to be carried out as sums run over all states of the system. Assuming a non-metallic material with a finite gap between valence and conduction manifold, we can rearrange the linear response of the electronic density as

$$\begin{aligned} \Delta n(\boldsymbol{r}) &= 2 \sum_{c,v} \psi^*_v(\boldsymbol{r}) \frac{1}{\varepsilon_v - \varepsilon_c} \langle \boldsymbol{r} \,|\, c \rangle \langle c \,|\, \Delta V_{\mathrm{eff}} \,|\, v \rangle \\ &= 2 \sum_{v} \psi^*_v(\boldsymbol{r}) \underbrace{\left\langle \boldsymbol{r} \middle| \sum_{c} \frac{1}{\varepsilon_v - \varepsilon_c} \middle| c \right\rangle \langle c \,|\, \Delta V_{\mathrm{eff}} \,|\, v \rangle}_{|\Delta v\rangle}, \end{aligned} \tag{I.27}$$

where c and v index states from the conduction manifold and valence manifold respectively and $|\Delta v\rangle$ captures the linear response of states in the valence manifold. In a Sternheimer-type equation all dependencies of quantities from the conduction manifold cancel and upon the usage of projectors $P_c = |c\rangle\langle c|$ and $P_c = 1 - P_v$, we find

$$(H - \varepsilon_v)\,|\Delta v\rangle = (P_v - 1)\Delta V_{\text{eff}}\,|v\rangle\ . \tag{I.28}$$

Finally, the set of equations I.26 to I.28 defines a self-consistent loop in terms of valence states only. Using this approach circumvents taking conduction states into account. Most importantly, an efficient protocol to determine all parts of the force constant matrix from equation I.21 is established.

I.5 Electron-phonon coupling

A possible way to describe the coupling of electronic and nucleic degrees of freedom is achieved by introducing a formal coupling potential dependent on the nucleus displacements $\boldsymbol{u}$ to any order:

$$H_{\text{el-n}} = \sum_{\boldsymbol{k}\boldsymbol{q}mn} V_{\boldsymbol{k}\boldsymbol{q}mn}(\boldsymbol{u})\hat{c}^\dagger_{\boldsymbol{k}+\boldsymbol{q}m}\hat{c}_{\boldsymbol{k}n}\,, \tag{I.29}$$

where we used second quantisation. In an *ab initio* approach only the first-order coupling can be determined efficiently. Thus, once again we will deal with a linear approximation.

Invoking the Kohn-Sham fomulation of DFT, an expansion of the effective potential with respect to the nuclear displacement $\Delta u_{\varkappa p}$ of nucleus $\varkappa$ in unit cell p from their equilibrium position $u^0_{\varkappa p}$ reads

$$V_{\text{eff}}(\boldsymbol{u}) = V_{\text{eff}}(\boldsymbol{u}^0) + \sum_{\boldsymbol{R}i} \frac{\partial V_{\text{eff}}}{\partial u_{\boldsymbol{R}i}} u_{\boldsymbol{R}i}\,. \tag{I.30}$$

Using the difference between the effective potential at any set of $\boldsymbol{u}$ and the equilibrium positions $\boldsymbol{u}^0$ and the Fourier transform, we can write the coupling potential as matrix element and find

$$H_{\text{el-n}} = \sum_{\boldsymbol{k}\boldsymbol{q}mni} \left\langle \boldsymbol{k}+\boldsymbol{q}m \left| \frac{\partial V_{\text{eff}}}{\partial u_{\boldsymbol{q}i}} \right| \boldsymbol{k}n \right\rangle u_{\boldsymbol{q}i}\hat{c}^\dagger_{\boldsymbol{k}+\boldsymbol{q}m}\hat{c}_{\boldsymbol{k}n}\,. \tag{I.31}$$

After quantisation and normal-mode decomposition of the displacement according to equations I.23 and I.24 we find a linear displacement-density coupling

$$\begin{aligned} \hat{H}_{\text{e-ph}} &= \frac{1}{\sqrt{N}} \sum_{\boldsymbol{k}\boldsymbol{q}mn\nu} g_{\boldsymbol{k}\boldsymbol{q}mn\nu}\left(\hat{b}^\dagger_{-\boldsymbol{q}\nu} + \hat{b}_{\boldsymbol{q}\nu}\right)\hat{c}^\dagger_{\boldsymbol{k}+\boldsymbol{q}m}\hat{c}_{\boldsymbol{k}n} \\ \text{using}\quad g_{\boldsymbol{k}\boldsymbol{q}mn\nu} &= \frac{1}{\sqrt{2\omega_{\boldsymbol{q}\nu}}} \sum_i e_{\boldsymbol{q}i\nu} \frac{1}{\sqrt{M_i}} \left\langle \boldsymbol{k}+\boldsymbol{q}m \left| \frac{\partial V_{\text{eff}}}{\partial u_{\boldsymbol{q}i}} \right| \boldsymbol{k}n \right\rangle\ . \end{aligned} \tag{I.32}$$

The calculation of the electron-phonon coupling matrix $\mathbf{g}$ is straight forward from DFPT and carried out in the self-consistent calculation of equation I.28. Hence, the *ab initio* version is readily available.

As established in sections I.2.2 and I.4, electrons can be represented in the localised basis of Wannier functions and phonons in the basis of atomic displacements. Both formulations allow for arbitrary density in reciprocal sampling of the tight-binding matrix and dynamical matrix via Fourier transformation. This is advantageous for the subsequent calculation of properties arising from electron-phonon interactions since those often require very high resolutions in the electronic $\boldsymbol{k}$-space and phononic $\boldsymbol{q}$-space. In order to set up a full model in the language of localised orbitals and atomic displacements, we use the formulation following the version used in the EPW code [41–44]. It determines the electron-phonon coupling via the calculation of the electron-phonon vertex using a Wannier representation:

$$\begin{aligned} g_{\boldsymbol{k}\boldsymbol{q}mn\nu} &= \sum_{\boldsymbol{R}i\boldsymbol{R}'\alpha\beta} e_{\boldsymbol{q}\nu i} U^*_{\boldsymbol{k}+\boldsymbol{q}\alpha m} g_{\boldsymbol{R}\boldsymbol{R}'\alpha\beta i} U_{\boldsymbol{k}\beta n} e^{\mathrm{i}(\boldsymbol{q}\boldsymbol{R}+\boldsymbol{k}\boldsymbol{R}')} \\ \text{and} \quad g_{\boldsymbol{R}\boldsymbol{R}'\alpha\beta i} &= \frac{1}{NN'} \sum_{\boldsymbol{k}\boldsymbol{q}mn\nu} e^*_{\boldsymbol{q}\nu i} U_{\boldsymbol{k}+\boldsymbol{q}\alpha m} g_{\boldsymbol{k}\boldsymbol{q}mn\nu} U^*_{\boldsymbol{k}\beta n} e^{-\mathrm{i}(\boldsymbol{q}\boldsymbol{R}+\boldsymbol{k}\boldsymbol{R}')} \,, \end{aligned} \tag{I.33}$$

where the band mixing matrices $\mathbf{U}_{\boldsymbol{k}+\boldsymbol{q}}$ and $\mathbf{U}^\dagger_{\boldsymbol{k}}$ enter via the transformation to Wannier functions of the vertex in equation I.32. Physically, these matrices describe the change to linear order to the hopping amplitude from orbital α to orbital β at $\boldsymbol{R}'$ for an atomic displacement i at $\boldsymbol{R}$.

I.6 Influence of electron-phonon coupling on phonons

Up until this point, we were dealing with systems which are not subject to any electron addition or removal. The described *ab initio* approaches of DFT and DFPT ar erigid to the sense that the number of electrons in the system has to be changed before the self-consistent solution can be determined and physical properties can be inferred. This will unfortunately lead to huge costs in compute time since all steps have to be redone for any specific doping level. Here, we will introduce a framework to determine changes in phonon dispersion as a consequence of doping, i.e. how charges renormalise phonons.

Using a similar approach to Green's functions for electrons, a displacement-displacement correlation function can be written down. We will refer to it as phonon Green's function $\boldsymbol{\mathcal{D}}$. In combination with a phonon self-energy $\boldsymbol{\Pi}$, the Dyson-type equation

$$\tilde{\mathcal{D}}_{\boldsymbol{q}\mu\nu}(\omega)^{-1} = \mathcal{D}^{-1}_{\boldsymbol{q}\mu\nu}(\omega) - \Pi_{\boldsymbol{q}\mu\nu}(\omega) \tag{I.34}$$

is obtained. We distinguish between the full Green's function $\tilde{\boldsymbol{\mathcal{D}}}$ and the bare Green's function $\boldsymbol{\mathcal{D}}$. The latter can be expressed in terms of the eigenvalue $\omega_{\boldsymbol{q}\nu}$ of the dynamical matrix $\mathbf{D}_{\boldsymbol{q}}$ as

$$\mathcal{D}_{\boldsymbol{q}\mu\nu}(\omega) = \frac{2\omega_{\boldsymbol{q}\nu}}{\omega^2 - \omega^2_{\boldsymbol{q}\nu}} \delta_{\mu\nu} \,. \tag{I.35}$$

With this insight, we can write

$$\begin{aligned} \tilde{\mathcal{D}}^{-1}_{\boldsymbol{q}\mu\nu}(\omega) &= \frac{\omega^2 - \omega^2_{\boldsymbol{q}\nu}}{2\omega_{\boldsymbol{q}\nu}} \delta_{\mu\nu} - \Pi_{\boldsymbol{q}\mu\nu}(\omega) \\ &= \frac{(\omega^2 - \omega^2_{\boldsymbol{q}\nu})\delta_{\mu\nu} - 2\sqrt{\omega_{\boldsymbol{q}\mu}\omega_{\boldsymbol{q}\nu}}\Pi_{\boldsymbol{q}\mu\nu}}{2\sqrt{\omega_{\boldsymbol{q}\mu}\omega_{\boldsymbol{q}\nu}}} \,, \end{aligned} \tag{I.36}$$

where the second line is given in a more symmetrical version. It is possible to rewrite this as a Dyson-type equation for the dynamical matrix as well due to the implicative relation between the poles of the Green's function and the screened dispersion. Using the static case of $\omega = 0$, we find

$$\tilde{D}^{-1}_{\boldsymbol{q}\mu\nu} = \omega^2_{\boldsymbol{q}\nu}\delta_{\mu\nu} - 2\sqrt{\omega_{\boldsymbol{q}\mu}\omega_{\boldsymbol{q}\nu}}\Pi_{\boldsymbol{q}\mu\nu}\,. \tag{I.37}$$

Via diagonalisation, the eigenvectors and screened phonon frequencies are accessible. It is noteworthy that the calculations carried out to arrive at these formulae above can be carried out in a Cartesian basis as well. This comes with the advantage that the eigenvectors can be interpreted as displacement of individual atoms instead of collective displacements.

In second order perturbation theory [45, 46], the leading contribution to the phonon self-energy is given as

$$\Pi_{\boldsymbol{q}\mu\nu} = \frac{2}{N}\sum_{\boldsymbol{k}mn} g^*_{\boldsymbol{k}\boldsymbol{q}mn\mu}\frac{f(\varepsilon_{\boldsymbol{k}+\boldsymbol{q}m}) - f(\varepsilon_{\boldsymbol{k}n})}{\varepsilon_{\boldsymbol{k}+\boldsymbol{q}m} - \varepsilon_{\boldsymbol{k}n}}\tilde{g}_{\boldsymbol{k}\boldsymbol{q}mn\nu}\,, \tag{I.38}$$

where the screened coupling $\tilde{g}$ is used. Finally, upon separating the dependence on phonon dispersion in the electron-phonon coupling $d_{\boldsymbol{k}\boldsymbol{q}mn\mu} = \sqrt{2\omega_{\boldsymbol{q}\mu}}g_{\boldsymbol{k}\boldsymbol{q}mn\mu}$ and $\tilde{d}_{\boldsymbol{k}\boldsymbol{q}mn\nu} = \sqrt{2\omega_{\boldsymbol{q}\nu}}\tilde{g}_{\boldsymbol{k}\boldsymbol{q}mn\nu}$, we find

$$\begin{aligned} \tilde{D}_{\boldsymbol{q}\mu\nu} &= \omega^2_{\boldsymbol{q}\nu}\delta_{\mu\nu} + \Pi'_{\boldsymbol{q}\mu\nu} \\ \text{and}\quad \Pi'_{\boldsymbol{q}\mu\nu} &= \frac{2}{N}\sum_{\boldsymbol{k}mn} d^*_{\boldsymbol{k}\boldsymbol{q}mn\mu}\frac{f(\varepsilon_{\boldsymbol{k}+\boldsymbol{q}m}) - f(\varepsilon_{\boldsymbol{k}n})}{\varepsilon_{\boldsymbol{k}+\boldsymbol{q}m} - \varepsilon_{\boldsymbol{k}n}}\tilde{d}_{\boldsymbol{k}\boldsymbol{q}mn\nu}\,. \end{aligned} \tag{I.39}$$

Using this small trick, we find an expression, where phonon dispersion, screened dynamical matrix and phonon self-energy appear in separated terms of the Dyson-type equation.

Now, we want to pay special attention to the formal equivalence of the static phonon energy $\boldsymbol{\Pi}$ and the electronic contribution to the dynamical matrix in DFPT. The change of the latter contains an identical expression to the phonon self-energy:

$$\Delta D_{\boldsymbol{q}\mu\nu} = 2\sqrt{\omega_{\boldsymbol{q}\mu}\omega_{\boldsymbol{q}\nu}}\frac{2}{N}\sum_{\boldsymbol{k}mn} g^*_{\boldsymbol{k}\boldsymbol{q}mn\mu}\frac{f(\varepsilon_{\boldsymbol{k}+\boldsymbol{q}m}) - f(\varepsilon_{\boldsymbol{k}n})}{\varepsilon_{\boldsymbol{k}+\boldsymbol{q}m} - \varepsilon_{\boldsymbol{k}n}}g^{\text{eff}}_{\boldsymbol{k}\boldsymbol{q}mn\nu} \tag{I.40}$$

Here, the superscript "eff" to the electron-phonon coupling once again refers to the self-consistently determined version—in this case by DFPT. This connection between formulations opens a path to renormalise phonons according to the underlying changes in a model system upon change of parameters. We will use this in the exploration of monolayers of TMDCs and constructed bilayers in chapter III.

I.7 Deriving critical temperatures in phonon-driven superconductivity

One of the most fascinating properties of general quantum lattice models as introduced above is that they are able to contain a multitude of many-body instabilities, which often have their

very own research field (see for instance the discussions in chapter II and [47, 48] for polarons). We call such effects *many-body* due to the description in the framework of quasi-particles arising from many-body theory. It is common for materials to have a multitude of such instabilities and corresponding phases. By now it is known that the interplay can be competing [49–53], coexisting [53, 54] or even cooperative [55–57].

Here, we turn our attention to the superconductivity as discovered in mercury by K. Onnes in 1911 [58, 59]. This opened up a way to go from the assumption of "freezing out the lattice" to the understanding that lattice dynamics actually are essential in driving superconductivity [60, 61]. The field took a path along macroscopic and phenomenological theories until focusing on lattice induced effective potentials and the idea of pair formation ending in a first microscopic description now known as BCS theory (attributed to Bardeen, Cooper and Schriefer) in 1957 [62–66]. Here, we will use a generalisation of BCS theory taking the retarded nature of the underlying interaction—an electron propagates, moves ions accumulating a positive charge to attract a second electron—into account [67, 68].

The starting point of the Eliashberg theory is a diagrammatic treatment of the dynamical electron self-energy. Any effects of retardation in the phonon-mediated interaction between electrons is therefore taken into account explicitly. Using formulations of L. Gor'kov and Y. Nambu a starting point can be formulated via the introduction of anomalous Green's functions in addition to normal Green's functions. The anomalous Green's functions carry information of pair creation and annihilation [30, 69]. These Green's function are equivalently labeled as Gor'kov propagators in a diagramatic framework. The vanishing character of the non-interacting anomalous propagator hinders a perturbative solution of the problem. Consequently, a solution has to be formulated non-perturbatively in a self-consistent approach. The assumption of an existing perturbation series leads as a final result to the Eliashberg spectral function [68, 70, 71]

$$\alpha^2F(\omega) = N(0)\frac{\sum\limits_{\boldsymbol{kq}mn\nu}\left|g^2_{\boldsymbol{kq}mn\nu}\right|\delta(\omega_{\boldsymbol{q}\nu}-\omega)\delta(\varepsilon_{\boldsymbol{k}n})\delta(\varepsilon_{\boldsymbol{k}+\boldsymbol{q}m})}{\sum\limits_{\boldsymbol{kq}mn}\delta(\varepsilon_{\boldsymbol{k}n})\delta(\varepsilon_{\boldsymbol{k}+\boldsymbol{q}m})}\,, \tag{I.41}$$

which combines the double Fermi-surface average of the squared electron-phonon coupling α^2 with the phonon density of states $F(\omega)$. The newly introduced $N(0)$ denotes the electronic density of states at the Fermi level. This spectral function usually is determined via *ab initio* calculations. We will use it to determine a scalar quantity as measure for the effective electron coupling strength:

$$\lambda = 2\int_0^\infty \mathrm{d}\omega\,\frac{\alpha^2F(\omega)}{\omega} \tag{I.42}$$

Additionally, we can construct an Einstein spectrum as an effective phonon frequency via the established choice of a logarithmic average

$$\omega_{\log} = \exp\left[\frac{2}{\lambda}\int_0^\infty \mathrm{d}\omega\,\frac{\alpha^2F(\omega)\log(\omega)}{\omega}\right]. \tag{I.43}$$

Last but not least, within the Eliashberg theory, an instantaneous Coulomb interaction $\mu = N(0)U$ is defined. It incorporates physical effects opposing superconductivity. Within the

calculation of the electron-phonon spectral function, bosonic Matsubara frequencies as well as a numerical cut-off to ensure feasibility are introduced. As a consequence, the Coulomb interaction has to be scaled [72] according to

$$\mu^* = \frac{\mu}{1 + \mu \log\left(\frac{\varepsilon_{\mathrm{pl}}}{\omega_{\mathrm{ph}}}\right)} \,. \tag{I.44}$$

Within the logarithm the time-scales related to the plasma frequency $\varepsilon_{\mathrm{pl}}$ and lattice dynamics ω_{ph} is introduced. Thus, the different scale of propagation times is taken into account.

Here we decided to denote the electronic scale as plasma frequency $\varepsilon_{\mathrm{pl}}$ and want to relate ω_{ph} to the high-frequency cut-off in α^2F as prototypical energy scales of the studied system.

In order to facilitate usage of Eliashberg's framework, W. L. McMillan approximated the critical temperature as it can be derived from the above equations [73, 74]

$$T_{\mathrm{c}} = \frac{\omega_{\log}}{1.2} \exp\left[\frac{-1.04(1+\lambda)}{\lambda - 0.62\lambda\mu^* - \mu^*}\right] . \tag{I.45}$$

This expression got expanded by P. B. Allen and R. C. Dynes [70] with two correcting prefactors:

$$\begin{gathered} f_1 = \left(1 + \left(\frac{\lambda}{\Lambda_1}\right)^{3/2}\right)^{1/3} \quad \text{and} \quad f_2 = 1 + \frac{\left(\frac{\omega_{2\mathrm{nd}}}{\omega_{\log}} - 1\right)\lambda^2}{\lambda^2 + \Lambda_2^2} \\ \Lambda_1 = 2.46(1 + 3.8\mu^*) \,, \quad \Lambda_2 = 1.82(1 + 6.3\mu^*)\frac{\omega_{2\mathrm{nd}}}{\omega_{\log}} \,, \\ \text{and} \quad \omega_{2\mathrm{nd}} = \left\langle \omega^2 \right\rangle^{1/2} = \left(\frac{2}{\lambda}\int_0^\infty \mathrm{d}\omega\, \alpha^2F(\omega)\omega\right)^{1/2} \end{gathered} \tag{I.46}$$

As extensively discussed by P. B. Allen and R. C. Dynes, the factor f_1 serves as a correction in the limit of strong electron-phonon coupling, i.e. $\lambda \gtrsim 1.5$. f_2 on the other hand makes use of the relation between the shape of the electron-phonon spectral function α^2F and the ratio $\omega_{\log}/\omega_{2\mathrm{nd}}$ of logarithmic average frequency ("0^{th}" order momentum) and the square root of the second momentum. Thus, f_1 serves as a strong-coupling correction, whereas f_2 is a shape correction.

It is noteworthy that McMillan's formula for the critical temperature was developed on niobium only. Surprisingly, it performs rather well for almost any material. In a similar fashion, the above corrections by Allen and Dynes are a empirical adaptions to numerical data [70]. Additionally, it also stands as a subject to in-depth research and analysis whether the approximations in the development of Eliashberg theory, McMillan's formula and the Allen-Dynes correction are valid for two dimensional materials.

As a final remark to this chapter, it is noteworthy that the idea of phonon-mediated superconductivity can be extended in other directions, too. Specifically, thoughts and efforts are taken in the direction of "paramagnon"-driven superconductivity with FLEX theory for instance. This explores the idea of substituting the exchange boson from phonons to paramagnons. In a strict sense this deviates not only in the origin of the boson but also in its lack of a sharp well-defined spectrum [75].

I.8 Influence of electron-phonon coupling on electrons

Section I.3 introduced the set of Hedin's equations within the GW approximation, where only electron-electron interaction is accounted for in the screening process. We saw during the discussion of lattice vibrations that in general the underlying potential of nuclei varies. With the extension from the Green's function as used in Hedin's equations G^{Hed}, it is possible to define a Dyson equation encapsulating formally the effects of electron-phonon interaction as well:

$$G(1,2) = G^{\mathrm{Hed}}(1,2) + G^{\mathrm{Hed}}(1,3) \star \Sigma_{\mathrm{ep}}(3,4) \star G(4,2)\,, \tag{I.47}$$

where the newly introduced self-energy arising form electron-phonon interaction has three contributions. Derived from a full perturbation theory treatment, they read

$$\begin{aligned} \Sigma_{\mathrm{ep}} &= \Sigma^{\mathrm{FM}} + \Sigma^{\mathrm{DW}} + \Sigma^{\mathrm{dGW}}\,, \\ \Sigma^{\mathrm{FM}}(1,2) &= \mathrm{i}\hbar G(1,3) \star \Gamma(3,2;4) W_{\mathrm{ph}}(4,1^+)\,, \\ \Sigma^{\mathrm{DW}}(1,2) &= v(1,3) \star \left[\langle \hat{n}(3)\rangle - \left\langle \hat{n}^{\mathrm{Hed}}(3)\right\rangle\right]\delta(2,3) \quad \text{and} \\ \Sigma^{\mathrm{dGW}}(1,2) &= \Sigma_{\mathrm{e}}(1,2) - \Sigma_{\mathrm{e}}^{\mathrm{GW}}(1,2)\,. \end{aligned} \tag{I.48}$$

The first contribution labeled Fan-Migdal* self-energy Σ^{FM} uses Γ as full electron-phonon vertex and the phononically screened potential W_{ph}. Σ^{DW} is attributed to Debye and Waller, incorporating a difference between the electron density of fixed nuclei n^{Hed} † and electronic density if lattice degrees of freedom are included. Lastly, Σ^{dGW} holds the formal correction to the GW self-energy arising from slight differences when calculated on fixed nuclei.

The Debeye-Waller self-energy is a static contribution and has the character of a time-independent correction to the crystal potential [76–78]. The GW self-energy correction in a similar covers effects of change within the Green's function and electron density, if electron-phonon interaction is taken into account.

In contrast to the other two contributions, the Fan-Migdal term corrects the electronic excitation energies dynamically. The convolution of Green's function and phononically screened Coulomb potential encapsulates effects of dynamic lattice polarisation. In practice, we will use the Fan-Migdal self-energy as it is implemented in the EPW code [41, 43], which comes with some approximations to the involved quantities. Like before in section I.3, we approximate $\Gamma(1,2;3) = \delta(1,3)\delta(2,3)$, which is why the Fan-Migdal self-energy colloquially is viewed as "phonon screened GW":

$$\Sigma^{\mathrm{FM}}(1,2) = \mathrm{i}\sum_{\mu\nu}\int \frac{\mathrm{d}\omega}{2\pi}\frac{\mathrm{d}^3 q}{\Omega_{\mathrm{BZ}}} e^{-\mathrm{i}\omega(t_2 - t_1^+)} G(1,2) g^*_{\boldsymbol{q}\mu}(\boldsymbol{r}_2,\omega)\mathscr{D}_{\boldsymbol{q}\mu\nu}(\omega) g_{\boldsymbol{q}\nu}(\boldsymbol{r}_1,\omega) \tag{I.49}$$

In order to determine the remaining quantities, the Green's function will be approximated by the Kohn-Sham Green's function for fixed nuclei, the phonon propagator will be used in its adiabatic form and the frequency dependence of the electron-phonon coupling will be neglected.

*We adopt the combination label of "Fan self-energy" and "self-energy in the Migdal approximation" into Fan-Migdal self-energy as coined by [40].

†In relation to Hedin's equations and hence superscripted accordingly.

With these approximations, an analytical expression can be determined as

$$\Sigma^{\mathrm{FM}}_{\boldsymbol{k}m}(\omega) = \frac{1}{N_{\boldsymbol{q}}} \sum_{\boldsymbol{q}n\nu} |g_{\boldsymbol{k}\boldsymbol{q}mn\nu}|^2 \left(\frac{f(\varepsilon_{\boldsymbol{k}+\boldsymbol{q}n})}{\omega - (\varepsilon_{\boldsymbol{k}+\boldsymbol{q}n} - \omega_{\boldsymbol{q}\nu}) + \mathrm{i}\eta} + \frac{1 - f(\varepsilon_{\boldsymbol{k}+\boldsymbol{q}n})}{\omega - (\varepsilon_{\boldsymbol{k}+\boldsymbol{q}n} + \omega_{\boldsymbol{q}\nu}) + \mathrm{i}\eta} \right). \tag{I.50}$$

In order to see direct relation with *ab initio* band structures, we have to determine the spectral function. In general this can be calculated from the self-energy in a straight forward manner:

$$A(\boldsymbol{k}, \omega) = -\frac{1}{\pi} \sum_j \frac{\mathrm{Im}[\Sigma_{\boldsymbol{k}j}(\omega)]}{(\omega - \varepsilon_{\boldsymbol{k}j} - \mathrm{Re}[\Sigma_{\boldsymbol{k}j}(\omega)])^2 + (\mathrm{Im}[\Sigma_{\boldsymbol{k}j}(\omega)])^2} \tag{I.51}$$

Thus, as soon as the self-energy has been calculated, the spectral function can be inferred.

I.9 Cumulant expansion

Taking a step back, we should recall that in the GW approximation as well as in the approximation of the Fan-Migdal self-energy, we assumed for simplicity that the interaction vertex is an identity. By doing so, information on quasi-particles is lost due to the linearity in the screened potential W (often even W_0, i.e. a one-shot screening). Specifically, the full cascade of satellites to the quasi-particle peak is lost beyond the first order [79, 80]. One possible way to recover the full satellite spectrum is the idea to write the Green's function in the time domain as $G(t) = G_0 \mathrm{e}^{C(t)}$, where G_0 is the Green's function of an independent particle or a quasi-particle and C is the cumulant [81]. This way, an infinite series of diagrams can bes summed over, leading to the possibility to recovering higher-order spectral features. In a full form, the time-dependent Green's function is given as [82, 83]

$$G(\boldsymbol{k}, t) = -\mathrm{i} Z_{\boldsymbol{k}} \Theta(t) \cdot \exp(\mathrm{i}(-\varepsilon_{\boldsymbol{k}} + \mu + \Delta_{\boldsymbol{k}} + \mathrm{i}\eta)t) \cdot \exp(O_{\boldsymbol{k}}(t)) \,, \tag{I.52}$$

where the individual terms are

$$Z_{\boldsymbol{k}} = \exp\left(- \int_{-\infty}^{\infty} \mathrm{d}\omega \frac{|\mathrm{Im}[\Sigma(\boldsymbol{k}, \omega + \varepsilon_{\boldsymbol{k}})]|}{\pi \omega^2} \right), \tag{I.53}$$

$$\Delta_{\boldsymbol{k}} = \int_{-\infty}^{\infty} \mathrm{d}\omega \frac{|\mathrm{Im}[\Sigma(\boldsymbol{k}, \omega + \varepsilon_{\boldsymbol{k}})]|}{\pi \omega} \tag{I.54}$$

$$\text{and} \quad O_{\boldsymbol{k}}(t) = \int_{-\infty}^{\infty} \mathrm{d}\omega \frac{|\mathrm{Im}[\Sigma(\boldsymbol{k}, \omega + \varepsilon_{\boldsymbol{k}}]|}{\pi \omega^2} e^{-\mathrm{i}\omega t} \,. \tag{I.55}$$

The prefactor $Z_{\boldsymbol{k}}$ renormalises the expression. Within the first exponential, $\Delta_{\boldsymbol{k}}$ shifts the quasi-particle dispersion $\varepsilon_{\boldsymbol{k}}$. The last term, $O_{\boldsymbol{k}}(t)$ contains physics leading to the induction of shakeoff bands, i.e. the cascade of satellites.

I.10 Polarons

Up until this point, we assumed that changes in the electronic and phononic properties of the material keep the crystal structure itself unchanged. It is, however, possible that a different

arrangement of the nuclei corresponds to a new configuration of lowest energy, if an external influence like electric fields, stress or doping come into play [84–92]. In the context of coupled electrons and phonons, charge density waves and polarons are typical phenomena. They can be distinguished easily by the extend of the distortion to the crystal structure. Periodic changes are visible for charge density waves whereas polarons manifest only locally.

On a very basic level, a polaron is a charge carrier self-trapped in a lattice distortion created by their presence. By today various directions and theories in order to describe polarons were explored. One of the most prominent theories was introduced by H. Fröhlich [64, 93–97] and focuses on long-range coupling between electrons and phonons, leading to what is called large polarons*. The Fröhlich Hamiltonian is closely related to the Hamiltonian for quantum lattice models we use. It consists of purely electronic and phononic terms as well as an electron-phonon coupling term. The latter of which contains an approximation to the electron-phonon coupling matrix upon introducing the Fröhlich coupling constant α as a material specific scalar parameter rather than a complex coupling matrix. The same constant can be used to determine the polaron self-energy approximately.

A second well-established approach to polarons is the ansatz coined by Holstein [98–101]. It originates in the description of local electron-phonon coupling to a flat optical phonon mode. Due to the local character of the electron-phonon coupling and the connected short-range character of it, strong lattice deformations close to the electron are possible. Thus, Holstein polarons often are smaller than Fröhlich polarons but do not necessarily have to be. If tuned, the coupling will directly influence the size of the polaron. For weak coupling, electrons remain itinerant and lattice distortions spread over multiple unit cells. Thus, a large Holstein polaron is formed. Increasing the coupling to the intermediated range will lead to polaronic narrowing in the electronic bands. Reaching the strong coupling range, electrons induce a sharp, local distortion and become fully self-trapped. In analogy to the Fröhlich coupling parameter α, the parameter λ usually expressed by the polaron binding energy and the inverse electron band width is used to categories the coupling strength.

In this work, we will focus on transition metal dichalcogenide materials (see the following section I.11). Their relatively flat d-bands, valley structure at the K- and Q-/Λ- points of the Brillouin zone and pronounced electron-phonon coupling make them great sandboxes to explore the physics of Holstein polarons [87, 89].

Generally speaking, the full polaron problem is accessible via a model ansatz following Fröhlich or Holstein. They even incorporate effects leading to bipolarons, multiphonon dressing or multipolarons. This is contrasted by the way of choice in *ab initio* approaches, which take the Migdal route by often including only the lowest-order diagrams involving single phonons [67, 102, 103]. Thus, working with models enables a non-perturbative study of polaron formation whereas perturbative Migdal theory allows for a quasiparticle approach. Thus, while the Holstein model provides a full framework capable of describing (small) polaron formation in TMDCs, the Fan-Migdal self-energy corresponds only to the weak-coupling limit treated perturbatively. In chapter II we will use the Fan-Migdal formalism (see section I.8) to capture quasiparticle renormalisation in MoS_2, while keeping in mind that strong short-range coupling require more intricate approaches.

*"Large" and "small" in this context is usually referred to as the ratio between the extend of the polaron and the lattice constant of the material.

I.11 The material class of transition metal dichalcogenides

Recent years saw the advent and uprising of 2D materials. Multiple experimental techniques have been developed to prepare single layers or extract them from a bulk [104–108]. A development which arguably started in 1947 when P.R. Wallace studied the electronic bands of graphite and theorised about the electronic structure of a single layer of carbon atoms [109], which was labelled as "graphene" much later [110]. Jumping in time to 2004; K.S. Novoselvo, A.K. Geim et al. successfully exfoliated a monolayer of graphene using tools as simple as adhesive tape [111]. This original technique of graphene exfoliation in order to obtain monolayers made use of the inherent structure of graphite. In contrast to the diamond structure of carbon, in graphite only two dimensions bind the carbon atoms covalently whereas the third direction binds the layers of carbon atoms only with week electrostatic van-der-Waals forces. This is what actually allows us to use graphite in pencils as a crystal material, from which it is easy to rub off tiny flakes of graphene and splinters of graphite in order to write. Not being exclusive to graphite, this kind of bulk structure can be observed in a multitude of materials [112]. Consequently, this class of 2D materials is coined and referred to as van-der-Waals materials.

It stands to reason that the most well-known of these materials is graphene. Albeit it's visual simplicity with a honeycomb lattice and no out-of-plane extension, the number of model system which can be realised with it appear to be as many as there are sand corns in a dessert: nanotubes of various diameter and coordination, bilayer, trilayer and multilayer systems, twisted graphene multilayers, dressed graphene or decorated graphene [113–118]. The field of low dimensional materials is still rapidly evolving and huge focus and effort is being made experimentally and theoretically in the material family of transition metal dichalcogenides.

Rather surprisingly*, the first monolayer extraction of a TMDC material was done via chemical exfoliation in 1986 [119]. An exfoliation using adhesive tape followed just one year after the success with graphene in 2005 for a wider range of materials by K.S. Novoselov et al. [104]. In 2015 the "gold standard" followed by G.Z. Magda et al. [120], who used the chemical affinity of the chalcogens to bind stronger with gold than with the neighbouring layer of the bulk. Most importantly this kind of technique allows for much larger flakes to be extracted than adhesive tape exfoliation. Nowadays steps towards automation and industrialisation of the adhesive tape exfoliation method make fast progress towards removal of time consuming manual inspection of samples [121, 122]. Work towards large production is fruitful in mechanical exfoliation with adhesive tape mostly in graphene [123] and gold in TMDCs [124]. The same direction of high yield in monolayer production is taken by liquid-phase exfoliation [125–127], where high purity is reachable simultaneously.

TMDCs are usually described by the chemical formula MX_2 [128, 129]. Here, M denotes the transition metal and X a chalcogen, which correspond to group VI B such as molybdenum and tungsten as well as group VI A such as sulphur, selenium and tellurium in the work presented below. The crystal structure consists of covalently bonded X-M-X trilayers stacked in the out-of-plane direction. Individual trilayers are bound via van-der-Waals forces along the same direction [130]. Note, that we refer to one such trilayer as MX_2 monolayer. Several polytypes exist, most notably the semiconducting 2H phase and the metallic 1T and distorted 1T' phases [131, 132]. The former of these is energetically favoured for MoS_2, $MoSe_2$, $MoTe_2$, WS_2, WSe_2 and WTe_2 [133, 134].

*at least to the author

In contrast to graphene, many TMDCs are intrinsic semiconductors with band gaps in the visible to near-infrared range [135, 136]. *Ab initio* calculations and effective tight-binding models show a pronounced thickness dependence of the electronic structure with respect to the number of TMDC layers, where an indirect-to-direct band gap transition is predicted when going from monolayer to bulk systems or vice versa [137–140]. The presence of heavy transition metal atoms leads to strong spin-orbit coupling, resulting in significant spin splittings of the valence and conduction band edges [141, 142]. In monolayers, the lack of inversion symmetry couples spin and valley degrees of freedom. A feature usually captured in $\boldsymbol{k} \cdot \boldsymbol{p}$ and tight-binding descriptions [143, 144]. Throughout this work, we will neglect the spin-orbit coupling for chapters III and IV. Reduced dielectric screening in two dimensions enhances many-body interactions [145–147]. Thus, the role of electron-electron and electron-phonon coupling is amplified.

Due to the reduced dimension of the materials, electronic screening can not happen in the direction perpendicular to the layer plane. Further, the density of states in these materials often shows strong van-Hove singularities. The combination of these prerequisites can lead to a competition of phases such as superconductivity and charge density waves. A wide variety of combinations between transition metals and chalcogens show charge density waves and superconductivity, where the specific combination changes for instance the occurrence of these phases along doping variation [145, 148, 149].

Bilayer systems occupy an intermediate position between monolayers and bulk crystals. Hence, they introduce additional degrees of freedom associated with stacking order and interlayer hybridisation [150–152]. Depending on the interlayer stacking, inversion symmetry can be restored or remain broken. This in turn leads to qualitative changes in the band structure [55]. For semiconducting TMDC bilayers, theoretical studies reveal tunable band alignment, modified spin-orbit splitting and layer-hybridised states, which can be further controlled by external electric fields [153, 154]. Those properties make TMDC bilayers an attractive platform for studying interaction driven phenomena [155, 156].

Picking up the previous line of thought on exotic phases in TMDCs again, the doping variation can be clearly separated in its nature from structural and thermal control parameters. It is thus complementing the stacking configuration, application of external electric field and the reduced dimensionality in monolayers and bilayers. There are several routes and techniques available to achieve doping variations such as electrostatic gating [157, 158], ionic-liquid [159] and electrolyte gating [129, 149, 160–162]. In contrast to chemical doping, these techniques offer a way to tune the doping continuously and reversibly. They directly influence the charge carrier density and the Fermi level. Subsequently, valley occupation and band renormalisation can be directly influenced. In this way a route to balancing and switching between electron-electron and electron-phonon interactions opens up and the charge density wave and superconductivity phases emerge [53, 145, 163]. Doping in TMDC systems is a suitable knob for correlated and collective phases, which can even be combined with the access to geometric degrees of freedom via twisting two layers against each other.

For layered and especially stackable materials the question may arise weather two layers are always as well aligned after stacking as they would be in a bulk material if grown as a crystal. Certainly, with enough training and precise equipment a level of skill can be achieved that a stacking done by hand reaches such proficiency. However, most of the time the layers will be mismatched either by a shift or a twist. The latter of which contains the possibility to realise

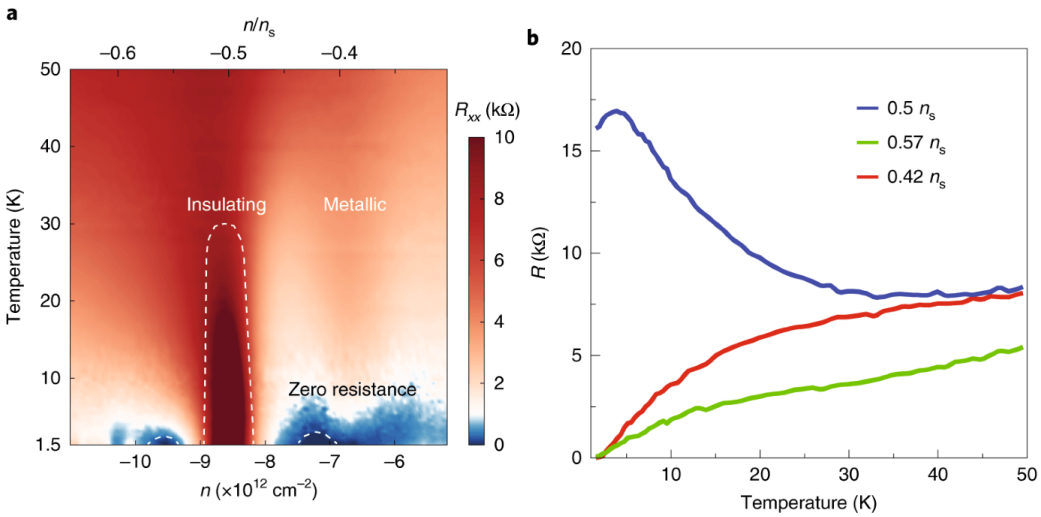

Figure I.1: *Exemplary observation of correlated phases in twisted WSe_2 at 5.1° and a displacement field of 0.45 V nm^{-1}. Subfigure a showcases a phase diagram of resistance if varied over doping and temperature. An insulating region as well as two domes of zero resistance are clearly visible. Subfigure b follows the resistance as function of temperature along the half-filling line through the insulating region, whereas the zero resistance lines (red and green) allow for a guess of the critical temeperature at 3 K. Reproduced with permission from Springer Nature [118].*

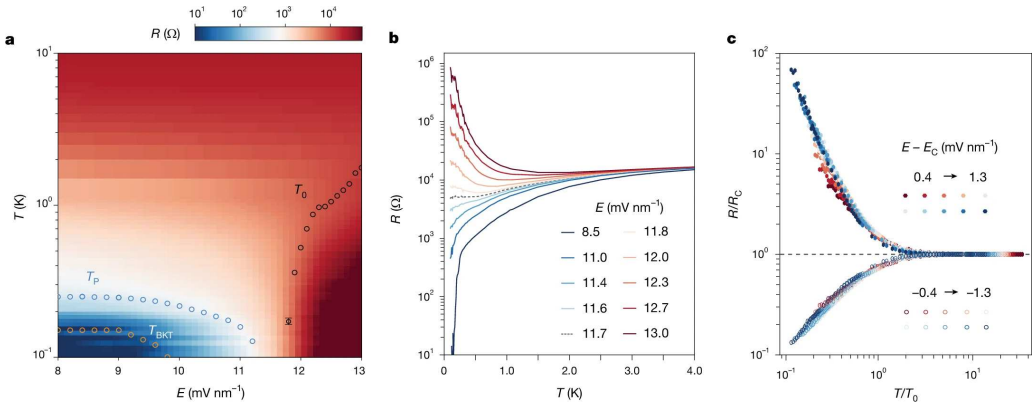

Figure I.2: *Exemplary observation of a superconductor to insulator transition in twisted WSe_2 at 3.65°. In Subfigure a zero-bias resistance R as a function of temperature T and electric field E at $\nu \approx 1$ without magnetic field is depicted. Linecuts of representative electric fields are given in subfigure b, highlighting the superconductor to insulator transition at $E_C = 11.7$ mV nm^{-1}. Subfigure c gives insight into the collaps of the normalised resistance R/R_C after scaling the temperature by the thermal activation temperature T_0. Reproduced with permission from Springer Nature [164].*

so called moiré patterns, i.e. long range periodicity [117, 165]. As a consequence the band edges in the compound undergo a periodic spatial variation. In contrast to twisted bilayer graphene, the intrinsic semiconducting properties of TMDCs give easy access to the formation of flat bands at moderate twist angles.

As teased above, a twisted bilayer is still susceptible to electron doping. In figure I.1 an exemplary measurement of twisted WSe_2 is reproduced, where interaction driven phases like strongly correlated Mott-physics and zero resistance* states were observed [118, 166]. Figure I.2 contrasts the early results of Wang et al. with a concise study of superconductivity in twisted WSe_2 [164], where fast progress is being made in understanding various aspects of the realised exotic phases [167, 168]. Further, properties of the electronic bands in moiré systems can be tuned via twist angle and the combination with doping, an external electric field or strain as well [169–173].

Synoptically, the material class of transition metal dichalcogenides opens a vast control panel with all the individual knobes and switches to be used in order to realise a range of physical effects. Due to this richness, one can set out to understand emerging phases, correlation effects and their interplay in a range of settings.

*Speculated but not concisely proven to be superconductivity.

II Preclusion of monopolarons in MoS_2

How utterly wondrous it is that a small collection of the universe's particles can rise up, examine themselves and the reality they inhabit... and illuminate mystery.

Brian Greene talking about going from simple to complex

In this chapter, we address the work done on the investigation of multipolaronic bound states in single-layer MoS_2. Specifically, my personal contribution on the preclusion of **mono**polaronic effects. In the framework of quantum-lattice models, I investigated how fingerprints of electron-phonon coupling may be visible in the electronic spectral function via electronic Fan-Migdal self-energy and cummulant expansion. In addition to the simulations carried out and presented, I actively contributed to the literature research on theoretical work regarding monopolarons and multipolarons and their spectral functions. Further, I helped writing the interpretation of theoretical results and combining them with the experimental interpretation to a full understanding of the observed effects. Here, I will elaborate in a more detailed manner than it was published in Physical Review X under the title "Inelastic Tunneling into Multipolaronic Bound States in Single-Layer MoS_2" [48]. Collaboration on this work was initiated by the experimental group from university Cologne, II. Physikalisches Institut. The publication in full-text is attached in appendix A. Section II.2 contains work solely conducted by me while section II.1 summarizes the work of the experimental team and section II.3 discusses the final result and multipolaron explanation with numerical results obtained by L. Paetzold.

Polarons themselves are a fascinating physical condensation of electron and lattice interplay. As laid out in section I.10, they sparked the interest to investigate their properties and underlying mechanism of their formation over decades in theoretical physicists just as much as in experimentalists. By now their properties are well studied although their experimental realisation and observation in low-dimensional materials remains sparse.

It is known that the electron-phonon coupling in TMDC materials plays a dominant role. Electron-lattice effects such as superconductivity and charge density waves are among the possible phases (see section I.11). The semiconducting MoS_2, when studied as a bulk material, showed mass enhancement of charge carriers often related to polaron formation, in this case specifically to multiple small Holstein polarons [87]. Follow-up studies were able to reproduce the spectral function in terms of the Fan-Migdal self-energy without small polaron formation [174] and even postulated that in monolayer MoS_2 no stable polarons form at all [102]. Motivated by these contrasting theoretical predictions, we want to revisit the polaron formation in a metallic MoS_2 monolayer. We see it as an ideal platform to test the polaron theory due to the enhanced electron-phonon coupling and the reduced dimensionality of the sample.

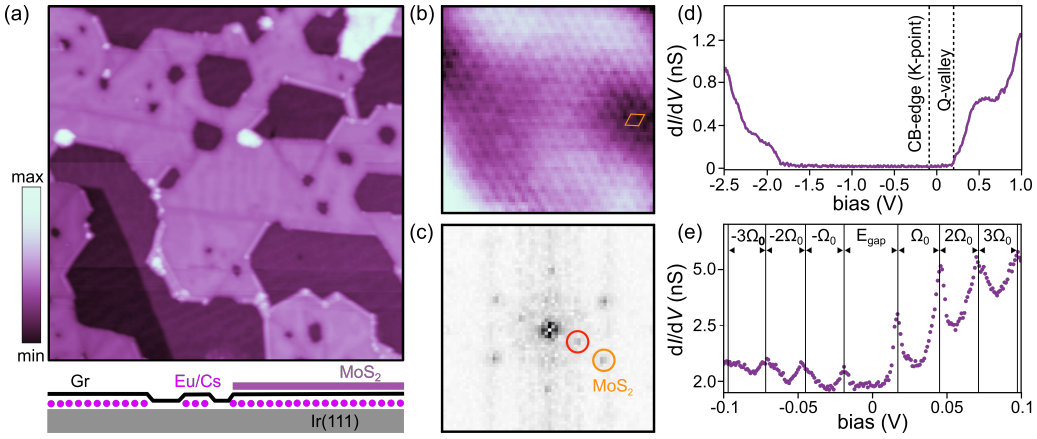

Figure II.1: *Experimental observations in metallic MoS_2. Subfigure (a) depicts a large-scale STM scan of the sample as sketched at the bottom; (b) gives an atomic resolution of the STM scan, making a superstructure; (c) shows a Fourier transform of (b) showing the reciprocal cell as well as a pronounced feature at half the reciprocal lattice size; (d) shows a large-bias STS of the sample indicating central features of the conduction manifold; (e) contrasts with a low.bias STS around the Fermi energy in relation to (d). Taken from van Efferen et al. [48] (CC BY 4.0)*

II.1 Experimental setup and observations

To access this regime experimentally, we reproduce the metallic MoS_2 monolayer system introduced by van Efferen et al. [47]: a monolayer of MoS_2 is placed on top of a graphene layer (Gr), which in turn was placed on top of an iridium (111) substrate (Ir(111)). It was observed that the intercalation with caesium and europium (Cs and Eu) between Gr and Ir(111) leads to a shift of the conduction band edge of MoS_2 below the Fermi level, which induces an insulator-metal transition.

With scanning tunnelling microscopy (STM) (see figure II.1), the surface of the grown material was investigated and a superstructure (2×2) was found. This structure was found to not be long-range coherent, ruling out the charge density wave phase. Scanning tunnelling spectroscopy (STS) reveals a series of peaks in $\mathrm{d}I/\mathrm{d}V$ centred around the 0 V bias, i.e. the Fermi energy of the system. The first peak above and below the Fermi level are separated by an energy gap $E_{\mathrm{gap}} = 41 \pm 7\,\mathrm{meV}$ and appear in outward direction in steps of $\Omega_0 = 24 \pm 4\,\mathrm{meV}$. This kind of spectrum can in general be associated to a many-body spectral function of an electronic state which couples to a phonon mode [175, 176]. Following this ansatz however, does not explain the spectrum in full detail due to not offering an explanation for the origin of the energy states closest to the Fermi level nor a reason for the dominance of a single phonon energy in the observed spectra. In total, strong evidence for a localised state induced by coupling of additional charge carriers and acoustic phonons is observed, thus hinting at the realisation of a polaronic state in metallic MoS_2.

II.2 Ab initio studies

Following the conclusion that polaron physics lead to the observed scanning tunnelling spectra, we want to understand in depth the underlying mechanisms at play. We apply the well-established *ab initio* polaron theory [102, 103]. Although the MoS_2 monolayer is positioned on top of a graphene layer on an iridium substrate and intercalated with Cs and Eu in experiment, we will investigate in our simulations the TMDC monolayer as free-standing. Any effects by the substrate beyond electron doping are not preserved this way. As a starting point of our studies, we use the explanation of spectral features as effects originating in Fan-Migdal physics (see section I.8) as observed and explained in [87, 174].

II.2.1 Polaron states in metallic MoS_2

In figure II.2 (a), we depict the electronic band structure of a free-standing monolayer of MoS_2 doped with $0.1\,e^-/\text{u.c.}$. Spin-orbit coupling is included, leading to a six band Wannier construction. The close-up panel (c) details the dispersion around the Fermi level, colour coding the bands according to spin. It shows an occupied K-valley in both spin states and a Q-valley occupied in one spin state. It is noteworthy that this situation is reversed at the Q'-point due to the symmetry of the system and spin-orbit coupling.

In addition, we show the acoustic phonon dispersion of the system in figure II.2 (b). This differs from figure III.3 by softening of the orange LA branch and an avoided crossing between the M-point and the K-point with the blue TA mode. The black ZA mode appears unchanged except for a slight imaginary dispersion around the Γ-point. As a linewidth of the phonon branches, we depict the modulus of the squared electron-phonon coupling $\left|g^2_\nu(\boldsymbol{q})\right|$ after summation over all electronic indices. We observe the strongest coupling for M-point phonons in the softened LA branch, offering an explanation for the change of the phonon dispersion due to the added charge carriers in the system.

Last but not least, figure II.2 (d) depicts the spectral function as obtained from the Fan-Migdal self-energy in the same energy and momentum range as subfigure (c). Upon close inspection of the K-valley, we observe a slightly more prominent splitting in both spin states as well as so called phonon-cuts in the parabolic dispersion as highlighted by the inset. The bottom of the Q-valley is washed out due to spectral broadening.

All results and observation in figure II.2 are in line with the findings in [174]. One major difference we find here, is the imaginary phonon dispersion around the Γ-point in figure II.2. This small detail points toward a system instability related to lattice relaxation, i.e. upon doping the system, the crystal structure is no longer in equilibrium.

The most important difference between the system studied here and the experimental findings however is the occupation of the Q-valley. As pointed out above in section II.1, the experimental results suggest that the Q-valley is unoccupied [48] and rather well separated from the Fermi level.

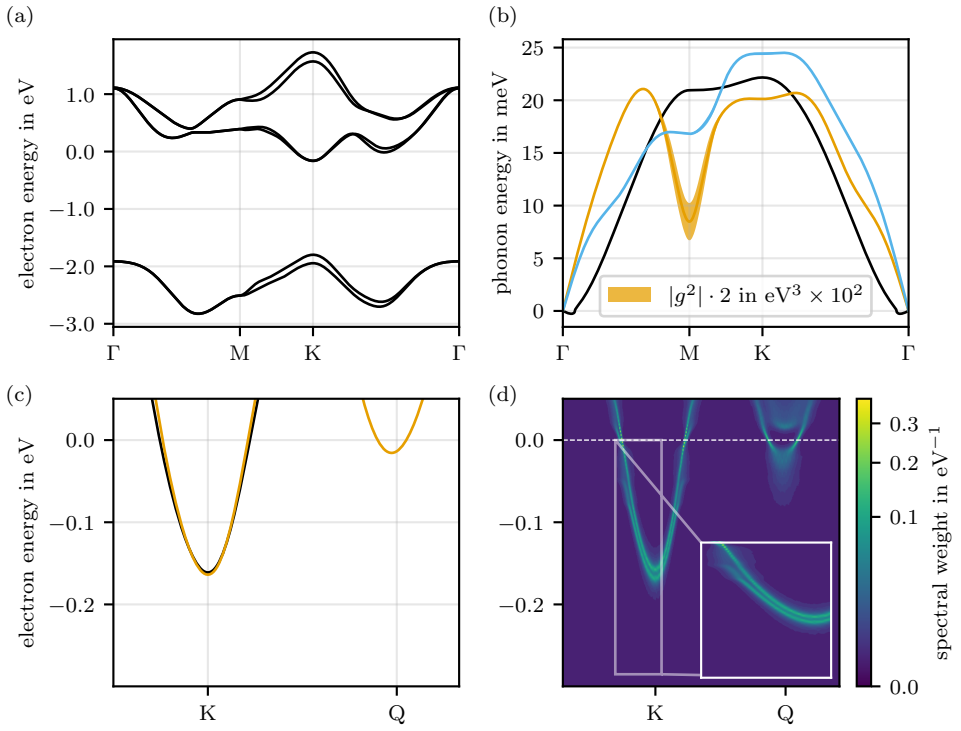

Figure II.2: *Electronic band structure of MoS_2 including spin-orbit coupling (a) and zoom-in to the energy window between conduction band edge and Fermi level as well as reciprocal path round K-valley and Q-valley highlighting spin splitting between black and orange band (c). Acoustic phonon dispersion with k- and mode resolved electron-phonon coupling as linewidth (b). Spectral function as obtained from Fan-Migdal self-energy detailing phonon-cuts in the K-valley and spectral weight redistribution of the Q-valley bottom (d).*

II.2.2 Removal of polaronic fingerprints

It turns out that on an *ab initio* level, the problem of unoccupied Q-valley and suggested lattice instabilities can be resolved simultaneously. Upon relaxation of the doped system, a slight increase of the lattice constant from $a = 3.185\,\text{Å}$ to $a' = 3.234\,\text{Å}$ as well as slight shift by $0.024\,\text{Å}$ of sulphur atoms into the monolayer plane occurs. Figure II.3 gathers the subsequent changes in electronic and phononic structure.

Now in full agreement with the experimental observation, the Q-valley lies above the Fermi level while the K-valley remains occupied according to figure II.3 (a). Comparing subplots (c) of figures II.2 and II.3 we observe that the relaxation leads to a separation of the K-valley minimum and the Q-valley minimum. In figure II.3 (b) the phonon dispersion no longer shows imaginary dispersion around the zone-center and electron-phonon coupling is of two magnitudes smaller as compared to figure II.2 (b). Any phonon-mediated effects like spectral weight distribution as seen in figure II.2 (d) are now fully absent in figure II.3 (d).

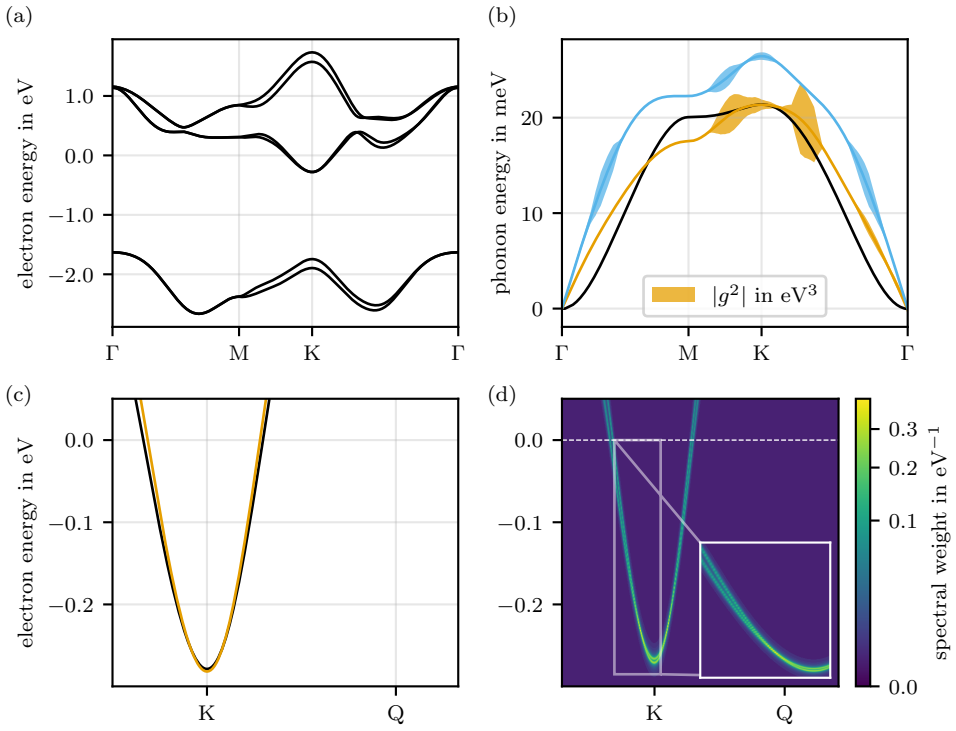

Figure II.3: *Electronic band structure of MoS_2 including spin-orbit coupling (a) and zoom-in to the energy window between conduction band edge and Fermi level as well as reciprocal path round K-valley and Q-valley (c). Acoustic phonon dispersion with k- and mode resolved electron-phonon coupling as linewidth (b). Spectral function as obtained from Fan-Migdal self-energy detailing phonon-cuts in the K-valley and spectral weight redistribution of the Q-valley bottom (d).*

Comparatively, we interpret the change in lattice structure, electronic structure and phononic structure as combinatorial effects towards the suppression of electron-phonon coupling. Thus, any signs of polaron formation are removed.

II.2.3 Cumulant expansion

In figure II.1 (e) the observation of a cascade of peak-features around the Fermi level is documented. We detailed in sections I.8 and I.9, that the spectral function as it can be invoked from the Fan-Migdal self-energy fails to reproduce a series of polaronic band replica. Thus, as a last check, we apply the cumulant expansion technique to the simulation setting closer to experiment to understand whether the spectral features can be recovered.

We infer the renormalising prefactor $Z_{\boldsymbol{k}}$ from the *ab initio* Fan-Migdal self-energy. This is possible due to the equivalence of both Fan-Migdal approach and cumulant expansion in first order of the latter. In the setup of occupied K-valley and unoccupied Q-valley, we find at the K-point $Z_K \approx 0.9$. This indicates that there is a redistribution of 10 % of spectral weight to

satellites. The STS measurements show that the satellite peaks contain much more than 10 % of the spectral weight, which is visible to the naked eye already. Thus, an explanation based on cumulant theory is not possible either.

II.3 Conclusion and final interpretation

With the results of figure II.3 and section II.2.3 we do not find any hints towards the formation of polarons in metallic MoS_2 monolayers as included in the *ab initio* approach to polaron and Fan-Migdal physics. We demonstrated that either the features of electron-phonon interaction can be realised while sacrificing a close relation with the experiment or the physical parameters as determined by the experiment are kept fixed and no significant electron-phonon interaction is predicted theoretically. Thus, we pose the question whether the experimental results stem from physics beyond the **mono**polaron explanation.

To address the question, we adapt our idea and consider polaronic structures beyond the single self-trapped electron, i.e. polarons containing two or more electrons. For so called **multi**polarons to form, the Coulomb repulsion of charge carriers has to be overcome by the effective attractive potential of the lattice distortion.

The spectral properties of multipolaronic states are much less understood however. We gain insights by comparison of the better-studied bipolaron case [177, 178]. In the Holstein model (see section I.10), an increase in electron-phonon coupling leads to equidistant, phonon-induced replica separated by an energy gap $E_{\mathrm{gap}} = 2\varepsilon_{\mathrm{pol}}$. Here the Fermi energy is centered in the gap and peaks corresponding to electron removal (addition) lie below (above) [179, 180]. Such features are expected to be generic for interacting many-polaron systems [178, 181–183] and qualitatively match the experimental observations.

This line of thought is followed with a different approach in a newly developed *ab initio* electron-lattice downfolding approach tailored towards the relaxation of supercell structures [184]. in agreement with W.H. Sio and F. Giustino [185], no stable lattice distortions upon adding one electron into a MoS_2 monolayer were found. An addition of four electrons, however, distorts supercells of different sizes (6×6, 12×12 and 18×18) in a stable manner. Unfolding the band structure from the supercell to a unit cell, we find dispersionless shake-off bands within the band gap, which can be associated to the broken symmetry beacuse of the polaron distortion. By analysing the structure factor [184] a peak at the M-point is found and a decomposition into normal modes reveals the origin at a dominant LA mode in the vicinity of the M-point. The phonon energy of 28 meV coincides with experiment and stands in line with previous findings [174]. Amn analysis of the free energy with respect to the lattice distortion along the relaxation direction reveals that the symmetric phase now is only a local minimum and the polaron configuration is energetically favourable. Due to the real space structure of the multipolaronic distortion as a 2×2 superstructure, we further conclude that the polaronic states are a precursor to a charge density wave phase which will form under further electron doping to the monolayer. At this point, the interested reader is pointed to the full discussion of model calculations by L. Pätzold as printed in the full-text publication [48] in appendix A.

With the theoretical preclusion of monopolarons and the finding that multi-electron doping leads to stable local lattice deformations, we interpret the energy gap $E_{\mathrm{gap}} \approx 40\,\mathrm{meV}$ as binding

Table II.1: *Fractional coordinates of MoS_2 for Fan-Migdal self-energy calculations. n_i are coefficients to the lattice vectors $\boldsymbol{a}_i$. The left table lists the coordinates before relaxation, the right table after relaxation.*

atom	n_1	n_2	n_3
S	2/3	1/3	0.104196
Mo	1/3	2/3	0.0
S	2/3	1/3	-0.104196

atom	n_1	n_2	n_3
S	2/3	1/3	0.102627
Mo	1/3	2/3	0.0
S	2/3	1/3	-0.102627

energy of the multipolaron and the equidistant spacing of the peak series as shake-off peaks due to strong coupling with an M-phonon of energy $\Omega_0 \approx 24\,\mathrm{meV}$.

II.4 Computational details

Density functional theory calculations were performed using the Quantum Espresso codes [10–12]. The lattice constant for a hexagonal Bravais lattice was set to $a = 3.1851\,\text{Å}$ and later to $a' = 3.2342\,\text{Å}$ for relaxation after doping; fractional coordinates are listed in table II.1. The layers were artificially separated by $c = 15\,\text{Å}$. Plane wave functions were cut at 100 Ry. Fermi-Dirac smearing with a width of 0.001 Ry was employed and a total charge of $-0.1\,e^-/\text{u.c.}$ was set. The pseudo potentials used the PBE functional [186]. Electron density and energy levels were determined on a dense $18 \times 18 \times 1$ Monkhorst-Pack grid. Density functional perturbation theory was carried out on a $6 \times 6 \times 1$ $\boldsymbol{q}$-grid.

The EPW code [41, 43, 44, 187] performed the Wannier construction (using Wannier90 [24, 27, 28]) and extrapolated the electron-phonon coupling matrix to a $72 \times 72 \times 1$ $\boldsymbol{k}$-grid and $48 \times 48 \times 1$ $\boldsymbol{q}$-grid. Subsequent calculation of the electron spectral function in the Fan-Migdal approximation was carried out on a dense $\boldsymbol{k}$-path along $\Gamma \to M \to K \to \Gamma$ and the underlying $\boldsymbol{q}$-grid spanned $96 \times 96 \times 1$ points.

III Stacking-induced phenomena in transition metal dichalcogenide bilayers

The pleasure of finding things out

Title of an interview transcript of R.P. Feynman [188]

By combining *ab initio* calculations with many-body theory for quantum lattice models we will explore a total of 32 semiconducting TMDC materials. Largely focusing on the evolution of superconductivity parameters with electron doping to the system. First, we discuss how material-realistic quantum lattice models (see sections I.2, I.4 and I.5) are obtained for monolayer TMDCs built from molybdenum and tungsten (Mo and W) in combination with silicon, selenium and tellurium (S, Se and Te). We study these monolayer systems within Eliashberg theory. Afterwards, we describe the approach to the construction of bilayer quantum lattice models and apply Eliashberg theory once again.

As established in section I.7 and chapter II, there is a wide range of possible phases to be realised in different scenarios within the family of TMDC materials. Now, we will focus on the phonon-driven superconducting phase as it can be predicted from Eliashberg theory and want to hint at charge density wave phases. It is rather fascinating that via a multitude of ways, a superconducting phase may be reached [53–57] or hindered [49–53]. A recent study in $NbSe_2$ revealed that chemical doping with molybdenum atoms to get $Nb_{1-x}Mo_xSe_2$ influences the superconductivity significantly [189]. This kind of doping however is rather strict in nature, gives fixed results after crystal growth and *ab initio* calculation have to use large unit cells. When introducing and discussion general properties of TMDCs (see section I.11), we described the possibility of doping them strongly with continuous doping approaches. With previous work done by M. Rösner [190] an *ab initio* study of MoS_2 predicted that superconductivity and a charge density wave phase can be reached. Shortly after W. Shi et al. [191]demonstrated that the superconducting phase in molybdenum-based TMDCs can be reached via ionic gating. A multitude of other routes of doping were taken experimentally as well. For instance to study superconductivity in ion-gated MoS_2 [192], hydrogenation in MoS_2 [193], gating via electric field in MoS_2 [194] and electrolyte gating in WS_2 [195].

III.1 Downfolding of electronic bands

As discussed in section I.2 we want to reduce the complexity of the electronic model obtained from *first principle* calculations by choosing a relevant submanifold of electronic bands. It is

a standard approach by now to project to a three-band basis for our chosen TMDCs. The initial projections to d_{z^2}, d_{xy} and $d_{x^2-y^2}$ of Mo and W by calculation of the projected density of states. In figure III.1, for instance, we show the k-resolved density of states in a MoS_2 monolayer to orbitals of d-character in Mo. We see that the valance band is dominated by d_{z^2} character at the Brillouin zone center, shifting to $d_{x^2-y^2}$ and d_{xy} character at the K-point. In the conduction band, the band minimum at the K-point shows maximal d_{z^2} weight and significant $d_{x^2-y^2/xy}$ character everywhere else. This behaviour is well reproduced for all transition metals in our considerations, where the influence of varying chalcogen type on the distribution of the orbital weights appears negligible. See appendix B for the remaining five elemental combinations. Thus, we choose one valence band and two conduction bands as electronic submanifold.

We depict in figure III.2 the band structure after Wannier construction (orange dashed lines) which shows identical electronic energy dispersions as the underlying *ab initio* band structure. On the right, we also show the resulting Wannier orbitals. They are localised on the transition metal atom and show d_{z^2}, d_{xy} and $d_{x^2-y^2}$ character as it is to be expected from the projected band structure. Due to the crystal structure the orbital lobes are slightly morphed if compared to their counterparts in atomic hydrogen. Nevertheless, we will refer to the Wannier orbitals as d_{i}-type with $i \in \{z^2, xy, x^2-y^2\}$. Once again, all considered material combinations show similar localisation and structure of Wannier orbitals.

We see immediately from the dispersion of the lowest conduction band that besides the conduction band minimum (CBM) there is a second, local minimum forming around the middle of the path $K \to \Gamma$, which is commonly denoted as Λ*. Upon electron doping into the system, we can therefore first occupy the K-valley and upon further increase the Λ-valley. We will see that the energy difference between these two minima $\Delta E_{K\Lambda}$ is a pointer towards how resilient the lattice structure is under doping. Table III.1 lists $\Delta E_{K\Lambda}$ against the monolayer material. Notably, the exchange of the chalcogen atoms along the period of this group shows a dip of

*Sometimes Q is used, too. Both notations are somewhat interchangeable in 2d systems since they are identical in a 2d Brillouin zone.

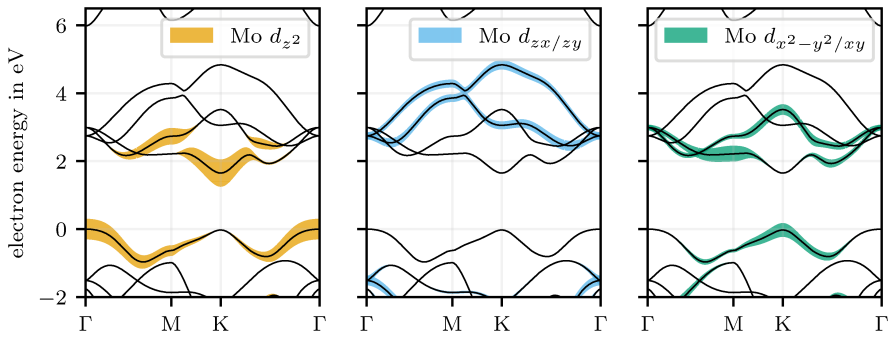

Figure III.1: *Projected density of states of MoS_2, k-resolved along the high-symmetry path. The height of the shown color belts indicates the orbital weight of the labeled transition metal orbitals. Domination of d_{z^2}, d_{xy} and $d_{x^2-y^2}$ in a three-band subspace around the band gap is clearly visible.*

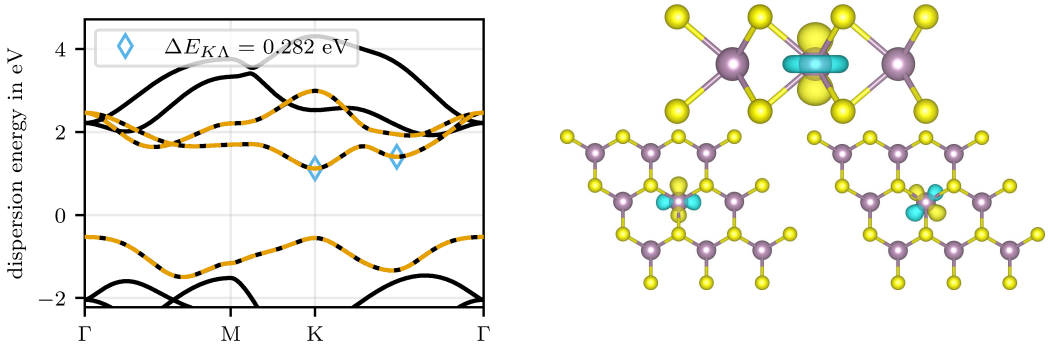

Figure III.2: *Wannier construction in monolayer MoS_2. The left plot shows the ab initio band structure on the left (black solid lines) with Wannier model (orange dashed lines) on top, where the energy difference between the conduction band K- and Λ-valley (blue markers) is given. On the right, the three resulting Wannier orbitals are depicted, showing clear resemblance of the initial projections to d_{z^2} and d_{xy/x^2-y^2} orbitals.*

$\Delta E_{K\Lambda}$ for selenium and the transition metals influence the extend of the energy differences. The optimized in-plane lattice parameter a_0 increases along the period of chalcogens whereas we see little influence of the transition metal due to changes appearing on mÅ level.

III.2 Force-constant model and phonon renormalisation

Section I.4 established the underlying theory of how force-constant models are extracted from DFPT calculations. Figure III.3 shows the phonon dispersion of the acoustic branches as they can be extracted from the force-constants. It comes to no surprise that the band width reduces with increasing atomic weight of the constituent atoms. In all materials shown here, the TA-mode crosses the ZA-mode around the M-point, where only for MoS_2, it crosses around the K-point again and rises in energy above the ZA-mode. This behaviour at the Brillouin zone boundary thus is unique. However, we observe identical behaviour for the LA-mode in WTe_2.

Due to the direct connection between force-constants and the dynamical matrix via a mass-coefficient, such models are an easy way to store information about lattice dynamics. It is possible to use *ab initio* theory (as lined out in section I.4) to perform a study of the influence doping has on the phonon dispersion. Here, however, we go a different path using a multi-particle approach as already introduced in section I.6.

We use the above established downfolded electronic model in order to construct an *ab initio* description of electron-phonon interactions for Wannier orbitals. By usage of the less complex electronic model, the matrix of electron-phonon coupling is reduced in size and complexity. As established in section I.6, adding charge carriers to the system, a screening of the Coulomb interaction as well as the electron-phonon coupling will be induced. This screening leads to

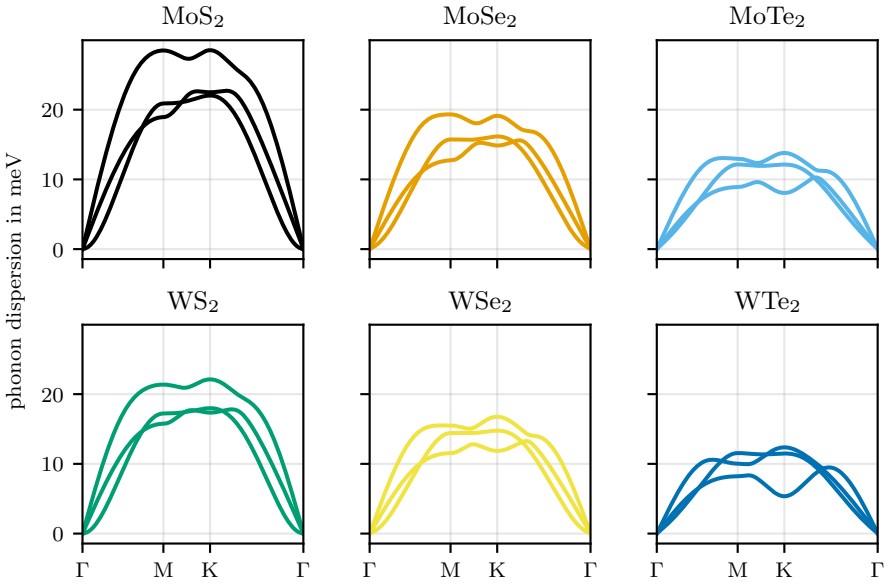

Figure III.3: *Phonon dispersion of monolayer TMDCs—material as indicated by the subfigure's title. A clear chemical trend of dispersion width reduction with increasing mass of constituent atoms is visible.*

significant renormalisation of the phonon dispersion. Often, if the phonon dispersion is pushed downwards in energy, this is referred to as phonon-softening.

Starting from the monolayer TMDCs without added charge carriers, the renormalisation can be tuned continuously. Here, we want tor restrict the doping level such that the renormalisation does not yet lead to imaginary phonon energies. Thereby, we keep the application of Eliashberg theory and the estimation of the critical temperature by McMillan's approach viable (see section I.7). Table III.1 lists the charge carrier density for which we observe the phonon-softening to imaginary phonon-dispersion indicative of a lattice instability as n_{inst}. In figure III.4 we show the renormalised phonon dispersions for MoS_2 for no doping as well as the doping levels of $0.14\,e^-/\text{u.c.}$ and $0.15\,e^-/\text{u.c.}$, where the softened M-phonon crosses into imaginary frequency range. We observe that the ZA phonon is unchanged by phonon renormalisation and the TA phonon shows small changes. In contrast to this, the LA phonon is renormalised the strongest. While the reduction around the K-point is pushing the LA branch below the other acoustic modes, this can still be viewed as a moderate change if compared to the extend of renormalisation visible around the M-point.

III.3 Monolayer materials and charge instabilities

It is well-established for TMDC materials, that charge-density wave phases (CDW) emerge upon adding charge carriers to the system [84, 85, 88, 91, 92]. As visible in figure III.4, the phonons in a given monolayer material continue softening upon doping the system further

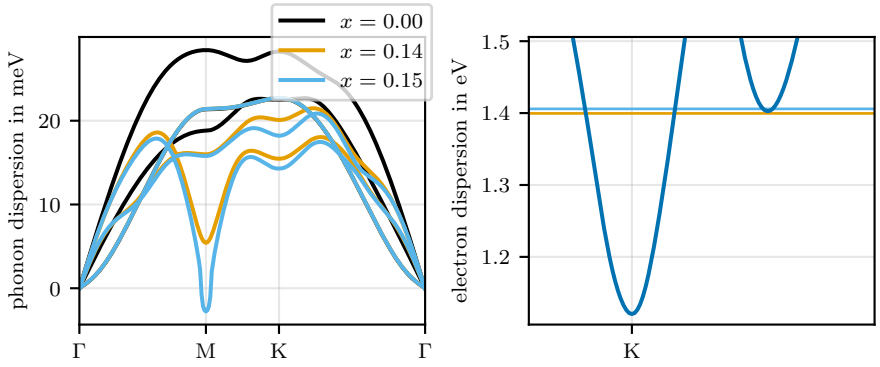

Figure III.4: *The left plot shows the renormalisation of the phonon dispersion in monolayer MoS_2 with varying doping level given by x in units of electrons per unit cell ($^{e^-}/_{\text{u.c.}}$). Around the M-valley, the softening of the LA and TA phonon mode is observed to be most prominent. The conduction band manifold close around the K and Λ valley and the Fermi level for the depicted doping levels indicated by horizontal lines is given in the right plot.*

and further. In the case of depicted MoS_2 monolayer, the softened M-phonon crosses the 0 meV line* for a doping between 0.14 - 0.15 $^{e^-}/_{\text{u.c.}}$ into "imaginary" dispersion range. These imaginary pockets are interpreted as lattice instabilities towards a more stable arrangement of atoms. For Γ-pockets a change of lattice constant or atom arrangement within the unit cell is to be expected. In contrast to this, M-pockets are attributed to the formation of a charge-density wave as a 2×2 superstructure.

In our case all monolayer materials show identical behaviour with respect to electron doping and induced phonon softening. In table III.1 we gather the range of doping levels for which the crossing towards the charge density wave instability is observed. The trend along the change of chalcogens is almost identical with the most stable structure involving sulphur. Changing the constituent transition metal appears to change the overall susceptibility towards phonon softening, i.e. tungsten based TMDCs are destabilised for less doping in general.

The correlation observable between the instability doping n_{inst} and the energy level of the two lowest lying valleys of the valence band $\Delta E_{K\Lambda}$ might be misleading in an interpretation with the idea that the population of the Λ-valley results in CDW-instabilities. However, upon inspection of the Fermi levels in the doped systems it becomes clear that this can not be true in a general sense. The Λ-valley is occupied only for WS_2 and in MoS_2 and WSe_2 first states can be populated upon doping into the CDW-instability. In contrast $MoSe_2$, $MoTe_2$ and WTe_2 have Fermi levels lying well below the Λ-valley, wherefore these electronic states are not occupied. Table III.1 lists the energy difference between Fermi level at the instability doping and the energy of the Λ-valley. We conclude here that it is scattering processes which create the CDW and they are not a Fermi surface effect with the opening of more Fermi pockets. Hence, CDW and SC are not mutually exclusive phenomena as already outlined in section I.7.

*The part of the phonon dispersion lying below this line comes numerically as imaginary solution due to the eigenvalues of the dynamical matrix ω^2 being negative.

Table III.1: *Energy difference of conduction band minima, instability level of electron doping and equilibrium lattice parameter in TMDC materials.*

material	$\Delta E_{K\Lambda}$ in eV	n_{inst} in $^{e^-}/_{\text{u.c.}}$	$\Delta E_{\Lambda\text{F}}^{\text{inst}}$ in eV	a_0 in Å
MoS_2	0.282	0.14 - 0.15	-0.003	3.186
$MoSe_2$	0.184	0.09 - 0.10	0.015	3.323
$MoTe_2$	0.258	0.12 - 0.13	0.015	3.572
WS_2	0.218	0.11 - 0.12	-0.032	3.187
WSe_2	0.150	0.05 - 0.06	0.003	3.323
WTe_2	0.326	0.07 - 0.08	0.099	3.575

III.4 Phonon-driven superconductivity in monolayers

Within figure III.5, we show once again the phonon dispersion of monolayer MoS_2 if doped with $0.14\,^{e^-}/_{\text{u.c.}}$. We add the information of electron-phonon coupling $|g^2|$ along the phonon branches as linewidth, standing in clear correspondence to the softening of M-phonons and K-phonons. From this depiction, we can analyse the electron-phonon spectral function α^2F for the corresponding doping value (red area) in the right subfigure. Only phonon density with significant coupling to electrons lead to peaks in α^2F, i.e. peaks do appear for instance from the orange and blue K-point with visible linewidth but not at the black branch. Further, upon increasing the doping, a shift towards lower phonon energies in α^2F is observable, which aligns with the continuous phonon softening as already seen in figure III.4. Additionally, the overall shift of the electron-phonon spectral function is observed in the evolution of $\omega_{\log}$ and $\omega_{2\text{nd}}$ as plotted in the lower left of figure III.6. From the evolution of $\omega_{\log}$, we determine that the center of the spectral function first moves to higher frequencies before it starts decreasing again when the phonon softening starts to dominate. $\omega_{2\text{nd}}$ gives us an intuition of how much the spectral weight is spread out. This decreases constantly for increasing doping, meaning that the spectral weight gets compressed to smaller frequency ranges. This behaviour is found in all investigated materials as can be seen in sections B.1 to B.5.

According to section I.7, we can now use our knowledge gained about the electron-phonon spectral function α^2F in order to determine the superconducting strength λ, the Einstein frequency $\omega_{\log}$ and the second momentum $\omega_{2\text{nd}}$. Figure III.6 contains the mentioned quantities for every electron doping in steps of $0.01\,^{e^-}/_{\text{u.c.}}$ until n_{inst} as indicated by the vertical dashed line. While the superconducting strength starts rapidly increasing for more than $0.1\,^{e^-}/_{\text{u.c.}}$, the logarithmic frequency average starts declining at the same time. Notably, the superconducting strength does not surpass the threshold of $\lambda \gtrsim 1.5$. Thus, the second momentum does not play a role here. Last but not least, the critical temperature for phonon-driven superconductivity is plotted for a range of screended Coulomb potentials μ^*, which are colour coded accordingly. As it can be expected by the steep rise of λ, the critical temperature curves approximately follow an exponential increase. Often, a value of $\mu^* = 0.15$ is assumed due to lack of a full an concise determination of the screening. We find a maximal $T_c = 13.5\,\text{K}$ for doping close to n_{inst}.

In table III.2 we gather all the just described parameters for the investigated monolayers. For all of them a clear decreasing trend along the chalcogen column in the periodic table of elements is visible, i.e. the superconductivity strength λ, the Einstein frequency, the second

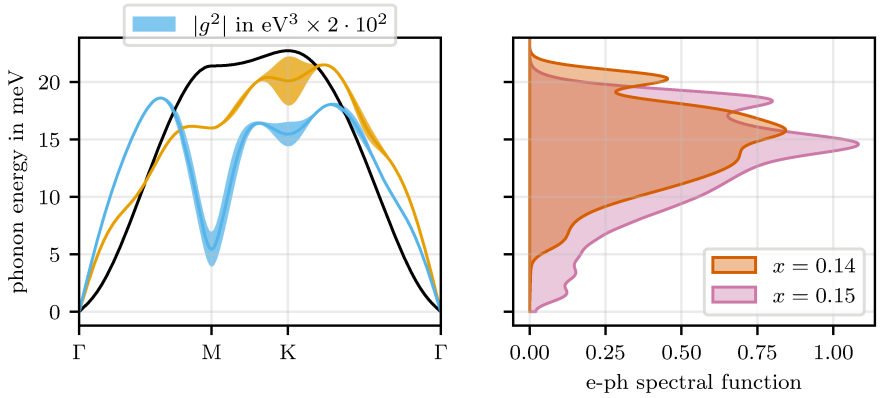

Figure III.5: *Phonon dispersion in monolayer MoS_2 for doping of $0.14\,^{e^-}/_{\text{u.c.}}$ is shown in the left panel, we add the information of electron phonon-coupling according to $|g^2|$ resolved in reciprocal space as linewidth of the phonon branches. The relation between softened parts of the phonon dispersion and coupling to the electrons is clearly visible. In the right panel, we depict the electron-phonon spectral function α^2F. The red and purple areas depict the shift of spectral weight towards lower phonon energies with increasing doping as can be judged by the movement of shaded area.*

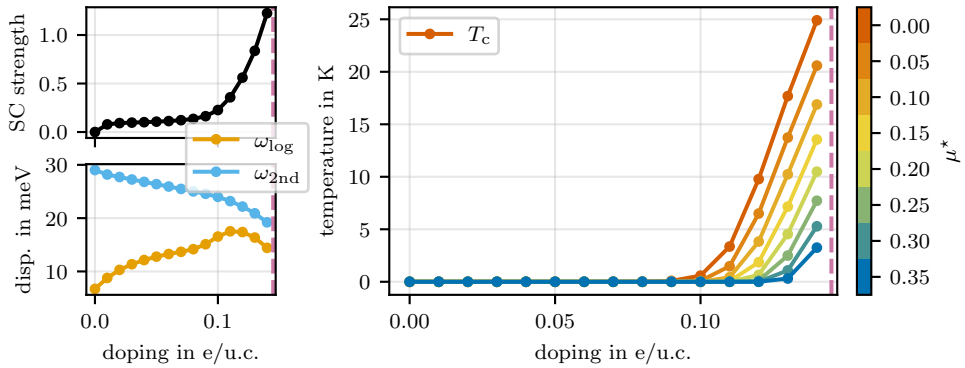

Figure III.6: *Curves of critical temperature for monolayer MoS_2. The upper left panel depicts the evolution of the superconducting strength λ with doping, where we observe a steep increase for more than $0.1\,^{e^-}/_{\text{u.c.}}$. In the lower left panel, the mode of the Einstein spectrum $\omega_{\log}$ and the second moment $\omega_{2\text{nd}}$ of the electron-phonon spectral function are depicted. The main panel shows curves of critical temperature for various correcting values of the Coulomb potential μ^*.*

Table III.2: *Critical temperature and parameters of electron-phonon coupling strength. The maximal critical temperature is extracted for $\mu^* = 0.15$ and all quantities are extracted at the highest doping just before the CDW instability.*

material	λ	$\omega_{\log}$ in meV	$\omega_{2\mathrm{nd}}$ in meV	$T_c^{\mathrm{max.}}$ in K
MoS_2	1.225	14.429	19.210	13.546
$MoSe_2$	0.883	8.844	13.297	4.434
$MoTe_2$	0.566	4,640	10.230	0.521
WS_2	2.618	8.125	13.647	18.634
WSe_2	1.680	4.650	8.135	6.759
WTe_2	0.259	5.490	9.560	0.000

moment $\omega_{2\mathrm{nd}}$ of the electron-phonon-spectral function α^2F and the critical temperature T_c are smaller in [M]Te_2 than in [M]S_2. The trend along the molybdenum-based TMDC monolayers stands in qualitative agreement with experimental findings of W. Shi et al [191]. In contrast to the chalcogen axis, heavier transition metals increase the superconductivity strength λ and the critical temperature T_c. Hence, we obtain the highest critical temperatures in WS_2 followed by MoS_2. For WTe_2 phonon-driven superconductivity appears to be suppressed entirely, i.e. $T_c = 0\,\mathrm{K}$.

III.5 Bilayer structures and assumption to the structure

Having established the physics present in monolayers of semiconducting TMDCs, we turn to the possibility os stacking two layers of them on top of each other. We will choose here from MoS_2, $MoSe_2$, WS_2 and WSe_2. This already gives a total number of ten bilayer materials. The combinations with identical materials are labeled as homobilayers whereas the ones with two different layers are called heterobilayers. By layering the materials, there are some configurations which are possible to form. Here we set the focus on so called AA, AB and BA stacking. Figure III.7 shows the mentioned stacking configurations. For homobilayers, AB and BA stacking are identical.

From the last column in table III.1 it becomes obvious that we will have to make some assumptions to the overall structure of the bilayers. In experiment one would have to either stack the two layers mechanically after exfoliation of monolayers. This comes with a mismatch in the lattice parameter between layers and unit cells will have hundreds or thousands of atoms in them. Here, we neglect this mismatch by using a unit cell with only six atoms, i.e. three per layer, and relax the structure on an *ab initio* level. It is noteworthy that this assumption corresponds to a possibility of growing the two layers on top of each other from the start.

For the scope of the thesis, we will not go beyond the stackings explained here, i.e. aligned bilayer structures. It is possible to anti-align the layers with respect to each other. Creating what is known as AA' stacking. In this configuration the hexagonal structure of both layers lies on top of each other and the transition metal of one layer is aligned with the chalcogens of the other layer—hence **anti**-alignment. In case it is possible to either align the transition metal or the chalcogen of one layer with the hexagon center of the other layer, aligning chalcogens with chalcogens (A'B) or metals with metals (AB').

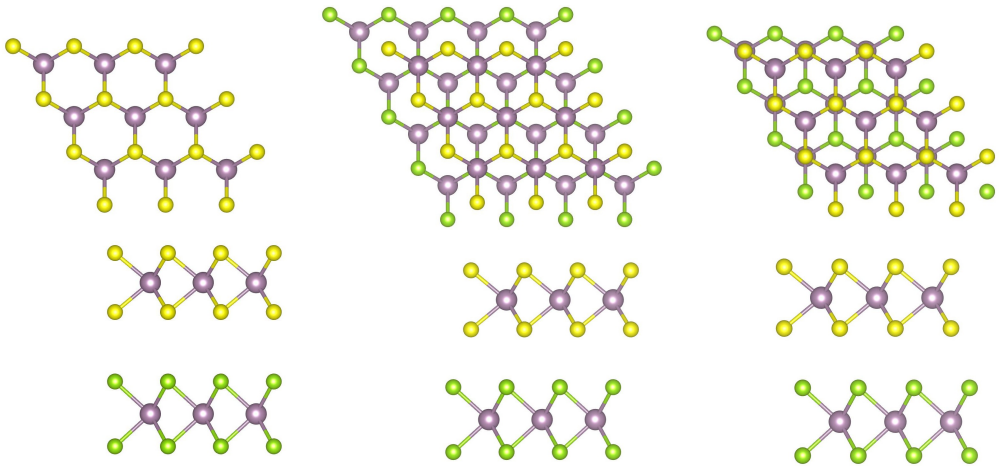

Figure III.7: *From left to right, the stacking configurations of bilayer materials are shown: AA, AB and BA. AA stacking is fully aligned; AB stacking has the metals of one layer in the hexagon center of the other layer as well as the chalcogens of the other layer in the hexagon center of the one layer, consequently one metal is aligned to sit on top of two chalcogens ; BA stacking changes the alignment of AB such that the previously aligned metal-chalcogen are now lying in the hexagon centers of the pairwise othe layer. For all pictures a* 3×3 *supercell was used.*

Due to the very low critical temperatures calculated for monolayer $MoTe_2$ and WTe_2 (see table III.2), we will exclude them from further discussion. Leaving us with a total of four monolayer materials. This results in eight homobilayer structures and 18 heterobilayer structures, listed in table III.3 and table III.4.

For the total of 24 bilayer materials, we do approximate the underlying model. On the purely electronic level, we perform a full *ab initio* band structure calculation and a subsequent Wannier construction in order to arrive at a downfolded electron-model. We use the same orbital projections per layer as before (d_{z^2}, d_{xy} and $d_{x^2-y^2}$; see figure III.2), which gives us a tight-binding description of each bilayer with six orbitals in total. In contrast to this, we do not perform full calculations within density functional perturbation theory for the phonons and neither go all the way to determine the electron-phonon coupling. Rather, we use the models obtained for the monolayers and combine them into a bilayer model. This assumption is based on the idea that appearing interlayer phonon modes, i.e. layer-breathing and layer-sheering modes [196], will not drive superconductivity in the systems. The system will only be interacting electronically this way.

III.6 Homobilayers

In a first step, we relax the bilayer materials on *ab initio* level, which gives us the insight that the stacking configuration of the bilayer will influence the material properties already, which becomes clear by comparing the lattice parameter a_0 between AA and AB stacking for each homobilayer in table III.3. One might expect that the AA-stacking configuration of the bilayers does not influence the lattice parameter as it can be seen by comparison with

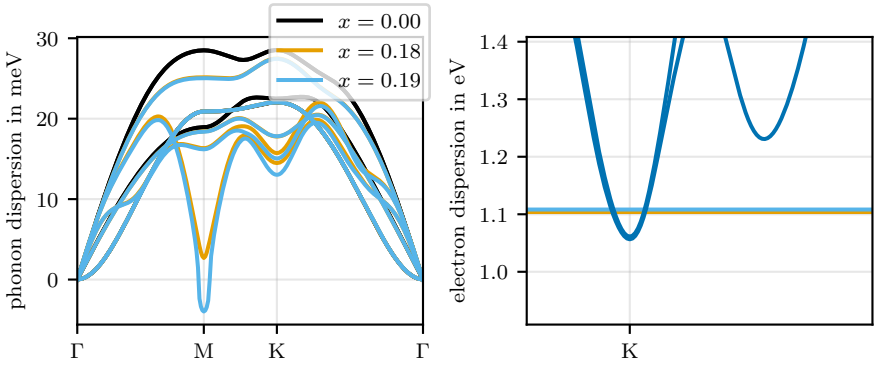

Figure III.8: *The left plot shows the renormalisation of the phonon dispersion in AA stacked MoS_2-Mo_2 with varying doping level. Around the M-valley, the softening of the phonon modes is observed to be most prominent. The conduction band manifold around the K and Λ valley and the Fermi level for the depicted doping levels indicated by horizontal lines is given in the right plot.*

table III.1. Interestingly, AB-stacking in contrast leads to a slight contraction of the crystal structure. An effect attributable to the alignment of "chalcogen pins" with hexagon empty space and "transition metal dips".

As mentioned above, we perform a Wannier construction projecting on a total of six orbitals. Similar to the monolayer materials, we get double the amount of conduction bands as we get valence bands, i.e. four and two. Using the phonons and the electron-phonon coupling as it can be constructed from the monolayer models, we can implement a renormalisation of the phonons under the influence of electron doping. For the example of AA stacked MoS_2-MoS_2, we find a instability doping n_{inst} of 0.18 - 0.19 $^{e^-}/_{\text{u.c.}}$ as visualised in figure III.8. Here, we also depict the phonon dispersion as it arises with no electron doping in black. It is identical to two copies of the monolayer phonons. Due to our approach of letting only the electrons of both layers interact with each other, we get a total of six accoustic phonons with 0 eV modes at the Γ-point. Once again, we can confirm here that the formation of a charge density wave is not correlated with the population of further electronic states in the Λ-valley since it is not reached by the Fermi levels as indicated by the horizontal light blue and orange lines in the right plot. Looking at the values determined in all homobilayers in table III.3, we see that AA stacking in S-based TMDCs and AB stacking in Se-based TMDCs is more stable against CDW formation.

We can further confirm that the softening of the M-point phonon comes with a strong electron-phonon coupling along the branch and the electron-phonon spectral-function α^2F shifts towards lower energies for higher doping (see figure III.9). Figure III.10 contains the full evolution of logarithmic-mean frequency $\omega_{\log}$ and frequency spread $\omega_{2\text{nd}}$ over the doping level. We observe once again a rapid fall-off towards the instability doping, while the electron-phonon coupling strength λ increases.

For all possible homobilayers, we list the final physical parameters in table III.3. In comparison with our findings for the monolayer materials, we observe an overall decrease in the electron-phonon coupling strength λ. The moments $\omega_{\log}$ and $\omega_{2\text{nd}}$ of the spectral function α^2F on the

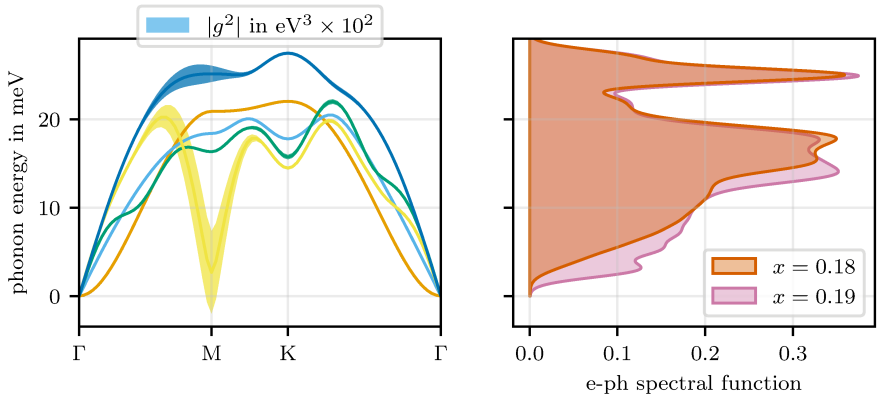

Figure III.9: *Phonon dispersion in AA stacked MoS_2-Mo_2 for doping of $0.18\,^{e^-}/_{\text{u.c.}}$ is shown in the left panel, we add the information of electron phonon-coupling according to $\left|g^2\right|$ resolved in reciprocal space as linewidth of the phonon branches. The relation between softened parts of the phonon dispersion and coupling to the electrons is clearly visible. In the right panel, we depict the electron-phonon spectral function α^2F in red for $x = 0.18\,^{e^-}/_{\text{u.c.}}$.*

other hand increase. This behaviour has its origin in the way the phonon-softening manifests here. Only one mode is affected the most, while others only change slightly as it becomes clear from looking at figure III.8. Thus, the spectral function α^2F is more spread out with higher $\omega_{2\text{nd}}$ and its center $\omega_{\log}$ is pulled upwards. The critical temperature T_c decreases rapidly for small λ, which can not be compensated by the larger frequency moments, leading to smaller values of T_c overall.

Table III.3: *Instability level of electron doping, equilibrium lattice parameter, superconductivity strength, Einstein spectrum frequency, second moment frequency and maximal critical temperature at $\mu^* = 0.15$ in TMDC homobilayer materials.*

material	n_{inst} in $^{e^-}/_{\text{u.c.}}$	a_0 in Å	λ	$\omega_{\log}$ in meV	$\omega_{2\text{nd}}$ in meV	$T_c^{\text{max.}}$ in K
MoS_2-MoS_2 AA	0.18 - 0.19	3.1855	0.830	13.629	20.771	5.861
MoS_2-MoS_2 AB	0.04 - 0.05	3.1569	0.693	15.063	20.681	3.800
$MoSe_2$-$MoSe_2$ AA	0.06 - 0.07	3.3230	0.502	11.370	17.099	0.670
$MoSe_2$-$MoSe_2$ AB	0.11 - 0.12	3.2876	0.682	12.073	15.254	2.877
WS_2-WS_2 AA	0.08 - 0.09	3.1874	0.710	11.061	17.702	3.022
WS_2-WS_2 AB	0.05 - 0.06	3.1606	0.559	14.939	20.676	1.578
WSe_2-WSe_2 AA	0.03 - 0.04	3.3227	1.091	4.479	9.087	3.483
WSe_2-WSe_2 AB	0.10 - 0.11	3.2892	0.752	9.030	12.291	2.945

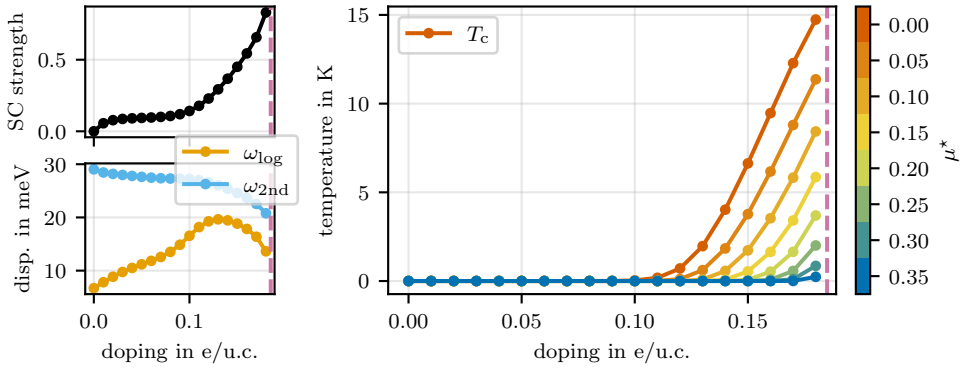

Figure III.10: *Curves of critical temperature for AA stacked MoS_2-MoS_2. The upper left panel depicts the evolution of the superconducting strength λ with doping. In the lower left panel, the logarithmic average $\omega_{\log}$ and the second moment $\omega_{2\mathrm{nd}}$ of the spectral function are plotted over doping. The main panel shows curves of critical temperature for various correcting values of the Coulomb potential μ^*.*

III.7 Heterobilayers

Switching the focus to more complex systems, we stack two different monolayers on top of each other. It is immediately clear from table III.4 that the stacking configuration here does influence the lattice parameter only slightly. However, we saw in table III.1 that the lattice constant is mostly determined by the constituent chalcogen atoms. Thus, it is rather counter-intuitive that the lattice parameter is shorter in MoS_2-WS_2 than it is in the corresponding monolayers and similar for $MoSe_2$-WSe_2. For all bilayer materials with a combination of sulfur in one layer and selenium in the other layer we observe a lattice constant of $a_0 \approx 3.22\,\text{Å}$. Hence, the chalcogens are most influential to the lattice constant once again.

The search for charge density wave reveals that compounds including selenium and tungsten tend to be less resilient, if not counteracted by molybdenum and sulphur, especially if combined as MoS_2. In contrast to the homobilayers we observe that the stacking order does not result in large variations of instability doping n_{inst} for most layer combinations. One deviation is present for MoS_2-WS_2 in AA-stacking to less resilience and for $MoSe_2$-WS_2 in AA-stacking to more resilience.

Turning our attention towards the critical temperature, we see that heterobilayers with identical chalcogen show highest $T_c^{\mathrm{max.}}$ for AA stacking. Whereas, for other heterostructures a trend towards AB stacking is favoured—the exception here is $MoSe_2$-WS_2 with AA stacking, which we attribute to the higher resilience against charge density wave formation.

III.8 Conclusion

We presented the study of the family of semiconducting monolayer TMDCs with respect to the question how strong electron-phonon driven superconductivity in these materials is and

Table III.4: *Instability level of electron doping, equilibrium lattice parameter, superconductivity strength, Einstein spectrum frequency, second moment frequency and maximal critical temperature at $\mu^* = 0.15$ in TMDC homobilayer materials.*

material	n_{inst} in $^{e^-}/_{\text{u.c.}}$	a_0 in Å	λ	$\omega_{\log}$ in meV	$\omega_{2\text{nd}}$ in meV	$T_c^{\text{max.}}$ in K
MoS_2-WS_2 AA	0.08 - 0.09	3.1572	1.414	12.670	17.816	14.697
MoS_2-WS_2 AB	0.12 - 0.13	3.1874	0.618	15.466	20.057	2.547
MoS_2-WS_2 BA	0.10 - 0.11	3.1587	1.196	13.029	18.268	11.804
$MoSe_2$-WSe_2 AA	0.07 - 0.08	3.2861	1.183	10.857	14.216	9.629
$MoSe_2$-WSe_2 AB	0.08 - 0.09	3.2885	1.146	10.598	14.119	8.919
$MoSe_2$-WSe_2 BA	0.09 - 0.10	3.2882	1.032	9.130	13.279	6.379
MoS_2-$MoSe_2$ AA	0.17 - 0.18	3.2174	0.596	13.139	17.855	1.857
MoS_2-$MoSe_2$ AB	0.19 - 0.20	3.2195	0.841	14.672	20.920	6.520
MoS_2-$MoSe_2$ BA	0.19 - 0.20	3.2198	0.639	15.234	20.819	2.864
WS_2-WSe_2 AA	0.11 - 0.12	3.2204	0.774	11.073	15.685	3.934
WS_2-WSe_2 AB	0.11 - 0.12	3.2219	0.854	10.942	15.694	5.046
WS_2-WSe_2 BA	0.10 - 0.11	3.2222	0.517	11.765	16.423	0.825
MoS_2-WSe_2 AA	0.19 - 0.20	3.2205	0.517	13.665	18.239	0.962
MoS_2-WSe_2 AB	0.20 - 0.21	3.2224	0.966	12.663	16.981	7.730
MoS_2-WSe_2 BA	0.19 - 0.20	3.2226	0.499	13.417	18.007	0.764
$MoSe_2$-WS_2 AA	0.16 - 0.17	3.2173	0.726	11.982	16.675	3.510
$MoSe_2$-WS_2 AB	0.12 - 0.13	3.2193	0.690	12.077	16.438	2.997
$MoSe_2$-WS_2 BA	0.13 - 0.14	3.2189	0.546	13.965	19.791	1.309

what kind of general trends appear among the different combinations of metals and chalcogens . It became apparent to us that lighter chalcogens , i.e. lower periods in the periodic table of elements, make for better tunability towards higher critical temperatures under electron doping due to higher electron-phonon coupling strength. Highest reachable temperatures in our approximations were 13.546 K in MoS_2 and 18.634 K in WS_2.

From there we decided to study bilayers of semiconducting TMDCs where only electronic interactions were allowed. This lead to the insight that homobilayer stacking suppresses electron-phonon coupling significantly. We find the highest critical temperature estimate for MoS_2-MoS_2 in AA configuration with 5.861 K. A trend within the critical temperature as it has for instance been seen for a charge density wave phase in $NbSe_2$ [49]. While for superconductivity in MoS_2 the opposite trend as documented by us has been observed [197], we attribute this to the naive approach of taking identical Coulomb potential correction μ^* for extraction of the critical temperature T_c. For results closer to experiment, often μ^* is now chosen to have higher values in monolayers than in monolayers due to the weaker dielectric screening and stronger Coulomb repulsion [198].

In heterobilayers, we find comparatively stronger electron-phonon coupling in some bilayer combinations. Most notably in MoS_2-WS_2 bilayers with 14.697 K in AA configuration and 11.804 K in BA configuration. Hence, the electron-phonon coupling strength and subsequent critical temperature for phonon-driven superconductivity stays highest in compounds involving mostly sulphur.

Table III.5: *Fundamental gap correction, instbility doping level and parameters of electron-phonon coupling as well as superconductivity in G_0W_0-corrected monolayers.*

material	ΔE_{gap} in eV	$\Delta E_{K\Lambda}$ in eV	n_{inst} in $^{\text{e}^-}/_{\text{u.c.}}$	λ	$\omega_{\log}$ in meV	$\omega_{2\text{nd}}$ in meV	$T_{\text{c}}^{\text{max.}}$ in K
MoS_2	0.909	0.165	0.12 - 0.13	2.129	12.975	17.760	23.984
$MoSe_2$	0.991	-0.051	0.09 - 0.10	2.151	9.669	12.698	17.953
WS_2	0.809	0.080	0.09 - 0.10	3.793	5.548	11.731	18.161
WSe_2	0.873	-0.136	0.12 - 0.13	2.012	8.258	10.835	14.357

With table III.3 and especially table III.4 we achieve a list of bilayer TMDCs with respect to CDW phase transition, superconductivity and a wide variety of possible crystal fields to choose from for engineering of electronic band structures. From a methodological point of few, we were able to build quantum lattice models of monolayer TMDCs on small 3-orbital models, where *a posteriori* doping was included to the model via many-body calculations and renormalisation. Additionally, we set up 6-orbital quantum-lattice models for TMDC bilayers including interlayer interactions in the electron sector only. We found that stable model predictions on phonon softening, possible transitions into a CDW phase and critical temperature curves for phonon-driven superconductivity as function of electron doping can be extracted. Thus, we enrich the model landscape for studying phonon-related properties of TMDC structure with minimal models. As a final remark, we would like to stretch that transition into possible CDW phases is not linked to the occupation of new valleys if doping is increased. Hence, this hints at the possibility that CDW and superconductivity are not mutually exclusive phenomena in semiconducting TMDCs.

III.9 One look beyond

Following the reasoning in section I.3, we extend our studies of monolayer materials by first correcting the electronic band structure within the GW-framework. As expected we observe an increase of the band gap within the material [199]. We list values determined for ΔE_{gap} in table III.5. Interestingly, for selenium-based TMDCs a change from a direct K-K band gap to a K-Λ band gap is observable. In addition, we see that the top valence band separates from the rest of the valence manifold. This is displayed for monolayer $MoSe_2$ in figure III.11.

The way we constructed the quantum-lattice models allows us to use the new electronic model in combination with the phononic model and the electron-phonon coupling. This means that on the model level, we implemented the effects of electron screening as described by GW physics. The updated electronic models influence directly how the phonon dispersion is renormalised for increased doping levels. The most significant change is a high resilience against charge density wave formation in WSe_2. The general structure of M-point instability however is not changed.

Comparing the parameters of electron-phonon coupling and superconductivity in table III.5 with the former values in tables III.1 and III.2, we see that the coupling strength λ is significantly increased for all monolayers. At the same time, the frequency moments $\omega_{\log}$ and $\omega_{2\text{nd}}$ drop a bit in comparison. In total, the critical temperature for $\mu^* = 0.15$ rises—in selenium based materials much more than in sulfur-based ones. Last but not least, by comparison of figures III.6

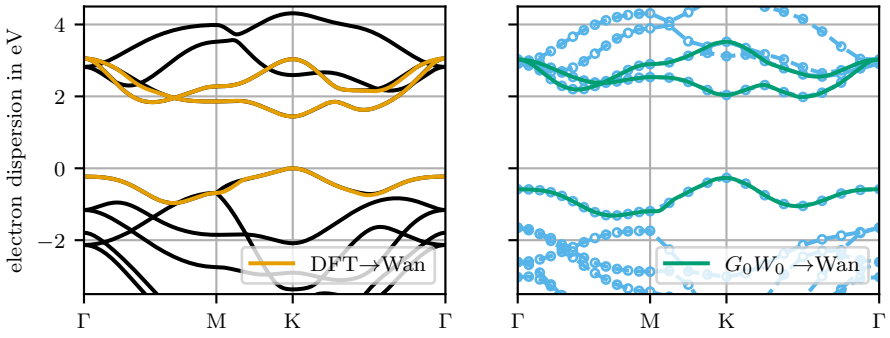

Figure III.11: *Electronic band structure of $MoSe_2$ monolayer as it can be obtained from directly from DFT and after correction by G_0W_0. Both versions are then downfolded to a three-band model via Wannier construction. The values of G_0W_0-corrected energy levels are indicated explicitly as they are calculated on a sparse path if compared with the DFT levels.*

and III.12 we see that the rise of λ and $\omega_{\log}$ for smaller doping levels directly results in a earlier increase of the critical temperature. At the same time a higher critical temperature is reached for doping levels just before the system goes into the charge density wave phase.

Here we see that already the change from Wannier tight-binding models based on *ab initio* density functional theory to such based on linear response many-body perturbation theory exhibit more notable electron-phonon physics. Namely, due to the correction of the electronic model by G_0W_0 energies, an increase in electron-phonon coupling strength is realised. This observation in our simple and straight-forward model application stands in line with efforts being made in the construction of GW perturbation theory (GWPT) in order to determine phonons and electron-phonon coupling in the same framework as the electronic structure [200, 201]. Thus, GWPT will be an analogous theory to density functional perturbation theory*.

III.10 Computational details

Density functional theory calculations were performed using the Quantum Espresso codes [10–12]. All calculations used a hexagonal Bravais lattice with lattice constant as listed in tables III.1, III.3 and III.4. The layers were artificially separated by $c = 15\,\text{Å}$ for monolayers and $c = 30\,\text{Å}$ for bilayers. Plane wave functions were cut at 100 Ry and no smearing was used. The pseudo potentials used the PBE functional [186]. Electron density and energy levels were determined on a dense $18 \times 18 \times 1$ Monkhorst-Pack grid. Density functional perturbation theory was carried out on a $6 \times 6 \times 1$ $\boldsymbol{q}$-grid.

The EPW code [41, 43, 44, 187] performed the Wannier construction (using Wannier90 [24, 27, 28]) and extrapolated the electron-phonon coupling matrix to a $60 \times 60 \times 1$ $\boldsymbol{k}$-grid and $30 \times 30 \times 1$ $\boldsymbol{q}$-grid.

*See for instance the efforts of the groups behind the Berkley code [201].

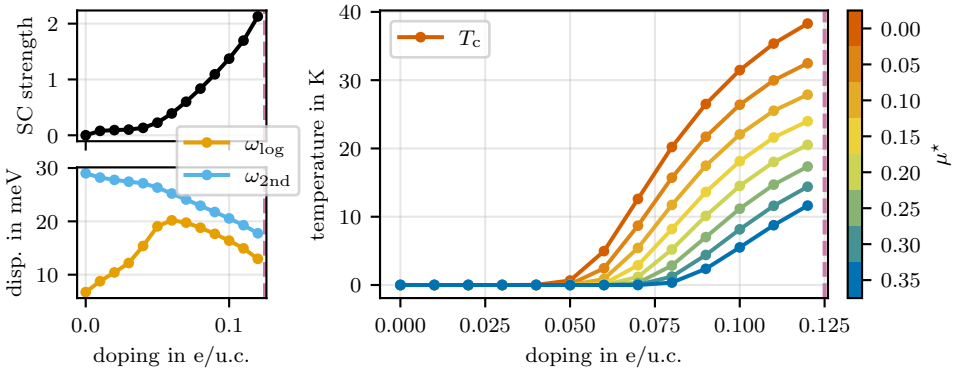

Figure III.12: *Curves of critical temperature for G_0W_0-corrected monolayer MoS_2. The upper left panel depicts the evolution of the superconducting strength λ with doping, with a rapid increase starting at $0.05\,^{e^-}/_{\mathrm{u.c.}}$. In the lower left panel, $\omega_{\log}$ and $\omega_{2\mathrm{nd}}$ of the electron-phonon spectral function are depicted. The main panel shows curves of critical temperature for various correcting values of the Coulomb potential μ^*.*

Renormalisation of phonons and calculations of Eliashberg electron-phonon spectral function as well as the critical temperature were carried out by using functionalities provided by the Python module elphmod [202]. The renormalisation calculations used a full $192 \times 192 \times 1$ k-grid and a irreducible $24 \times 24 \times 1$ q-grid with an electronic and phononic smearing of 0.015 eV. Force constant models were saved on a $6 \times 6 \times 1$ q-grid. Eliashberg calculations used a full $24 \times 24 \times 1$ k-grid and an irreducible $24 \times 24 \times 1$ q-grid as well as identical electron smearing and phononic smearing of 0.000 15 eV.

GW calculations as presented here were performed with the Yambo code [34, 203]. We used a "slab z" Coulomb cut-off geometry to account for the two-dimensional character of our materials, activated the random integration method for faster convergence and corrected seven valence bands and four conduction bands explicitly.

IV Interpolation approach to tight-binding models of twisted WSe_2

Come on let's twist again, like we did last summer
Yeah, let's twist again, like we did last year
Do you remember when, things were really hummin'
Yeah, let's twist again; twistin' time is here

Lyrics to the song ´Let's twist again' by Chubby Checker

It comes with little to no surprise that the electronic structure of a material is influenced by the lattice structure. In section I.11, we already laid out that for van-der-Waals materials there are several structural knobs and switches available to influence crystal on the nano scale. Influencing the structure in a rather continuous fashion is possible via the route of twisting two or more layers against each other. This influence is the core of what is called "twistronics"—twisting layered materials in order to influence and tune the electronic structure towards desired outcomes [204].

This field opened up when the first studies of twisted bilayer graphene were published. Here, R. Bistritzer and A.H. MacDonald described electronically flat bands in twisted bilayer graphene at an angle of 1.1° [205] and the measurement of superconductivity in this so called magic angle bilayer graphene (MATBG) by Y. Cao, P. Jarillo-Herero et al. [206]. The interest in this particular material is unbroken and new applications and findings are reported on a regular basis. The idea of using other van-der-Waals materials in order to study the physics of twisted, layered materials seems only natural. Here, we will address WSe_2 as exemplary material. Shown in figure I.1 already, twisted WSe_2 exhibits a rather rich phase diagram similar to MATBG [118], i.e. stripes of Mott-insulating phases alternating with domes of superconductivity. Pinning down the origin and final proof of the zero resistance states eluded the efforts of the authors and no claim of superconductivity could be made.

Quick effort and success was reported on the tight-binding modelling of TMDC materials, where work on monolayers and untwisted bilayers focussed on Slater-Koster-type hopping amplitudes [18, 207, 208] or a downfolding to 3 *p*-orbitals per chalcogen and 5 *d*-orbitals per transition metal were considered [209, 210]. These efforts were followed by first investigations of band structure modelling in twisted bilayer systems, e.g. a 2-band continuum model for twisted $MoTe_2$ by F. Wu et al. [211] and an adapted triangular lattice Hubbard model for twisted WSe_2 by J. Zang et al. [212]. A larger scale study on twisted heterobilayers involving MoS_2, $MoSe_2$, WS_2 and WSe_2 was carried out by V. Vitale et al. [213], who focussed once again on Slater-Koster-type modelling of hopping amplitudes. Last but not least, only a few

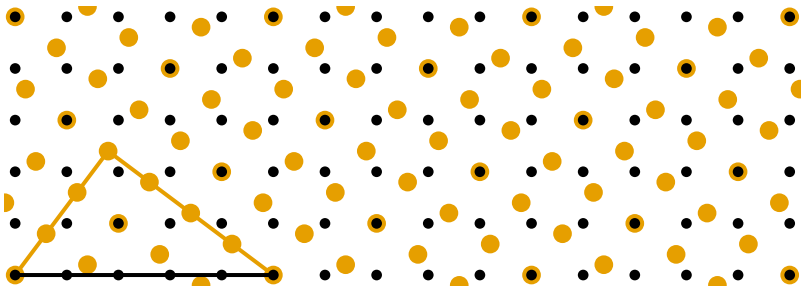

Figure IV.1: *Emergence of a moiré pattern upon twisting two square lattices against each other by 36.9°. Clear short-range periodicity is visible by spots, where the orange dots of one layer coincide with the black dots of the other.*

years back in 2024, V. Crépel and A. Millis published an article showing that after successfully setting up a tight-binding model for twisted homobilayers of TMDCs it is possible to perform a Wannier construction to capture essential physics with only a few orbitals inherent to the moiré lattice of the twisted system [214].

We set out on the idea that the superconductivity here might originate in electron-phonon interactions, i.e. it is phonon-driven superconductivity. Thus, the route of choice is almost identical to chapter III: define the individual parts of the model for electrons, phonons and their interaction. Here, we report on first efforts to interpolate a six-orbital downfolding in bilayer WSe_2. We will introduce central aspects of the spatial structure in twisted bilayer system in section IV.1 before turning to the description and study on how this spatial structure influences hopping amplitudes in section IV.2. Simultaneously, we set up the idea on how to construct tight-binding models of twisted bilayers from less-costly *ab initio* calculations. Section IV.3 will conclude our efforts and discuss results for non-corrugated twisted bilayers.

IV.1 Spatial features of twisted bilayers

Upon twisting two layers in a system against each other, the naive assumption would be that any periodicity is lost in the system. With a small thought experiment, we can already see that there is a chance to recover periodic structures. A Pythagorean triangle, i.e. cathetuses of length 3 and 4 and a hypotenuse of length 5, can easily be mapped to a bilayer system of two square lattices if seen from above. Imagine that in one layer, one walks along the hypotenuse for 5 unit cells. In the other layer, one walks along the first cathetus for 3 unit cells, turning by 90° on the square lattice and walking for 4 unit cells along the second cathetus. In both cases, one ends up in the same point in a two dimensional space. Figure IV.1 visualises this scenario with two square lattices in orange and black and an indication of the mentioned Pythagorean triangle. We note here that there is an even shorter periodicity arising. Upon close inspection the newly formed structure has a unit cell with $\sqrt{3}$ times the original square lattice parameter as can be deduced from the coinciding lattice points in the center of the indicated triangle.

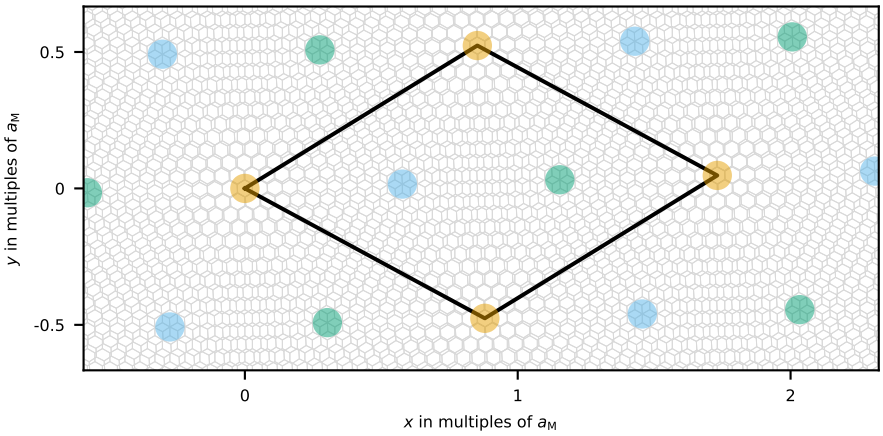

Figure IV.2: *Emergence of a moiré pattern upon twisting two hexagonal lattices (background) against each other by* 3.15°. *Orange shading indicates areas of stacking close to AA, blue and green indicate areas close to AB and BA respectively.*

Formalising this effect and conducting a large scale search for twist angles under which a new periodic structure is formed can be formalised. It is also not restricted to square lattice systems [215, 216]. Here we will investigate two hexagonal lattices of WSe_2 twisted against each other. In figure IV.2 we show the arising moiré structure for an exemplary twist angle of 3.15°. Upon analysing commensurate twist angles and the number of atoms in the resulting moiré unit cell, one can find the relation [216, 217]

$$a_\mathrm{M} = \frac{a}{2\sin(\theta/2)} \tag{IV.1}$$

between the length of the moiré cell a_M and original lattice parameter a as well as twist angle θ. This function defines a lower bound for a_M and correspondingly the number of atoms in the moiré unit cell.

In order to determine the twist angle for commensuration, we take a different route if compared to the prior ansatz of using geometric figures. We aim to align two vectors of identical length

$$\begin{aligned} &\boldsymbol{v}_1 = N\cdot\boldsymbol{a}_1 - \boldsymbol{a}_2 \quad \text{and} \quad \boldsymbol{v}_2 = (N+1)\cdot\boldsymbol{a}_1 + \boldsymbol{a}_2\,, \\ &\text{where} \quad \boldsymbol{a}_1 = a\begin{pmatrix}1\\0\end{pmatrix} \quad \text{and} \quad \boldsymbol{a}_2 = \frac{a}{2}\begin{pmatrix}-1\\\sqrt{3}\end{pmatrix} \\ &\text{with} \quad |\boldsymbol{a}_1| = |\boldsymbol{a}_2| = \sqrt{N^2+N+1}\,. \end{aligned}$$

We introduced here the integer $N \in \mathbb{N}$ and will refer to it as commensuration index. The above defined vectors point to two unit cells lying half the realised twist angle θ above and below the $\boldsymbol{a}_1$-direction. A straight forward calculation leads to

$$\theta = \arccos\left(\frac{N^2+N-\frac{1}{2}}{N^2+N+1}\right).$$

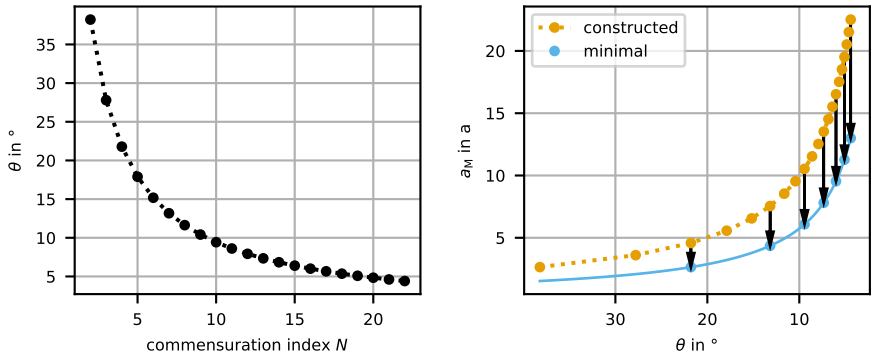

Figure IV.3: *Evolution of twist angle θ with increasing commensuration index N and moiré length of the resulting twisted bilayer. In the latter, the lengths according to the construction as well as the minimal lengths are indicated.*

One flaw of this construction protocol is shared with what we saw already in figure IV.1. In some instances, the lattice periodicity is shorter. As a byproduct lattice points of the two layers align within the assumed moire structure. Upon inspection, we see that for $\gcd(N-1,3)=3$ these smaller moiré cells are realised. The length of these cells coincides with the lower bound as defined in equation IV.1. In figure IV.3 we display the moiré length of our naive construction approach as well as the minimal lengths realisable.

Finally, one should ponder what happens to the system on a structural level after the twist is carried out. A clear answer to this question exists. Due to the locally varying stacking configuration, the interlayer separation distance will adapt accordingly and a corrugation of the bilayer accompanied by atomic reconstruction can be observed [218–221]. Thus, interlayer distance, lattice constant and binding angles change periodically on a local level.

IV.2 Lateral displacement

Taking a step back and looking at an untwisted bilayer system, it is possible to perform *ab initio* studies of the electronic structure not only at the high-symmetry stacking configurations laid out in section III.5 but also at any stacking configuration in between. We formalise the realisation of different configurations via a displacement vector

$$\boldsymbol{\delta} = \frac{\mu}{6}\cdot\boldsymbol{a}_1 + \frac{\nu}{6}\cdot\boldsymbol{a}_2\,,$$

with $\mu,\nu\in\{0,1,2,3,4,5\}$. We add this vector as a shift to the atomic positions of one WSe_2 layer and realise a total of 36 configurations. We depict subsequent *ab initio* calculation and Wannier construction identical to chapter III in figure IV.4. It is immediately clear that both manifolds undergo significant change upon lateral movement of the layers with respect to each other. Most prominently the variations around the K-point in the valence band and in the Σ-, K- and Λ-valley in the lowest conduction band will be of interest if systems will be doped slightly with electrons.

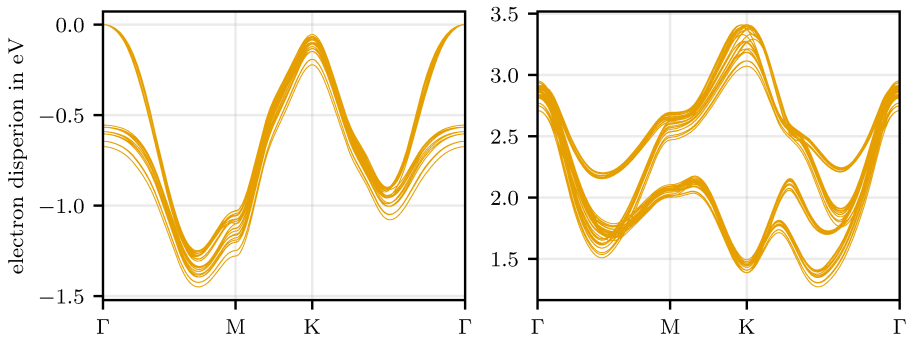

Figure IV.4: *Electronic dispersion in bilayer WSe_2 for the indicated 36 configurations of lateral shifting. All sets of bands are aligned to the respective highest occupied level's energy. Clear shifts of the energy levels in the valence manifold (left plot) and the conductance manifold (right plot) are visible.*

Now, combining the electronic downfolding to the d-type orbitals of tungsten and the accessibility of aligned bilayers in any stacking configurations, we will map out moiré cells of twisted bilayer WSe_2 in terms of local tight-binding models. To do so, we will first have to identify functional behaviour of the hopping matrix elements in the downfolded model [117, 165, 204, 209, 210, 218, 222]. We will use the indices $\alpha, \beta \in \left\{ d^{\mathrm{u}}_{z^2}, d^{\mathrm{u}}_{xy}, d^{\mathrm{u}}_{x^2-y^2}, d^{\mathrm{l}}_{z^2}, d^{\mathrm{l}}_{xy}, d^{\mathrm{l}}_{x^2-y^2} \right\}$ to identify simultaneously the d-orbital and whether it corresponds to the upper or lower layer in combination with the indices of the Wigner-Seitz cell i, j determining the direction and distance of hopping via $\boldsymbol{R}_{ij} = i \cdot \boldsymbol{a}_1 + j \cdot \boldsymbol{a}_2$:

$$t^{ij}_{\alpha\beta} \equiv t^{ij}_{\alpha\beta}(\boldsymbol{\delta}_{\mu\nu}) \tag{IV.2}$$

As a first step, we will have a look at the variation of the hopping parameters, if the displacement is fixed to lateral shifts. We distinguish between the intralayer parts of the hopping matrix and the interlayer parts, i.e. we split the 6×6-matrix in the orbital sectors into four 3×3 matrices [209, 210].

Figure IV.5 depicts on the left the matrix element of the on-site energy of d_{z^2}-orbital in the upper layer in the grid of the mentioned displacement raster. We extend the 6×6 raster in $\boldsymbol{a}_1$-direction and $\boldsymbol{a}_2$-direction in order to highlight the emerging periodic modulation since the boundaries match seamlessly together. As a green hexagon we indicate the Wigner-Seitz cell around the AA-stacking configuration. Thus, the black spots correspond to the case of AB-stacking, i.e the metal and subsequently the d_{z^2} orbital of the top layer is aligned with the chalcogen of the bottom layer (see figure III.7). Interestingly AA-stacking and BA-stacking show almost similar onsite energies, which we attribute to identical distance from the bottom-layer chalcogen. Similar behaviour can be observed for all combinations of the indices to $\mathbf{t}$. Hence, the intralayer terms can be described by the periodic modulation of a crystal field. We formalise this in a Fourier interpolation [218, 222–224]

$$\tilde{t}^{ij}_{\alpha\beta}(\boldsymbol{G}) = \frac{1}{N} \sum_{\mu\nu} t^{ij}_{\alpha\beta}(\boldsymbol{\delta}_{\mu\nu}) \exp(-\mathrm{i}\boldsymbol{\delta}_{\mu\nu}\boldsymbol{G}) \quad \text{with} \quad N = \#\{\mu\} \cdot \#\{\nu\}\,, \tag{IV.3}$$

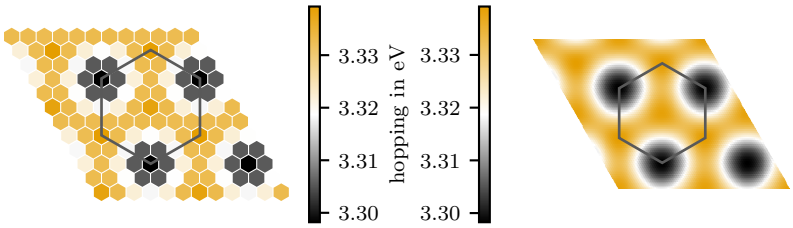

Figure IV.5: *Fourier interpolation of $d_{z^2} \to d_{z^2}$ intralayer hopping from the sampled grid to a continuum. The green hexagon indicates the extend of a Wigner-Seitz cell w.r.t the AA-stacked bilayer.*

where a set of $\boldsymbol{G}$ has to be chosen. Here we take $\boldsymbol{G}_{k\ell}$ with k, ℓ such that two hexagonal rings in reciprocal space are covered. Transforming back via

$$t^{ij}_{\alpha\beta}(\boldsymbol{\delta}) = \sum_{k\ell} \tilde{t}^{ij}_{\alpha\beta}(\boldsymbol{G}_{k\ell}) \exp(-\mathrm{i}\boldsymbol{G}_{k\ell}\boldsymbol{\delta}) \tag{IV.4}$$

allows for a free choice of $\boldsymbol{\delta}$, opening up the full space of displacements. Without loss of generality, we showcase in figure IV.5 how this interpolation to continuous $\boldsymbol{\delta}$ leads to a smooth surface for on-site $d_{z^2} \to d_{z^2}$ hoppping. Similar graphs can be drawn for any other combination of α, β, i and j.

Now, switching our attention to the interlayer hopping. The situation is a bit different in this case. Due to the binding of the two layers via electrostatic van-der-Waals forces, the hopping amplitude will follow a continuous function with a decaying hull. In figure IV.6, we depict this for interlayer $d_{z^2} \to d_{z^2}$ hopping. Due to the spatial structure of the involved d_{z^2}-orbitals, no angular structure in the evolution of the hopping amplitude can be observed. Since this is not the case for all combinations of orbitals (see figure IV.7), a continuous description of this kind of hopping can be achieved by means of splitting the radial and angular parts:

$$t_{\alpha\beta}(\boldsymbol{r}_{pq}) \equiv t_{\alpha\beta}(\rho_{pq}, \varphi_{pq}) = \sum_m c^{\alpha\beta}_m(\rho_{pq}) \exp(\mathrm{i}m\varphi_{pq}) \,, \tag{IV.5}$$

where $\boldsymbol{r}_{pq} = \boldsymbol{R}_{ij} + \boldsymbol{\delta}_{\mu\nu}$ combines the Wigner-Seitz vectors and the displacement into a continuous grid and recasts the index sets $\{i, j\}$ and $\{\mu, \nu\}$ into $\{p, q\}$. In order to determine the radial functions, we perform the inverse operation

$$c^{\alpha\beta}_m(\rho) = \sum_{\varphi_{pq}} t_{\alpha\beta}(\rho_{pq}, \varphi_{pq}) \exp(-\mathrm{i}m\varphi_{pq}) \Delta\varphi_{pq} \,, \tag{IV.6}$$

where the sampled hopping amplitudes are separated into slices of radii and the sum over angles is carried out over only those hopping amplitudes and corresponding angles in a given slice. The weights $\Delta\varphi_{pq}$ represent the Voronoi part of a full rotation along all realised angles. Depending on the width of the radius slice, an averaging effect takes place. As a final step, we model the real and imaginary part of the radial functions as polynomial with a Fermi hull and fit it to the obtained points:

$$c^{\alpha\beta}_m(\rho) \approx \frac{\mathrm{Pol}_\lambda(\rho)}{\mathrm{e}^{\sigma(\rho-\rho_{\mathrm{cut}})} + 1} \,, \tag{IV.7}$$

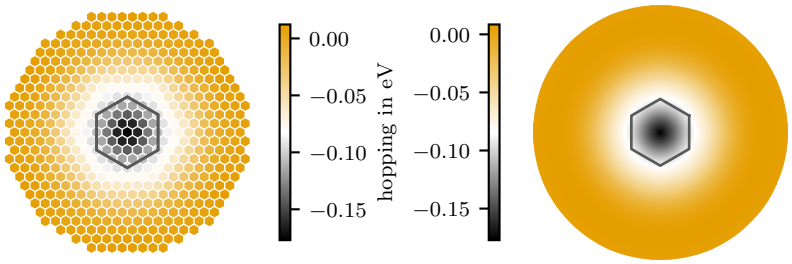

Figure IV.6: *Polar interpolation of $d^{\mathrm{u}}_{z^2} \to d^{\mathrm{l}}_{z^2}$ interlayer hopping from the sampled grid to a continuum. The green hexagon indicates the extend of a Wigner-Seitz cell w.r.t the AA-stacked bilayer.*

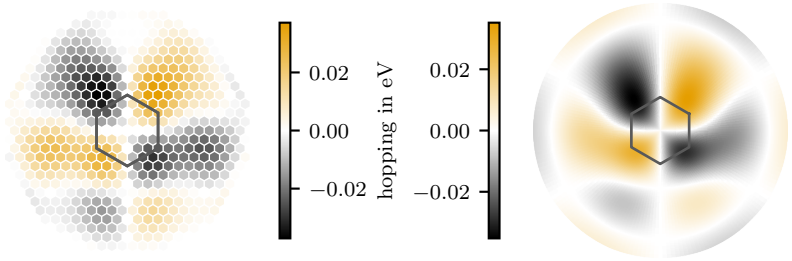

Figure IV.7: *Polar interpolation of $d^{\mathrm{u}}_{xy} \to d^{\mathrm{l}}_{x^2-y^2}$ interlayer hopping from the sampled grid to a continuum. The green hexagon indicates the extend of a Wigner-Seitz cell w.r.t the AA-stacked bilayer.*

where λ denotes the order of the polynomial, ρ_{cut} is the cut-off radius where the hull falls of and σ is the broadening of the fall-off.

Overall, the approaches for intralayer and interlayer hopping show close agreement. The shape of the spatial variation and the amplitude of the continuous version if compared to the sampled grid is clearly visible by the almost identical colour bars added in figures IV.5 to IV.7. With the above interpolation from a set of aligned structures to any rigid-shift displacement between two layer, we can take a look on the structure of a twisted bilayer.

Taking any pair of two orbitals present in the moiré cell of a twisted bilayer, we can determine a displacement vector between the two. in combination with the orbital type and the layer they are positioned in, we can determine all information necessary to plug into the interpolation functions from above. Thus, a full description of a tight-binding model in twisted bilayers can be inferred.

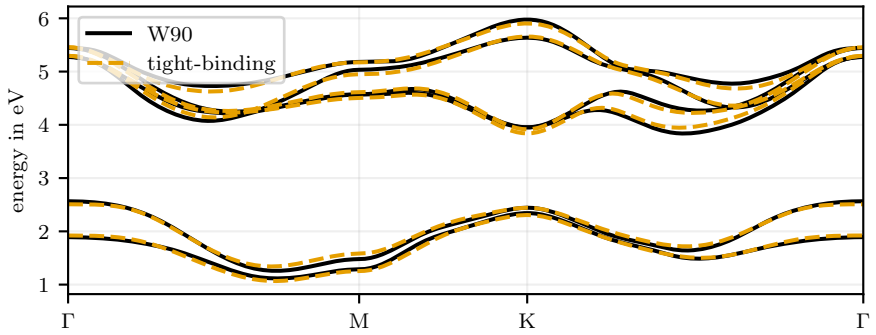

Figure IV.8: *Band structure of AA-stacked WSe_2 bilayer as it can be obtained from Wannier construction and our interpolation technique. Significant deviations are visible around the Λ-valley of the conduction band, while the general features are matched.*

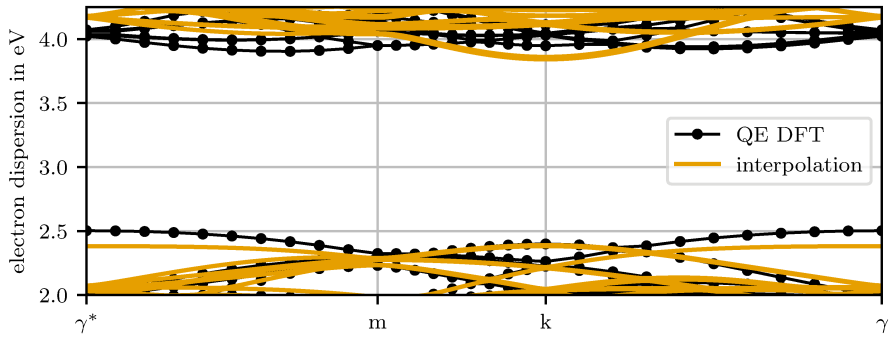

Figure IV.9: *Band structure of twisted WSe_2 bilayer. We depict large scale ab initio calculations and the dispersion obtained by interpolation. An overall qualitative match of the band structure can be seen in the valence manifold while the cunduction manifold is not reproduced beyond main features.*

IV.3 Flat bilayer systems

Now, having established a description of tight-binding elements depending only on the lateral displacement between two orbitals, we can try to describe moiré cells of various twist angles. We ant to draw the attention first to the trivial twist of 0°. The band structure of AA-stacked WSe_2 as obtained from Wannier construction and from our interpolation is shown in figure IV.8. Overall, we achieve good agreement. Yet, there are significant deviations in the conduction manifold around the Λ-valley and Σ-valley due to overestimation and around the K-valley due to underestimation. Hence, the energy difference especially between K-valley and Λ-valley is increased. Last but not least, we note that the energies of the top most valence band at the Γ-point are underestimated. This could not be resolved even after optimisation of the interpolation routines.

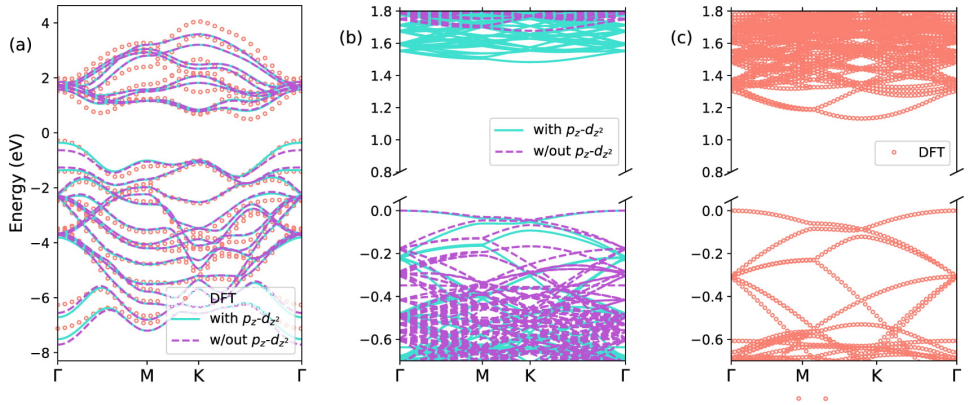

Figure IV.10: *Comparison of ab initio band structure and two constrcuted tight-binding models in untwisted AA-stacked MoS_2 (a) and twisted MoS_2 at $\theta = 7.3°$ (b) and (c). Taken from Vitale et al. [213] (CC BY 4.0)*

Figure IV.9 shows the band structure of twisted WSe_2 for a twist angle of 13.17°. The previously already observed shortcomings of the interpolation in the untwisted bilayer are further manifested here. We show the band structure as calculated along the reciprocal space path $\gamma^* - m - k - \gamma$, where the lower case letters emphasize the smaller size of the Brillouin zone of the twisted bilayer if compared to the aligned case and correspond in their meaning to the upper case letters. The valence band energies around the γ-point are underestimated just like the conduction band around the k-point. The overestimation of Λ- and Σ-valley in the conduction manifold extend to the γ-point as well now. While these deviations are of course clearly visible, we can also note that the overall structure of the top valence bands is matched qualitatively. Comparing our results and the match to *ab initio* calculations with work done by V. Vitale et al on twisted MoS_2, which we reproduce in figure IV.10, we see that similar matching of the valence manifold edge is possible. Further, we reproduce the conduction manifold edge closer in energy range while V. Vitale et al. [213] capture the structure better. Thus, good agreement is found with both approaches while more precision work has to be carried out at this point.

IV.4 Outlook

So far we found from literature and our own approaches that most interpolated band structures of twisted TMDC bilayers do agree at least qualitatively with the ones obtainable from *ab initio* calculations. While the approach of interpolating the tight-binding with various complexity is fruitful, i.e. we obtain decently detailed and matching result, further work and improvement on energetic precision has to be done. We speculate that the interpolation as discussed in section IV.2 and shown visually in figures IV.5 to IV.7 can be further improved. On one hand especially the energy scales do match closely while on the other hand cuts in the Fourier transform of intralayer hopping and averaging effects in the construction of the radial parameter for the interlayer hopping may sacrifice minor spatial resolution and subsequently lead to predictions not precise enough for the desired outcome.

Table IV.1: *Fractional coordinates of all atoms in the aligned WSe_2 bilayers. n_i are coefficients to the lattice vectors $\boldsymbol{a}_i$ and the integers μ, ν define the displacements realised.*

atom	n_1	n_2	n_3
Se	$1/3$	$2/3$	0.659349
W	$2/3$	$1/3$	0.605974
Se	$1/3$	$2/3$	0.552581
Se	$1/3 + \mu/6$	$2/3 + \nu/6$	0.447433
W	$2/3 + \mu/6$	$1/3 + \nu/6$	0.394040
Se	$1/3 + \mu/6$	$2/3 + \nu/6$	0.340665

Additionally, the idea of interpolation has to be extended beyond the lateral displacement of one layer with respect to local variation of interlayer distance due to corrugation effects. Hence, the full three dimensional shift and repositioning of any aligned bilayer configuration should be accessible in order to make predictions for real-world settings. Due to the continuous nature of the above established displacement field it stands to reason that the electronic structure of the system is going to be influenced in a continuous fashion as well.

Summa summarum, we can say that here we have proven the applicability of interpolating minimal 6-orbital tight-binding models in aligned TMDC bilayers to the use-case of twisted bilayer structures. Thus, a full treatment of chalcogen p-orbitals and transition metal d-orbitals is not necessary any longer. This effectively reduces the model by 16 orbitals or equivalently a factor of $6/22$.

IV.5 Computational details

Data generation of aligned WSe_2 bilayers was carried out in 36 *ab initio* calculations using the Quantum Espresso software package [10–12] and Wannier90 [24, 27, 28]. We employed the PBEsol functional, used a dense $18 \times 18 \times 1$ unshifted Monkhorst-Pack grid with $E_{\text{cut}} = 90\,\text{Ry}$, a conversion threshold of 1×10^{-10} and Methfessel-Paxton smearing with width $7.5 \times 10^{-5}\,\text{Ry}$. We used the predefined Bravais lattice index 4 for hexagonal lattices and set up the fractional coordinates as listed in table IV.1.

V Silicon adsorbate structures

改善

A central budo philosophy. 「かいぜん」, *read as "kaizen"; Continuous, small and consistent improvements applied to every aspect of training, fostering lifelong growth in skill, character and discipline.*

In contrast to the above discussed material class of transition metal dichalcogenides, we want to draw the attention to silicon carbide now. Similar to other 2D materials, a wide range of possibilities exist for usage of SiC. Already seen in the polytypes of SiC, infrared optical properties and infrared-active phonons modes exist with significant [225]. This reveals a rather interesting property of SiC because it opens up the possibility to control samples externally. Driving IR-active phonons in order to control atomic structure is an established route to induce lattice displacements and transient phases in condensed matter. It is possible due to resonant excitation and exploitation of anharmonic coupling to other structural coordinates [39, 226–229]. As a consequence of the structural influence, the electronic structure will be influenced as well.

Similar to graphene as touched upon in section I.11, SiC can be used as a host and substrate in a rich zoo of combinations with other materials. Among these is epitaxy and related influence of the SiC substrate on band gaps in graphene, group III-N membranes [230, 231]. The former of which can even be extensively studied when rare-earth metals are intercalated between

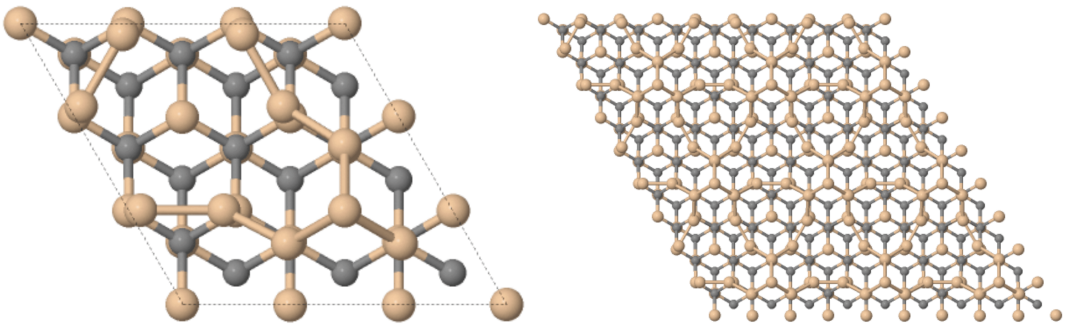

Figure V.1: *Top view of silicon-rich SiC—left as unit cell and right as* 3×3 *super cell structures. In the lower right half of the unit cell structure, the Si-tetramer is seen from above. In this view, it becomes clear that the adsorbate structure pushes the surrounding six silicon top-layer atoms outward, forming the pattern better visible in the super cell on the right.*

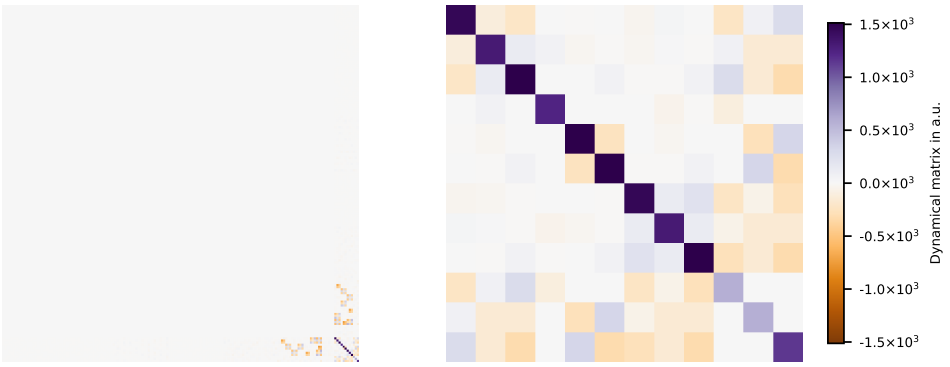

Figure V.2: *Visualisation of the dynamical matrix if restricted to linear response in the silicon tetramer only. Left: Full matrix including all not calculated entries. Right: Cut-out of the dynamical matrix corresponding to the entries connecting the four tetramer atoms.*

the SiC substrate and the graphene sheet, leading to functionalisation and band structure tuning [232–234].

Right here, we will have a first look on what might be referred to as overgrowing a SiC crystal. To be more precise, it is possible to saturate the SiC surface with an additional layer of Si and even over-saturating it. So called silicon-rich SiC is created. Crystallography studies [235, 236] were carried out and determined that a tetramer of silicon forms in a 3×3 supercell of SiC (see figure V.1 for a top-down view of the system). It is this tetramer adsorbate, its connection to the band structure of the material and the possibility of controlling the band structure by IR-pumping, which we want to understand here.

V.1 Estimation of oscillatory frequencies

In order to understand the tetramer's oscillation patterns and frequencies, we turn to DFPT (as introduced in section I.4) once again. Here, we would have to deal with a total of 58 atoms in a linear response calculation—which would lead to a 174×174 dynamical matrix. Within a linear response approach, we would determine the reaction of all 57 atoms, if one atom is moved slightly. Due to the on-top positioning of the Si-tetramer, we expect to see little to no response of atoms far away from the adsorbate structure. Thus, we reduce the complexity of the calculations carried out by neglecting the bulk silicon and carbon atoms as well as the added hydrogen atoms*.

We start from the symmetric structure of the tetramer and adlayer as given in references [235, 236]. After relaxing the structure, we find an equilibrium as depicted in figure V.1. The tetramer on top of the adlayer pushes the surrounding silicon atoms in an outward direction if seen from the tetramer (lower right of the left subfigure), which fully agrees with the crystallographic findings.

*These hydrogen atoms act as saturators for so called dangling bonds and passivate the lower edge of the crystal.

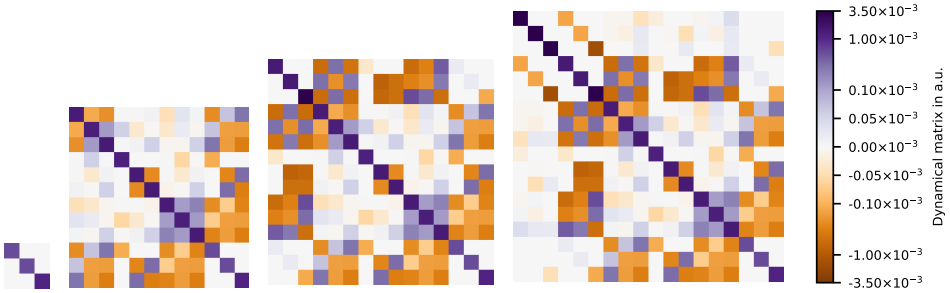

Figure V.3: *Visualisation of the dynamical matrix from atom-restricted DFPT calculations. From left to right, the dynamical matrix of the tetramer tip, the tetramer, the triangular pentamer and a connection of the latter into the SiC bulk is depicted.*

In order to reduce complexity and the usage of computational resources, we restrict the number of atoms for which the linear response calculation is performed. Figure V.2 shows the resulting dynamical matrix, if only the four atoms in the tetramer are considered. Looking at the full matrix (left plot in figure V.2), we see that the lower right block, where the entries of the four silicon atoms interacting with each other is visible in dark purple. A zoomed in version (depicted to the right) reveals—besides the purple diagonal—contributions of lower amplitude. An additional feature of figure V.2 is visible in the rows above the tetramer block and the columns to the left of it. DFPT as it is coded in Quantum Espresso [10–12] calculates the full linear response to the chosen subset of atoms. In physical terms this shows how the tetramer interacts with the silicon adlayer and the silicon carbide bulk. On the upper right of the full dynamical matrix, no entries are calculated. Thus, this block remains colourless and no information on the interaction within the adlayer and bulk is extracted. Based on the comparably small amplitude of these entries connecting the tetramer with the bulk, we aim for a suitable cut of the dynamical matrix. Figure V.3 shows (from left to right) the cuts to 1, 4, 5, and 6 atoms. One atom correspond to the tetramer tip, four atoms correspond to the tetramer, the fifth atom corresponds to the silicon atom of the adlayer lying directly under the center of the tetramer and the sixth atom is the continuation of this line to a silicon atom in the SiC bulk.

In a straight-forward diagonalisation, we can extract the oscillation frequencies. We depict in figure V.4, the evolution of calculated frequency eigenvalues, corresponding to the dynamical matrices visualised in figure V.3. While there is significant change upon including the fifth atom (going from the tetramer to the triangular pentamer structure), the connection into the SiC bulk adds lines rather than changing the existing ones. Hence, we choose to analyse the oscillation patterns to the cut dynamical matrix including the five silicon atoms of the pentamer.

V.2 Oscillations of the silicon adsorbate

Diagonalisation of the dynamical matrix gives direct access to the oscillation frequencies of phonon modes as well as eigenvectors related to it. In combination with the statistics of bosons,

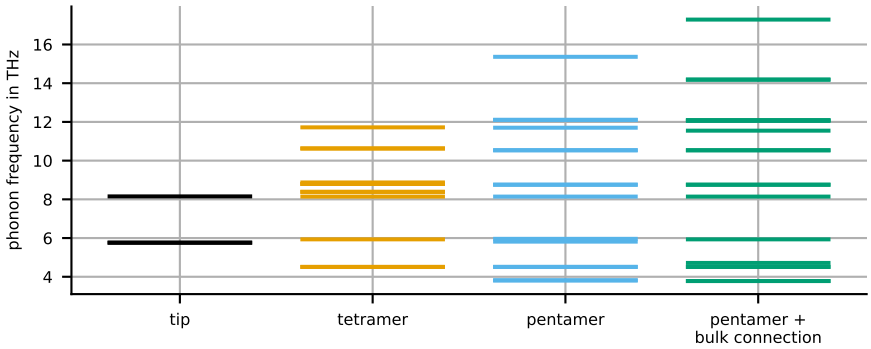

Figure V.4: *Oscillation frequencies of the silicon tetramer with increasing consideration of silicon atoms. While there is significant change observable between the tip, tetramer and pentamer spectrum, the inclusion of a connection to the bulk only minimally shifts existing lines between* 3 *and* 13 THz *but adds lines.*

we can determine the mean square displacement as

$$\left\langle \left| u_\nu^\alpha(jl,t) \right|^2 \right\rangle = \frac{\hbar}{2Nm_j} \sum_{\boldsymbol{q}} \frac{1+2n_\nu(\boldsymbol{q},T)}{\omega_\nu(\boldsymbol{q})} \left| e_\nu^\alpha(j,\boldsymbol{q}) \right|^2 .$$

This way, we obtain for all phonon modes ν three cartesian displacements α for every silicon atom considered j. The reciprocal lattice is restricted to $\boldsymbol{q} = \boldsymbol{\Gamma}$ and we set the temperature arbitrarily to $T = 300\,\mathrm{K}$. We restrict the dynamical matrix to the five silicon atoms of the pentameral structure.

After diagonalisation, we extract the mean square displacement and take the square root in order to achieve measurements for displacements. In figure V.5 we depict the in-plane rotational oscillation pattern at $\omega = 8.14\,\mathrm{THz}$. The five silicon atoms of the pentamer structure are highlighted as larger orange dots, whereas all other silicon and carbon atoms are shown as small black spots. With light blue and green arrows, we indicate the oscillation of the silicon atoms. Identical colours are equivalent to a movement with identical phase. Thus, for the pattern shown a clockwise motion for arrows in light blue and counter-clockwise motion for arrows in green is depicted.

The infrared laser within the experiment will be propagating along the z-axis. Therefore, oscillation in the THz regime with in-plane motion are favourable for pumping. All 15 modes of the pentamer lie in range for pumping and are infrared active by their symmetry. Table V.1 lists all modes with pattern labels descriptive of the observed motion and their frequencies. Out of the listed modes, we find that the squeezing movements at 8.76 THz (see figures E.7 and E.8) and the rotational movement at 8.14 THz as depicted in figure V.5 are purely in-plane. Additionally, modes at 12.11 THz (see figures E.2 and E.3) have dominanting in-plane oscillation patterns.

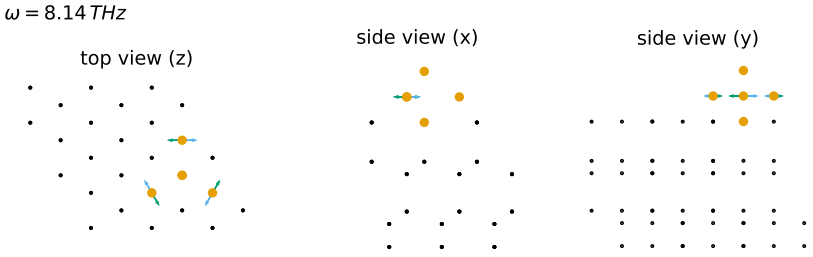

Figure V.5: *In-plane rotational oscillation pattern of the triangular pentamer structure in silicon-rich SiC with frequency* 8.14 THz*. Mean displacement is plotted as arrows in light blue and green and elongated by a factor of 2.5.*

Table V.1: *Oscillation patterns and frequencies of the silicon pentamer structure. Pattern labels are chosen descriptively of the motion.*

pattern	ω in THz	pattern	ω in THz	pattern	ω in THz
base vertical	15.36	top x-tilt	10.54	vertical breath	5.82
base x tilt	12.11	x squeeze	8.76	tip y tilt	4.51
base y tilt	12.11	y squeeze	8.76	tip x tilt	4.51
tetramer breath	11.70	rotation	8.14	x breath	3.81
top y tilt	10.54	all vertical	5.96	y breath	3.81

V.3 Outlook

Further investigation into silicon-rich SiC should be performed by means of nonlinear phononics as a route towards controlled structural manipulation. In experiments often a pumping of 5 - 10 % of the oscillation amplitude can be reached. This may include the modulation of electronic surface states, resonant surface bands, charge transfer and surface conductivity [227, 237, 238]. A different path may lead to structural switching and the drive into metastable configurations [239]. Last but not least the system may proof interesting as a hub for phonon-polariton interactions [240, 241].

Beyond these ultrafast avenues, silicon-rich SiC also represents a promising platform for quantitative theory to experiment comparison. The silicon tetramer and the localised nature of its vibrational modes make the system suited for *ab initio* studies of anharmonic force constants and phonon lifetimes within the framework of DFPT. Such characteristics allow the adlayer to serve as a microscopic test case for surface non-linear phononics, where localized degrees of freedom can be selectively addressed by mid-infrared driving [242, 243].

Within the above detailed discussion, we were able to identify and list a range of IR-active phonons modes in the silicon tetramer in silicon-rich SiC. Handing over this acquired knowledge to experimentalist, we are able to guide the efforts of finding suitable ranges for the wavelength of the IR-pump as well as determining oscillation modes most responsive to incident direction perpendicular to the SiC substrate.

Right now, we hand over our results as a rough guidance for first measurements to the experimental physics research group "Ultrafast Electron Dynamics" headed by Prof. Dr. I. Gierz in Regensburg. It serves as a first step towards a new collaboration on additional prototypical model strategies on electron-lattice effects.

V.4 Computational details

Density functional theory calculations were performed using the Quantum Espresso codes [10–12]. All calculations used a hexagonal Bravais lattice with lattice constant $a = 9.2847\,\text{Å}$ and $c = 30.0\,\text{Å}$. Plane wave functions were cut at $80\,\text{Ry}$ and Fermi-Dirac smearing with $\sigma = 1 \times 10^{-3}\,\text{Ry}$ was used. The pseudo potentials used the PBE functional [186]. Electron density and energy levels were determined on a $6 \times 6 \times 1$ Monkhorst-Pack grid. Density functional perturbation theory was carried out as a Γ-point only calculation.

VI Closure

サイエンス　イズ　エレガント。
Science is elegant.

Xeno Houston Wingfield in Dr. Stone

What preceded followed a sequence of questions rather than a predefined destination. Along the way, different materials, models, and levels of description were brought into focus, sometimes to confirm expectations, sometimes to quietly dissolve them. What remains at the end is not a single result, but a pattern: that carefully chosen approximations, when guided by physical intuition and material realism, tend to reduce apparent complexity. Making science truly elegant.

Chapters II and III focus on electron–phonon interactions in transition metal dichalcogenides, moving from specific questions to more general modelling frameworks. In chapter II, experimentally motivated claims of polarons in metallic MoS_2 are examined using a combination of *ab initio* calculations and many-body approaches beyond simple perturbation theory. The analysis shows that, the formation of monopolarons can be excluded while a lattice distortion can be stabilised in a downfolded model with multiple charge carriers. Thus, offering an interpretation of the origin of measured scanning tunnelling spectra. Chapter III extends the discussion to mono- and bilayer TMDC systems. By constructing downfolded quantum-lattice models derived from first principles, phonon-mediated superconductivity is analysed across a wide range of materials and stacking configurations. The results highlight how stacking and layer composition influence renormalisation of lattice dynamics and superconducting tendencies under doping. Simultaneously, it is demonstrated that physically meaningful effective models can be formulated without explicitly retaining interlayer phonon modes.

Chapters IV and V broaden the perspective beyond pristine, aligned systems. Chapter IV addresses twisted bilayers of WSe_2 and introduces a scalable interpolation approach for tight-binding models in large moiré supercells based on *ab initio* calculations of aligned bilayers. The spatial structure of the resulting hopping processes is analysed in detail, providing a practical framework for studying electronic structure in twisted systems where direct first-principles calculations become infeasible. Chapter V turns to adsorbate-induced lattice dynamics and investigates vibrational modes of a silicon adsorbate on silicon-rich SiC using density functional perturbation theory. By identifying infrared-active oscillations, this chapter illustrates how local modifications can be used to probe and control lattice degrees of freedom, complementing the earlier focus on layered and extended systems.

Looking ahead, there are several routes to take and dive deeper into the field, some of which we already touched. Starting off, moiré-induced flat bands and correlation effects in twisted TMDCs are emerging as tunable platforms for Mott physics, Wigner crystallisation and correlated insulators [167, 168, 244]. In terms of the electron-phonon coupling, increasing

focus is set on regimes where phonons cooperate or compete with Coulomb interactions rather than acting as a weak perturbation [245]. Material design with respect to heterostructures investigates correlations as tunable via stacking order, interlayer hybridisation and dielectric environment mostly in twisted moiré heterobilayers [244, 246]. Lastly, steps beyond the single-particle descriptions are taken with growing use of *GW* approaches, dynamical mean field theory and hybrid approaches combined with downfolded models to capture strong-correlation effects quantitatively [201, 247].

Appendix

A Full text publication of van Efferen et al.

Here we provide for the sake of completeness the full-text publication of [48]. My personal contributions beyond discussions and contributing to the writing process are detailed in chapter II.

Inelastic Tunneling into Multipolaronic Bound States in Single-Layer MoS_2

Camiel van Efferen,[1] Laura Pätzold,[2] Tfyeche Y. Tounsi,[1] Arne Schobert,[2] Michael Winter,[2] Yann in 't Veld,[2] Mark Georger,[1] Affan Safeer,[1] Christian Krämer,[1] Jeison Fischer,[1] Jan Berges,[3] Thomas Michely,[1] Roberto Mozara,[2] Tim Wehling,[2,4] and Wouter Jolie[1,*]

[1]*II. Physikalisches Institut, Universität zu Köln, Zülpicher Straße 77, 50937 Köln, Germany*
[2]*I. Institut für Theoretische Physik, Universität Hamburg, Notkestraße 9-11, 22607 Hamburg, Germany*
[3]*U Bremen Excellence Chair, Bremen Center for Computational Materials Science, and MAPEX Center for Materials and Processes, Universität Bremen, 28359 Bremen, Germany*
[4]*The Hamburg Centre for Ultrafast Imaging, Luruper Chaussee 149, 22761 Hamburg, Germany*

(Received 21 August 2024; revised 14 April 2025; accepted 17 June 2025; published 29 July 2025)

Polarons are quasiparticles that arise from the interaction of electrons or holes with lattice vibrations. Though polarons are well studied across multiple disciplines, experimental observations of polarons in two-dimensional crystals are sparse. We use scanning tunneling microscopy and spectroscopy to measure inelastic excitations of polaronic bound states emerging from coupling of nonpolar zone-boundary phonons to Bloch electrons in *n*-doped metallic single-layer MoS_2. The latter is kept chemically pristine via contactless chemical doping. Tunneling into the vibrationally coupled polaronic states leads to a series of evenly spaced peaks in the differential conductance on either side of the Fermi level. Combining density functional (perturbation) theory with a recently developed *ab initio* electron-lattice downfolding technique, we show that the energy spacing stems from the longitudinal-acoustic phonon mode that flattens at the Brillouin zone edge and is responsible for the formation of stable multipolarons in metallic MoS_2.

DOI: 10.1103/l8lg-ny6m

Subject Areas: Condensed Matter Physics

I. INTRODUCTION

Electron-phonon coupling is known to play a dominant role in metallic transition metal dichalcogenides, leading to various correlated ground states such as charge density waves and superconductivity [1,2]. Such correlation phenomena are also induced in the intrinsic semiconductor MoS_2 when its conduction band is filled with electrons. A charge density wave, which couples conduction electrons to unstable phonon modes, has been reported for electron-doped MoS_2 [3–7]. Further increases of the electron density through ionic liquid gating led to the observation of a superconducting dome, under which electrons condense into Cooper pairs via electron-phonon interactions [3,8–12]. Finally, at even higher charge carrier concentrations the entire crystal lattice becomes unstable, leading to an electronically driven structural phase transition from the 1H to the 1T structure [13].

Polarons represent local manifestations of electron-phonon coupling [14]. These many-body quasiparticles form when charge carriers interact strongly with the ionic lattice, creating a localized state in absence of a defect [15]. A polaron is generally able to move through the lattice, though it drags a deformation of the lattice with it, enhancing its effective mass. This mass enhancement has been observed in bulk MoS_2 doped with rubidium using angle-resolved photoemission spectroscopy (ARPES) and was attributed to the formation of multiple Holstein polaron bands [16]. A follow-up *ab initio* study could however reproduce the experimental spectral function without small polaron formation, but using the Fan-Migdal perturbative self-energy. This approach, which is geared toward the weak coupling limit, suggested that the mass renormalization stems from interactions with two different M-point phonons [17]. The phonons couple electronic states close to the conduction band minima at K and K' with states near Q' and Q. These local minima of the conduction band are only $\approx$100 meV higher than the global conduction band minimum and also partly filled in the ARPES experiment [16].

The proposed importance of the local minimum at Q for polaron formation in bulk MoS_2 poses the question whether polarons can actually form in single-layer (SL) MoS_2, since the energy difference between K and Q is much larger in *n*-doped SLs [18–20]. In addition, a recent theoretical study postulated that stable polarons do not form in SL MoS_2 [21], although only monopolarons were considered in these calculations. The physics of multipolarons, i.e., bound states formed by two or more electrons coupled to phonons,

*Contact author: wjolie@ph2.uni-koeln.de

is in general much less studied, though it is postulated to become dominant in cases of suppressed Coulomb potentials and sufficiently large electron-phonon coupling [22,23]. While signatures of plasmonic polarons have been observed in highly defective SLs of MoS_2 [19], the observation of polarons in defect-free SL MoS_2 remains elusive.

Here, we investigate the role of electron-phonon coupling and its link to multipolarons in SL MoS_2 on a graphene (Gr) on Ir(111) substrate using scanning tunneling microscopy (STM), scanning tunneling spectroscopy (STS), first-principles density functional (perturbation) theory calculations, and a newly developed multiscale technique based on downfolding for electron-phonon coupled systems [24]. Intercalating Cs and Eu between Gr and Ir(111) shifts the conduction band of MoS_2 below the Fermi energy E_F, thus inducing an insulator-metal transition [18]. This enables us to study the intrinsic properties of metallic SL MoS_2, which rests on a weakly interacting substrate (Gr).

II. RESULTS

A. Scanning tunneling spectroscopy

An STM topograph of metallic SL MoS_2 is shown in Fig. 1(a), displaying the typical morphology. The MoS_2 islands have merged during growth, forming extended networks, with defect-free areas ranging in size from 50 to 700 nm^2. These areas are separated by grain boundaries, which are imaged as dark stripes when tunneling in the conduction band of MoS_2. In addition, faint stripes can be recognized on and next to MoS_2, which stems from minor density variations in the Eu intercalation layer below graphene, as discussed previously [18].

Our first experimental observation related to electron-phonon physics is a weak local superstructure appearing in atomically resolved STM images, presented in Fig. 1(b). While the superstructure is locally visible in real space, there is no long-range coherence of the charge density, ruling out the presence of a charge density wave. The corresponding Fourier transformation in Fig. 1(c) reveals a broad feature close to the (2×2) spot in reciprocal space. This intensity has no structural origin, as intercalated Cs forms a disordered structure after annealing, while intercalated Eu forms a $c(4 \times 2)$ superstructure with respect to graphene. These intercalation patterns are not visible on MoS_2, as both Cs and Eu layers are intercalated below graphene [18]. As we will show below, multipolarons in MoS_2 are expected to generate local lattice distortions with the same dominant wave vector as the local (2×2) superstructure observed experimentally.

A dI/dV spectrum showing the band gap of MoS_2 is depicted in Fig. 1(d). The spectrum shows an apparent onset of the conduction band above the Fermi level. However, since the conduction band minimum of doped SL MoS_2 lies at the K point [3,20], the high parallel

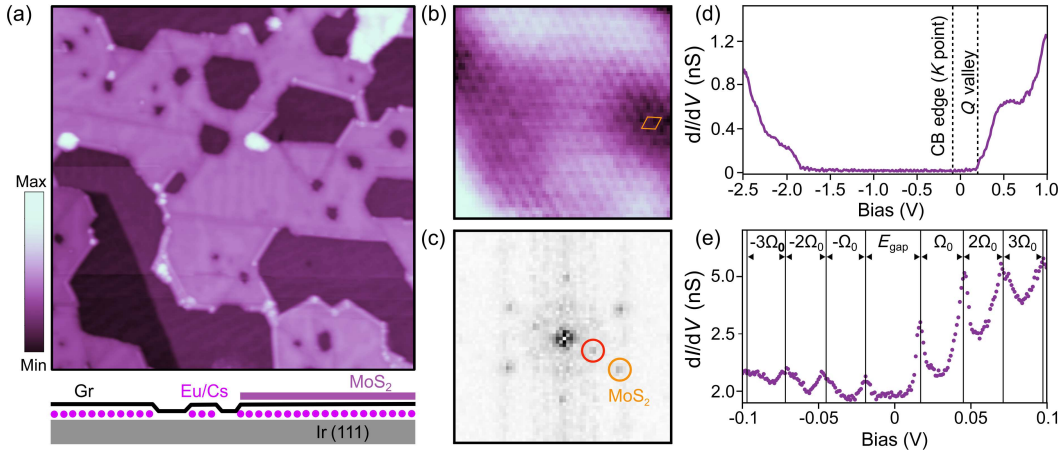

FIG. 1. Electronic structure of SL MoS_2. (a) Large-scale STM image of SL MoS_2/Gr/Eu/Ir(111). A step edge in the Ir substrate can be seen in the bottom left. The Eu intercalation has slight density modulations which lead to the stripes visible through MoS_2 and Gr. (b) Atomic resolution image of MoS_2, revealing a local superstructure. The MoS_2 unit cell is indicated. (c) Fourier transformation of (b), showing the six spots of the reciprocal MoS_2 lattice together with additional features at wave vectors close to half the size of the reciprocal lattice. Both features are marked with circles. (d) Large-bias dI/dV spectrum of single-layer MoS_2 on Gr/Eu/Ir(111). The conduction band (CB) edge at the K point of the Brillouin zone and the onset of the valley at 0.2 eV near the Q point are indicated. (e) Low-bias STM dI/dV spectrum, revealing peak-dip features and a gap at the Fermi level, characteristic for metallic SL MoS_2. STM or STS parameters: (a) 100×100 nm^2, $V_{set} = 2.5$ V, $I_{set} = 50$ pA; (b) 5×5 nm^2, $V_{set} = 0.1$ V, $I_{set} = 500$ pA; (d) $V_{set} = 1$ V, $I_{set} = 500$ pA, $V_{mod} = 15$ mV; (e) $V_{set} = 0.1$ V, $I_{set} = 500$ pA, $V_{mod} = 1$ mV, smoothed using the Savitzky-Golay method. For all spectra $f_{mod} = 877$ Hz.

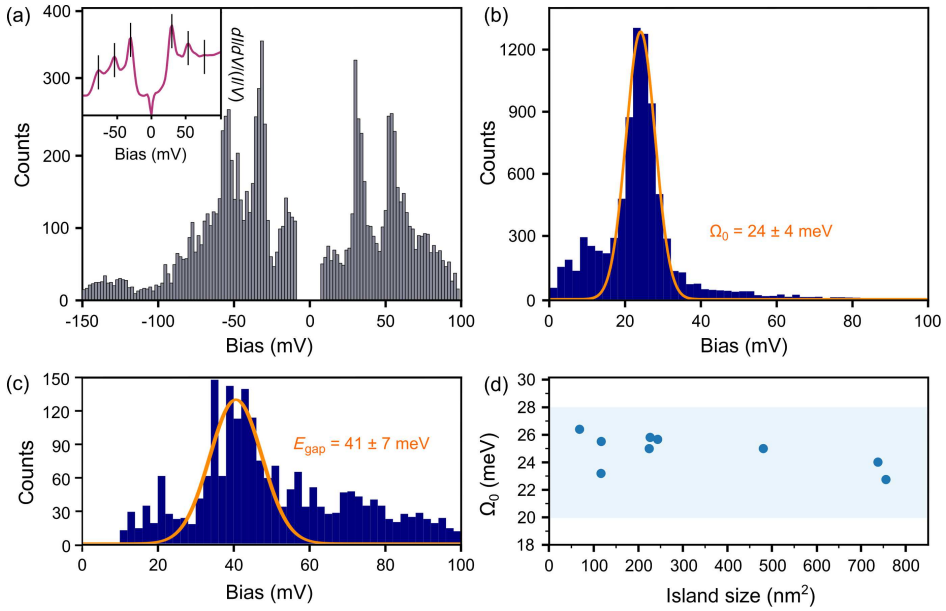

FIG. 2. Statistical analysis of peak-dip features in dI/dV spectra. (a),(b) Histograms of 2935 dI/dV spectra acquired on different locations, at different temperatures (0.4–6.5 K) and on MoS_2 areas of different sizes, using different samples [multiple MoS_2/Gr/Eu/Ir(111) samples and one MoS_2/Gr/Cs/Ir(111) sample] and tips (Au and PtIr). In (a) the peak locations are plotted. To analyze the data, the dI/dV spectra were smoothed and normalized. The inset in (a) shows a dI/dV spectrum after this procedure, with the locations of peaks found by a peak finding algorithm marked. In (b) the energetic distances between neighboring peaks (excepting the peaks closest to the Fermi level) are plotted. A Gaussian fit to the peak yields $\Omega_0 = 24 \pm 4$ meV. (c) Histogram of the distribution of the energetic distance between the first peaks on either side of the Fermi level. A Gaussian fit to the peak yields $E_{\mathrm{gap}} = 41 \pm 7$ meV. (d) Average distance between neighboring peaks Ω_0 for spectra taken on MoS_2 islands of different sizes. The island size is the coherent island area taking into account edges, grain boundaries, and constrictions smaller than 10 nm. The shaded area represents $\Omega_0 = 24 \pm 4$ meV.

momentum $k_{||}$ of the quasiparticles leads to a strongly reduced tunneling probability, unless the tip-sample distance is severely reduced [25,26]. Indeed, the low-bias dI/dV spectrum in Fig. 1(e) reveals a finite spectral intensity in the occupied states, separated from the unoccupied states by a gap at E_F. Comparable spectra are measured on Cs-intercalated samples. On account of the n doping of the Gr substrate layer by the Eu atoms, the MoS_2 conduction band edge is shifted to −90 meV below the Fermi energy, while the local minimum at Q lies 200 meV above the Fermi energy [18]. These energies were experimentally determined using quasiparticle interference (QPI) maps as well as comprehensive tunneling spectroscopy [25,26].

A particular aspect of the spectrum in Fig. 1(e) is the presence of peak-dip features close to E_F. These are seen to manifest as a series of evenly spaced peaks, present below and above E_F. The peaks are spaced by a fixed energy Ω_0, with a larger gap of width E_{gap} separating the states around E_F. The peak-dip features are absent in semiconducting MoS_2; see Appendix C.

To better understand the behavior of the peaks, we have analyzed approximately 3000 dI/dV spectra taken on islands of different size and on two different metallic MoS_2 samples—with either Eu or Cs intercalated below Gr. We included spectra taken in a temperature range between 0.4 and 6.5 K. In Fig. 2(a), the resulting peak positions are plotted in a histogram. The peaks have a clear tendency to be located at symmetric positions with respect to the Fermi energy (0 V), such as ±32 and ±55 mV. We further analyze the single spectra and find that the spacing between peaks located above and below the Fermi energy has a Gaussian distribution, with a mean value and standard deviation of $\Omega_0 = 24 \pm 4$ meV; see Fig. 2(b). We therefore interpret all these peaks as harmonics of a bosonic mode Ω_0 instead of independent excitations. When we check for the size of E_{gap} across all investigated spectra, see Fig. 2(c), we find considerably more fluctuations than for the peak spacing. The distribution does have a marked peak, which fitted with a Gaussian gives $E_{\mathrm{gap}} = 41 \pm 7$ meV.

We have checked in Fig. 2(d) that there is no dependence of Ω_0 on the size of the coherent island. Since the grain boundaries that divide the different regions of the MoS_2 islands are charged relative to their surroundings, band bending effects take place perpendicular to them, isolating

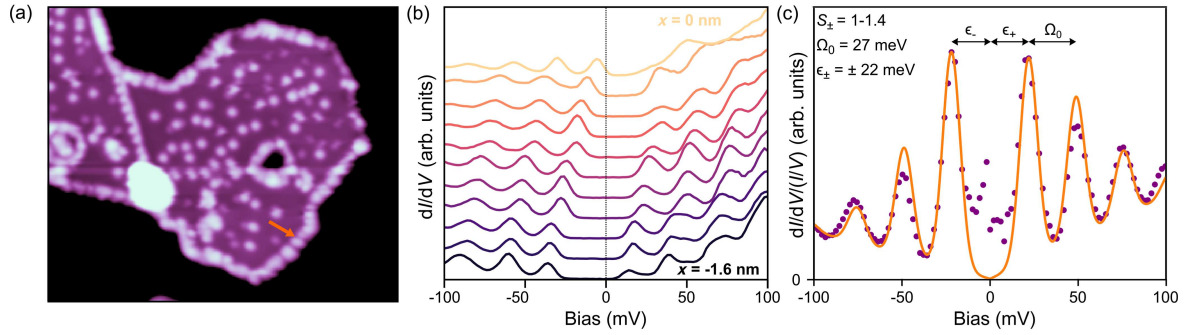

FIG. 3. Tunneling through localized polaronic states. (a) STM image of an SL MoS_2 island on Gr/Cs/Ir(111). Adsorbed Cs atoms are visible on the island, grain boundaries, and edges as bright dots. (b) dI/dV spectra taken along the orange arrow in (a), with $x = 0$ nm corresponding to the spectrum closest to the edge. Spectra are offset for clarity. (c) Low-bias $dI/dV/(I/V)$ spectrum with peaks above and below the Fermi level (purple dots). A fit based on Ref. [28] is shown as an orange line. Fitting parameters: the Huang-Rhys factor $S_- = 1$ ($S_+ = 1.4$) for the resonances in the occupied (unoccupied) states, the phonon energy $\Omega = 27$ meV, the location of the polaronic state $\varepsilon = \pm 22$ meV, the full width at half maximum of the states $\Gamma = 7$ meV, $l \leq 10$. A linear offset is included to account for (inelastic) tunneling processes that involve the MoS_2 band. STM or STS parameters: (a) 40×33 nm^2, $V_{\mathrm{set}} = 1.0$ V, $I_{\mathrm{set}} = 100$ pA; (b),(c) $V_{\mathrm{set}} = 100$ mV, $I_{\mathrm{set}} = 1.1$ nA, $V_{\mathrm{mod}} = 2$ mV, $f_{\mathrm{mod}} = 877$ Hz.

the different parts of the structure from one another [27]. The sample is thus composed of many areas of differing size, all of which show the same peak spacing Ω_0, ensuring that the peak-dip features are not related to area-dependent effects like confinement. The peaks are also independent of quasiparticle scattering effects within the metallic MoS_2 band; see Appendix D.

B. Effect of charge inhomogeneities

While the relative energy spacing of the peaks is locally reproducible, their absolute energetic positions vary depending on the location of data acquisition. These variations are especially pronounced close to charge inhomogeneities. To visualize this finding, we measure dI/dV spectra on metallic MoS_2 with additional Cs atoms adsorbed on top, shown in Fig. 3(a). The Cs adatoms are imaged with the STM as bright spots, which are preferentially decorating the island edges and grain boundaries. Because of the small electronegativity of Cs, the adatoms donate electrons to their environment, n-doped MoS_2. Cs is also intercalated between graphene and Ir(111) to further ensure that MoS_2 is metallic; see Appendix E. Taking a series of dI/dV spectra along the line drawn in Fig. 3(a), we can track the behavior of the peak-dip features as the tip moves toward the island edge. The spectra are plotted in Fig. 3(b). The peaks are seen to bend collectively upward near the edge of the island in a range of 1.6 nm, while not crossing the Fermi energy and thus retaining a finite gap E_{gap}.

The behavior in close vicinity to randomly placed Cs atoms on the MoS_2 islands is found to be more complex, see Appendix F, likely due to the inhomogeneous electrostatic environment there.

C. Modeling inelastic tunneling processes

Given the experimental evidence, we can conclude that tunneling in metallic SL MoS_2 is strongly affected by the existence of a bosonic mode of energy $\Omega_0 = 24 \pm 4$ meV, leading to pronounced satellite peaks in tunneling spectra. Since SL MoS_2 hosts multiple flat phonon bands near the edges of its Brillouin zone, with energies of 20–30 meV [29], the bosonic mode Ω_0 is likely a phonon. While the satellites are pinned to the peaks $\varepsilon_\pm$ defining E_{gap}, the latter is found to continuously shift up or down in energy relative to the Fermi energy, depending on the electrostatic environment. These observations point toward an inelastic tunneling process for the satellites, while E_{gap} seems related to an intrinsic property of metallic MoS_2.

Inelastic tunneling processes can lead to characteristic satellites in dI/dV when electrons tunneling through a localized level experience strong electron-phonon coupling. This has been established for STM junctions in 1D and 0D systems [30–32], in particular for molecules on surfaces [33–35] and in tunneling devices based on semiconductor quantum wells [36]. In these systems, a series of resonant peaks spaced by the energy of the vibronic mode are observed in conductance spectra, in close resemblance to our observations. To obtain information related to these inelastic tunneling processes, we fit our peak-dip features to the many-body spectral function of a discrete electronic state with energy $\varepsilon_\pm$ coupled to a bosonic phonon mode Ω_0 [28,37]:

$$A(\omega) = 2\pi \sum_{l=1}^{\infty} \left[\left(e^{-S_\pm} \frac{S_\pm^l}{l!} \right) \delta(\hbar\omega - \varepsilon_\pm \mp \Omega_0 l) \right]. \quad (1)$$

From the fit we obtain the Huang-Rhys factor $S_{\pm}$, which is related to the electron-phonon coupling strength $g = \sqrt{S_{\pm}}\Omega_0$ and l being an integer. We obtain Huang-Rhys factors of $S_- = 1$ and $S_+ = 1.4$ for the resonances in the occupied and unoccupied states of the spectrum in Fig. 3(c), respectively. We find a range of $S_{\pm} = 1$–3, using several representative spectra; see Appendix G. Though the model is able to adequately describe the experimental spectra and points to strong electron-phonon coupling involving a well-defined mode Ω_0, it does not provide an explanation for the origin of the energy states $\varepsilon_{\pm}$ around E_F, nor why a single phonon energy is dominating in the experimental spectrum.

D. Polaronic deformations in metallic MoS_2

To unveil the origin of the pronounced peak-dip features observed in STS, we performed a theoretical analysis combining density functional theory (DFT) and density functional perturbation theory (DFPT) with a recently developed *ab initio* electron-lattice downfolding technique which facilitates relaxations of large supercells [24] (see Appendix B for more information) and compared to the scenarios put forward in Refs. [16,17].

The ARPES study of Ref. [16] revealed dip-peak features in the photoemission spectral function, that were explained in Ref. [17] as Fan-Migdal self-energy effects stemming from scattering of electrons between K and Q' as well as K' and Q valleys. Following this idea, we calculate the Fan-Migdal self-energy and show the resulting electronic spectral function for the system at hand in Appendix H. For a Fermi level such that K and Q valleys of the SL MoS_2 conduction band are occupied, we find kinks and gaps in the spectral function, very similar to Ref. [17]. However, our STS experiments (see Fig. 1) locate the Q valley ~150 meV above the Fermi level. In this situation, the gaps in the electronic spectral function disappear; see Appendix H. Hence, the peak-dip features seen here in STS [Figs. 1(e), 2, and 3] are not explicable by the Fan-Migdal self-energy. This points toward the possibility that strong coupling physics is at work, here.

One natural explanation, given the shape of the STS spectra in Fig. 3, would be polarons in the intermediate to strong coupling regime. Within the mean-field approximation, the polaron is a self-consistent localization of additional charges in the system, and this localization can be captured by DFT when self-interaction errors are eliminated [38]. Our downfolded-model approach incorporates DFT and DFPT, closely relates to the approach of Ref. [38] in the case of a single electron being added to the system, and by construction contains no self-interaction terms.

For a single electron being doped into an SL MoS_2 supercell up to sizes of 18×18, we did not find a localized polaron state—in line with Ref. [21]. The situation changes, however, with more than one electron being doped into the supercell: At four or more additional electrons in an 18×18 supercell, we find that n-doped SL MoS_2 is unstable toward multipolaronic deformations, as can be seen in the relaxed structure depicted in Fig. 4(a). The stability of the deformation depends on the amount of doping in the system; see Appendix I. In Fig. 4(b) we show the total energy as a function of displacement for the multipolaronic deformation of four additional electrons in the supercell, revealing an energy gain of up to 25 meV per additional electron in the supercell. This energy gain corresponds to the formation energy when doping charges localize [39], giving a total binding energy of about 100 meV for the multipolaronic distortion shown in Fig. 4(a). Because of the omission of explicit Coulomb interactions between charge carriers in our model [24], the resulting displacement pattern as well as the corresponding multipolaronic binding energy are shown to be essentially independent of the supercell size as long as the displacement pattern can be accommodated in the supercell; see Appendix J for calculations with four additional electrons on supercell sizes 6×6, 12×12, and 18×18.

To understand which phonons contribute to the multipolaronic deformation found in our lattice relaxations, we calculated the structure factor $\langle S(\mathbf{q}) \rangle$ [see Fig. 4(c)] [24]. It represents the Fourier transform of the atomic structure, provides an estimation of the momentum-dependent scattering intensity, and encodes the polaron-associated atomic displacements. The structure factor reveals that the deformation is peaked in reciprocal space around the M point, which corresponds to the (2×2) spot with respect to the reciprocal MoS_2 lattice. As to be expected for a localized distortion pattern, there is a finite range of $\mathbf{k}$ points contributing with different weights, with the ratio of the contribution from K compared to M corresponding to about 30%. A decomposition of the displacement pattern into normal modes (see Appendix K) shows that the longitudinal-acoustic (LA) mode dominates the polaronic displacements at the distortion-relevant $\mathbf{k}$ points. The phonon dispersion shown in Fig. 4(d) reveals a flat phonon band at the Brillouin zone edge, with the LA mode flattening between K and M at around 28 meV. This phonon energy agrees well with the experimental observation of the bosonic energy of $\Omega_0 = 24 \pm 4$ meV.

To further understand the implications of the multipolaronic deformations, we examined the corresponding electronic structure. In Fig. 4(e) we depict the undistorted band structure (blue) and the unfolded band structure in the distorted phase (orange). The weights of the unfolded bands were calculated as the overlap of the electronic wave functions (with the same wave vector) of the deformed and the undeformed system. These overlaps are visualized on a logarithmic color scale as well as via the size of the markers. Dashed lines indicate the corresponding Fermi level of the undistorted (blue) and the distorted system (orange). In both band structures, the dispersive states of the Q valley are not occupied, which resembles the situation of our experiments (cf. Fig. 1 and

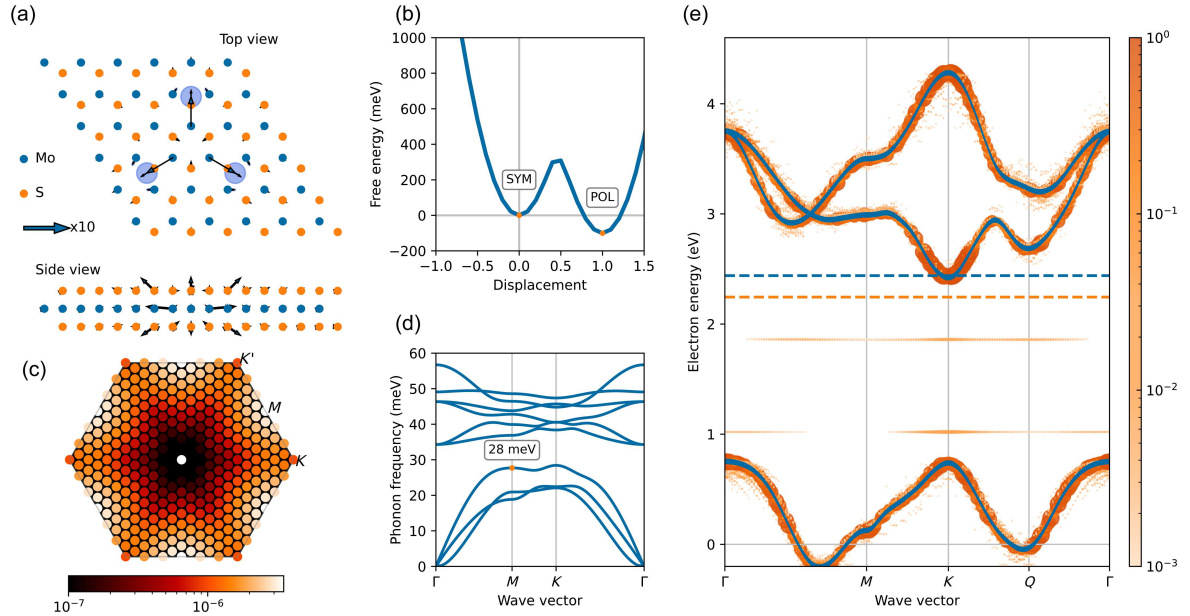

FIG. 4. Multipolaronic deformations in metallic SL MoS_2. (a) Enlargement of relaxed crystal structure based on *ab initio* model calculations on an 18×18 supercell with a lattice constant of 3.19 Å at an electronic doping of $0.0124e^-$ per formula unit of MoS_2. The doping is slightly increased compared to the one used in DFT + DFPT calculations ($0.01e^-/MoS_2$) and results in four additional electrons per supercell. The displacements visualized by arrows are rescaled by a factor of 10 for better visibility. Blue circles indicate the localization of the additional electrons. (b) Total energy as function of displacement for the polaronic deformation shown in (a). The relaxation started from the symmetric phase (SYM) and shows a minimum at the displacement corresponding to the multipolaronic deformation (POL). The resulting total energy gain of ≈100 meV equals the binding energy of the multipolaronic distortion. (c) Structure factor $S(\mathbf{q})$ for the relaxed geometry seen in (a). The high intensity around the M points of the phononic Brillouin zone shows that the modes located there contribute the most to the polaronic deformation. (d) Phonon bands obtained via DFPT. The LA phonon mode that contributes the most to the polaronic deformation is marked by its energy at the M point. The phonon bands are obtained at an electronic doping of $0.01e^-/MoS_2$. (e) Band structure of low-energy subspace as obtained by DFT (blue) and after the *ab initio* model relaxation (orange). The weights of the unfolded bands correspond to the logarithmic color bar and the size of the markers. The relaxed band structure has been unfolded from the supercell to the unit cell, revealing the opening of small gaps due to the formation of dispersionless states associated with the symmetry breaking due to the polaronic deformation, which also lowers the Fermi energy (dashed lines).

Ref. [18]). A close inspection of the spectral weight of the distorted structure inside the gap of the undistorted system, however, reveals localized (i.e., flat in k space) states with contributions from K and Q. The charge density of these states is localized precisely in the region of strong polaronic displacements as visualized in Fig. 4(a). The occurrence of in-gap localized polaronic states featuring hybridization of K- and Q-valley states is well in line with the dominant contribution of LA M-point phonons to the polaronic relaxation: The momentum difference $K'Q$ as well as KQ' corresponds to ΓM (see Appendix L), and the electron-phonon coupling matrix element scattering conduction band electrons between K and Q points is particularly strong for the LA M-point phonon [3,4].

It is intriguing to note that this coupling is active and leads to a polaronic state even though the Q point is not occupied [Fig. 4(e)]. As mentioned above, the Fan-Migdal self-energy in the deformed structure does not reveal any M-point phonon satellites in such a situation (see Appendix H) [17,39], showing that the polaronic deformations found in the relaxations and the spectral footprint of phonons in experiment are thus a strong coupling phenomenon. While the precise energetic minimum of the dispersive band at Q will depend on variations of the doping level and the lattice constant, the suggested scenario is qualitatively robust as long as sufficiently many electrons are doped into the system (cf. Appendix I for an illustration of the case with three additional electrons).

III. DISCUSSION

To bring our work into context, we can rule out certain polaronic scenarios based on our observations. The energetic shifts of the peaks in response to localized charges are incompatible with purely inelastic tunneling processes, which would lead to the appearance of symmetrically

distributed steps or peaks in the dI/dV signal on either side of the Fermi level (at energies $\pm n\Omega_0$) [33,40]. In the same vein, renormalization of the electron bands with a particular phonon mode can be excluded as well, as it would lead to mass-enhanced (flatter) bands at fixed energies relative to E_F [41], as observed, for instance, in surface-doped bulk MoS_2 with ARPES [16]. In our case, the spectral energy shifts induced by charges within the layer, together with the statistical distribution of the peaks, strongly suggest that the two peaks closest to the Fermi energy have a different origin.

Our experimental analysis reveals that the peaks observed in STS spectra have equidistant spacings, $\Omega_0 = (24 \pm 4)$ meV. As the spacing corresponds to the quasiparticle energy, the simplest interpretation would be that phonon modes with energy Ω_0 dominate. It is also in line with our theoretical calculations, which find that the LA phonon mode, which flattens between K and M at around 28 meV, dominates the multipolaronic displacements. A second possibility would be a contribution of (optical) phonons with an energy close to twice (or, in general, multiples of) Ω_0, as suggested theoretically in Ref. [17] for bulk MoS_2. We can, however, rule out this scenario for SL MoS_2 as we observe peaks well above the highest energy of a single phonon mode. In addition, we find no significant contribution to the polaronic deformation stemming from optical phonon modes in our calculations.

Our calculations revealed stable multipolaronic states, i.e., complexes of more than one polaron. These polaron complexes can be viewed as precursors of the charge density wave emerging in MoS_2 under strong electron doping, where the periodic lattice distortion bases on the LA M phonon and its strong coupling to K and Q electrons [3,4,6,7]. The appearance of the multipolarons in STM here is thus considerably different from polarons in 2D semiconductors such as $CoCl_2$ [42,43]. There, a depression in the apparent height is observed due to the weak screening of the local charge. The interpretation of multipolarons being precursors of the charge density wave in MoS_2 is consistent with the appearance of a weak local (2×2) superstructure in our STM images. We expect that further doping will lead to a global periodic lattice distortion accompanied by a (2×2) charge density wave superstructure with respect to the MoS_2 lattice.

A. Characteristics of multipolaronic spectra

The spectral properties associated with multipolaronic states are less understood than the well-studied theoretical framework of the single polaron problem, yet the comparison to the better studied bipolaron case allows us to speculate about the spectral features exhibited by multipolarons.

For the Holstein model of the simplest two-site polaron system, the spectral intensity is characterized by the emergence of a series of equidistant, phonon-induced replica peaks above and below an energy gap E_{gap} when increasing the electron-phonon-coupling strength [44]. This energy gap is equal to the binding energy $2\varepsilon_{pol}$ between two monopolarons in the strong coupling limit, $E_{gap} = 2\varepsilon_{pol}$, with the corresponding Fermi energy positioned precisely in the middle of the gap. The peaks below the Fermi energy correspond to electron removal from an occupied (bi)polaronic state, while the peaks above the Fermi energy are associated with electron addition to (bi) polaronic states. These characteristics are expected to hold true generally for any interacting many-polaron system on a lattice and fit qualitatively well to the characteristics of our experimentally observed STS spectra. Similar spectra of equidistant, phonon-induced peak structures [45] separated by an energy gap are reported in other theoretical works, such as the study of the Holstein many-polaron model via cluster perturbation theory [46], the quantum Monte Carlo and exact diagonalization treatment of the 1D spinless Holstein model of a many-polaron system [47], as well as the dynamical mean field theory and exact diagonalization treatment of the Holstein bipolaron at half filling [48].

Under account of the direct comparison between the bipolaron case and our proposed multipolaron case, we can thus estimate the multipolaronic binding energy as $E_{gap} \approx 40$ meV from our STS spectra, which is in the same order of magnitude as the multipolaronic binding energy of $\sim$100 meV derived from our qualitative theory comparison in Fig. 4(b).

While our statistical analysis in Fig. 2(a) shows a preference for symmetric peaks around the Fermi energy, in line with the expected spectral features of multipolaronic states, clear energy shifts are observed in the vicinity of local charges. For the spectra in the vicinity of Cs adsorbates (see Figs. 3 and 8), the entire series of spectral peaks shifts rigidly in the vicinity of Cs without strong changes in the gap size. Because of charge transfer from Cs to MoS_2 and the underlying graphene, we expect strong electric fields around the Cs atoms. We suspect that band bending due to these electric fields is the reason behind the shifts in the spectra seen in the Cs-decorated case, while the energy gap remains essentially unchanged. Based on these observations, the large scatter in E_{gap} as seen in Fig. 2(c) is likely not caused by charge inhomogeneities. Possible origins are structural disorder or variations in the intercalation layer.

B. Limits and plausibility of the downfolding approach

For further verification of our multipolaron interpretation, it is important to justify the use of the downfolding approach in our theoretical analysis. The proposed multipolaronic states might still be altered by electron-electron interaction effects which are included neither in the Holstein model of (bi)polarons nor in our downfolding model: Nonlocal exchange enhances electron-phonon coupling vertices and could stabilize polaron complexes involving less than the proposed four electrons. At the

same time, electron-electron interactions can lead to correlation effects beyond the effective mean-field treatment of the polaronic state considered here.

In freestanding 2D semiconductors as well as 2D semiconductors in a weakly screened environment, long-range Coulomb interactions could counteract the proposed multipolaron state, since the formation of bipolarons and by extension multipolarons is limited to a certain range of the ratio between the electron-phonon coupling and the Coulomb repulsion interaction strength [22,23]. Therefore, for strong Coulomb interaction, the formation of multipolarons is suppressed.

Though strong Coulomb interactions are observed in semiconducting MoS_2 when charges localize within grain boundaries [49,50], here we are adding charge carriers into the conduction band of *n*-doped MoS_2 on top of a metallic substrate. In consequence, the MoS_2 on substrate system is conducting and can effectively screen charges within the layer. This is experimentally confirmed as a reduced extension of band bending effects in real space as compared to semiconducting MoS_2 [18]. In consequence, long-range Coulomb interactions emerging from the formation of multipolaronic states will be effectively screened in our metallic system. So it stands to reason that the possibility of multipolaron formation should be further supported.

While a full account of Coulomb effects remains to be given, we also note that for the downfolding approach used here, many contributions of interaction terms are shown to be canceling out [24]. Because of that, the Born-Oppenheimer potential energy surfaces of a variety of metallic charge density wave materials have been reproduced to a high degree of accuracy. Although the substrate is not explicitly included in our theoretical analysis, omitting the long-range Coulomb interactions (such as polaron-polaron repulsion) in the downfolding model implicitly describes the aforementioned substrate-induced screening effects on the charges and therefore on the multipolaronic states within the layer. Effectively, the MoS_2 sample in our model equals a "metallic" setup with quenched long-range interactions, which would explain the qualitative agreement regarding the binding energies between our calculations and the experiment.

These arguments provide evidence that our proposed scenario of multipolaronic binding concluded from our downfolding calculations is a reasonable assumption to make, given the clear spectral similarities to literature without the full account of electron-electron interaction and regarding the validity of our downfolding approach in metallic charge density wave materials.

To the best of our knowledge, the problem of electronic spectra resulting from multipolaronic states under full account of the electron-electron interaction has not been addressed for real materials so far, and we hope that our study triggers a closer theoretical investigation.

IV. SUMMARY

In summary, our results demonstrate that multipolaronic states emerging from the coupling of charge carriers to a well-defined phonon mode can be measured via STM in *n*-doped metallic SL MoS_2. A local superstructure resembling a (2×2) is observed experimentally. In dI/dV spectra, two strong resonances are observed on either side of the Fermi level, together with inelastic phonon replica evenly spaced by an energy of $\Omega_0 = 24 \pm 4$ meV. By combining density functional (perturbation) theory with a recently developed *ab initio* electron-lattice downfolding technique, we find that the MoS_2 lattice has a strong tendency toward localized deformations with a finite range of wave vectors around the *M* point contributing to the distortion, which can be interpreted as a multipolaron involving four (or more) electrons. By revealing the effects of large electron-phonon coupling on the tunneling spectra of 2D materials, we expect that our findings create new research opportunities into 2D (multi)polaron complexes.

ACKNOWLEDGMENTS

We acknowledge funding from the Deutsche Forschungsgemeinschaft (DFG, German Research Foundation) through CRC 1238 (Project No. 277146847, subprojects A01 and B06). J. F. acknowledges financial support from the DFG through Project No. FI 2624/1-1 (Project No. 462692705) within the SPP 2137. J. B. acknowledges financial support from the DFG through Germany's Excellence Strategy (University Allowance, EXC 2077, Project No. 390741603, University of Bremen). Financial support by the DFG priority program SPP2244 is acknowledged by M. W., T. W. (Project No. 43274199), and W. J. (Project No. 535290457). L. P. and T. W. thank the DFG for funding through the research unit QUAST FOR 5249 (Project No. 449872909; Project P5). Arne Schobert, Y. in 't V., and T. W. acknowledge funding and support from the DFG through the cluster of excellence "CUI: Advanced Imaging of Matter" of the Deutsche Forschungsgemeinschaft (DFG EXC 2056, Project No. 390715994). The authors gratefully acknowledge the computing time made available to them on the high-performance computer "Lise" at the NHR Center NHR@ZIB under the Project No. hhp00063. This center is jointly supported by the Federal Ministry of Education and Research and the state governments participating in the NHR [51].

APPENDIX A: EXPERIMENTAL METHODS

The samples were grown *in situ* in two preparation chambers with base pressure $p < 5 \times 10^{-10}$ mbar. Ir(111) is cleaned by 1.5 keV Ar^+ ion sputtering and annealing to a temperature of 1550 K. Gr is grown on Ir(111) in two steps. First, the Ir is exposed to ethylene until saturation, followed

by 1370 K thermal decomposition in order to obtain well-oriented Gr islands. Afterward, the sample is exposed to 2000 L ethylene at 1370 K for 600 s, which yields a complete single-crystal Gr layer [52]. SL MoS_2 is grown by Mo deposition in an elemental S pressure of 1×10^{-8} mbar [53]. Subsequently, the sample is annealed to 1050 K in the same S background pressure. Cs was evaporated using a direct current evaporator to heat a Cs dispenser in ultrahigh vacuum. During evaporation, the MoS_2/Gr/Ir(111) sample was kept at 570 K. After intercalation, the sample was flashed to 730 K to remove residual Cs from the surface. Details about the Eu intercalation can be found in Ref. [18].

STM and STS were carried out in two ultrahigh vacuum systems at a temperature of 0.4–6.5 K after *in situ* transfer of the samples from the preparation chamber.

APPENDIX B: CALCULATION DETAILS

DFT calculations were performed with QUANTUM ESPRESSO [54] using the PBE approximation for the exchange-correlation potential [55] and norm-conserving pseudo-potentials from the PSEUDODOJO database [56,57]. Plane waves until an energy cutoff of 100 Ry were included and a Fermi-Dirac-type smearing of 0.001 Ry was imposed. We considered a doping of $0.01e^-/MoS_2$, which corresponds to a dopant density of 1.14×10^{13} cm^{-2}. We included a vacuum of approximately 12 Å above the monolayer. We used an 18×18 **k**-point grid for the unit cell. Relaxation of the (un)doped unit cell for fixed cell height yielded the lattice constant of 3.23 Å (3.19 Å). We used these unit cell structures and their lattice constants as the starting point of all subsequent calculations.

For the DFPT calculations via QUANTUM ESPRESSO, we used a 6×6 **q**-point grid. For the determination of the electron-phonon coupling we employed the EPW code [58]. Three energy bands around the Fermi energy were transformed into the Wannier basis starting from orbitals of Mo d_{z^2}, $d_{x^2-y^2}$, and d_{xy} character. Spectral function calculations in Appendix H were carried out on top of the three band Wannier model extended to include spin-orbit coupling within the EPW code including possible Fan-Migdal contributions to the self-energy. A dense **q**-point grid (192×192) was used. Smearing in electron-phonon coupling summation and energy-conserving delta functions was set to 0.002 eV.

The relaxations on large supercells (18×18) were facilitated by the downfolding strategies from Ref. [24], which have been implemented in the ELPHMOD package [59]. The same parameters as in DFT were used except for the **k**-point grid, which corresponds to a Γ-only calculation on the 18×18 supercell.

We used the "model III" variant with exclusion of electron-electron interactions of the downfolding strategy of Ref. [24], where its equivalence to DFT had been established for a variety of metallic charge density wave materials. Full equivalence would require recalculation of model parameters (charge self-consistency). The Landau-Pekar model provides a formally equivalent description of DFT polarons, with the equivalence becoming exact in the Fröhlich limit [38]. In the Fröhlich model, the polaronic self-energy within the self-consistent many-body approach provides the Landau-Pekar solution to the Fröhlich polaron, and thus at least the formal solution to the polaron problem in DFT and in downfolding model III [39]. Thus our approach captures localization and static renormalization effects encoded in the polaronic self-energy. The Fan-Migdal self-energy adds dynamical renormalization of the energy levels.

APPENDIX C: ABSENCE OF PEAK-DIP FEATURES IN SEMICONDUCTING MoS_2

We only observed the peak-dip features in dI/dV spectra measured on metallic MoS_2. Figure 5 shows a dI/dV spectrum measured on MoS_2/Gr/O/Ir(111), close to the conduction band minimum. Oxygen is known to shift the conduction band of MoS_2 to higher energies, making MoS_2 semiconducting [18]. The band edge is smooth, without pronounced additional features. The absence of peak-dip features is in line with the absence of polarons in semiconducting MoS_2.

APPENDIX D: DELOCALIZED QUASIPARTICLE SCATTERING IN METALLIC MoS_2

Standing waves are observed when mapping the dI/dV signal in real space; see Fig. 6. These are related to QPI, arising from electron scattering near the MoS_2 K point [18]. A dI/dV spectrum spatially averaged over the entire area under investigation still exhibits pronounced peak-dip features; see Fig. 6. This ensure that these peak-dip features are not related to local density variations due to QPI.

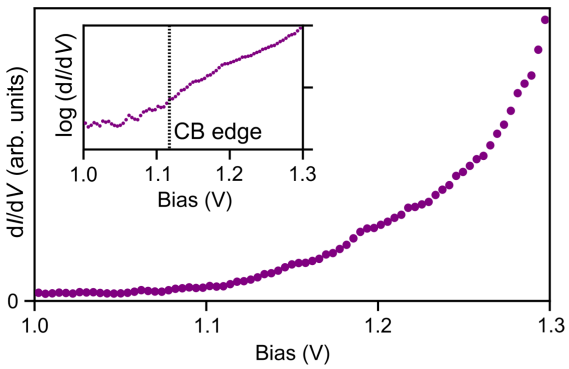

FIG. 5. Absence of peak-dip features in semiconducting MoS_2. In semiconducting MoS_2, here on a Gr/O/Ir(111) substrate, the band edge is smooth. No peak-dip features are seen. STM or STS parameters: $V_{set} = 1.35$ V, $I_{set} = 1.0$ nA, $V_{mod} = 5$ mV.

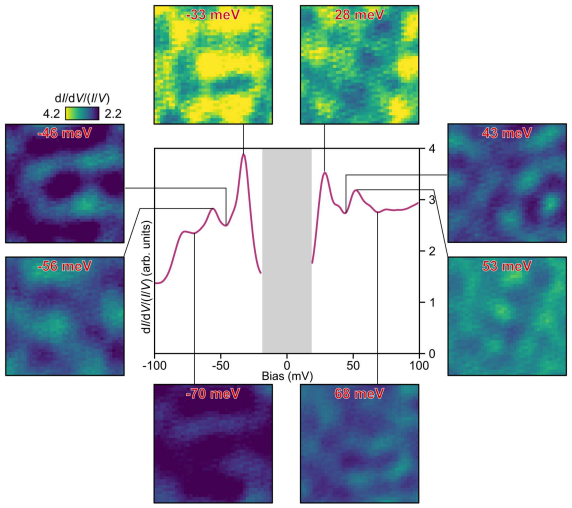

FIG. 6. Delocalized quasiparticle scattering in metallic MoS_2. Conductance maps of a large, defect-free area of MoS_2. The normalized spectrum in the center is spatially averaged over the whole investigated area. While the characteristic resonances are visible, they are delocalized, leading to an increase or decrease of the conductance at any point in the area. The patterns that are visible are related to QPI in MoS_2. STM or STS parameters: 10×10 nm^2, $V_{\mathrm{set}} = 0.1$ V, $I_{\mathrm{set}} = 1.0$ nA, $V_{\mathrm{mod}} = 2$ mV, $f_{\mathrm{mod}} = 877$ Hz.

APPENDIX E: DOPING LEVEL OF Cs INTERCALATED SAMPLE

In the conductance map of graphene in Fig. 7(a), standing wave patterns can be observed, which arise from QPI of the graphene electrons. A Fourier transform, shown in Fig. 7(b), reveals triangular scattering patterns around the K and K' points. The size of these triangular pockets is determined by intervalley scattering within the Dirac cones and is thus directly linked to the constant energy contours of the graphene band structure at the energy of the measurement [60]. At 25 meV, we find that the width of the trigonally warped Dirac cone, measured from $\Gamma \rightarrow K \rightarrow M$ is 0.374 Å^{-1}. Comparing this value to the fully Cs-intercalated data of Ref. [60], we estimate that $E_D \approx -0.9$ eV, with E_D the Dirac point of graphene. Compared to the Dirac point of graphene in the undoped MoS_2/Gr/Ir(111) system ($E_D = 0.25$ eV) [61], this shift is in considerable excess of the energy needed to bring the MoS_2 conduction band below the Fermi level [18,26].

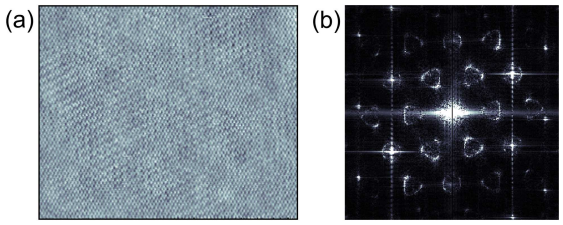

FIG. 7. Scattering pattern in Cs-intercalated graphene. (a) Conductance ($\mathrm{d}I/\mathrm{d}V$) map and (b) corresponding Fourier transformation of Cs-doped graphene. STM or STS parameters: (a) 17×14 nm^2, $V_{\mathrm{set}} = 25$ mV, $I_{\mathrm{set}} = 1.0$ nA, $V_{\mathrm{mod}} = 25$ mV.

APPENDIX F: SPECTRA MEASURED CLOSE TO Cs ATOMS ON MoS_2

Additional spectra measured close to Cs atoms on MoS_2 are presented in Fig. 8. They are recorded along the line in Fig. 8(a) and shown as color plot in Fig. 8(b), which visualizes the $\mathrm{d}I/\mathrm{d}V$ intensity as a function of position and bias voltage.

Again we find that the peaks shift considerably in energy, while not crossing the Fermi energy. Compared to Fig. 3(b), the behavior of the spectra is shown to be more complex. This behavior is likely due to the highly complex combination of (multi)polaron physics and the inhomogeneous electrostatic environment close to the Cs adatoms.

APPENDIX G: ELECTRON-PHONON COUPLING STRENGTH FROM CONDUCTANCE SPECTRA

Figure 9 shows additional spectra measured on MoS_2. We observe a variation in the intensity of the peak-dip features. This variation leads to a scatter in the Huang-Rhys factor S_+. The phonon energy Ω_0 is not affected by the intensity variations. A constant phonon energy is in line with our interpretation that one phonon mode dominates the spectral intensity.

APPENDIX H: SPECTRAL FUNCTION WITH FAN-MIGDAL SELF-ENERGY CONTRIBUTIONS AND CUMULANT EXPANSION

From the analytical expression for the Fan-Migdal self-energy and for the spectral function (see, e.g., Ref. [17]) we can understand the presence or absence of phonon-induced kinks and band cuts in the electronic K valley depending on whether K and Q valleys or only the K valleys are occupied by dopant electrons (see Fig. 10):

$$\Sigma_{\mathbf{k}j}(\omega) = \frac{1}{N_{\mathbf{q}}} \sum_{\mathbf{q}i\nu} |g^{\nu}_{ij}(\mathbf{k},\mathbf{q})|^2 \left(\frac{f(\varepsilon_i^{\mathbf{k}+\mathbf{q}})}{\omega - (\varepsilon_i^{\mathbf{k}+\mathbf{q}} - \omega_\nu^{\mathbf{q}}) + \mathrm{i}\eta} + \frac{1 - f(\varepsilon_i^{\mathbf{k}+\mathbf{q}})}{\omega - (\varepsilon_i^{\mathbf{k}+\mathbf{q}} + \omega_\nu^{\mathbf{q}}) + \mathrm{i}\eta} \right), \tag{H1}$$

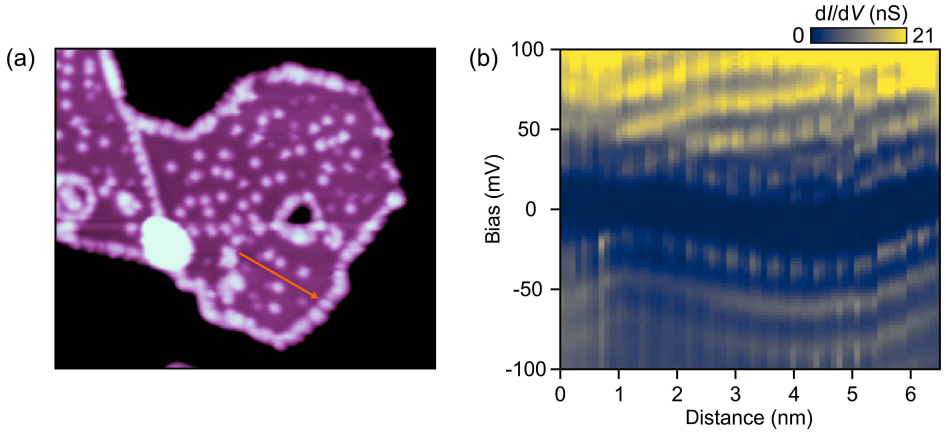

FIG. 8. Effect of an inhomogeneous electrostatic environment. (a) STM image of an SL MoS_2 island on Gr/Cs/Ir(111) with adsorbed Cs atoms. The arrow marks the position of data acquisition. (b) dI/dV intensity as a function of position and bias voltage. STM or STS parameters: (a) 40×33 nm^2, $V_{set} = 1.0$ V, $I_{set} = 100$ pA; (b) $V_{set} = 100$ mV, $I_{set} = 1.1$ nA, $V_{mod} = 2$ mV, $f_{mod} = 877$ Hz.

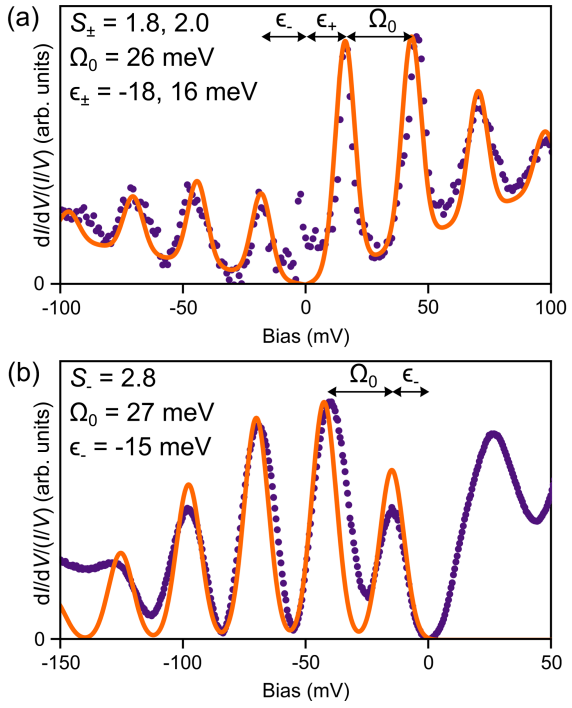

FIG. 9. Variation in the inelastic tunneling processes. (a), (b) Two conductance spectra taken on defect-free areas of MoS_2/Gr/Eu/Ir(111) are shown. The spectra are fitted using the model of Eq. (1) in the main text [28]. STM or STS parameters: (a) $V_{set} = 0.1$ V, $I_{set} = 500$ pA, $V_{mod} = 1$ mV; (b) $V_{set} = 0.1$ V, $I_{set} = 500$ pA, $V_{mod} = 5$ mV.

$$A(\mathbf{k},\omega) = -\frac{1}{\pi}\sum_j \mathrm{Im}[G(\mathbf{k},\omega)] = -\frac{1}{\pi}\sum_j \frac{\mathrm{Im}[\Sigma_{\mathbf{k}j}(\omega)]}{(\omega-\varepsilon_j^{\mathbf{k}}-\mathrm{Re}[\Sigma_{\mathbf{k}j}(\omega)])^2+(\mathrm{Im}[\Sigma_{\mathbf{k}j}(\omega)])^2}. \tag{H2}$$

The self-energy Σ has poles at $\omega = \varepsilon_i^{\mathbf{k}+\mathbf{q}} - \omega_\nu^{\mathbf{q}} - i\eta$ in the first fraction, which affect the occupied part of the spectrum due to the Fermi function in the numerator $f(\varepsilon_i^{\mathbf{k}+\mathbf{q}})$. Because of the factor $1 - f(\varepsilon_i^{\mathbf{k}+\mathbf{q}})$, the second term in Σ acts only on the unoccupied part of the spectrum. Therefore, the band cuts and kinks below the Fermi level originating from phonon-induced scattering between K and Q valleys can be realized only if the Q valley is occupied. A visual representation is given in Fig. 10.

The Fan-Migdal self-energy fails to reproduce the full series of polaronic replica in the spectral function even in systems with strong polarons. Using the cumulant expansion approach (similar to Refs. [62,63]), a full cascade of replica can be obtained. In the framework of the cumulant expansion, the Green's function can be written as

$$G(\mathbf{k},t) = -iZ_{\mathbf{k}}\Theta(t)e^{i(-\varepsilon_{\mathbf{k}}+\mu+\Delta_{\mathbf{k}}+i\eta)t}e^{O_{\mathbf{k}}(t)}, \tag{H3}$$

where

$$O_{\mathbf{k}}(t) = \int_{-\infty}^{\infty} d\omega \frac{|\mathrm{Im}[\Sigma(\mathbf{k},\omega+\varepsilon_{\mathbf{k}})]|}{\pi\omega^2}e^{-i\omega t} \tag{H4}$$

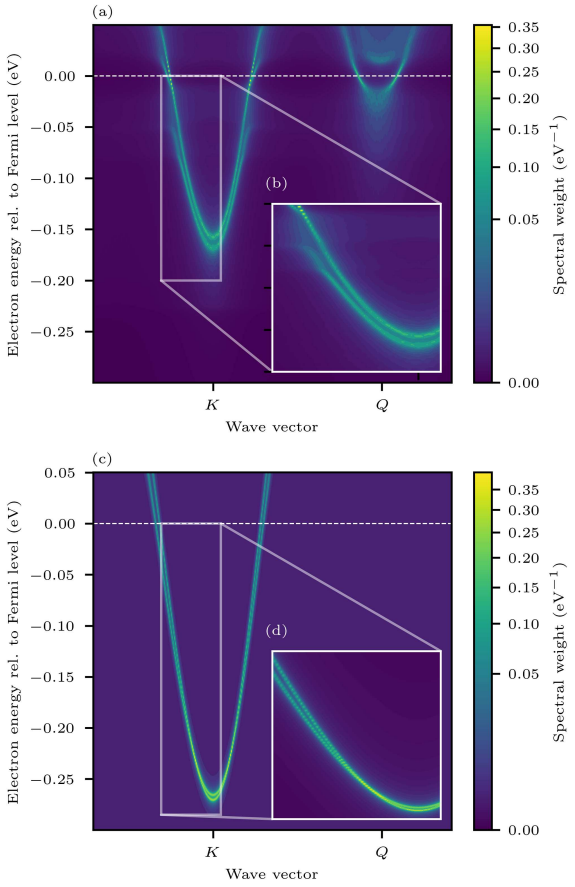

FIG. 10. Conduction band spectral function with Fan-Migdal self-energy at different valley occupations. (a), (b) K and Q valleys are occupied. (c), (d) Only K valleys but not Q valleys are occupied. Hence, the phonon-induced kinks and band cuts visible in (b) are no longer realized in (d).

captures the induction of shakeoff bands,

$$\Delta_{\mathbf{k}} = \int_{-\infty}^{\infty} d\omega \frac{|\mathrm{Im}[\Sigma(\mathbf{k}, \omega + \varepsilon_{\mathbf{k}})]|}{\pi\omega} \tag{H5}$$

shifts the quasiparticle dispersion, and

$$Z_{\mathbf{k}} = \exp\left(-\int_{-\infty}^{\infty} d\omega \frac{|\mathrm{Im}[\Sigma(\mathbf{k}, \omega + \varepsilon_{\mathbf{k}})]|}{\pi\omega^2}\right) \tag{H6}$$

acts as a renormalizing factor. By construction, to first order in the perturbation strength the Fan-Migdal self-energy and the cumulant expansion must give the same contribution. $Z_{\mathbf{k}}$ can thus be extracted from the *ab initio* Fan-Migdal self-energy. In the case of occupied K valley and unoccupied Q valley, we obtain $Z_K \approx 0.9$. Therefore, the maximal redistributable spectral weight in a cumulant expansion treatment is bound to approximately 10%. This goes against the experimental observations depicted in Fig. 3(c), where spectral weight redistribution is much larger than 10%. In conclusion, neither the Fan-Migdal self-energy nor a cumulant expansion treatment explains the polaronic replica seen in experiment. Thus, a monopolaron explanation can be ruled out here.

APPENDIX I: METASTABLE POLARONIC DEFORMATIONS

The resulting size and shape of the polaronic deformation depend on the amount of doping in the investigated 18×18 MoS_2 supercell. While Fig. 4 of the main text shows the instability of n-doped SL MoS_2 toward multipolaronic deformations when introducing four additional electrons into the supercell, a doping of only three additional electrons results in metastable polaronic deformations in n-doped MoS_2; see Fig. 11. The relaxed structure in Fig. 11(a) shows the breaking of the rotational and of most (vertical) mirror plane symmetries of the system. A doping below three additional electrons in the supercell does not result in any instability toward localized polaronic deformations.

APPENDIX J: DEPENDENCE ON SUPERCELL SIZE

Our analysis shows nearly no dependence of the multipolaronic displacement pattern and the corresponding total energy gain on the size of the supercell used in the simulation. We show the relaxed crystal structures for a doping of four additional electrons on supercell sizes of 6×6, 12×12, and 18×18 in Fig. 12 (for 18×18, see Fig. 4 as well). For each supercell with a size large enough to contain the multipolaronic distortion, the relaxation results in the same displacement pattern as shown in Fig. 4 of the main text. Below each relaxed crystal structure, the corresponding total energy as a function of the displacement can be found. The energy gained by the relaxation into the multipolaronic displacement equals a binding energy of about 100 meV and proves independent of the supercell size as well. This constancy of the binding energy is to be expected as a direct consequence of the omission of explicit Coulomb interactions between charge carriers in our downfolding model. For supercell sizes 12×12 and 18×18, the energy barrier between the symmetric structure and the multipolaronic distortion is comparable as well, while it is shown to be smaller for 6×6.

APPENDIX K: DECOMPOSITION OF POLARONIC DISTORTION INTO NORMAL MODES

The structure factor of the stable polaronic deformations [see Fig. 4(c) in the main text] reveals a finite range of $\mathbf{k}$ points contributing to the localized distortion pattern, with

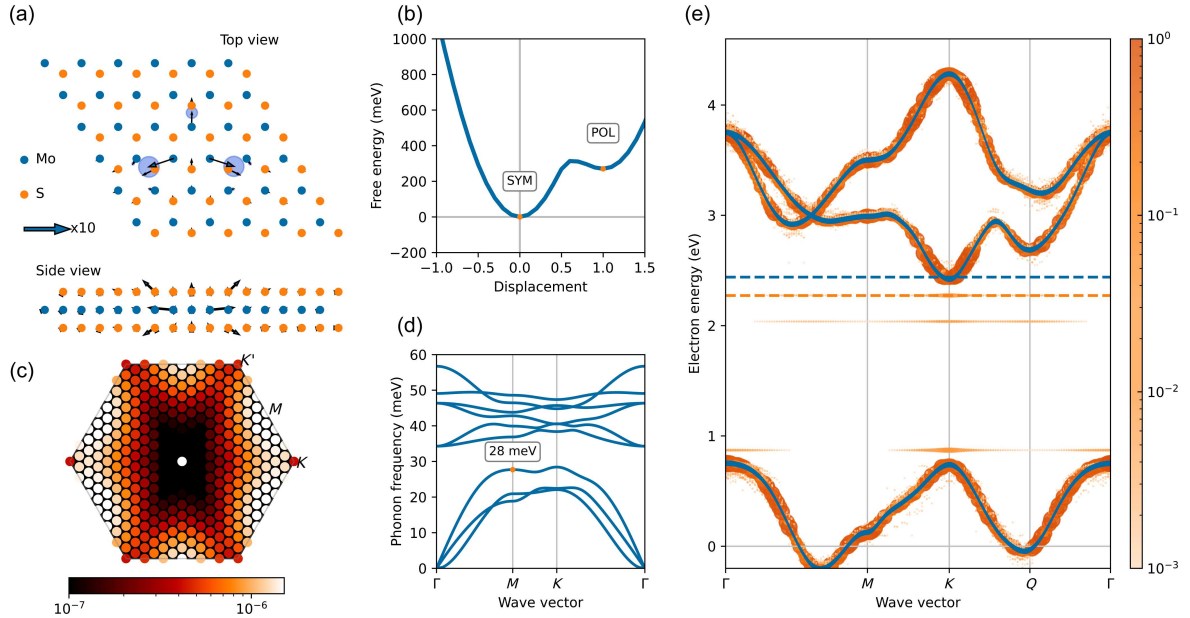

FIG. 11. Doping dependence of polaronic deformations. This figure was created in analogy to Fig. 4 of the main text; see there for more detailed information on the panels. (a) Enlargement of relaxed crystal structure based on *ab initio* model calculations on an 18×18 supercell with a lattice constant of 3.19 Å at an electronic doping of $0.0093e^-$ per formula unit of MoS_2. The doping results in three additional electrons per supercell and blue circles indicate the localization of these additional electrons. We find a metastable polaronic deformation and a lowering of the symmetry of the system. (b) Total energy as function of displacement for the metastable polaronic deformation shown in (a). (c) Structure factor $S(\mathbf{q})$ for the relaxed geometry seen in (a), which also shows the lowering of the symmetry. (d) Phonon bands obtained via DFPT at an electronic doping of $0.01e^-/MoS_2$. (e) Band structure of low-energy subspace as obtained by DFT (blue) and after the *ab initio* model relaxation (orange). The polaron formation is accompanied by the appearance of dispersionless states deep inside the gap which pull down the Fermi level (dashed lines).

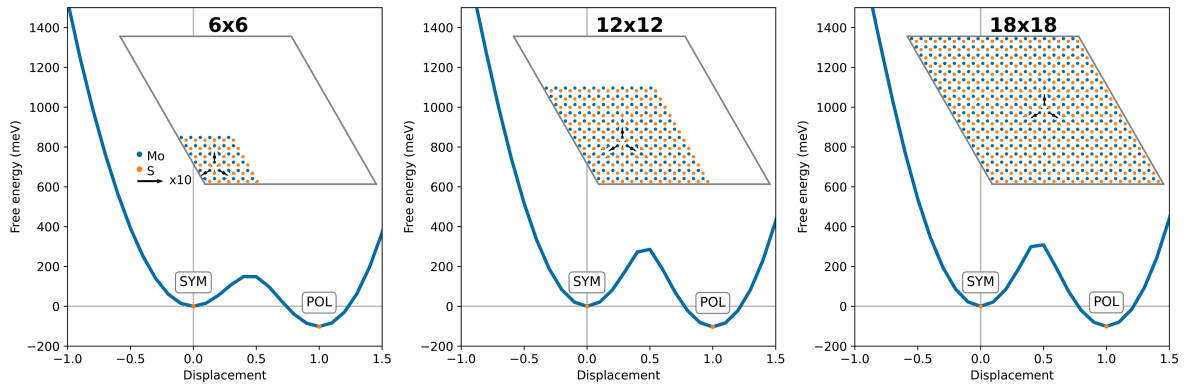

FIG. 12. Independence of the displacement pattern and the corresponding energy gain on the supercell size. For the different supercell sizes 6×6, 12×12, and 18×18, the same stable displacement pattern can be found for a doping of four additional electrons in the supercell; see relaxed crystal structures at the top. This holds true as long as the size of the supercell can accommodate the size of the multipolaronic displacement. For all simulated supercells, the relaxation into the displacement pattern results in the essentially same binding energy of about 100 meV due to not accounting for electron-electron interactions in our model; see the corresponding total energy as a function of the displacement shown below each structure.

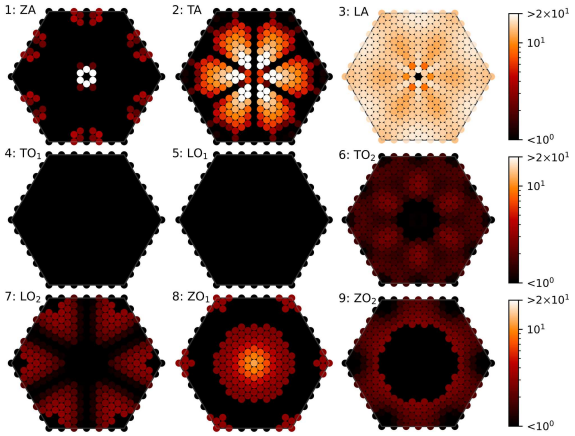

FIG. 13. Decomposition of the stable polaronic distortion into normal modes. Since the structure factor in Fig. 4(c) of the main text shows a range of $\mathbf{k}$ points contributing to the localized distortion pattern, peaking around the M point, the contributions of each normal mode to the structure factor are analyzed. The stable polaronic displacement pattern in Fig. 4(a) of the main text is decomposed into the nine normal modes, which are each labeled at the top. The bounds of the logarithmic color bar are chosen for the best visibility of each relevant contribution. The only notable contribution between the K and M point stems from the LA mode (plot 3, upper right), which therefore dominates the localized polaronic displacements with four additional electrons doped.

a peak in reciprocal space around the M point. To analyze the contributions stemming from each normal mode, the decomposition of the polaronic displacement pattern in Fig. 4 of the main text into normal modes is shown in Fig. 13 (modes are labeled). The most notable contribution around the relevant $\mathbf{k}$ points stems from the LA mode (see upper right-hand panel), which therefore dominates the polaronic displacements resulting from the doping of four additional electrons into the system. The phonon dispersion [see Fig. 4(d)] shows a flattening of the LA mode around approximately 28 meV between K and M, which agrees well with the experimental observation of the bosonic energy of $\Omega_0 = 24 \pm 4$ meV.

APPENDIX L: MOMENTUM DIFFERENCES *KQ* AND Γ*M*

To visualize how phonons with crystal momentum of the M point scatter electrons between Q and K points, we sketch the Brillouin zone of MoS_2 with the high-symmetry points M, K (K'), and Q (Q') in Fig. 14. The vector connecting Γ with M equals the distance between Q' and K or between Q and K'. The blue shaded background of the Brillouin zone shows the squared modulus of the electron-phonon coupling between the conduction band and the LA mode as a function of electronic momentum $\mathbf{k}$. It quantifies

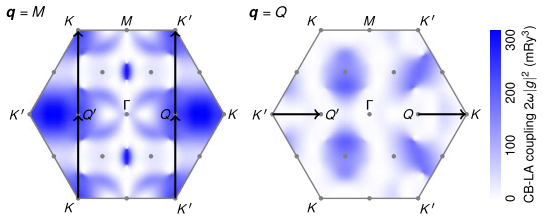

FIG. 14. Visualization of the equality between the crystal momentum of M-point phonons and the distance between Q (Q') and K' (K) point in the Brillouin zone of MoS_2. The relevant high-symmetry points Γ, M, K (K'), and Q (Q') are labeled. It is clear that the wave vector between Γ and M corresponds to the distance between Q' and K or between Q and K'; see left-hand plot of the figure. The squared modulus of the electron-phonon coupling between the conduction band and the LA mode as a function of $\mathbf{k}$ is visualized via the blue shaded background of the Brillouin zone and quantifies the scattering of electrons from $\mathbf{k}$ to $\mathbf{k} + \mathbf{q}$. In case of $\mathbf{q} = M$, the coupling strength shows significant contributions around the relevant regions. The connection between K and Q is additionally also possible via $\mathbf{q} = Q$, for which the electron-phonon coupling strength shows no relevant contributions.

the scattering of electrons from $\mathbf{k}$ to $\mathbf{k} + \mathbf{q}$, where $\mathbf{q}$ is the phonon momentum and fixed. In the case of $\mathbf{q} = M$ (see left-hand panel), the coupling strength in the relevant $\mathbf{k}$ regions (near the starting points of the arrows) is significant. There are further $\mathbf{q}$ values that connect the different conduction band valleys, namely $\mathbf{q} = Q$ and Q' (see right-hand panel), which connect Q to K and K' to Q' and vice versa. However, here the electron-phonon coupling in the relevant $\mathbf{k}$ regions is comparably smaller.

[1] M. M. Ugeda, A. J. Bradley, Y. Zhang, S. Onishi, Y. Chen, W. Ruan, C. Ojeda-Aristizabal, H. Ryu, M. T. Edmonds, H.-Z. Tsai, A. Riss, S.-K. Mo, D. Lee, A. Zettl, Z. Hussain, Z.-X. Shen, and M. F. Crommie, *Characterization of collective ground states in single-layer* $NbSe_2$, Nat. Phys. **12**, 92 (2016).

[2] L. J. Li, E. C. T. O'Farrell, K. P. Loh, G. Eda, B. Özyilmaz, and A. H. Castro Neto, *Controlling many-body states by the electric-field effect in a two-dimensional material*, Nature (London) **529**, 185 (2016).

[3] Y. Ge and A. Y. Liu, *Phonon-mediated superconductivity in electron-doped single-layer* MoS_2*: A first-principles prediction*, Phys. Rev. B **87**, 241408(R) (2013).

[4] M. Rösner, S. Haas, and T. O. Wehling, *Phase diagram of electron-doped dichalcogenides*, Phys. Rev. B **90**, 245105 (2014).

[5] P. Garcia-Goiricelaya, J. Lafuente-Bartolome, I. G. Gurtubay, and A. Eiguren, *Emergence of large nonadiabatic effects induced by the electron-phonon interaction on the complex vibrational quasiparticle spectrum of doped monolayer* MoS_2, Phys. Rev. B **101**, 054304 (2020).

[6] M. K. Bin Subhan, A. Suleman, G. Moore, P. Phu, M. Hoesch, H. Kurebayashi, C. A. Howard, and S. R. Schofield, *Charge density waves in electron-doped molybdenum disulfide*, Nano Lett. **21**, 5516 (2021).

[7] G. Marini and M. Calandra, *Phonon mediated superconductivity in field-effect doped molybdenum dichalcogenides*, 2D Mater. **10**, 015013 (2022).

[8] J. M. Lu, O. Zheliuk, I. Leermakers, N. F. Q. Yuan, U. Zeitler, K. T. Law, and J. T. Ye, *Evidence for two-dimensional Ising superconductivity in gated* MoS_2, Science **350**, 1353 (2015).

[9] D. Costanzo, S. Jo, H. Berger, and A. F. Morpurgo, *Gate-induced superconductivity in atomically thin* MoS_2 *crystals*, Nat. Nanotechnol. **11**, 339 (2016).

[10] Y. Saito, Y. Nakamura, M. S. Bahramy, Y. Kohama, J. Ye, Y. Kasahara, Y. Nakagawa, M. Onga, M. Tokunaga, T. Nojima, Y. Yanase, and Y. Iwasa, *Superconductivity protected by spin-valley locking in ion-gated* MoS_2, Nat. Phys. **12**, 144 (2016).

[11] Y. Fu, E. Liu, H. Yuan, P. Tang, B. Lian, G. Xu, J. Zeng, Z. Chen, Y. Wang, W. Zhou, K. Xu, A. Gao, C. Pan, M. Wang, B. Wang, S.-C. Zhang, Y. Cui, H. Y. Hwang, and F. Miao, *Gated tuned superconductivity and phonon softening in monolayer and bilayer* MoS_2, npj Quantum Mater. **2**, 52 (2017).

[12] D. Costanzo, H. Zhang, B. A. Reddy, H. Berger, and A. F. Morpurgo, *Tunnelling spectroscopy of gate-induced superconductivity in* MoS_2, Nat. Nanotechnol. **13**, 483 (2018).

[13] H. L. Zhuang, M. D. Johannes, A. K. Singh, and R. G. Hennig, *Doping-controlled phase transitions in single-layer* MoS_2, Phys. Rev. B **96**, 165305 (2017).

[14] D. Emin, *Polarons* (Cambridge University Press, Cambridge, England, 2012).

[15] C. Franchini, M. Reticcioli, M. Setvin, and U. Diebold, *Polarons in materials*, Nat. Rev. Mater. **6**, 560 (2021).

[16] M. Kang, S. W. Jung, W. J. Shin, Y. Sohn, S. H. Ryu, T. K. Kim, M. Hoesch, and K. S. Kim, *Holstein polaron in a valley-degenerate two-dimensional semiconductor*, Nat. Mater. **17**, 676 (2018).

[17] P. Garcia-Goiricelaya, J. Lafuente-Bartolome, I. G. Gurtubay, and A. Eiguren, *Long-living carriers in a strong electron–phonon interacting two-dimensional doped semiconductor*, Commun. Phys. **2**, 81 (2019).

[18] C. van Efferen, C. Murray, J. Fischer, C. Busse, H.-P. Komsa, T. Michely, and W. Jolie, *Metal-insulator transition in monolayer* MoS_2 *via contactless chemical doping*, 2D Mater. **9**, 025026 (2022).

[19] F. Caruso, P. Amsalem, J. Ma, A. Aljarb, T. Schultz, M. Zacharias, V. Tung, N. Koch, and C. Draxl, *Two-dimensional plasmonic polarons in n-doped monolayer* MoS_2, Phys. Rev. B **103**, 205152 (2021).

[20] E. Khestanova, T. Ivanova, R. Gillen, A. D'Elia, O. N. Gallego Lacey, L. Wysocki, A. Grüneis, V. Kravtsov, W. Strupinski, J. Maultzsch, V. Kandyba, M. Cattelan, A. Barinov, J. Avila, P. Dudin, and B. V. Senkovskiy, *Robustness of momentum-indirect interlayer excitons in* MoS_2/WSe_2 *heterostructure against charge carrier doping*, ACS Photonics **10**, 1159 (2023).

[21] W. H. Sio and F. Giustino, *Polarons in two-dimensional atomic crystals*, Nat. Phys. **19**, 629 (2023).

[22] G. Verbist, M. A. Smondyrev, F. M. Peeters, and J. T. Devreese, *Strong-coupling analysis of large bipolarons in two and three dimensions*, Phys. Rev. B **45**, 5262 (1992).

[23] R. L. Frank, E. H. Lieb, R. Seiringer, and L. E. Thomas, *Bipolaron and n-polaron binding energies*, Phys. Rev. Lett. **104**, 210402 (2010).

[24] A. Schobert, J. Berges, E. G. C. P. van Loon, M. A. Sentef, S. Brener, M. Rossi, and T. O. Wehling, *Ab initio electron-lattice downfolding: Potential energy landscapes, anharmonicity, and molecular dynamics in charge density wave materials*, SciPost Phys. **16**, 046 (2024).

[25] C. Zhang, Y. Chen, A. Johnson, M.-Y. Li, L.-J. Li, P. C. Mende, R. M. Feenstra, and C.-K. Shih, *Probing critical point energies of transition metal dichalcogenides: Surprising indirect gap of single layer* WSe_2, Nano Lett. **15**, 6494 (2015).

[26] C. Murray, W. Jolie, J. A. Fischer, J. Hall, C. van Efferen, N. Ehlen, A. Grüneis, C. Busse, and T. Michely, *Comprehensive tunneling spectroscopy of quasifreestanding* MoS_2 *on graphene on* Ir(111), Phys. Rev. B **99**, 115434 (2019).

[27] C. Murray, C. van Efferen, W. Jolie, J. A. Fischer, J. Hall, A. Rosch, A. V. Krasheninnikov, H.-P. Komsa, and T. Michely, *Band bending and valence band quantization at line defects in* MoS_2, ACS Nano **14**, 9176 (2020).

[28] K. A. Cochrane, J.-H. Lee, C. Kastl, J. B. Haber, T. Zhang, A. Kozhakhmetov, J. A. Robinson, M. Terrones, J. Repp, J. B. Neaton, A. Weber-Bargioni, and B. Schuler, *Spin-dependent vibronic response of a carbon radical ion in two-dimensional* WS_2, Nat. Commun. **12**, 7287 (2021).

[29] H. Tornatzky, R. Gillen, H. Uchiyama, and J. Maultzsch, *Phonon dispersion in* MoS_2, Phys. Rev. B **99**, 144309 (2019).

[30] U. Lundin and R. H. McKenzie, *Temperature dependence of polaronic transport through single molecules and quantum dots*, Phys. Rev. B **66**, 075303 (2002).

[31] M. Galperin, M. A. Ratner, and A. Nitzan, *Inelastic electron tunneling spectroscopy in molecular junctions: Peaks and dips*, J. Chem. Phys. **121**, 11965 (2004).

[32] G. A. Skorobagatko, *Resonant polaron-assisted tunneling of strongly interacting electrons through a single-level vibrating quantum dot*, Phys. Rev. B **85**, 075310 (2012).

[33] B. C. Stipe, M. A. Rezaei, and W. Ho, *Single-molecule vibrational spectroscopy and microscopy*, Science **280**, 1732 (1998).

[34] K. J. Franke and J. I. Pascual, *Effects of electron-vibration coupling in transport through single molecules*, J. Phys. Condens. Matter **24**, 394002 (2012).

[35] N. Krane, C. Lotze, G. Reecht, L. Zhang, A. L. Briseno, and K. J. Franke, *High-resolution vibronic spectra of molecules on molybdenum disulfide allow for rotamer identification*, ACS Nano **12**, 11698 (2018).

[36] N. Zou and K. A. Chao, *Inelastic electron resonant tunneling through a double-barrier nanostructure*, Phys. Rev. Lett. **69**, 3224 (1992).

[37] N. S. Wingreen, K. W. Jacobsen, and J. W. Wilkins, *Resonant tunneling with electron-phonon interaction: An exactly solvable model*, Phys. Rev. Lett. **61**, 1396 (1988).

[38] W. H. Sio, C. Verdi, S. Poncé, and F. Giustino, *Ab initio theory of polarons: Formalism and applications*, Phys. Rev. B **99**, 235139 (2019).

[39] J. Lafuente-Bartolome, C. Lian, W. H. Sio, I. G. Gurtubay, A. Eiguren, and F. Giustino, *Ab initio self-consistent many-body theory of polarons at all couplings*, Phys. Rev. B **106**, 075119 (2022).

[40] L. Vitali, M. A. Schneider, K. Kern, L. Wirtz, and A. Rubio, *Phonon and plasmon excitation in inelastic electron tunneling spectroscopy of graphite*, Phys. Rev. B **69**, 121414(R) (2004).

[41] S. Moser, L. Moreschini, J. Jaćimović, O. S. Barišić, H. Berger, A. Magrez, Y. J. Chang, K. S. Kim, A. Bostwick, E. Rotenberg, L. Forro, and M. Grioni, *Tunable polaronic conduction in anatase* TiO_2, Phys. Rev. Lett. **110**, 196403 (2013).

[42] H. Liu, A. Wang, P. Zhang, C. Ma, C. Chen, Z. Liu, Y.-Q. Zhang, B. Feng, P. Cheng, J. Zhao, L. Chen, and K. Wu, *Atomic-scale manipulation of single-polaron in a two-dimensional semiconductor*, Nat. Commun. **14**, 3690 (2023).

[43] M. Cai, M.-P. Miao, Y. Liang, Z. Jiang, Z.-Y. Liu, W.-H. Zhang, X. Liao, L.-F. Zhu, D. West, S. Zhang, and Y.-S. Fu, *Manipulating single excess electrons in monolayer transition metal dihalide*, Nat. Commun. **14**, 3691 (2023).

[44] E. V. L. de Mello and J. Ranninger, *Dynamical properties of small polarons*, Phys. Rev. B **55**, 14872 (1997).

[45] J. Ranninger, *Spectral properties of small-polaron systems*, Phys. Rev. B **48**, 13166 (1993).

[46] M. Hohenadler, G. Wellein, A. Alvermann, and H. Fehske, *Many-polaron problem by cluster perturbation theory*, Physica (Amsterdam) **378-380B**, 64 (2006).

[47] M. Hohenadler, D. Neuber, W. von der Linden, G. Wellein, J. Loos, and H. Fehske, *Photoemission spectra of many-polaron systems*, Phys. Rev. B **71**, 245111 (2005).

[48] M. Capone, P. Carta, and S. Ciuchi, *Dynamical mean field theory of polarons and bipolarons in the half-filled Holstein model*, Phys. Rev. B **74**, 045106 (2006).

[49] W. Jolie, C. Murray, P. S. Weiß, J. Hall, F. Portner, N. Atodiresei, A. V. Krasheninnikov, C. Busse, H. P. Komsa, A. Rosch, and T. Michely, *Tomonaga-Luttinger liquid in a box: Electrons confined within* MoS_2 *mirror-twin boundaries*, Phys. Rev. X **9**, 011055 (2019).

[50] C. van Efferen, J. Fischer, T. A. Costi, A. Rosch, T. Michely, and W. Jolie, *Modulated Kondo screening along magnetic mirror twin boundaries in monolayer* MoS_2, Nat. Phys. **20**, 82 (2024).

[51] https://www.nhr-verein.de/unsere-partner

[52] J. Coraux, A. T. N'Diaye, M. Engler, C. Busse, D. Wall, N. Buckanie, F.-J. Meyer zu Heringdorf, R. van Gastel, B. Poelsema, and T. Michely, *Growth of graphene on* Ir(111), New J. Phys. **11**, 039801 (2009).

[53] J. Hall, B. Pielić, C. Murray, W. Jolie, T. Wekking, C. Busse, M. Kralj, and T. Michely, *Molecular beam epitaxy of quasi-freestanding transition metal disulphide monolayers on van der Waals substrates: A growth study*, 2D Mater. **5**, 025005 (2018).

[54] P. Giannozzi *et al.*, *QUANTUM ESPRESSO: A modular and open-source software project for quantum simulations of materials*, J. Phys. Condens. Matter **21**, 395502 (2009).

[55] J. P. Perdew, K. Burke, and M. Ernzerhof, *Generalized gradient approximation made simple*, Phys. Rev. Lett. **77**, 3865 (1996).

[56] D. R. Hamann, *Optimized norm-conserving Vanderbilt pseudopotentials*, Phys. Rev. B **88**, 085117 (2013).

[57] M. van Setten, M. Giantomassi, E. Bousquet, M. Verstraete, D. Hamann, X. Gonze, and G.-M. Rignanese, *The PSEUDODOJO: Training and grading a 85 element optimized norm-conserving pseudopotential table*, Comput. Phys. Commun. **226**, 39 (2018).

[58] S. Poncé, E. Margine, C. Verdi, and F. Giustino, *EPW: Electron–phonon coupling, transport and superconducting properties using maximally localized Wannier functions*, Comput. Phys. Commun. **209**, 116 (2016).

[59] J. Berges, A. Schobert, E. G. C. P. van Loon, M. Rösner, and T. O. Wehling, *ELPHMOD: PYTHON modules for electron-phonon models* (2017), 10.5281/zenodo.5919991.

[60] D. Dombrowski, W. Jolie, M. Petrović, S. Runte, F. Craes, J. Klinkhammer, M. Kralj, P. Lazić, E. Sela, and C. Busse, *Energy-dependent chirality effects in quasifree-standing graphene*, Phys. Rev. Lett. **118**, 116401 (2017).

[61] N. Ehlen, J. Hall, B. V. Senkovskiy, M. Hell, J. Li, A. Herman, D. Smirnov, A. Fedorov, V. Y. Voroshnin, G. Di Santo *et al.*, *Narrow photoluminescence and Raman peaks of epitaxial* MoS_2 *on graphene*/Ir(111)., 2D Mater. **6**, 011006 (2018).

[62] S. Ulstrup, Y. in 't Veld, J. A. Miwa, A. J. H. Jones, K. M. McCreary, J. T. Robinson, B. T. Jonker, S. Singh, R. J. Koch, E. Rotenberg, A. Bostwick, C. Jozwiak, M. Rösner, and J. Katoch, *Observation of interlayer plasmon polaron in* graphene/WS_2 *heterostructures*, Nat. Commun. **15**, 3845 (2024).

[63] J. J. Kas, J. J. Rehr, and L. Reining, *Cumulant expansion of the retarded one-electron green function*, Phys. Rev. B **90**, 085112 (2014).

B Monolayer materials

B.1 $MoSe_2$

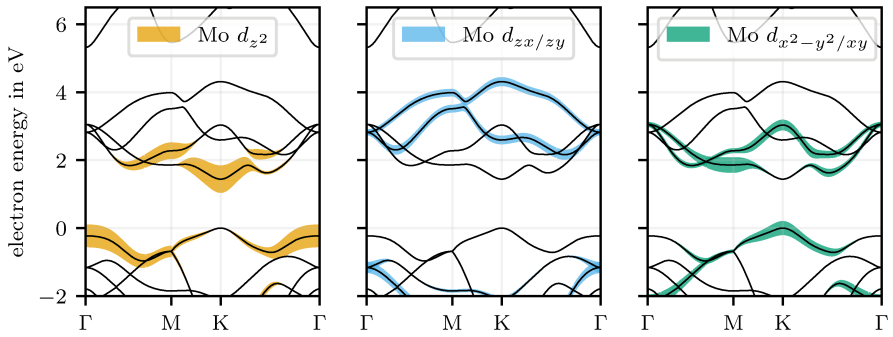

Figure B.1: *Projected bands of $MoSe_2$.*

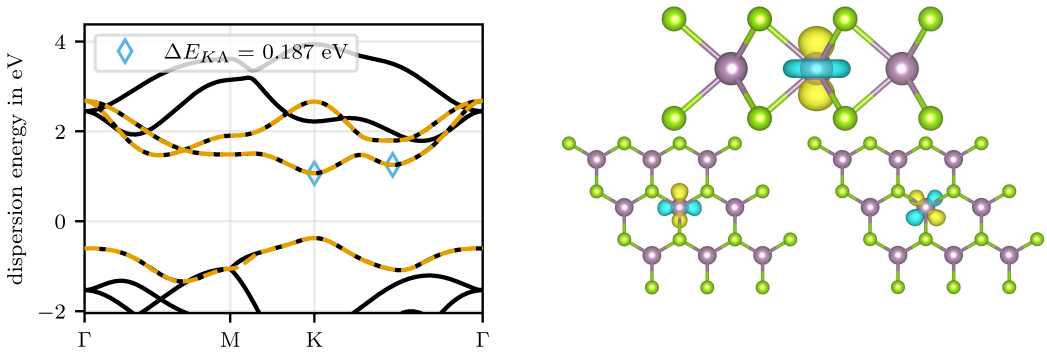

Figure B.2: *Wannier model of $MoSe_2$; Resulting electronic dispersion in a three band model and Wannier orbitals.*

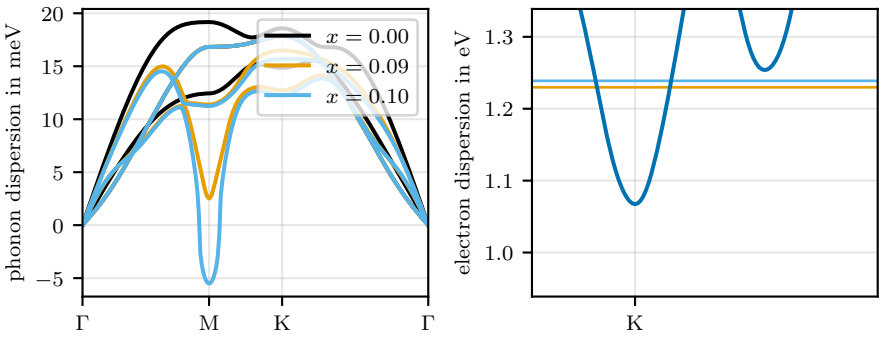

Figure B.3: *Phonon renormalisation under electron doping in $MoSe_2$ next to the electronic band structure with indication of Fermi level for given doping levels.*

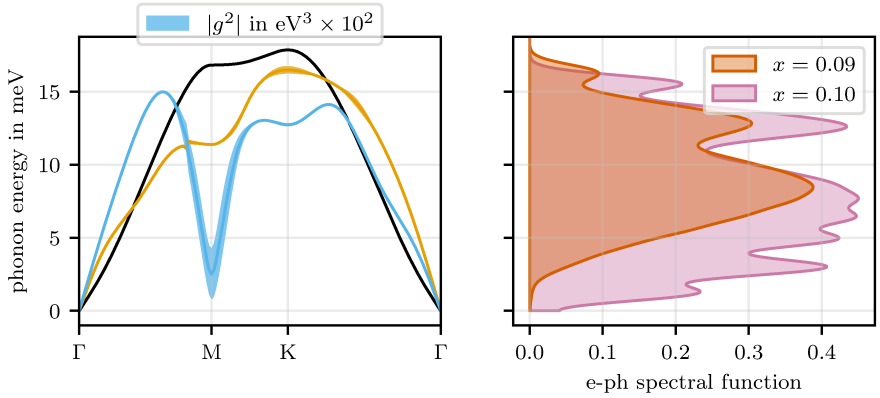

Figure B.4: *Electron-phonon coupling resolved to the accoustic phonon branches and electron-phonon spectral-function around the doping instability of $MoSe_2$.*

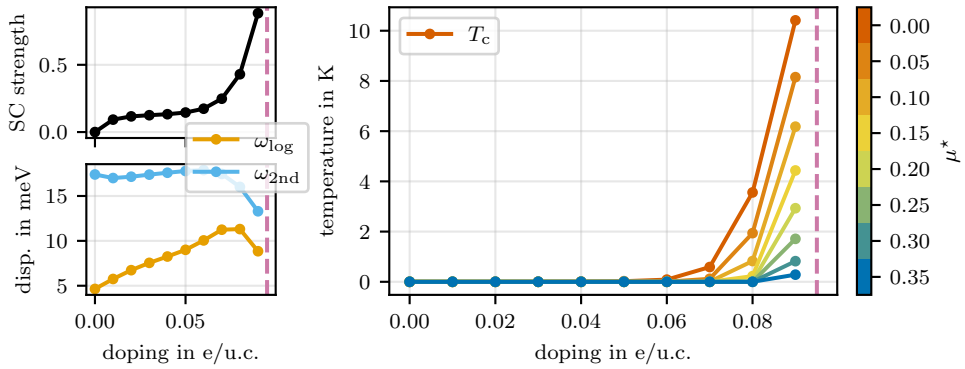

Figure B.5: *Electron-phonon coupling strength, frequency moments and critical temperature for superconductivity of $MoSe_2$.*

B.2 $MoTe_2$

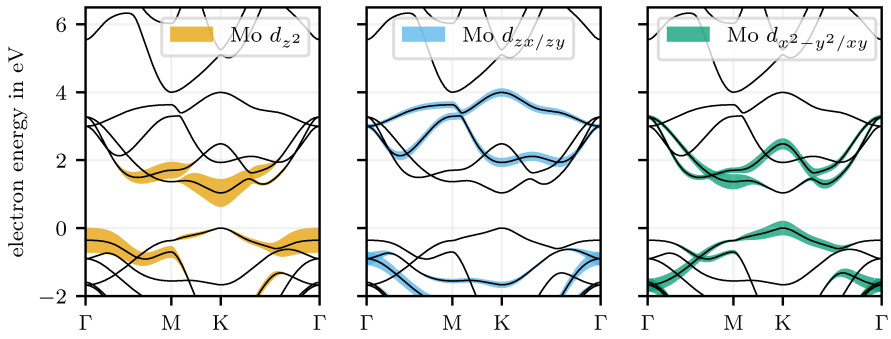

Figure B.6: *Projected bands of $MoTe_2$.*

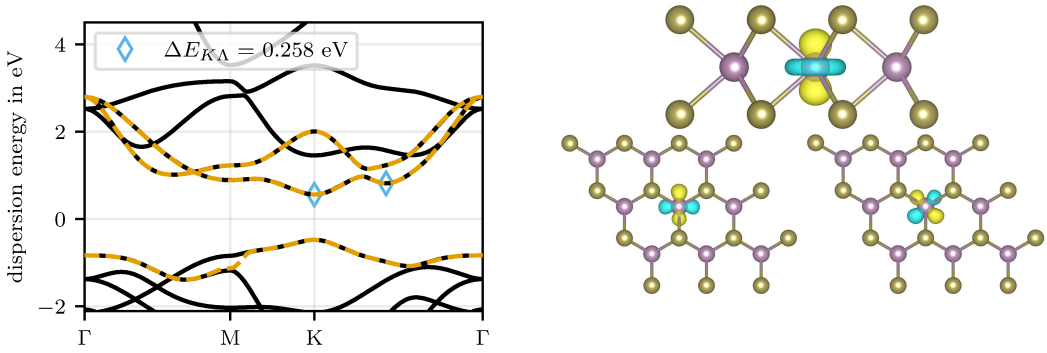

Figure B.7: *Wannier model of $MoTe_2$; Resulting electronic dispersion in a three band model and Wannier orbitals.*

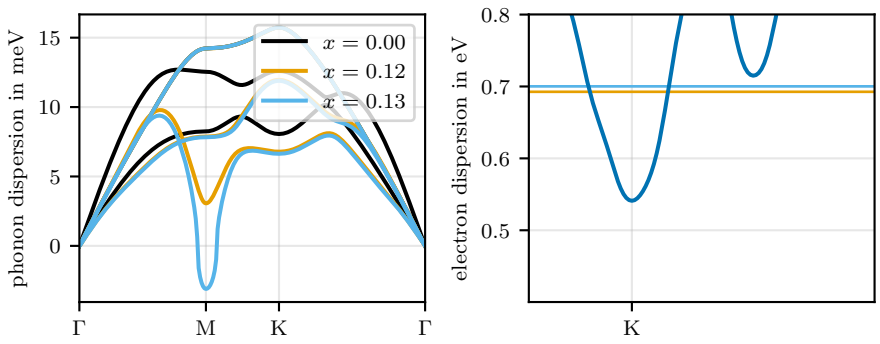

Figure B.8: *Phonon renormalisation under electron doping in $MoTe_2$ next to the electronic band structure with indication of Fermi level for given doping levels.*

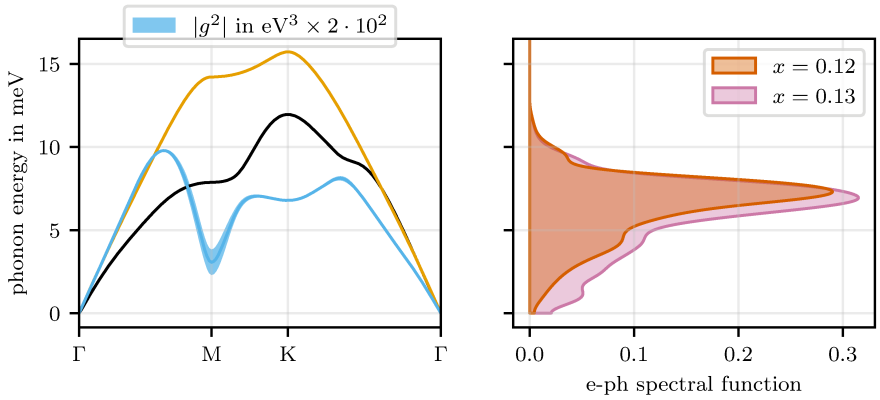

Figure B.9: *Electron-phonon coupling resolved to the accoustic phonon branches and electron-phonon spectral-function around the doping instability of $MoTe_2$.*

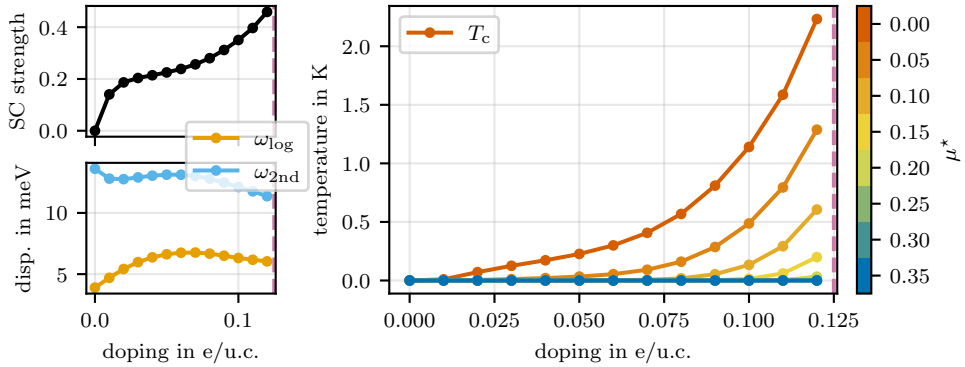

Figure B.10: *Electron-phonon coupling strength, frequency moments and critical temperature for superconductivity of $MoTe_2$.*

B.3 WS_2

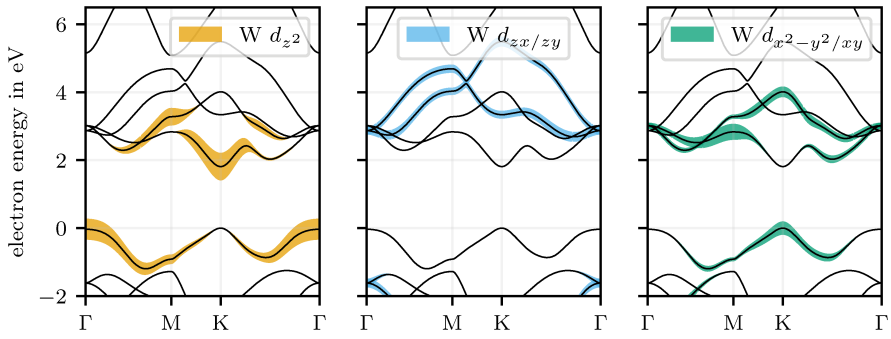

Figure B.11: *Projected bands of WS_2.*

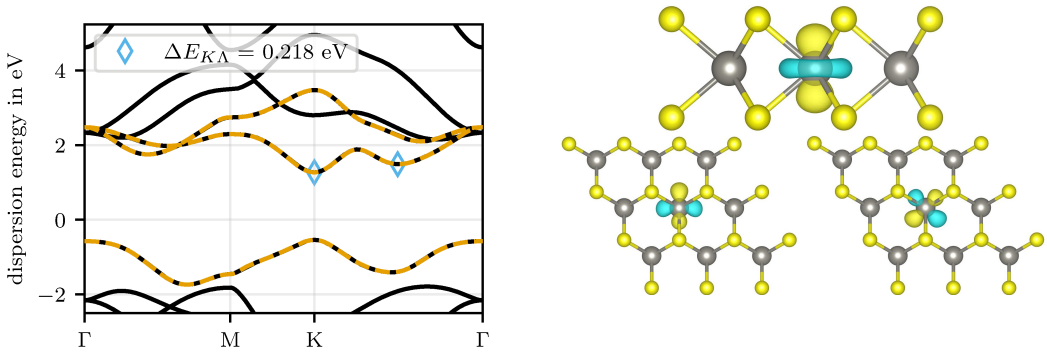

Figure B.12: *Wannier model of WS_2; Resulting electronic dispersion in a three band model and Wannier orbitals.*

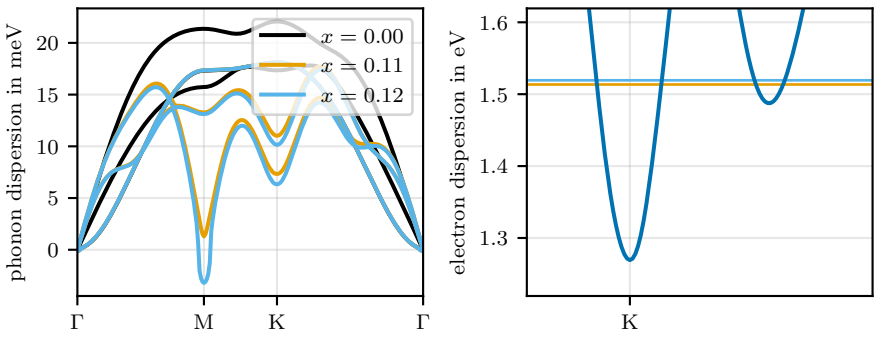

Figure B.13: *Phonon renormalisation under electron doping in WS_2 next to the electronic band structure with indication of Fermi level for given doping levels.*

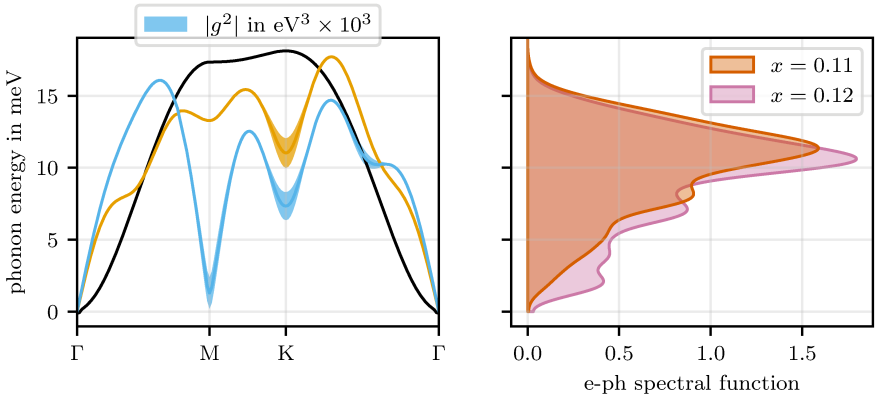

Figure B.14: *Electron-phonon coupling resolved to the accoustic phonon branches and electron-phonon spectral-function around the doping instability of WS_2.*

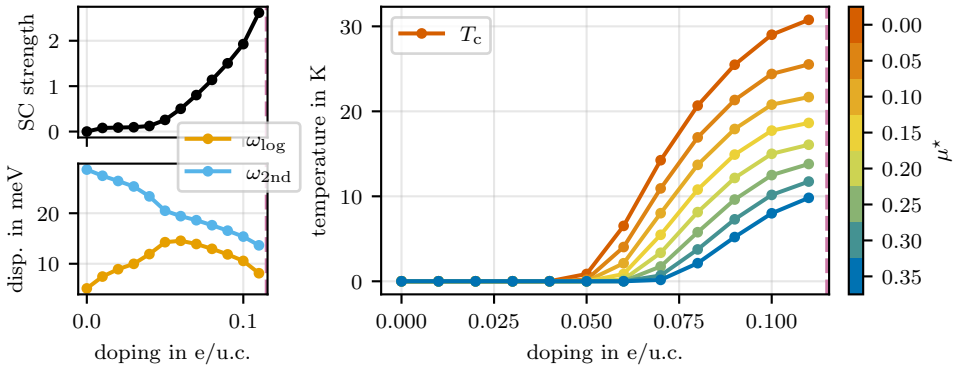

Figure B.15: *Electron-phonon coupling strength, frequency moments and critical temperature for superconductivity of WS_2.*

B.4 WSe_2

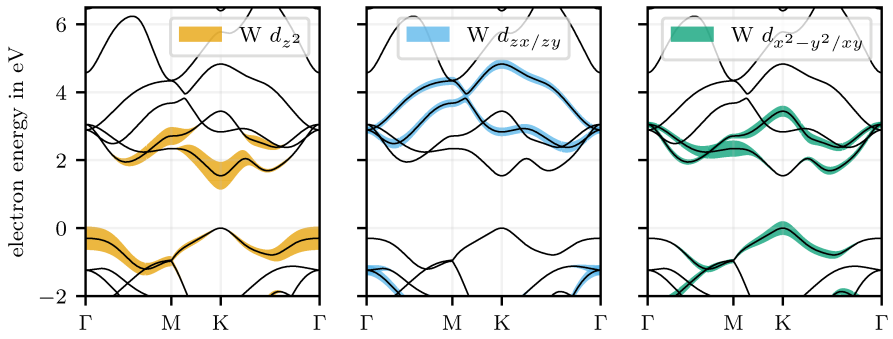

Figure B.16: *Projected bands of WSe_2.*

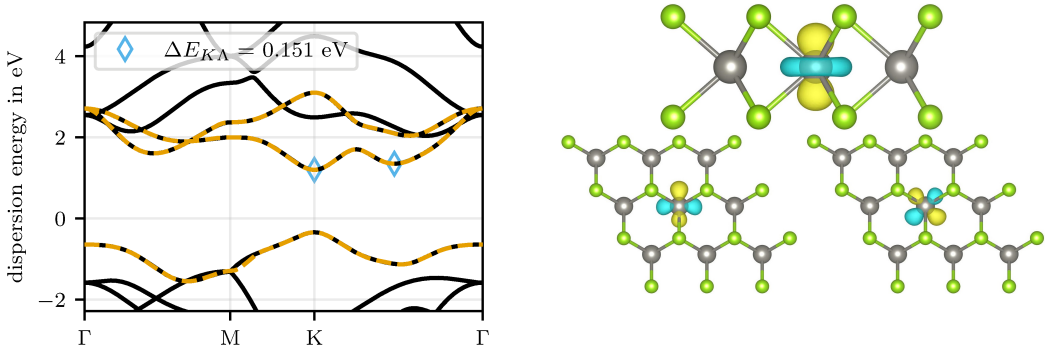

Figure B.17: *Wannier model of WSe_2; Resulting electronic dispersion in a three band model and Wannier orbitals.*

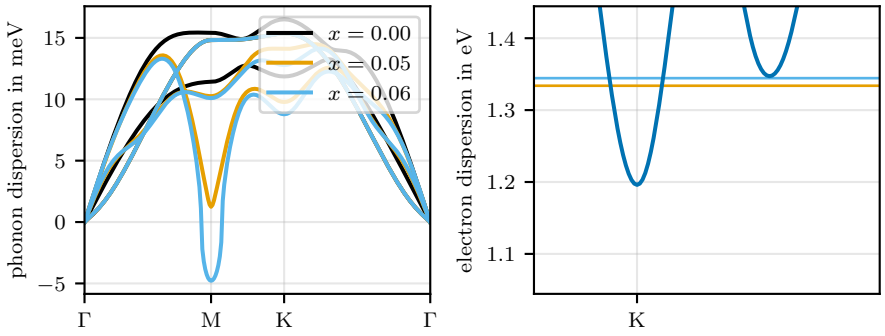

Figure B.18: *Phonon renormalisation under electron doping in WSe_2 next to the electronic band structure with indication of Fermi level for given doping levels.*

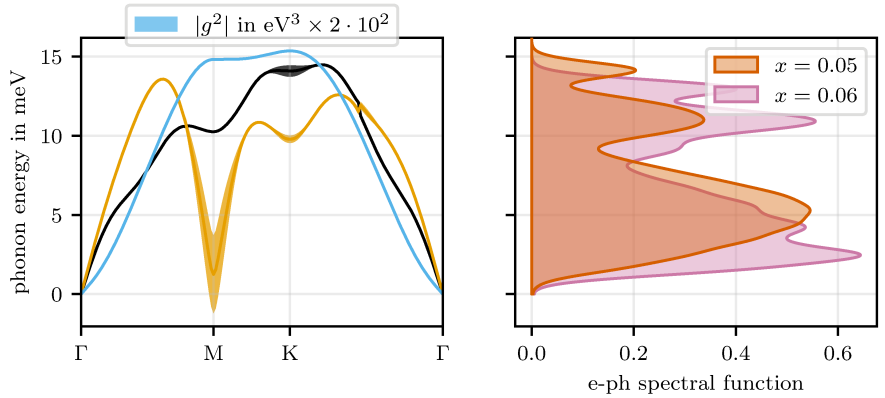

Figure B.19: *Electron-phonon coupling resolved to the accoustic phonon branches and electron-phonon spectral-function around the doping instability of WSe_2.*

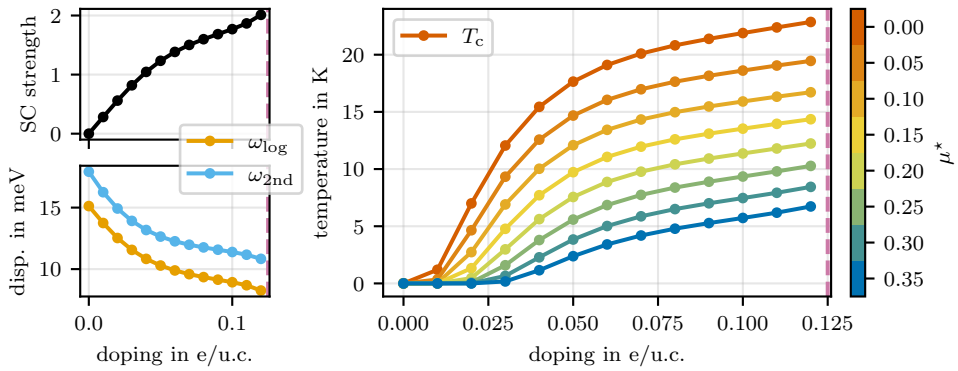

Figure B.20: *Electron-phonon coupling strength, frequency moments and critical temperature for superconductivity of WSe_2.*

B.5 WTe_2

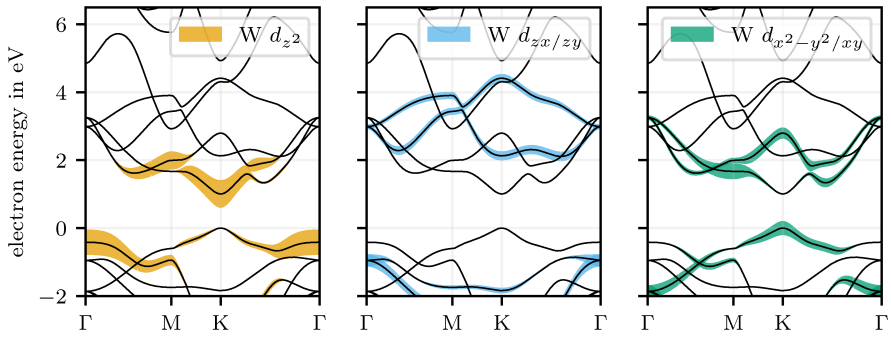

Figure B.21: *Projected bands of WTe_2.*

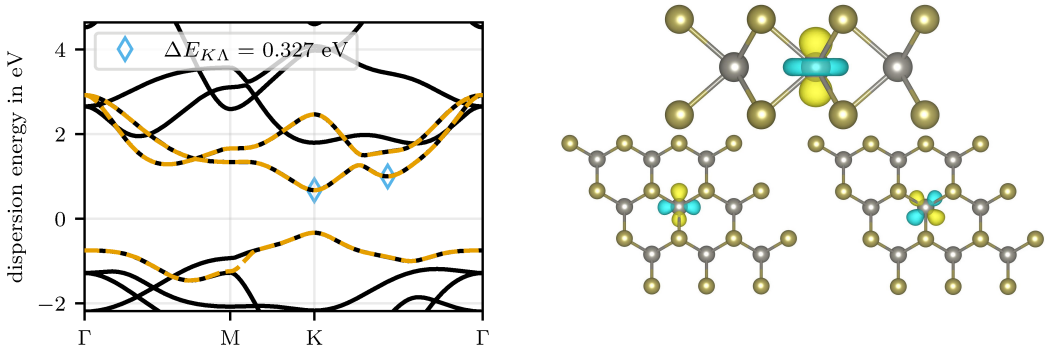

Figure B.22: *Wannier model of WTe_2; Resulting electronic dispersion in a three band model and Wannier orbitals.*

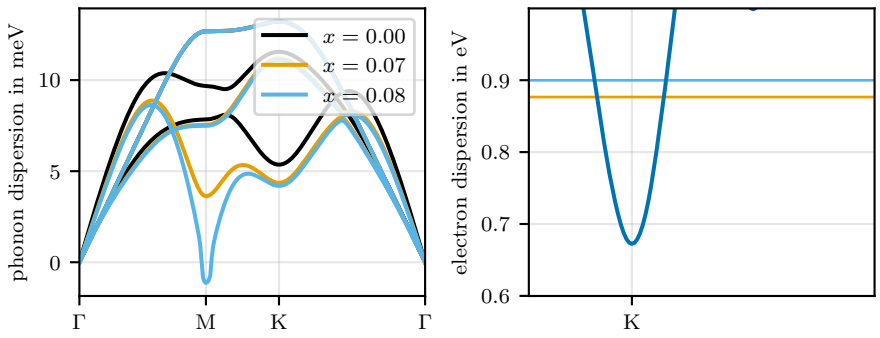

Figure B.23: *Phonon renormalisation under electron doping in WTe_2 next to the electronic band structure with indication of Fermi level for given doping levels.*

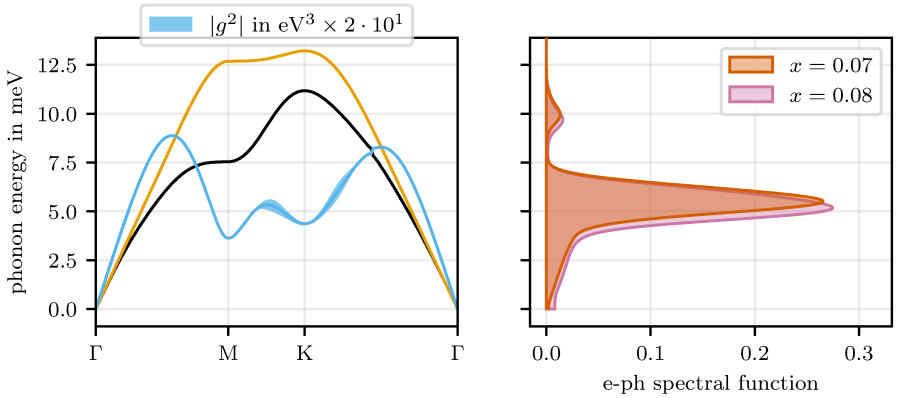

Figure B.24: *Electron-phonon coupling resolved to the accoustic phonon branches and electron-phonon spectral-function around the doping instability of WTe_2.*

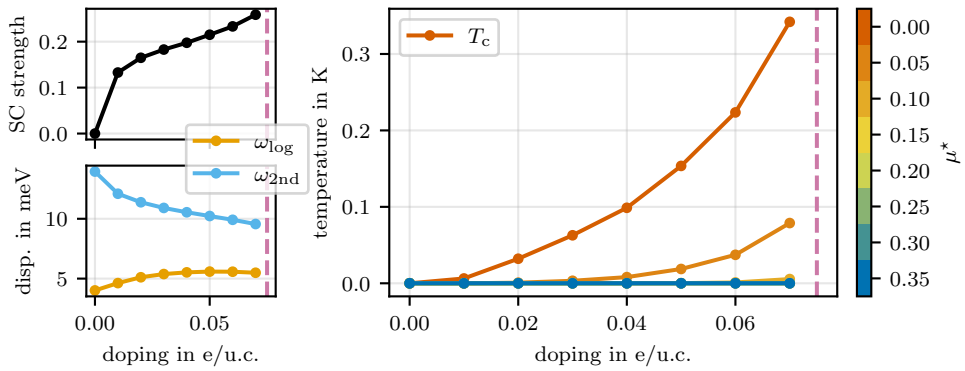

Figure B.25: *Electron-phonon coupling strength, frequency moments and critical temperature for superconductivity of WTe_2.*

B.6 MoS_2 – G_0W_0

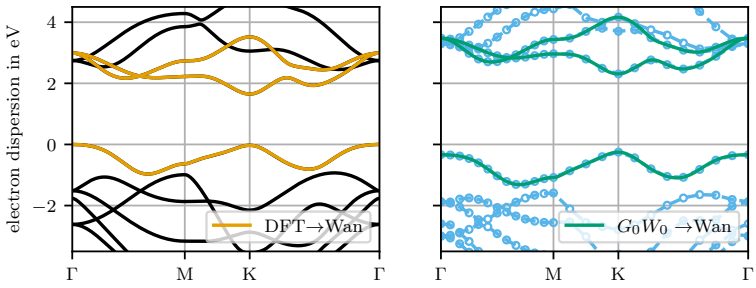

Figure B.26: *DFT and G_0W_0 band structure of monolayer MoS_2 as well as the downfolded Wannier model.*

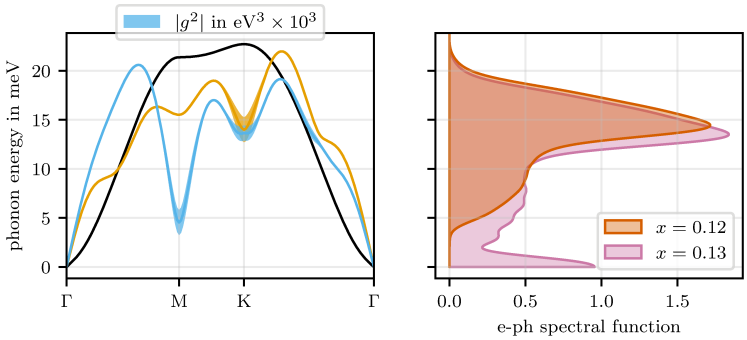

Figure B.27: *Electron-phonon coupling resolved to the accoustic phonon branches and electron-phonon spectral-function around the doping instability of G_0W_0-corrected MoS_2.*

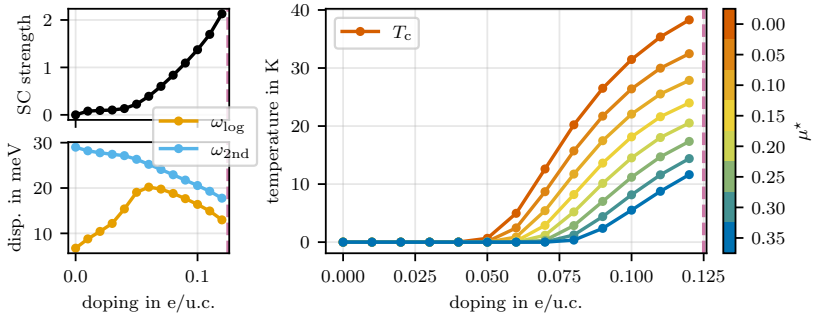

Figure B.28: *Electron-phonon coupling strength, frequency moments and critical temperature for superconductivity of G_0W_0-corrected MoS_2.*

B.7 $MoSe_2$ – G_0W_0

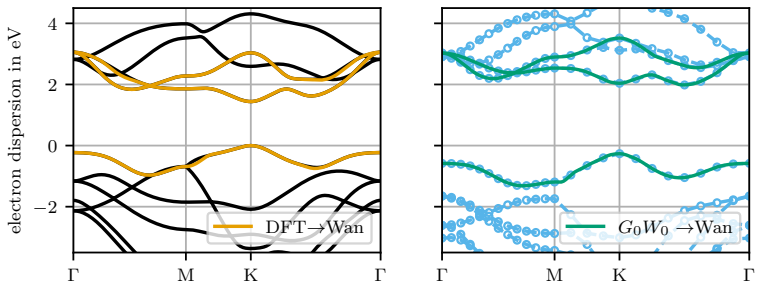

Figure B.29: *DFT and G_0W_0 band structure of monolayer $MoSe_2$ as well as the downfolded Wannier model.*

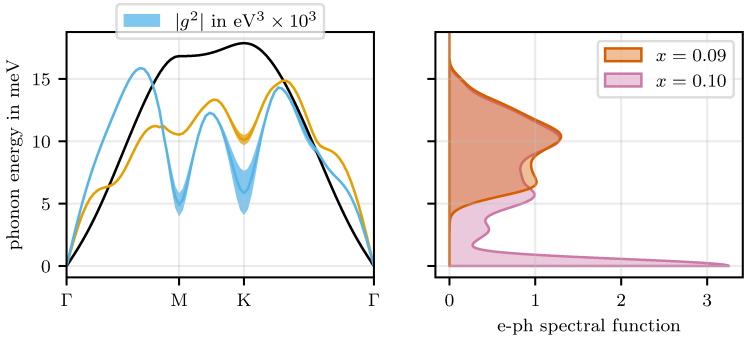

Figure B.30: *Electron-phonon coupling resolved to the accoustic phonon branches and electron-phonon spectral-function around the doping instability of G_0W_0-corrected $MoSe_2$.*

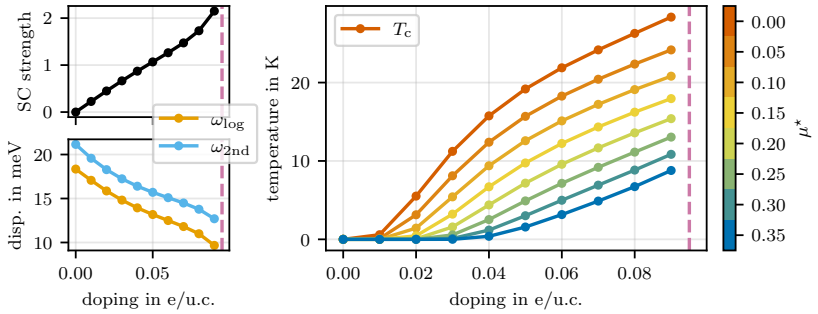

Figure B.31: *Electron-phonon coupling strength, frequency moments and critical temperature for superconductivity of G_0W_0-corrected $MoSe_2$.*

B.8 WS_2 – G_0W_0

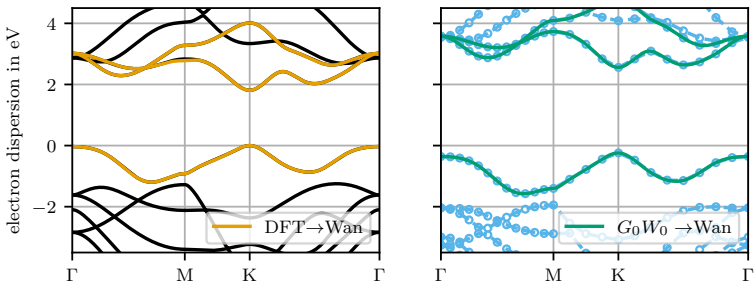

Figure B.32: *DFT and G_0W_0 band structure of monolayer WS_2 as well as the downfolded Wannier model.*

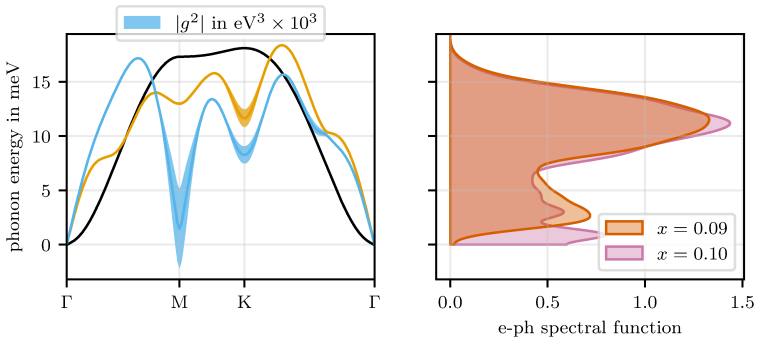

Figure B.33: *Electron-phonon coupling resolved to the accoustic phonon branches and electron-phonon spectral-function around the doping instability of G_0W_0-corrected WS_2.*

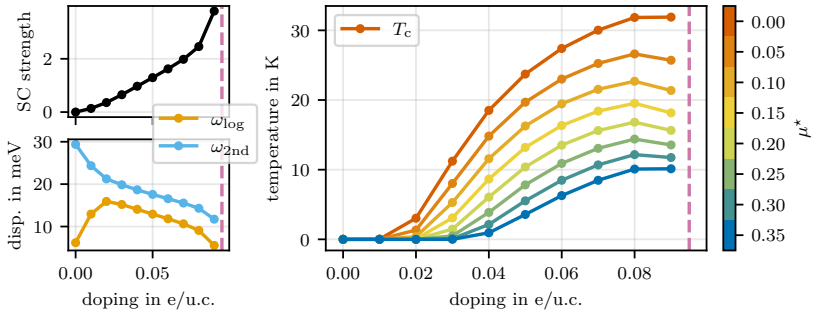

Figure B.34: *Electron-phonon coupling strength, frequency moments and critical temperature for superconductivity of G_0W_0-corrected WS_2.*

B.9 WSe_2 – G_0W_0

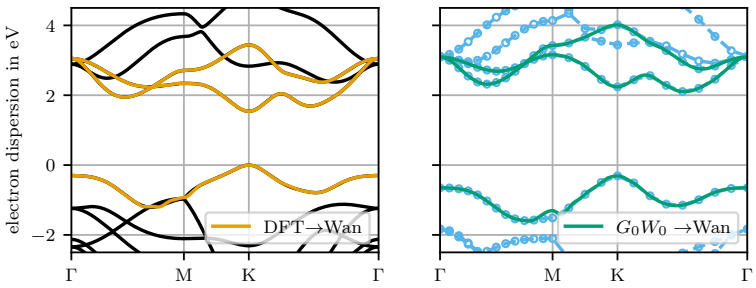

Figure B.35: *DFT and G_0W_0 band structure of monolayer WSe_2 as well as the downfolded Wannier model.*

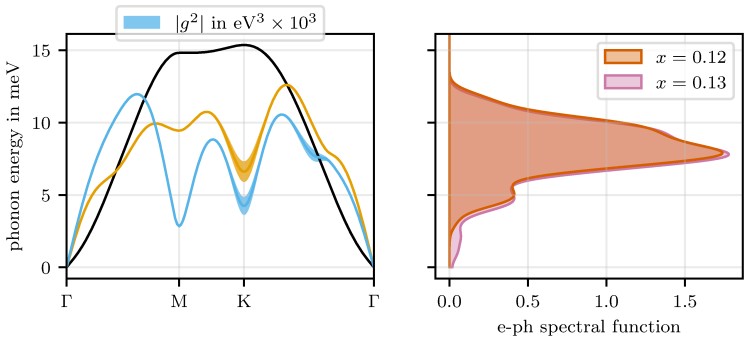

Figure B.36: *Electron-phonon coupling resolved to the accoustic phonon branches and electron-phonon spectral-function around the doping instability of G_0W_0-corrected WSe_2.*

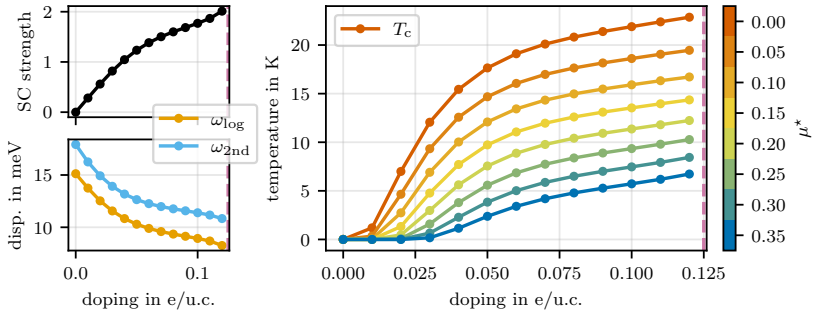

Figure B.37: *Electron-phonon coupling strength, frequency moments and critical temperature for superconductivity of G_0W_0-corrected WSe_2.*

C Homobilayer

C.1 MoS_2-MoS_2 - AB

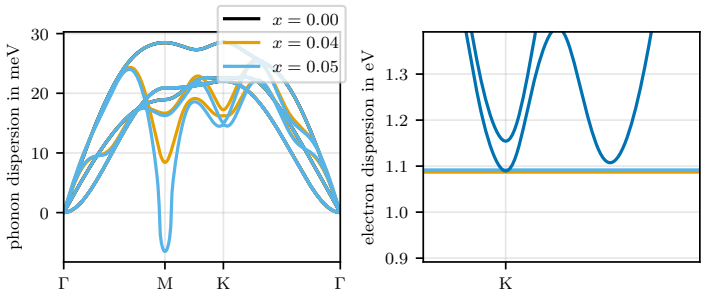

Figure C.1: *Phonon renormalisation under electron doping in AB MoS_2-MoS_2 next to the electronic band structure with indication of Fermi level for given doping levels.*

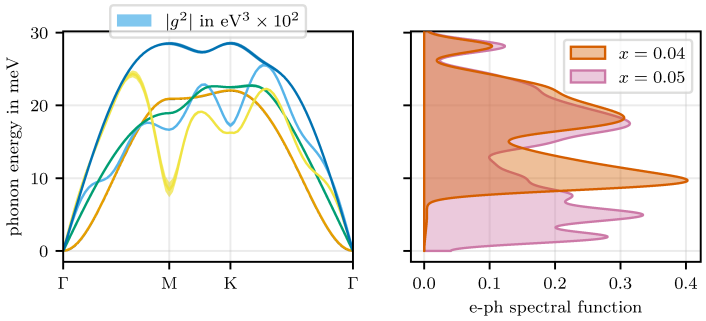

Figure C.2: *Electron-phonon coupling resolved to the accoustic phonon branches and electron-phonon spectral-function around the doping instability of AB MoS_2-MoS_2.*

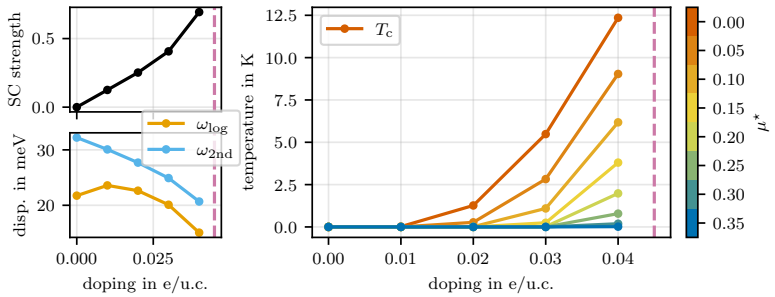

Figure C.3: *Electron-phonon coupling strength, frequency moments and critical temperature for superconductivity of AB MoS_2-MoS_2.*

C.2 $MoSe_2$-$MoSe_2$ - AA

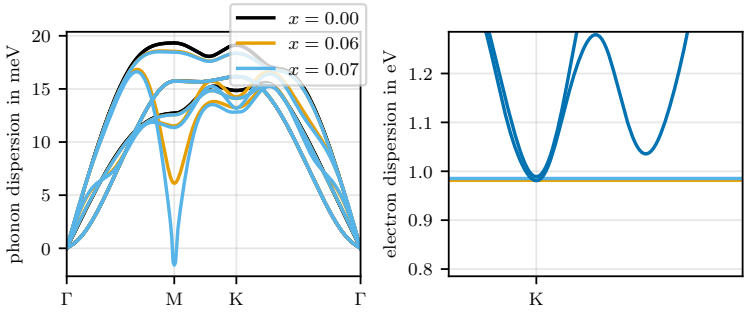

Figure C.4: *Phonon renormalisation under electron doping in AA $MoSe_2$-$MoSe_2$ next to the electronic band structure with indication of Fermi level for given doping levels.*

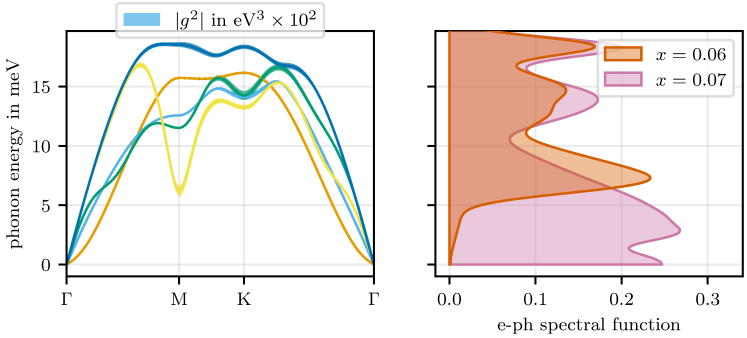

Figure C.5: *Electron-phonon coupling resolved to the accoustic phonon branches and electron-phonon spectral-function around the doping instability of AA $MoSe_2$-$MoSe_2$.*

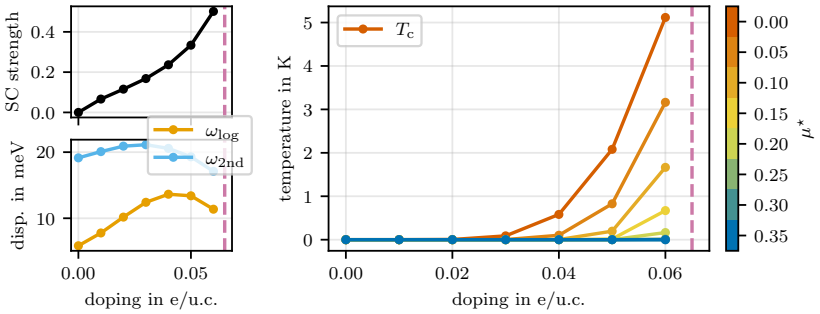

Figure C.6: *Electron-phonon coupling strength, frequency moments and critical temperature for superconductivity of AA $MoSe_2$-$MoSe_2$.*

C.3 $MoSe_2$-$MoSe_2$ - AB

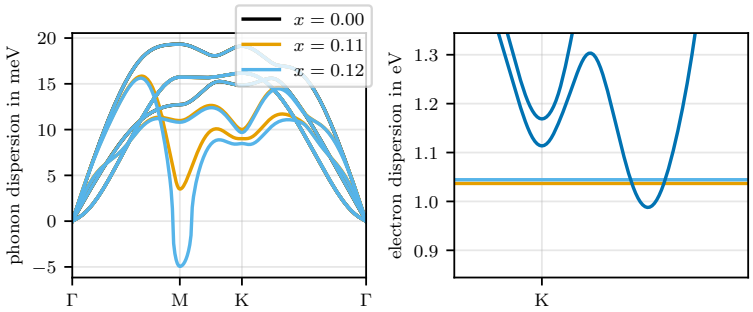

Figure C.7: *Phonon renormalisation under electron doping in AB $MoSe_2$-$MoSe_2$ next to the electronic band structure with indication of Fermi level for given doping levels.*

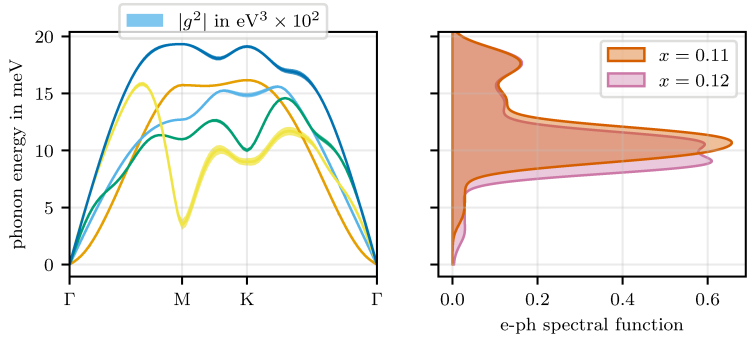

Figure C.8: *Electron-phonon coupling resolved to the accoustic phonon branches and electron-phonon spectral-function around the doping instability of AB $MoSe_2$-$MoSe_2$.*

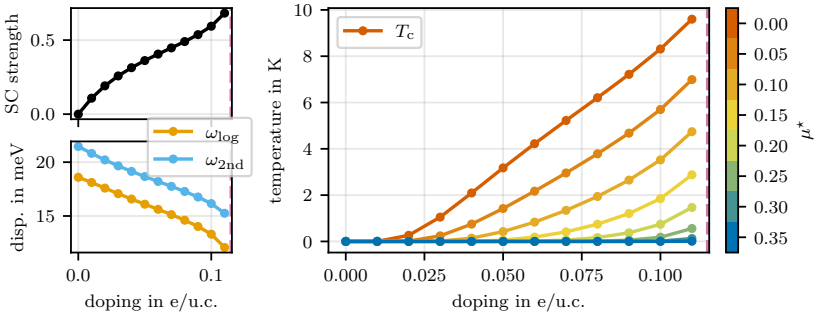

Figure C.9: *Electron-phonon coupling strength, frequency moments and critical temperature for superconductivity of AB $MoSe_2$-$MoSe_2$.*

C.4 WS_2-WS_2 - AA

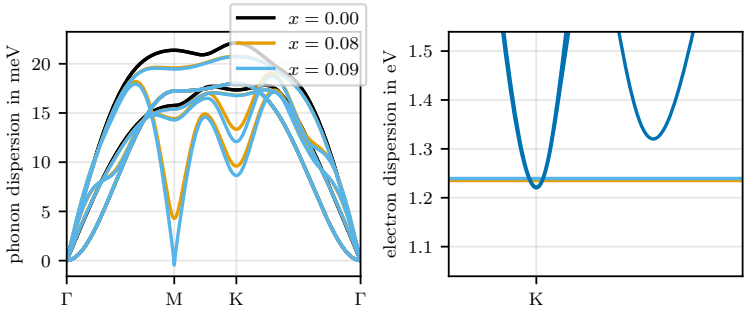

Figure C.10: *Phonon renormalisation under electron doping in AA WS_2-WS_2 next to the electronic band structure with indication of Fermi level for given doping levels.*

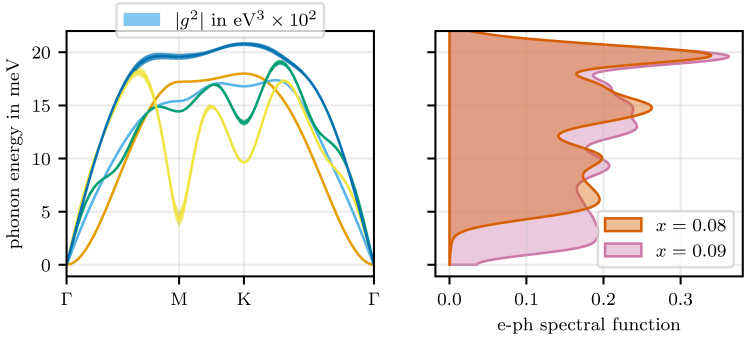

Figure C.11: *Electron-phonon coupling resolved to the accoustic phonon branches and electron-phonon spectral-function around the doping instability of AA WS_2-WS_2.*

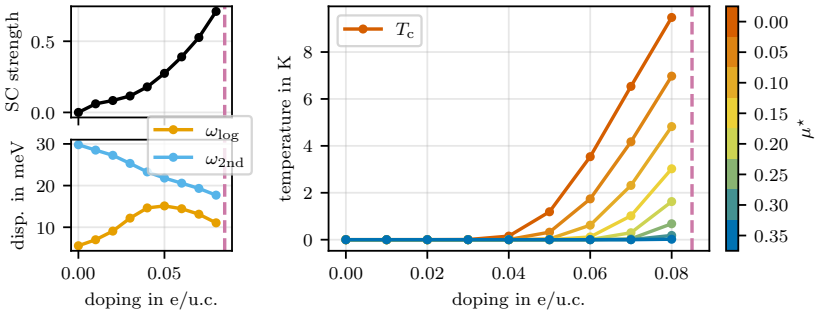

Figure C.12: *Electron-phonon coupling strength, frequency moments and critical temperature for superconductivity of AA WS_2-WS_2.*

C.5 WS_2-WS_2 - AB

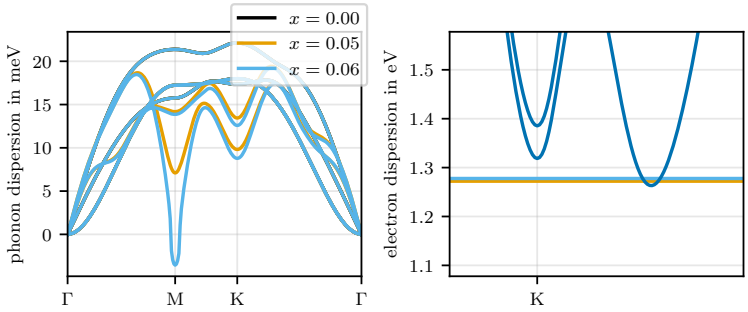

Figure C.13: *Phonon renormalisation under electron doping in AB WS_2-WS_2 next to the electronic band structure with indication of Fermi level for given doping levels.*

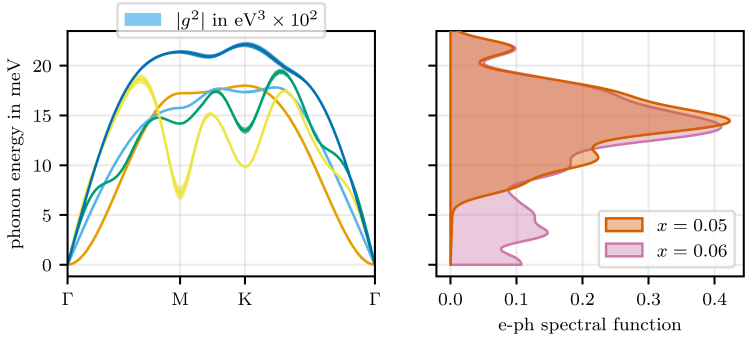

Figure C.14: *Electron-phonon coupling resolved to the accoustic phonon branches and electron-phonon spectral-function around the doping instability of AB WS_2-WS_2.*

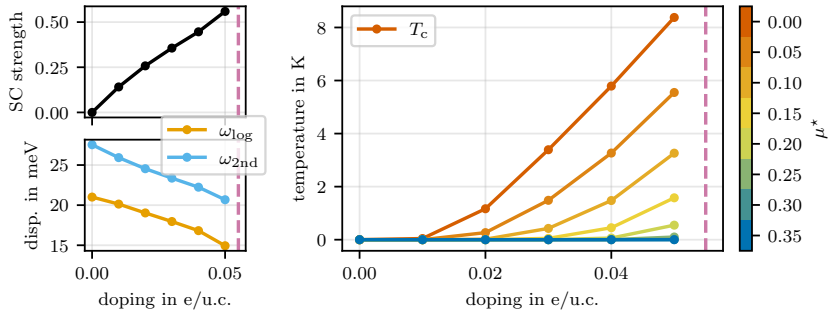

Figure C.15: *Electron-phonon coupling strength, frequency moments and critical temperature for superconductivity of AB WS_2-WS_2.*

C.6 WSe_2-WSe_2 - AA

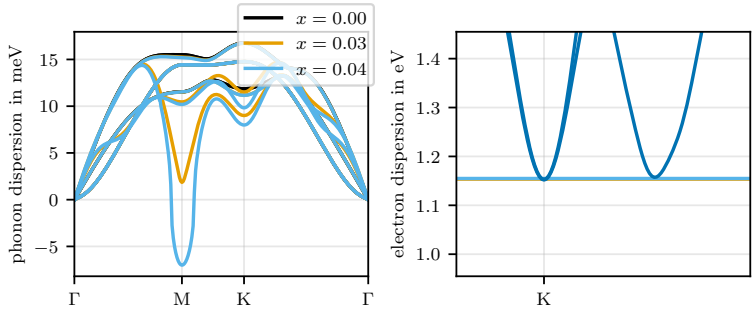

Figure C.16: *Phonon renormalisation under electron doping in AA WSe_2-WSe_2 next to the electronic band structure with indication of Fermi level for given doping levels.*

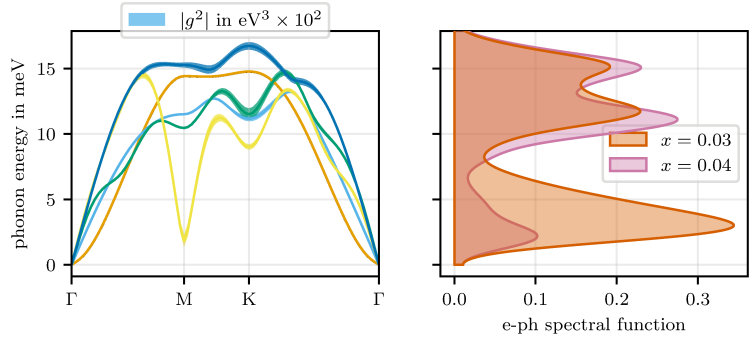

Figure C.17: *Electron-phonon coupling resolved to the accoustic phonon branches and electron-phonon spectral-function around the doping instability of AA WSe_2-WSe_2.*

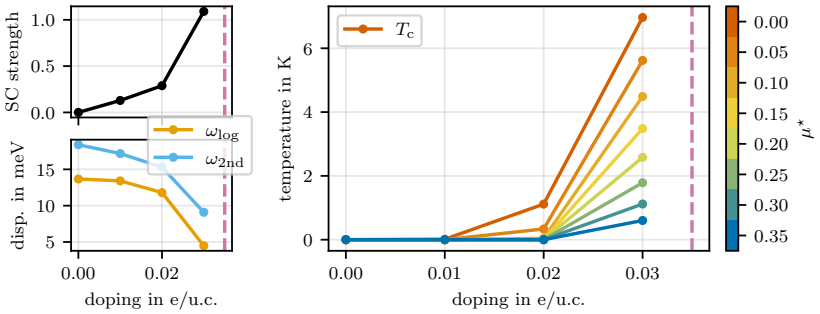

Figure C.18: *Electron-phonon coupling strength, frequency moments and critical temperature for superconductivity of AA WSe_2-WSe_2.*

C.7 WSe_2-WSe_2 - AB

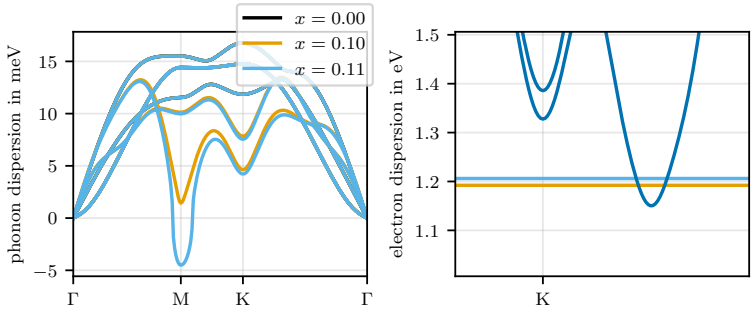

Figure C.19: *Phonon renormalisation under electron doping in AB WSe_2-WSe_2 next to the electronic band structure with indication of Fermi level for given doping levels.*

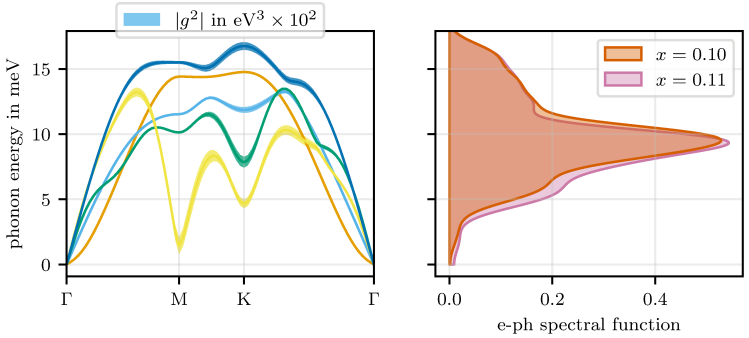

Figure C.20: *Electron-phonon coupling resolved to the accoustic phonon branches and electron-phonon spectral-function around the doping instability of AB WSe_2-WSe_2.*

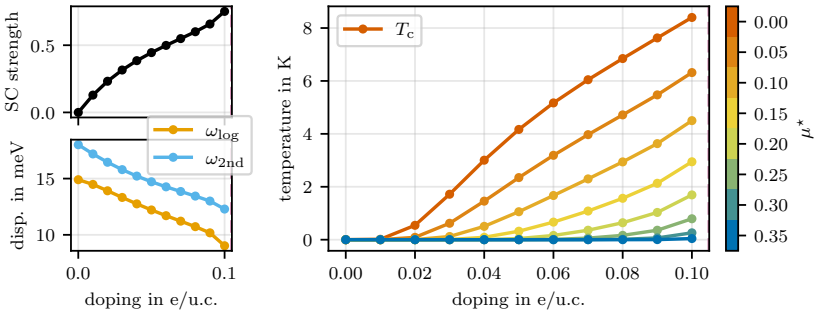

Figure C.21: *Electron-phonon coupling strength, frequency moments and critical temperature for superconductivity of AB WSe_2-WSe_2.*

D Heterobilayer

D.1 MoS_2-WS_2 - AA

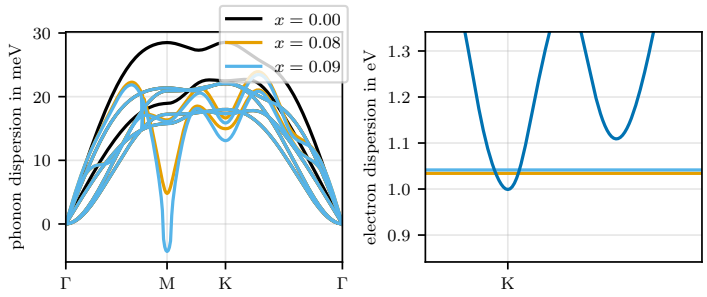

Figure D.1: *Phonon renormalisation under electron doping in AA MoS_2-WS_2 next to the electronic band structure with indication of Fermi level for given doping levels.*

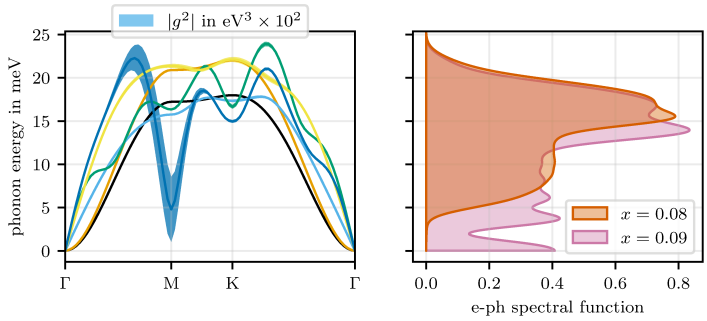

Figure D.2: *Electron-phonon coupling resolved to the accoustic phonon branches and electron-phonon spectral-function around the doping instability of AA MoS_2-WS_2.*

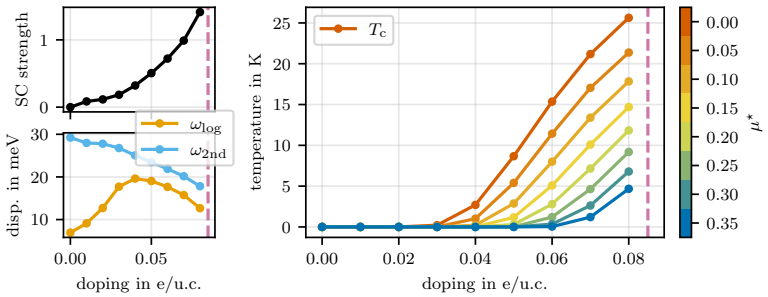

Figure D.3: *Electron-phonon coupling strength, frequency moments and critical temperature for superconductivity of AA MoS_2-WS_2.*

D.2 MoS_2-WS_2 - AB

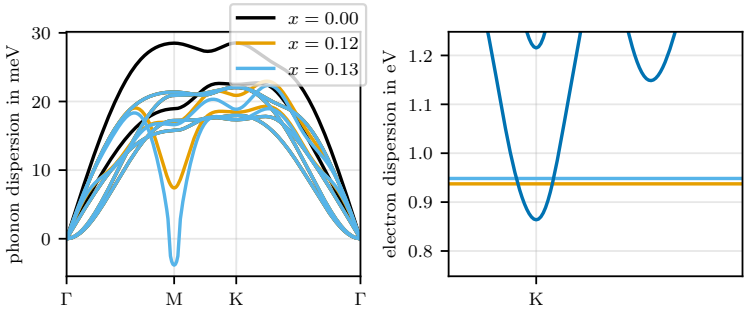

Figure D.4: *Phonon renormalisation under electron doping in AB MoS_2-WS_2 next to the electronic band structure with indication of Fermi level for given doping levels.*

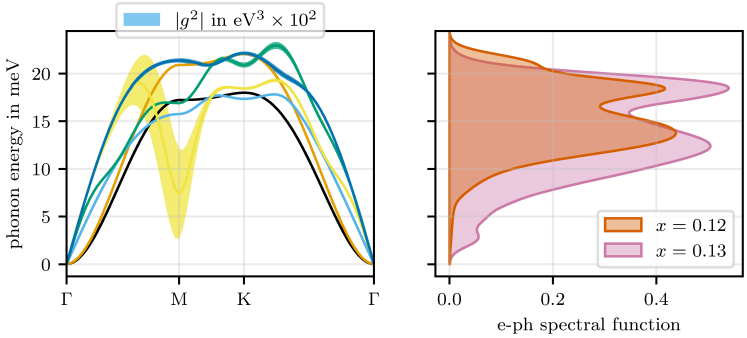

Figure D.5: *Electron-phonon coupling resolved to the accoustic phonon branches and electron-phonon spectral-function around the doping instability of AB MoS_2-WS_2.*

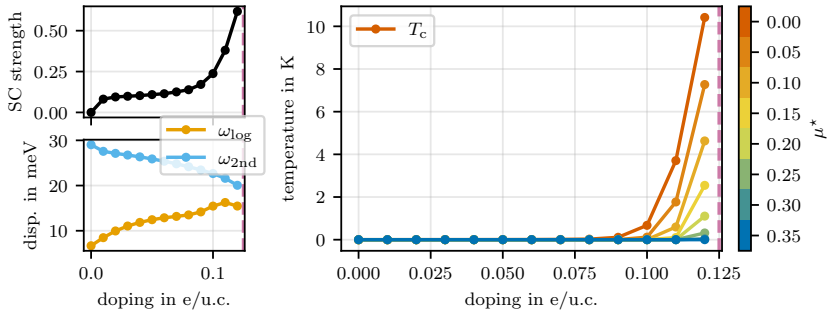

Figure D.6: *Electron-phonon coupling strength, frequency moments and critical temperature for superconductivity of AB MoS_2-WS_2.*

D.3 MoS_2-WS_2 - BA

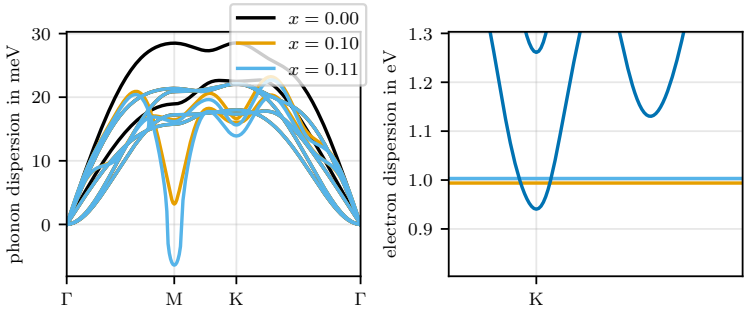

Figure D.7: *Phonon renormalisation under electron doping in BA MoS_2-WS_2 next to the electronic band structure with indication of Fermi level for given doping levels.*

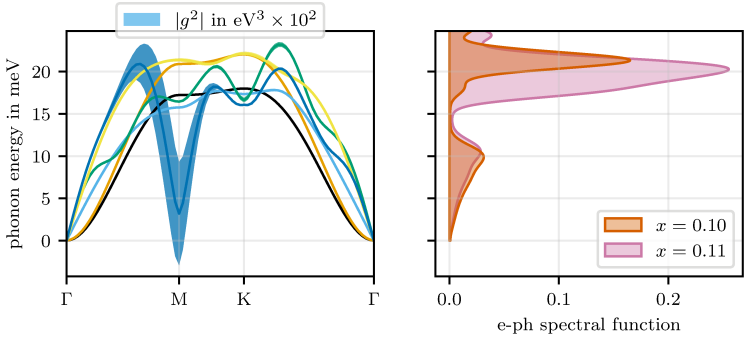

Figure D.8: *Electron-phonon coupling resolved to the accoustic phonon branches and electron-phonon spectral-function around the doping instability of BA MoS_2-WS_2.*

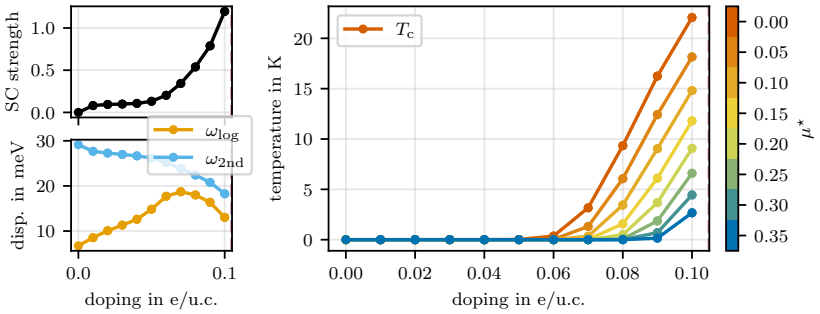

Figure D.9: *Electron-phonon coupling strength, frequency moments and critical temperature for superconductivity of BA MoS_2-WS_2.*

D.4 $MoSe_2$-WSe_2 - AA

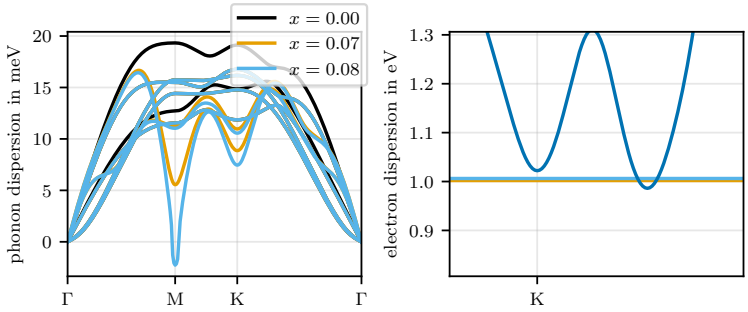

Figure D.10: *Phonon renormalisation under electron doping in AA $MoSe_2$-WSe_2 next to the electronic band structure with indication of Fermi level for given doping levels.*

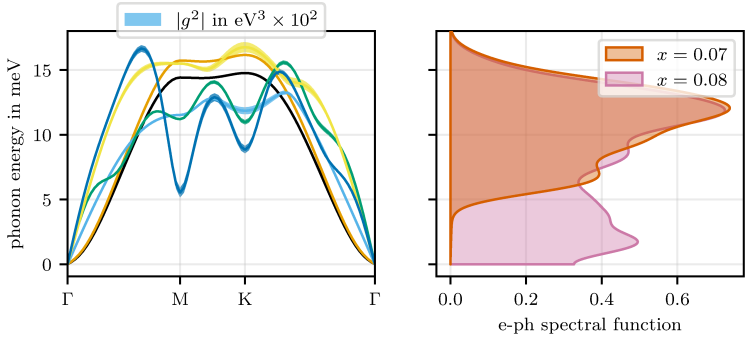

Figure D.11: *Electron-phonon coupling resolved to the accoustic phonon branches and electron-phonon spectral-function around the doping instability of AA $MoSe_2$-WSe_2.*

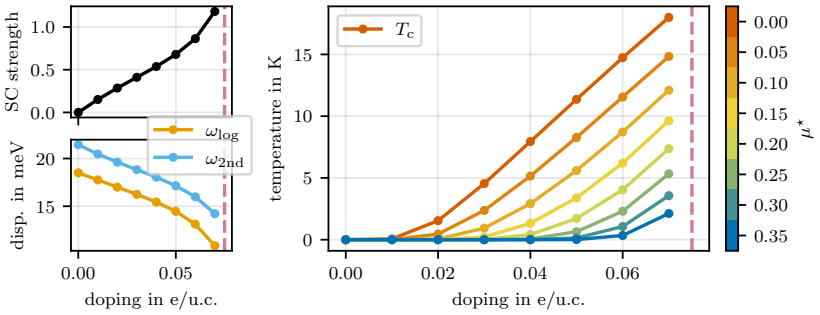

Figure D.12: *Electron-phonon coupling strength, frequency moments and critical temperature for superconductivity of AA $MoSe_2$-WSe_2.*

D.5 $MoSe_2$-WSe_2 - AB

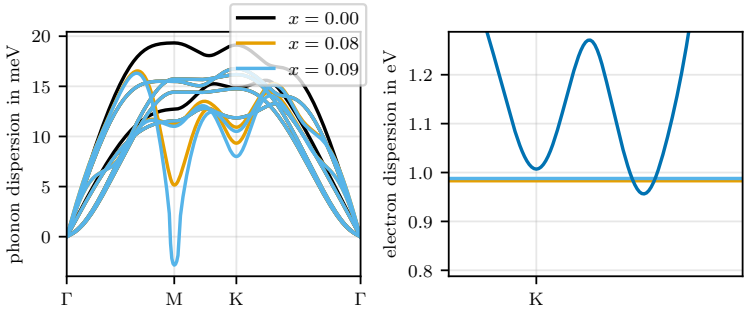

Figure D.13: *Phonon renormalisation under electron doping in AB $MoSe_2$-WSe_2 next to the electronic band structure with indication of Fermi level for given doping levels.*

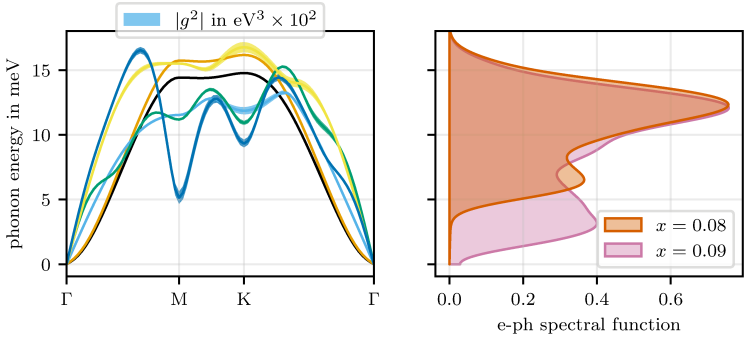

Figure D.14: *Electron-phonon coupling resolved to the accoustic phonon branches and electron-phonon spectral-function around the doping instability of AB $MoSe_2$-WSe_2.*

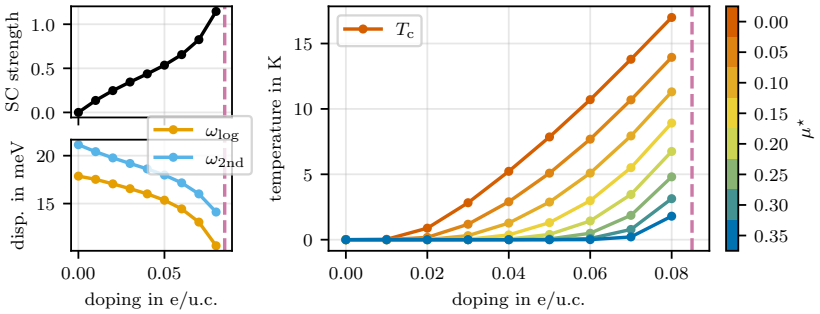

Figure D.15: *Electron-phonon coupling strength, frequency moments and critical temperature for superconductivity of AB $MoSe_2$-WSe_2.*

D.6 $MoSe_2$-WSe_2 - BA

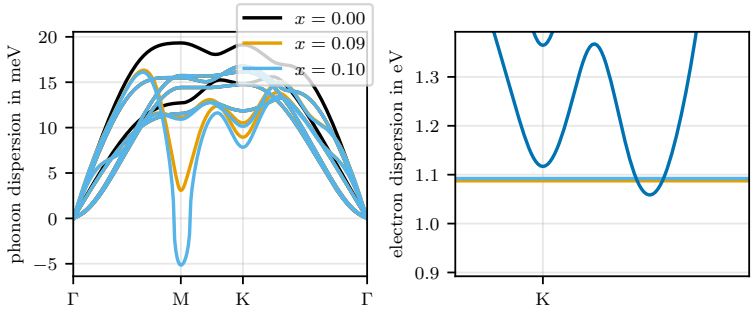

Figure D.16: *Phonon renormalisation under electron doping in BA $MoSe_2$-WSe_2 next to the electronic band structure with indication of Fermi level for given doping levels.*

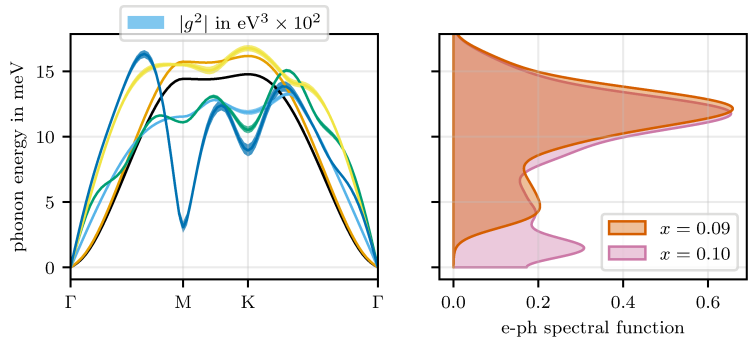

Figure D.17: *Electron-phonon coupling resolved to the accoustic phonon branches and electron-phonon spectral-function around the doping instability of BA $MoSe_2$-WSe_2.*

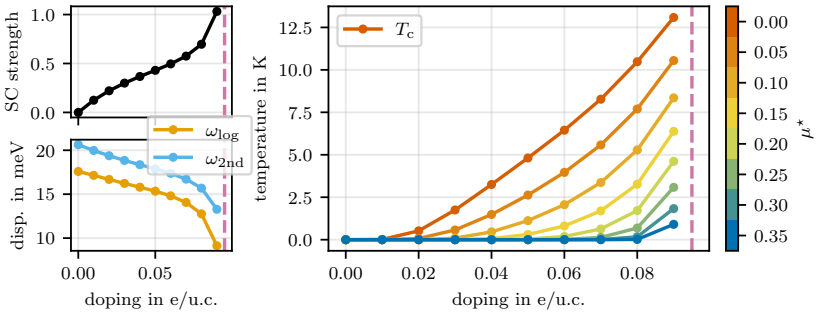

Figure D.18: *Electron-phonon coupling strength, frequency moments and critical temperature for superconductivity of BA $MoSe_2$-WSe_2.*

D.7 MoS_2-$MoSe_2$ - AA

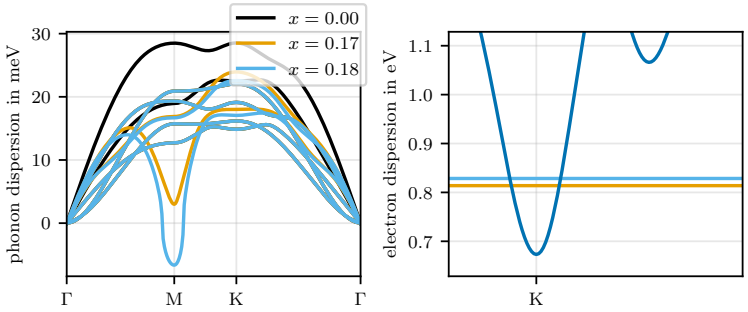

Figure D.19: *Phonon renormalisation under electron doping in AA MoS_2-$MoSe_2$ next to the electronic band structure with indication of Fermi level for given doping levels.*

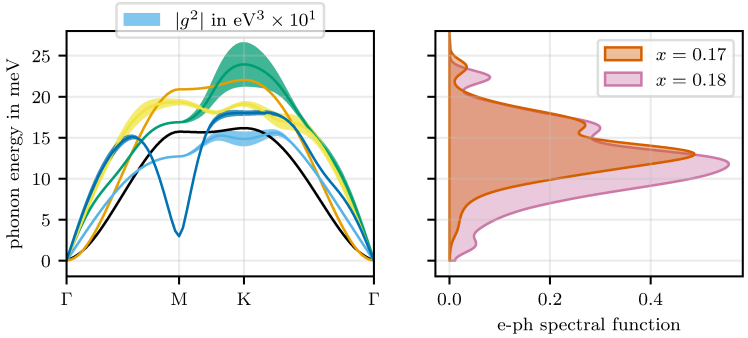

Figure D.20: *Electron-phonon coupling resolved to the accoustic phonon branches and electron-phonon spectral-function around the doping instability of AA MoS_2-$MoSe_2$.*

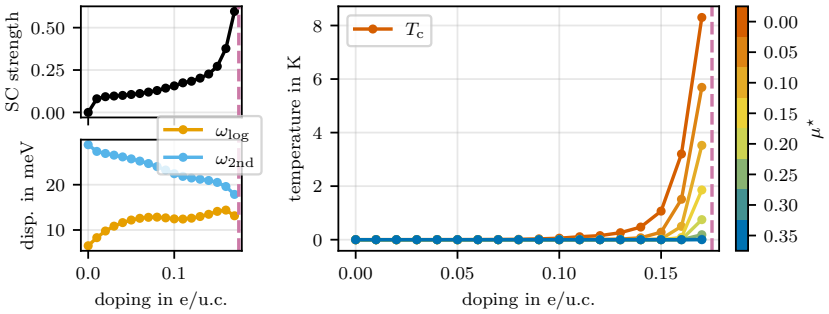

Figure D.21: *Electron-phonon coupling strength, frequency moments and critical temperature for superconductivity of AA MoS_2-$MoSe_2$.*

D.8 MoS_2-$MoSe_2$ - AB

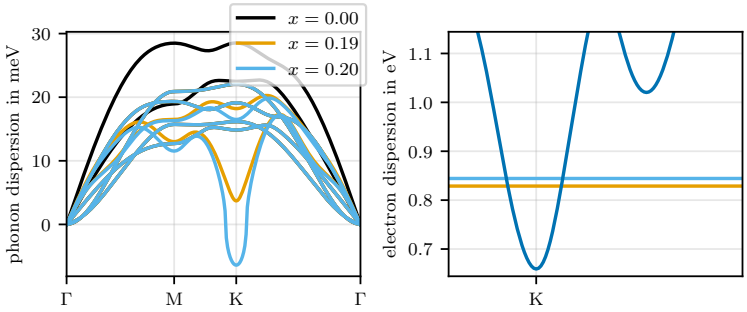

Figure D.22: *Phonon renormalisation under electron doping in AB MoS_2-$MoSe_2$ next to the electronic band structure with indication of Fermi level for given doping levels.*

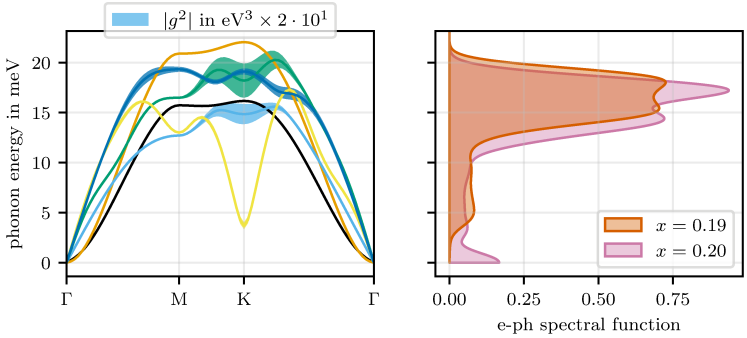

Figure D.23: *Electron-phonon coupling resolved to the accoustic phonon branches and electron-phonon spectral-function around the doping instability of AB MoS_2-$MoSe_2$.*

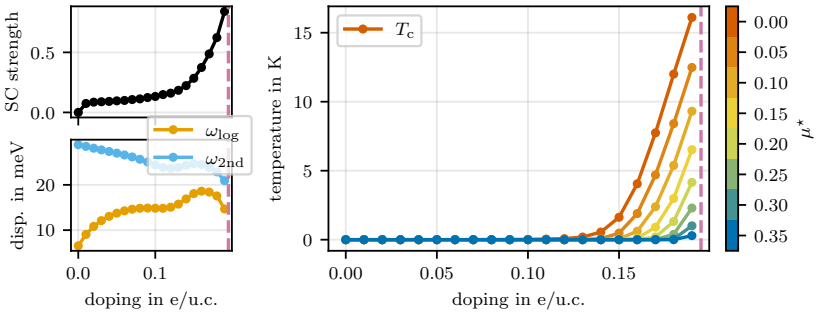

Figure D.24: *Electron-phonon coupling strength, frequency moments and critical temperature for superconductivity of AB MoS_2-$MoSe_2$.*

D.9 MoS_2-$MoSe_2$ - BA

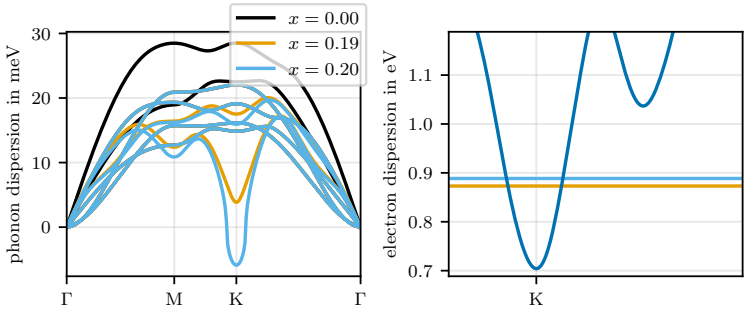

Figure D.25: *Phonon renormalisation under electron doping in BA MoS_2-$MoSe_2$ next to the electronic band structure with indication of Fermi level for given doping levels.*

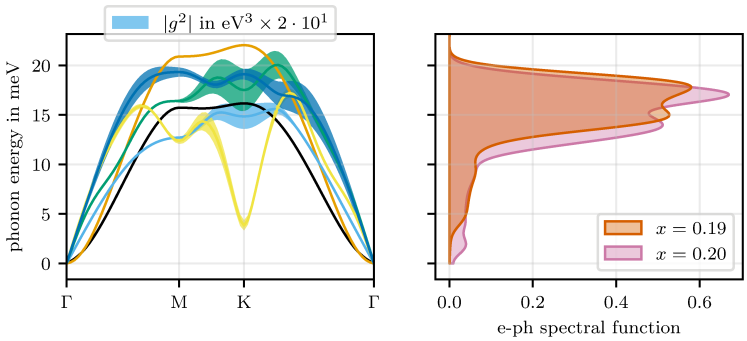

Figure D.26: *Electron-phonon coupling resolved to the accoustic phonon branches and electron-phonon spectral-function around the doping instability of BA MoS_2-$MoSe_2$.*

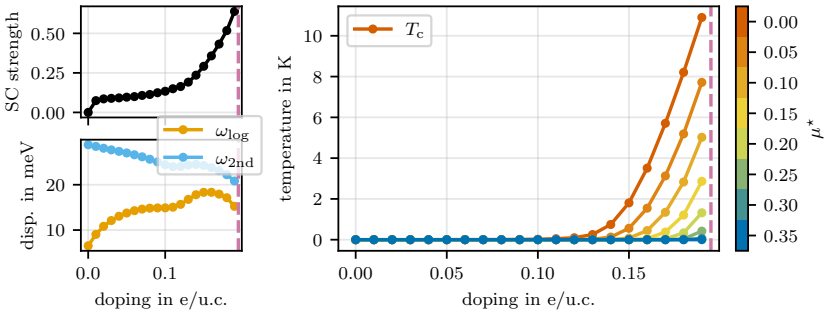

Figure D.27: *Electron-phonon coupling strength, frequency moments and critical temperature for superconductivity of BA MoS_2-$MoSe_2$.*

D.10 WS_2-WSe_2 - AA

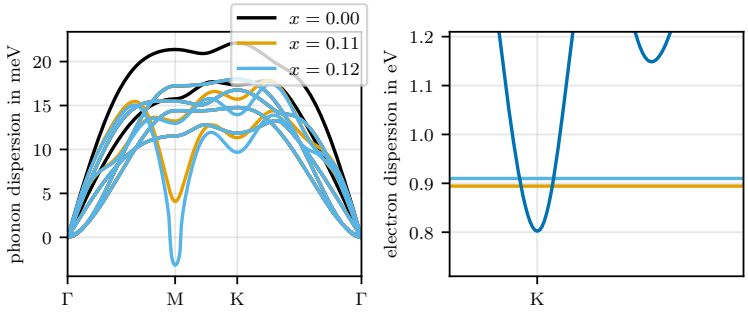

Figure D.28: *Phonon renormalisation under electron doping in AA WS_2-WSe_2 next to the electronic band structure with indication of Fermi level for given doping levels.*

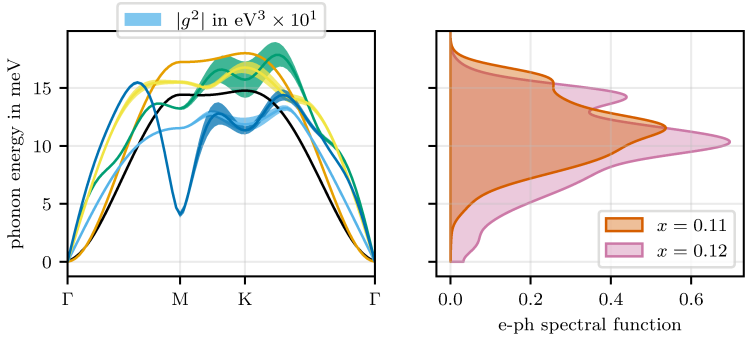

Figure D.29: *Electron-phonon coupling resolved to the accoustic phonon branches and electron-phonon spectral-function around the doping instability of AA WS_2-WSe_2.*

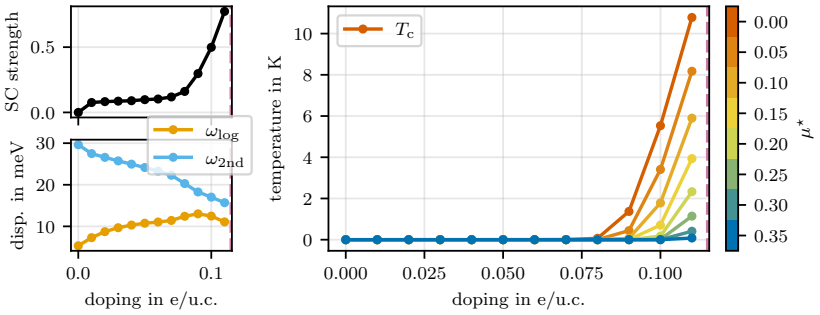

Figure D.30: *Electron-phonon coupling strength, frequency Wments and critical temperature for superconductivity of AA WS_2-WSe_2.*

D.11 WS_2-WSe_2 - AB

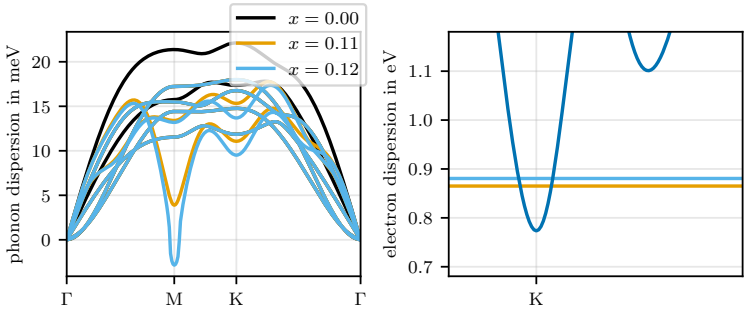

Figure D.31: *Phonon renormalisation under electron doping in AB WS_2-WSe_2 next to the electronic band structure with indication of Fermi level for given doping levels.*

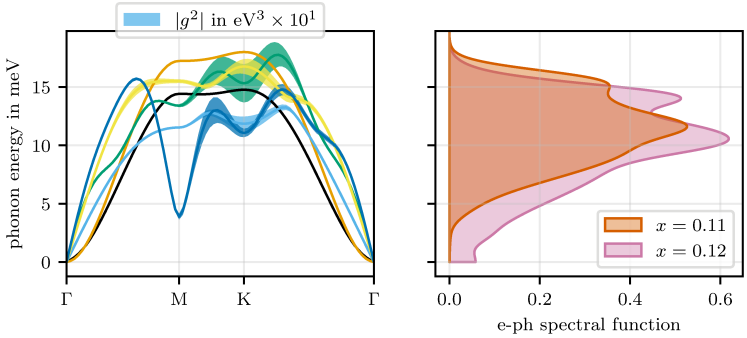

Figure D.32: *Electron-phonon coupling resolved to the accoustic phonon branches and electron-phonon spectral-function around the doping instability of AB WS_2-WSe_2.*

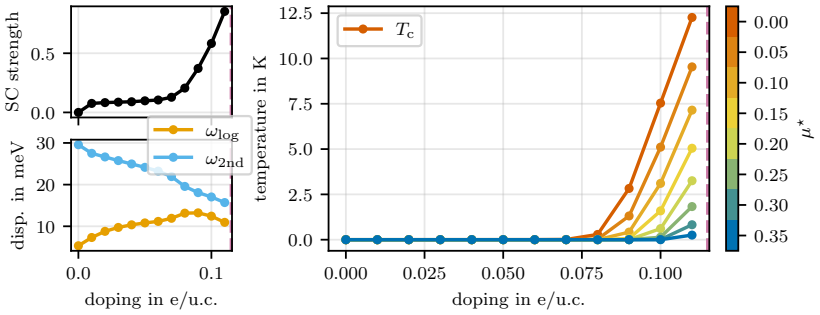

Figure D.33: *Electron-phonon coupling strength, frequency Wments and critical temperature for superconductivity of AB WS_2-WSe_2.*

D.12 WS_2-WSe_2 - BA

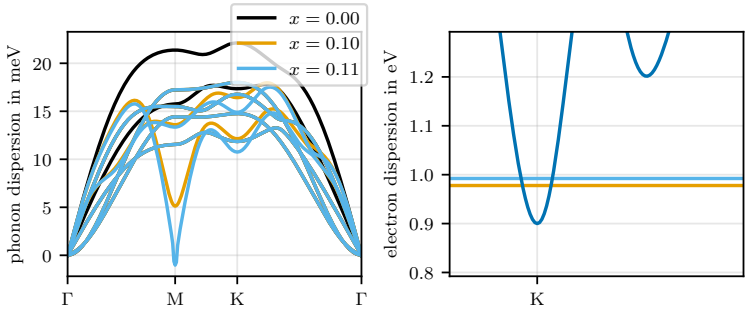

Figure D.34: *Phonon renormalisation under electron doping in BA WS_2-WSe_2 next to the electronic band structure with indication of Fermi level for given doping levels.*

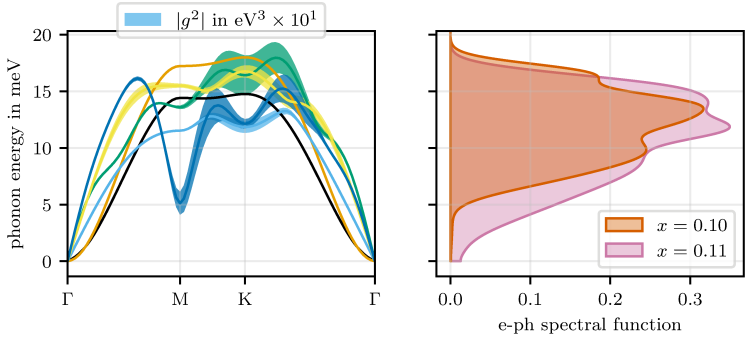

Figure D.35: *Electron-phonon coupling resolved to the accoustic phonon branches and electron-phonon spectral-function around the doping instability of BA WS_2-WSe_2.*

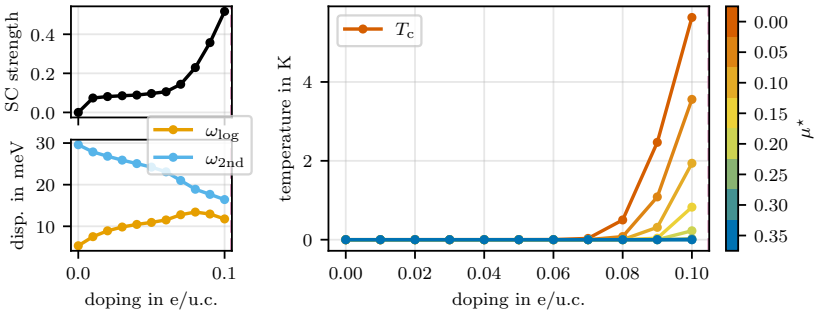

Figure D.36: *Electron-phonon coupling strength, frequency Wments and critical temperature for superconductivity of BA WS_2-WSe_2.*

D.13 MoS_2-WSe_2 - AA

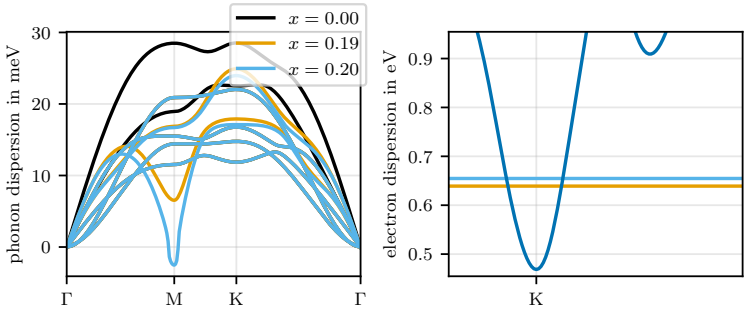

Figure D.37: *Phonon renormalisation under electron doping in AA MoS_2-WSe_2 next to the electronic band structure with indication of Fermi level for given doping levels.*

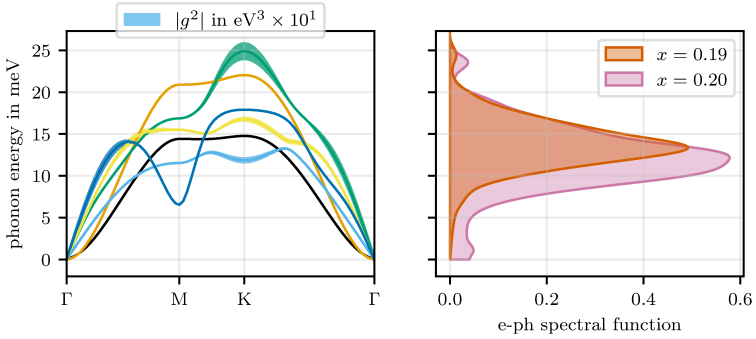

Figure D.38: *Electron-phonon coupling resolved to the accoustic phonon branches and electron-phonon spectral-function around the doping instability of AA MoS_2-WSe_2.*

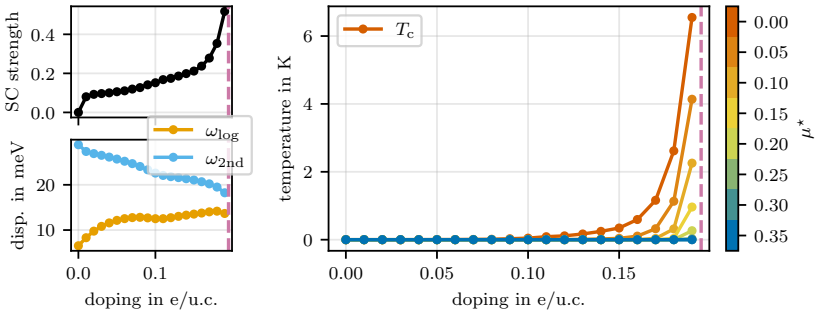

Figure D.39: *Electron-phonon coupling strength, frequency Wments and critical temperature for superconductivity of AA MoS_2-WSe_2.*

D.14 MoS_2-WSe_2 - AB

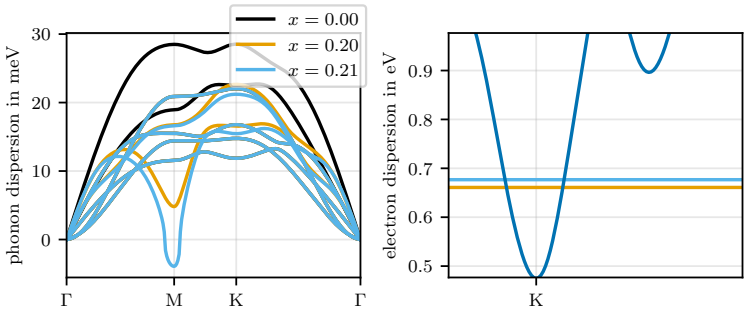

Figure D.40: *Phonon renormalisation under electron doping in AB MoS_2-WSe_2 next to the electronic band structure with indication of Fermi level for given doping levels.*

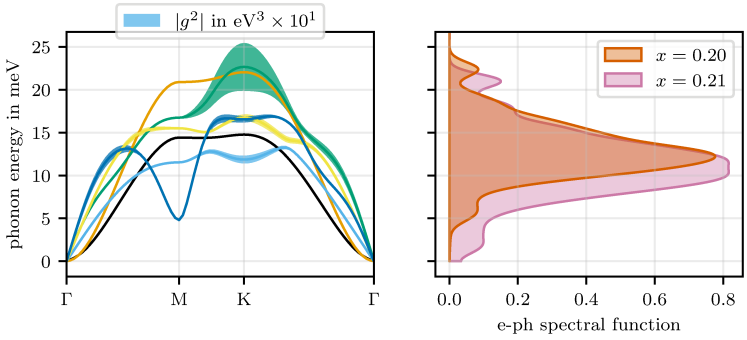

Figure D.41: *Electron-phonon coupling resolved to the accoustic phonon branches and electron-phonon spectral-function around the doping instability of AB MoS_2-WSe_2.*

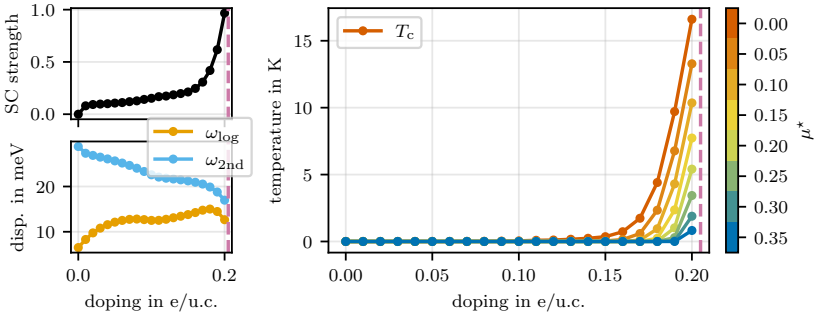

Figure D.42: *Electron-phonon coupling strength, frequency Wments and critical temperature for superconductivity of AB MoS_2-WSe_2.*

D.15 MoS_2-WSe_2 - BA

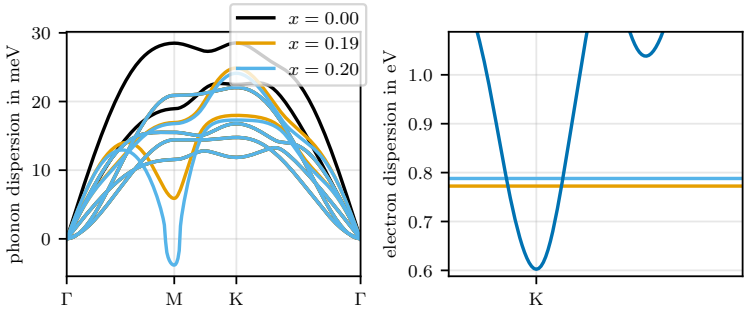

Figure D.43: *Phonon renormalisation under electron doping in BA MoS_2-WSe_2 next to the electronic band structure with indication of Fermi level for given doping levels.*

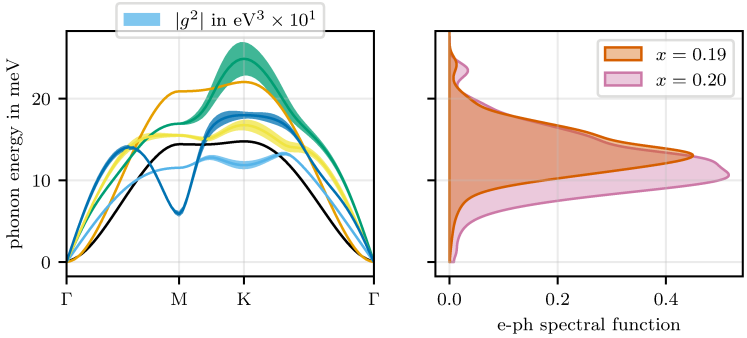

Figure D.44: *Electron-phonon coupling resolved to the accoustic phonon branches and electron-phonon spectral-function around the doping instability of BA MoS_2-WSe_2.*

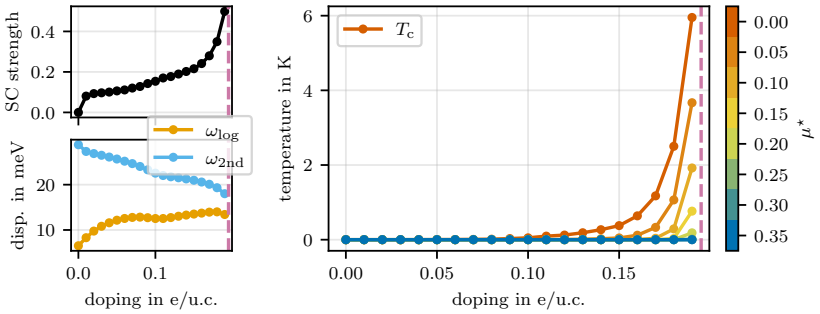

Figure D.45: *Electron-phonon coupling strength, frequency Wments and critical temperature for superconductivity of BA MoS_2-WSe_2.*

D.16 $MoSe_2$-WS_2 - AA

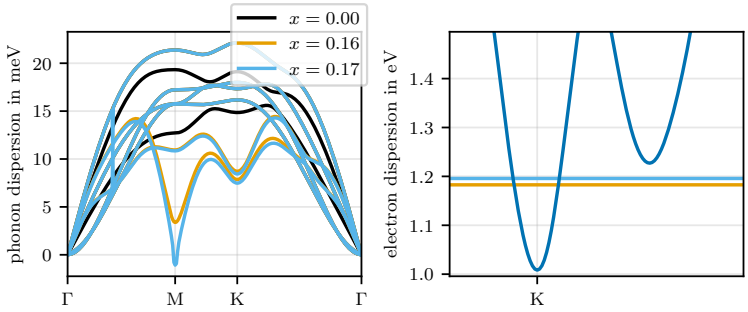

Figure D.46: *Phonon renormalisation under electron doping in AA $MoSe_2$-WS_2 next to the electronic band structure with indication of Fermi level for given doping levels.*

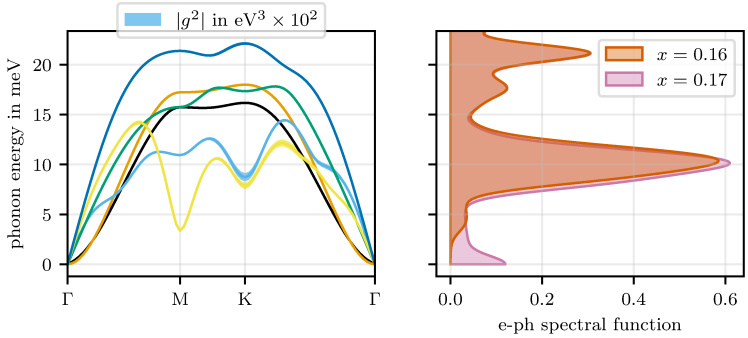

Figure D.47: *Electron-phonon coupling resolved to the accoustic phonon branches and electron-phonon spectral-function around the doping instability of AA $MoSe_2$-WS_2.*

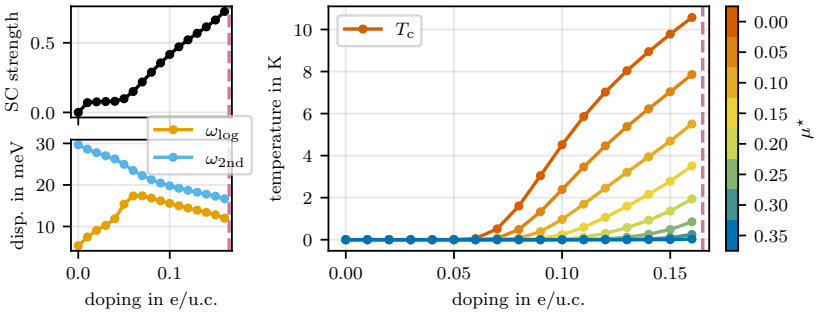

Figure D.48: *Electron-phonon coupling strength, frequency Wments and critical temperature for superconductivity of AA $MoSe_2$-WS_2.*

D.17 $MoSe_2$-WS_2 - AB

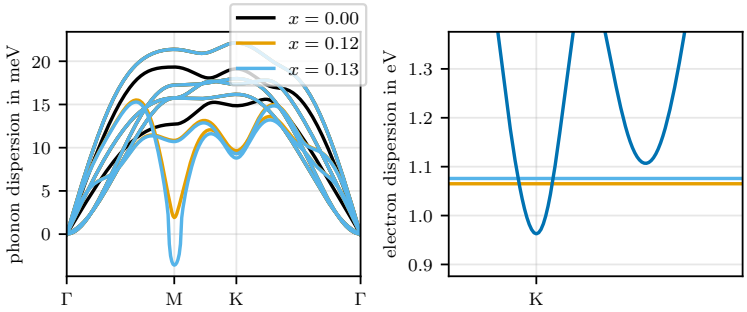

Figure D.49: *Phonon renormalisation under electron doping in AB $MoSe_2$-WS_2 next to the electronic band structure with indication of Fermi level for given doping levels.*

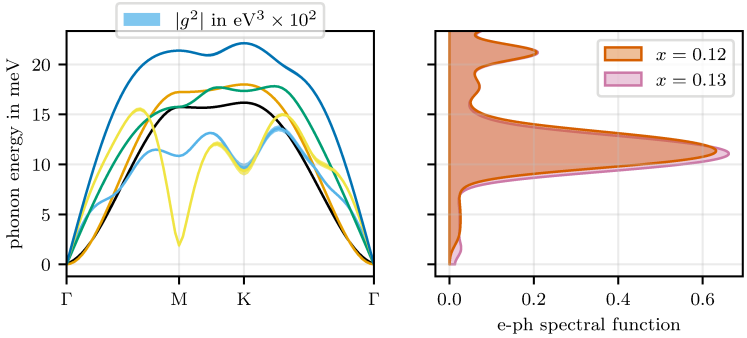

Figure D.50: *Electron-phonon coupling resolved to the accoustic phonon branches and electron-phonon spectral-function around the doping instability of AB $MoSe_2$-WS_2.*

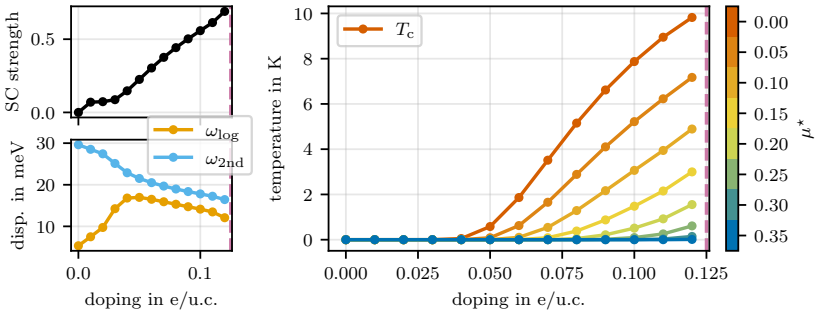

Figure D.51: *Electron-phonon coupling strength, frequency Wments and critical temperature for superconductivity of AB $MoSe_2$-WS_2.*

D.18 $MoSe_2$-WS_2 - BA

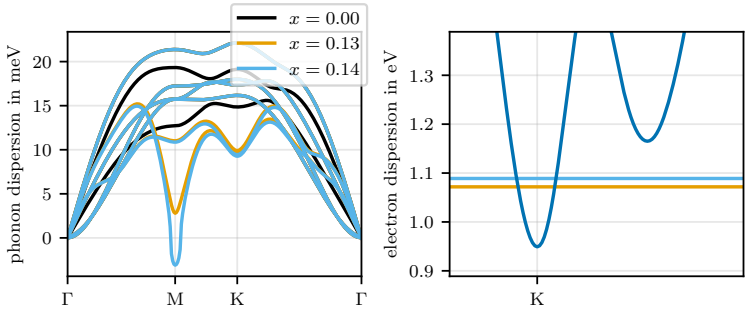

Figure D.52: *Phonon renormalisation under electron doping in BA $MoSe_2$-WS_2 next to the electronic band structure with indication of Fermi level for given doping levels.*

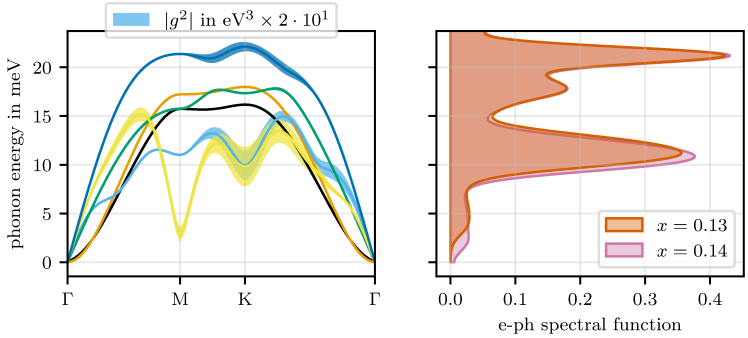

Figure D.53: *Electron-phonon coupling resolved to the accoustic phonon branches and electron-phonon spectral-function around the doping instability of BA $MoSe_2$-WS_2.*

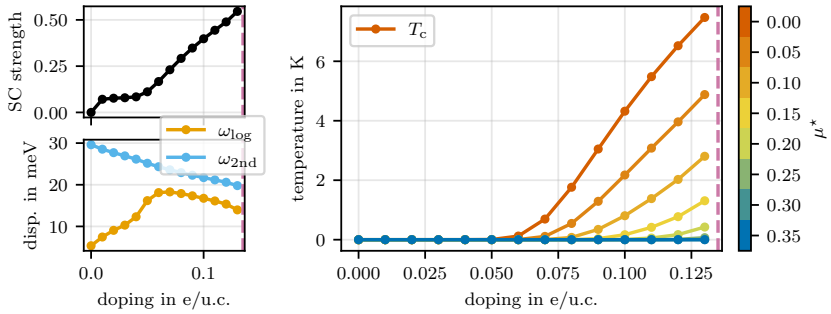

Figure D.54: *Electron-phonon coupling strength, frequency Wments and critical temperature for superconductivity of BA $MoSe_2$-WS_2.*

E Oscillation patterns of the silicon adsorbate in SiC

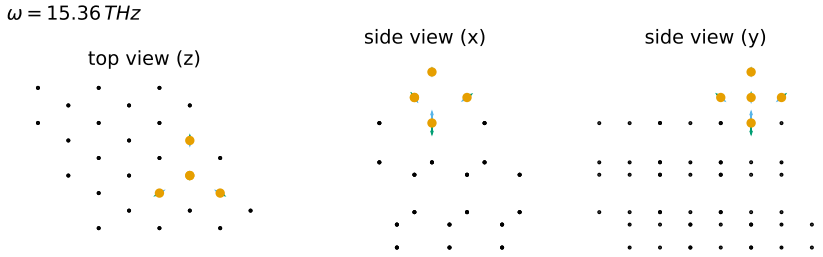

Figure E.1: *Oscillation of the silicon adsorbate in Si-rich SiC showing a dominant vertical motion of the base.*

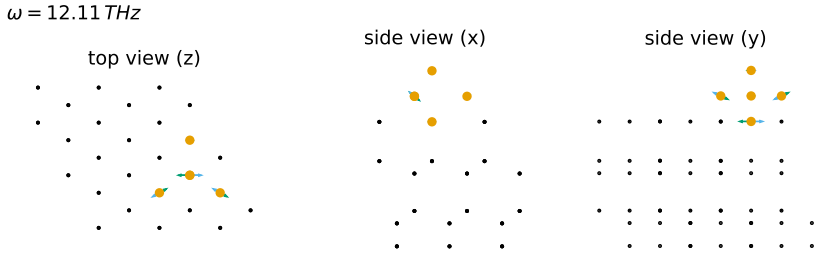

Figure E.2: *Oscillation of the silicon adsorbate in Si-rich SiC showing a tilting motion of the base in x-direction.*

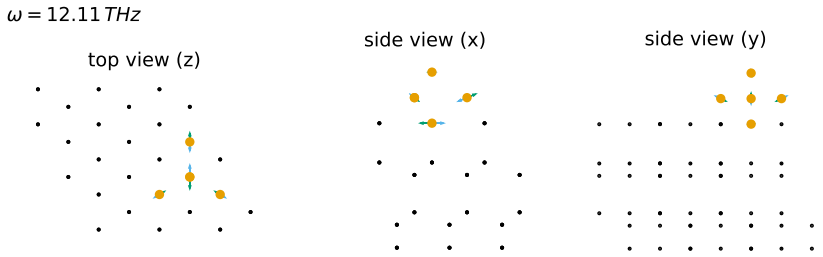

Figure E.3: *Oscillation of the silicon adsorbate in Si-rich SiC showing a tilting motion of the base in y-direction.*

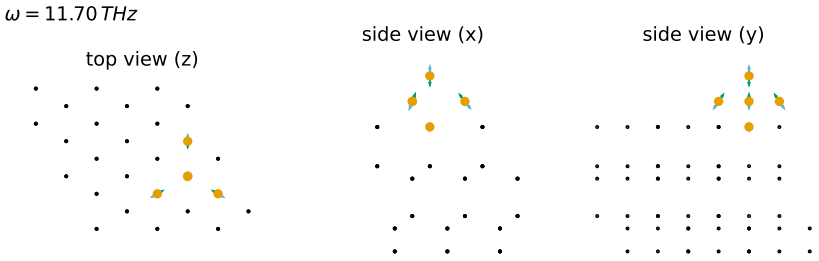

Figure E.4: *Oscillation of the silicon adsorbate in Si-rich SiC showing a breathing motion of the tripod.*

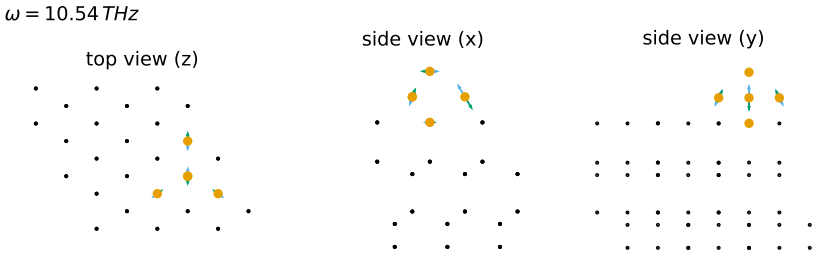

Figure E.5: *Oscillation of the silicon adsorbate in Si-rich SiC showing a tilting motion of the top in y-direction.*

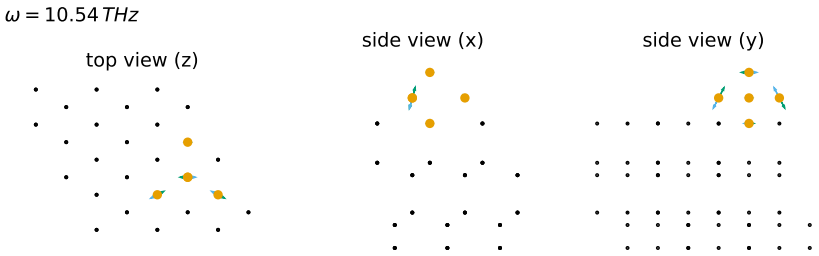

Figure E.6: *Oscillation of the silicon adsorbate in Si-rich SiC showing a tilting motion of the top in x-direction.*

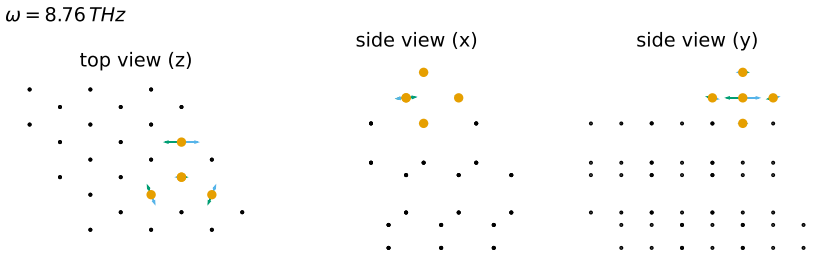

Figure E.7: *Oscillation of the silicon adsorbate in Si-rich SiC showing a squeezing motion of the tripod in x-direction.*

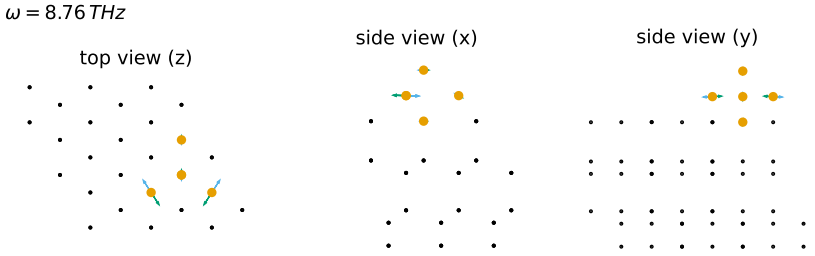

Figure E.8: *Oscillation of the silicon adsorbate in Si-rich SiC showing a squeezing motion of the tripod in y-direction.*

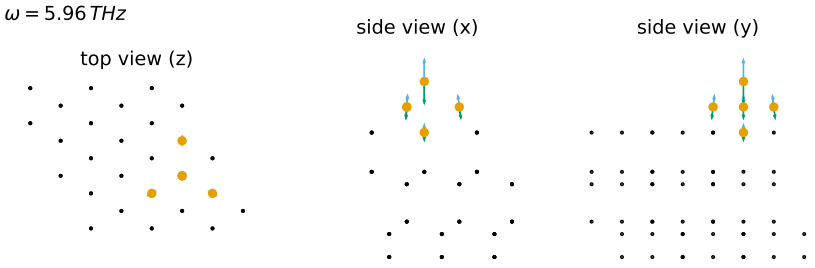

Figure E.9: *Oscillation of the silicon adsorbate in Si-rich SiC showing a motion of the adsorbate in z-direction.*

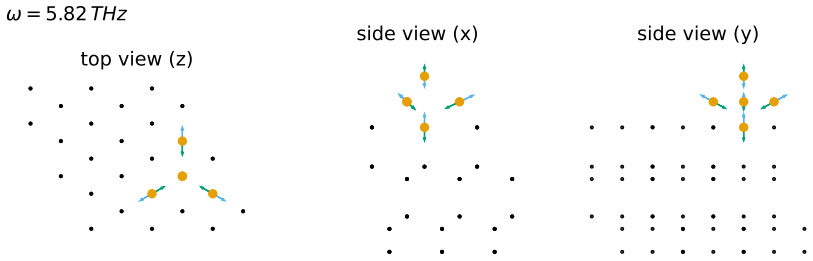

Figure E.10: *Oscillation of the silicon adsorbate in Si-rich SiC showing a squeezing motion of the tripod in z-direction.*

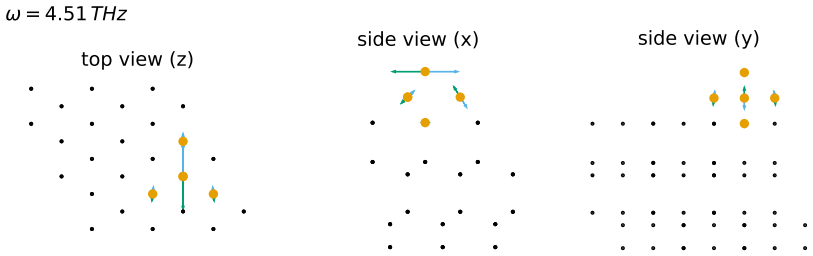

Figure E.11: *Oscillation of the silicon adsorbate in Si-rich SiC showing a tilting motion of the tip in y-direction.*

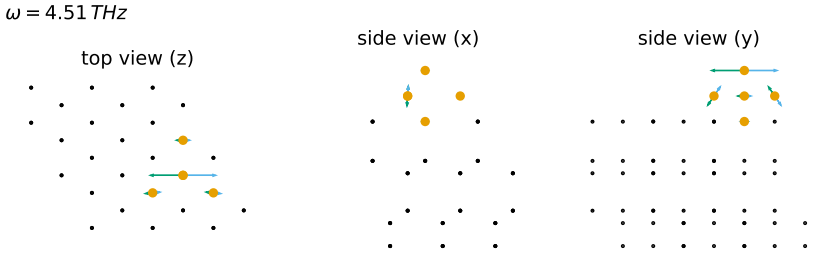

Figure E.12: *Oscillation of the silicon adsorbate in Si-rich SiC showing a tilting motion of the tip in x-direction.*

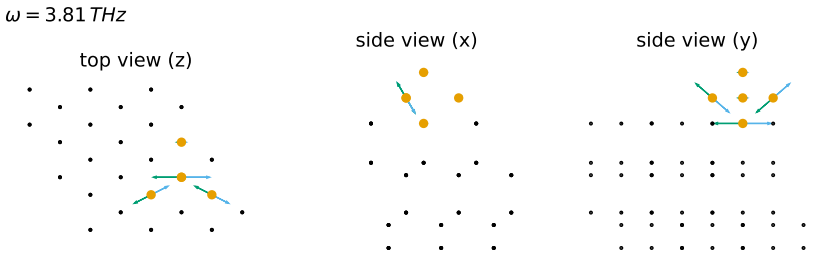

Figure E.13: *Oscillation of the silicon adsorbate in Si-rich SiC showing a breathing motion of the tripod in x-direction.*

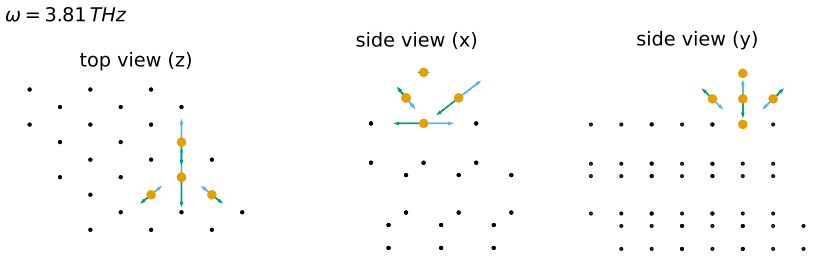

Figure E.14: *Oscillation of the silicon adsorbate in Si-rich SiC showing a squeezing motion of the tripod in y-direction.*

Bibliography

[1] A. Altland and B. D. Simons. 'Condensed Matter Field Theory'. In: second. Cambridge University Press, 2010. Chap. 2 Second Quantization, pp. 76–79. DOI: 10.1017/CBO9780511789984.

[2] R. M. Martin, L. Reining and D. M. Ceperley. *Interacting Electrons: Theory and Computational Approaches*. Cambridge University Press, 2016.

[3] R. Martin. *Electronic Structure: Basic Theory and Practical Methods*. Cambridge University Press, 2020. ISBN: 9781108429900. URL: https://books.google.fr/books?id=wvXvDwAAQBAJ.

[4] M. Born and R. Oppenheimer. 'Zur Quantentheorie der Molekeln'. In: *Annalen der Physik* 389.20 (1927), pp. 457–484. DOI: 10.1002/andp.19273892002.

[5] P. Hohenberg and W. Kohn. 'Inhomogeneous Electron Gas'. In: *Phys. Rev.* 136 (3B Nov. 1964), B864–B871. DOI: 10.1103/PhysRev.136.B864.

[6] L. H. Thomas. 'The calculation of atomic fields'. In: *Mathematical Proceedings of the Cambridge Philosophical Society* 23.5 (1927), pp. 542–548. DOI: 10.1017/S0305004100011683.

[7] E. Fermi. 'Un metodo statistico per la determinazione di alcune proprietà dell' atomo'. In: *Rend. Lincei* 6 (1927), pp. 602–607.

[8] E. Fiorini and G. Gallavotti. 'The Accademia dei Lincei to E. Fermi on the occasion of the 110th anniversary of his birthday'. In: *Rendiconti Lincei* 22.4 (Dec. 2011). This reference contains a translation of E. Fermi's original work in Italian., pp. 277–306. ISSN: 1720-0776. DOI: 10.1007/s12210-011-0141-5.

[9] R. O. Jones. 'Density functional theory: Its origins, rise to prominence, and future'. In: *Rev. Mod. Phys.* 87 (3 Aug. 2015), pp. 897–923. DOI: 10.1103/RevModPhys.87.897.

[10] P. Giannozzi et al. 'QUANTUM ESPRESSO: a modular and open-source software project for quantum simulations of materials'. In: *Journal of Physics: Condensed Matter* 21.39 (2009), 395502 (19pp). URL: http://www.quantum-espresso.org.

[11] P. Giannozzi et al. 'Advanced capabilities for materials modelling with QUANTUM ESPRESSO'. In: *Journal of Physics: Condensed Matter* 29.46 (2017), p. 465901. URL: http://stacks.iop.org/0953-8984/29/i=46/a=465901.

[12] P. Giannozzi et al. 'Quantum ESPRESSO toward the exascale'. In: *The Journal of Chemical Physics* 152.15 (2020), p. 154105. DOI: 10.1063/5.0005082.

[13] W. Kohn and L. J. Sham. 'Self-Consistent Equations Including Exchange and Correlation Effects'. In: *Phys. Rev.* 140 (4A Nov. 1965), A1133–A1138. DOI: 10.1103/PhysRev.140.A1133.

[14] M. Levy, J. P. Perdew and V. Sahni. 'Exact differential equation for the density and ionization energy of a many-particle system'. In: *Phys. Rev. A* 30 (5 Nov. 1984), pp. 2745–2748. DOI: 10.1103/PhysRevA.30.2745.

[15] J. F. Janak. 'Proof that $\frac{\partial E}{\partial n_i} = \epsilon$ in density-functional theory'. In: *Phys. Rev. B* 18 (12 Dec. 1978), pp. 7165–7168. DOI: 10.1103/PhysRevB.18.7165.

[16] J. P. Perdew and M. Levy. 'Physical Content of the Exact Kohn-Sham Orbital Energies: Band Gaps and Derivative Discontinuities'. In: *Phys. Rev. Lett.* 51 (20 Nov. 1983), pp. 1884–1887. DOI: 10.1103/PhysRevLett.51.1884.

[17] L. J. Sham and M. Schlüter. 'Density-Functional Theory of the Energy Gap'. In: *Phys. Rev. Lett.* 51 (20 Nov. 1983), pp. 1888–1891. DOI: 10.1103/PhysRevLett.51.1888.

[18] J. C. Slater and G. F. Koster. 'Simplified LCAO Method for the Periodic Potential Problem'. In: *Phys. Rev.* 94 (6 June 1954), pp. 1498–1524. DOI: 10.1103/PhysRev.94.1498.

[19] C. Kittel. *Quantum theory of solids*. New York: Wiley, 1963.

[20] C. Kittel. *Introduction to Solid State Physics*. 8th ed. Wiley, 2004. ISBN: 9780471415268.

[21] J. Singleton. 'Band Theory and Electronic Properties of Solids'. In: *Band Theory and Electronic Properties of Solids*. Oxford University Press, Aug. 2001. ISBN: 9780198506454. DOI: 10.1093/oso/9780198506454.002.0001.

[22] G. H. Wannier. 'The Structure of Electronic Excitation Levels in Insulating Crystals'. In: *Phys. Rev.* 52 (3 Aug. 1937), pp. 191–197. DOI: 10.1103/PhysRev.52.191.

[23] P.-O. Löwdin. 'On the Non-Orthogonality Problem Connected with the Use of Atomic Wave Functions in the Theory of Molecules and Crystals'. In: *The Journal of Chemical Physics* 18.3 (Mar. 1950), pp. 365–375. ISSN: 0021-9606. DOI: 10.1063/1.1747632.

[24] N. Marzari and D. Vanderbilt. 'Maximally localized generalized Wannier functions for composite energy bands'. In: *Phys. Rev. B* 56 (20 Nov. 1997), pp. 12847–12865. DOI: 10.1103/PhysRevB.56.12847.

[25] N. Marzari et al. 'Maximally localized Wannier functions: Theory and applications'. In: *Rev. Mod. Phys.* 84 (4 Oct. 2012), pp. 1419–1475. DOI: 10.1103/RevModPhys.84.1419.

[26] A. A. Mostofi et al. 'An updated version of wannier90: A tool for obtaining maximally-localised Wannier functions'. In: *Computer Physics Communications* 185.8 (2014), pp. 2309–2310. ISSN: 0010-4655. DOI: 10.1016/j.cpc.2014.05.003.

[27] G. Pizzi et al. 'Wannier90 as a community code: new features and applications'. In: *Journal of Physics: Condensed Matter* 32.16 (Jan. 2020), p. 165902. DOI: 10.1088/1361-648X/ab51ff.

[28] I. Souza, N. Marzari and D. Vanderbilt. 'Maximally localized Wannier functions for entangled energy bands'. In: *Phys. Rev. B* 65 (3 Dec. 2001), p. 035109. DOI: 10.1103/PhysRevB.65.035109.

[29] F. Aryasetiawan et al. 'Frequency-dependent local interactions and low-energy effective models from electronic structure calculations'. In: *Phys. Rev. B* 70 (19 Nov. 2004), p. 195104. DOI: 10.1103/PhysRevB.70.195104.

[30] L. Hedin. 'New Method for Calculating the One-Particle Green's Function with Application to the Electron-Gas Problem'. In: *Phys. Rev.* 139 (3A Aug. 1965), A796–A823. DOI: 10.1103/PhysRev.139.A796.

[31] F. Aryasetiawan and O. Gunnarsson. 'The GW method'. In: *Reports on Progress in Physics* 61.3 (Mar. 1998), p. 237. DOI: 10.1088/0034-4885/61/3/002.

[32] P. Rinke et al. 'Exciting prospects for solids: Exact-exchange based functionals meet quasiparticle energy calculations'. In: *physica status solidi (b)* 245.5 (2008), pp. 929–945. DOI: 10.1002/pssb.200743380.

[33] H. Jiang. 'Structural and electronic properties of ZrX2 and HfX2 (X = S and Se) from first principles calculations'. In: *The Journal of Chemical Physics* 134.20 (May 2011), p. 204705. ISSN: 0021-9606. DOI: 10.1063/1.3594205.

[34] D. Sangalli et al. 'Many-body perturbation theory calculations using the yambo code'. In: *Journal of Physics: Condensed Matter* 31.32 (May 2019), p. 325902. DOI: 10.1088/1361-648X/ab15d0.

[35] P. Larson, M. Dvorak and Z. Wu. 'Role of the plasmon-pole model in the *GW* approximation'. In: *Phys. Rev. B* 88 (12 Sept. 2013), p. 125205. DOI: 10.1103/PhysRevB.88.125205.

[36] M. Stankovski et al. 'G^0W^0 band gap of ZnO: Effects of plasmon-pole models'. In: *Phys. Rev. B* 84 (24 Dec. 2011), p. 241201. DOI: 10.1103/PhysRevB.84.241201.

[37] R. P. Feynman. 'Forces in Molecules'. In: *Phys. Rev.* 56 (4 Aug. 1939), pp. 340–343. DOI: 10.1103/PhysRev.56.340.

[38] S. Baroni, P. Giannozzi and A. Testa. 'Green's-function approach to linear response in solids'. In: *Phys. Rev. Lett.* 58 (18 May 1987), pp. 1861–1864. DOI: 10.1103/PhysRevLett.58.1861.

[39] S. Baroni et al. 'Phonons and related crystal properties from density-functional perturbation theory'. In: *Rev. Mod. Phys.* 73 (2 July 2001), pp. 515–562. DOI: 10.1103/RevModPhys.73.515.

[40] F. Giustino. 'Electron-phonon interactions from first principles'. In: *Rev. Mod. Phys.* 89 (1 Feb. 2017), p. 015003. DOI: 10.1103/RevModPhys.89.015003.

[41] F. Giustino, M. L. Cohen and S. G. Louie. 'Electron-phonon interaction using Wannier functions'. In: *Phys. Rev. B* 76 (16 Oct. 2007), p. 165108. DOI: 10.1103/PhysRevB.76.165108.

[42] J. Noffsinger et al. 'EPW: A program for calculating the electron–phonon coupling using maximally localized Wannier functions'. In: *Computer Physics Communications* 181.12 (2010), pp. 2140–2148. ISSN: 0010-4655. DOI: 10.1016/j.cpc.2010.08.027.

[43] S. Poncé et al. 'EPW: Electron–phonon coupling, transport and superconducting properties using maximally localized Wannier functions'. In: *Computer Physics Communications* 209 (2016), pp. 116–133. ISSN: 0010-4655. DOI: 10.1016/j.cpc.2016.07.028.

[44] H. Lee et al. 'Electron–phonon physics from first principles using the EPW code'. In: *npj Computational Materials* 9.1 (Aug. 2023), p. 156. ISSN: 2057-3960. DOI: 10.1038/s41524-023-01107-3.

[45] J. Berges et al. 'Ab initio phonon self-energies and fluctuation diagnostics of phonon anomalies: Lattice instabilities from Dirac pseudospin physics in transition metal dichalcogenides'. In: *Phys. Rev. B* 101 (15 Apr. 2020), p. 155107. DOI: 10.1103/PhysRevB.101.155107.

[46] J. Berges et al. 'Phonon Self-Energy Corrections: To Screen, or Not to Screen'. In: *Phys. Rev. X* 13 (4 Oct. 2023), p. 041009. DOI: 10.1103/PhysRevX.13.041009.

[47] C. van Efferen et al. 'Metal-insulator transition in monolayer MoS2 via contactless chemical doping'. In: *2D Materials* 9.2 (Mar. 2022), p. 025026. DOI: 10.1088/2053-1583/ac5d0f.

[48] C. van Efferen et al. 'Inelastic Tunneling into Multipolaronic Bound States in Single-Layer MoS_2'. In: *Phys. Rev. X* 15 (3 July 2025), p. 031030. DOI: 10.1103/l8lg-ny6m.

[49] X. Xi et al. 'Strongly enhanced charge-density-wave order in monolayer NbSe2'. In: *Nature Nanotechnology* 10.9 (Sept. 2015). Study via layer thickness. No dping, no twist, pp. 765–769. ISSN: 1748-3395. DOI: 10.1038/nnano.2015.143.

[50] C.-S. Lian, C. Si and W. Duan. 'Unveiling Charge-Density Wave, Superconductivity, and Their Competitive Nature in Two-Dimensional NbSe2'. In: *Nano Letters* 18.5 (2018). PMID: 29652158, pp. 2924–2929. DOI: 10.1021/acs.nanolett.8b00237.

[51] P. M. Coelho et al. 'Charge Density Wave State Suppresses Ferromagnetic Ordering in VSe2 Monolayers'. In: *The Journal of Physical Chemistry C* 123.22 (2019), pp. 14089–14096. DOI: 10.1021/acs.jpcc.9b04281.

[52] L.-N. Wu et al. 'Superconductivity and charge density wave in transition metal chalcogenides: A first principle study'. In: *Physica E: Low-dimensional Systems and Nanostructures* 151 (2023), p. 115714. ISSN: 1386-9477. DOI: 10.1016/j.physe.2023.115714.

[53] W. Zhang et al. 'The coexistence and competition of charge-density wave and superconductivity in the electron-doped H- MX2 (M = Mo, W and X=S, Se)'. In: *Surfaces and Interfaces* 49 (2024), p. 104391. ISSN: 2468-0230. DOI: 10.1016/j.surfin.2024.104391.

[54] F. Zheng and J. Feng. 'Electron-phonon coupling and the coexistence of superconductivity and charge-density wave in monolayer $NbSe_2$'. In: *Phys. Rev. B* 99 (16 Apr. 2019), p. 161119. DOI: 10.1103/PhysRevB.99.161119.

[55] Q. Zhang et al. 'Spin polarization driven by a charge-density wave in monolayer $1T-TaS_2$'. In: *Phys. Rev. B* 90 (8 Aug. 2014), p. 081103. DOI: 10.1103/PhysRevB.90.081103.

[56] D. Bansal et al. 'Magnetically driven phonon instability enables the metal–insulator transition in h-FeS'. In: *Nature Physics* 16.6 (June 2020), pp. 669–675. ISSN: 1745-2481. DOI: 10.1038/s41567-020-0857-1.

[57] W. Zhang and J. Wu. 'Stacking order and driving forces in the layered charge density wave phase of 1T-MX2 (M = Nb, Ta and X = S, Se)'. In: *Materials Research Express* 10.4 (Apr. 2023), p. 046302. DOI: 10.1088/2053-1591/acc997.

[58] H. K. Onnes. *Commun. Phys. Lab. Univ. Leiden 120b, 122b, 124c*. 1911.

[59] H. K. Onnes. 'Further Experiments with Liquid Helium. D. On the Change of the Electrical Resistance of Pure Metals at very low Temperatures, etc. V. The Disappearance of the resistance of mercury'. In: *Through Measurement to Knowledge: The Selected Papers of Heike Kamerlingh Onnes 1853–1926*. Ed. by K. Gavroglu and Y. Goudaroulis. Dordrecht: Springer Netherlands, 1911, pp. 264–266. ISBN: 978-94-009-2079-8. DOI: 10.1007/978-94-009-2079-8_16.

[60] D. van Delft and P. Kes. 'The discovery of superconductivity'. In: *Physics Today* 63.9 (Sept. 2010), pp. 38–43. ISSN: 0031-9228. DOI: 10.1063/1.3490499.

[61] W. Meissner and R. Ochsenfeld. 'Ein neuer Effekt bei Eintritt der Supraleitfähigkeit'. In: *Naturwissenschaften* 21.44 (Nov. 1933), pp. 787–788. ISSN: 1432-1904. DOI: 10.1007/BF01504252.

[62] L. F. and L. H. 'The electromagnetic equations of the supraconductor'. In: *Proc. R. Soc. Lond. A* 149 (Mar. 1935), pp. 71–88. DOI: 10.1098/rspa.1935.0048.

[63] H. Fröhlich. 'Theory of the Superconducting State. I. The Ground State at the Absolute Zero of Temperature'. In: *Phys. Rev.* 79 (5 Sept. 1950), pp. 845–856. DOI: 10.1103/PhysRev.79.845.

[64] F. H. 'Interaction of electrons with lattice vibrations'. In: *Proc. R. Soc. Lond. A* 215 (Dec. 1952), pp. 291–298. DOI: 10.1098/rspa.1952.0212.

[65] L. N. Cooper. 'Bound Electron Pairs in a Degenerate Fermi Gas'. In: *Phys. Rev.* 104 (4 Nov. 1956), pp. 1189–1190. DOI: 10.1103/PhysRev.104.1189.

[66] J. Bardeen, L. N. Cooper and J. R. Schrieffer. 'Theory of Superconductivity'. In: *Phys. Rev.* 108 (5 Dec. 1957), pp. 1175–1204. DOI: 10.1103/PhysRev.108.1175.

[67] A. Migdal. 'Interaction between electrons and lattice vibrations in a normal metal'. In: *Sov. Phys. JETP* 34 (7).6 (Dec. 1958), p. 6.

[68] G. M. Eliashberg. 'Interactions between electrons and lattice vibrations in a superconductor'. In: *Sov. Phys. JETP* 11.3 (Sept. 1960), pp. 696–702. URL: http://www.jetp.ras.ru/cgi-bin/dn/e_011_03_0696.pdf.

[69] L. P. Gor'kov. 'On the energy spectrum of superconductors'. In: *Soviet Physics JETP* 34(7).3 (Sept. 1958), pp. 505–508. URL: http://www.jetp.ras.ru/cgi-bin/dn/e_007_03_0505.pdf.

[70] P. B. Allen and R. C. Dynes. 'Transition temperature of strong-coupled superconductors reanalyzed'. In: *Phys. Rev. B* 12 (3 Aug. 1975), pp. 905–922. DOI: 10.1103/PhysRevB.12.905.

[71] E. A. Drzazga et al. 'Characteristics of Superconducting State in Vanadium: the Eliashberg Equations and Semi-analytical Formulas'. In: *Journal of Superconductivity and Novel Magnetism* 31.4 (Apr. 2018), pp. 1029–1034. ISSN: 1557-1947. DOI: 10.1007/s10948-017-4295-y.

[72] P. Morel and P. W. Anderson. 'Calculation of the Superconducting State Parameters with Retarded Electron-Phonon Interaction'. In: *Phys. Rev.* 125 (4 Feb. 1962), pp. 1263–1271. DOI: 10.1103/PhysRev.125.1263.

[73] W. L. McMillan. 'Transition Temperature of Strong-Coupled Superconductors'. In: *Phys. Rev.* 167 (2 Mar. 1968), pp. 331–344. DOI: 10.1103/PhysRev.167.331.

[74] R. Dynes. 'McMillan's equation and the Tc of superconductors'. In: *Solid State Communications* 10.7 (1972), pp. 615–618. ISSN: 0038-1098. DOI: https://doi.org/10.1016/0038-1098(72)90603-5.

[75] D. J. Scalapino. 'A common thread: The pairing interaction for unconventional superconductors'. In: *Rev. Mod. Phys.* 84 (4 Oct. 2012), pp. 1383–1417. DOI: 10.1103/RevModPhys.84.1383.

[76] E. Antončík. 'On the theory of temperature shift of the absorption curve in nonpolar crystals'. In: *Cechoslovackij fiziceskij zurnal* 5.4 (Dec. 1955), pp. 449–461. ISSN: 1572-9486. DOI: 10.1007/BF01687209.

[77] J. P. Walter et al. 'Temperature Dependence of the Wavelength-Modulation Spectra of GaAs'. In: *Phys. Rev. Lett.* 24 (3 Jan. 1970), pp. 102–104. DOI: 10.1103/PhysRevLett.24.102.

[78] M. Cardona and M. L. W. Thewalt. 'Isotope effects on the optical spectra of semiconductors'. In: *Rev. Mod. Phys.* 77 (4 Nov. 2005), pp. 1173–1224. DOI: 10.1103/RevModPhys.77.1173.

[79] P. Mitrić et al. 'Spectral Functions of the Holstein Polaron: Exact and Approximate Solutions'. In: *Phys. Rev. Lett.* 129 (9 Aug. 2022), p. 096401. DOI: 10.1103/PhysRevLett.129.096401.

[80] P. Mitrić et al. 'Cumulant expansion in the Holstein model: Spectral functions and mobility'. In: *Phys. Rev. B* 107 (12 Mar. 2023), p. 125165. DOI: 10.1103/PhysRevB.107.125165.

[81] L. Hedin. 'On correlation effects in electron spectroscopies and the GW approximation'. In: *Journal of Physics: Condensed Matter* 11.42 (Oct. 1999), R489. DOI: 10.1088/0953-8984/11/42/201.

[82] J. J. Kas, J. J. Rehr and L. Reining. 'Cumulant expansion of the retarded one-electron Green function'. In: *Phys. Rev. B* 90 (8 Aug. 2014), p. 085112. DOI: 10.1103/PhysRevB.90.085112.

[83] S. Ulstrup et al. 'Observation of interlayer plasmon polaron in graphene/WS2 heterostructures'. In: *Nature Communications* 15.1 (May 2024), p. 3845. ISSN: 2041-1723. DOI: 10.1038/s41467-024-48186-4.

[84] Z.-G. Fu et al. 'Modulation of doping and biaxial strain on the transition temperature of the charge density wave transition in 1T-TiSe2'. In: *RSC Adv.* 6 (80 2016), pp. 76972–76979. DOI: 10.1039/C6RA13433E.

[85] M. J. Wei et al. 'Manipulating charge density wave order in monolayer $1T - TiSe_2$ by strain and charge doping: A first-principles investigation'. In: *Phys. Rev. B* 96 (16 Oct. 2017), p. 165404. DOI: 10.1103/PhysRevB.96.165404.

[86] S. Gao et al. 'Atomic-scale strain manipulation of a charge density wave'. In: *Proceedings of the National Academy of Sciences* 115.27 (2018), pp. 6986–6990. DOI: 10.1073/pnas.1718931115.

[87] M. Kang et al. 'Holstein polaron in a valley-degenerate two-dimensional semiconductor'. In: *Nature Materials* 17.8 (Aug. 2018), pp. 676–680. ISSN: 1476-4660. DOI: 10.1038/s41563-018-0092-7.

[88] J. G. Si et al. 'Charge-density-wave tuning in monolayer 1H-TaSe2by biaxial strain and charge doping'. In: *Europhysics Letters* 127.3 (Sept. 2019), p. 37001. DOI: 10.1209/0295-5075/127/37001.

[89] S. Bae et al. 'Universal Polaronic Behavior in Elemental Doping of MoS2 from First-Principles'. In: *ACS Nano* 18.50 (2024). PMID: 39622529, pp. 33988–33997. DOI: 10.1021/acsnano.4c08366.

[90] C. T. S. Cheung et al. 'Coexisting Charge Density Waves in Twisted Bilayer NbSe2'. In: *Nano Letters* 24.39 (2024). PMID: 39297477, pp. 12088–12094. DOI: 10.1021/acs.nanolett.4c02750.

[91] A. K. Kundu et al. 'Charge density waves and the effects of uniaxial strain on the electronic structure of 2H-NbSe2'. In: *Communications Materials* 5.1 (Oct. 2024), p. 208. ISSN: 2662-4443. DOI: 10.1038/s43246-024-00661-7.

[92] W.-C. Chiu et al. 'Strain-Induced Charge Density Waves with Emergent Topological States in Monolayer NbSe2'. In: *ACS Nano* 19.19 (2025). PMID: 40327834, pp. 18108–18116. DOI: 10.1021/acsnano.4c13478.

[93] H. Fröhlich, H. Pelzer and S. Zienau. 'XX. Properties of slow electrons in polar materials'. In: *Philosophical Magazine Series 1* 41 (1950), pp. 221–242. URL: https://api.semanticscholar.org/CorpusID:121859551.

[94] H. Fröhlich. 'Electrons in lattice fields'. In: *Advances in Physics* 3.11 (1954), pp. 325–361. DOI: 10.1080/00018735400101213.

[95] J. T. Devreese and A. S. Alexandrov. 'Fröhlich polaron and bipolaron: recent developments'. In: *Reports on Progress in Physics* 72.6 (May 2009), p. 066501. DOI: 10.1088/0034-4885/72/6/066501.

[96] W. Dybalski and H. Spohn. 'Effective Mass of the Polaron—Revisited'. In: *Annales Henri Poincaré* 21.5 (May 2020), pp. 1573–1594. ISSN: 1424-0661. DOI: 10.1007/s00023-020-00892-7.

[97] B. Guster et al. 'Fröhlich polaron effective mass and localization length in cubic materials: Degenerate and anisotropic electronic bands'. In: *Phys. Rev. B* 104 (23 Dec. 2021), p. 235123. DOI: 10.1103/PhysRevB.104.235123.

[98] S. I. Pekar. *Untersuchungen über die Elektronentheorie der Kristalle*. De Gruyter, 1954.

[99] T. Holstein. 'Studies of polaron motion: Part I. The molecular-crystal model'. In: *Annals of Physics* 8.3 (1959), pp. 325–342. ISSN: 0003-4916. DOI: https://doi.org/10.1016/0003-4916(59)90002-8.

[100] T. Holstein. 'Studies of polaron motion: Part II. The "small" polaron'. In: *Annals of Physics* 8.3 (1959), pp. 343–389. ISSN: 0003-4916. DOI: https://doi.org/10.1016/0003-4916(59)90003-X.

[101] C. P. J. Adolphs and M. Berciu. 'Going beyond the linear approximation in describing electron-phonon coupling: Relevance for the Holstein model'. In: *Europhysics Letters* 102.4 (June 2013), p. 47003. DOI: 10.1209/0295-5075/102/47003.

[102] W. H. Sio et al. 'Ab initio theory of polarons: Formalism and applications'. In: *Phys. Rev. B* 99 (23 June 2019), p. 235139. DOI: 10.1103/PhysRevB.99.235139.

[103] J. Lafuente-Bartolome et al. 'Ab initio self-consistent many-body theory of polarons at all couplings'. In: *Phys. Rev. B* 106 (7 Aug. 2022), p. 075119. DOI: 10.1103/PhysRevB.106.075119.

[104] K. S. Novoselov et al. 'Two-dimensional atomic crystals'. In: *Proceedings of the National Academy of Sciences* 102.30 (2005), pp. 10451–10453. DOI: 10.1073/pnas.0502848102.

[105] C. R. Dean et al. 'Boron nitride substrates for high-quality graphene electronics'. In: *Nature Nanotechnology* 5.10 (Oct. 2010), pp. 722–726. ISSN: 1748-3395. DOI: 10.1038/nnano.2010.172.

[106] P. Yang et al. 'Epitaxial growth of inch-scale single-crystal transition metal dichalcogenides through the patching of unidirectionally orientated ribbons'. In: *Nature Communications* 13.1 (June 2022), p. 3238. ISSN: 2041-1723. DOI: 10.1038/s41467-022-30900-9.

[107] Z. Li et al. 'Atomic Layer Deposition of Transition-Metal Dichalcogenides'. In: *Crystal Growth & Design* 24.5 (2024), pp. 1865–1879. DOI: 10.1021/acs.cgd.3c01044.

[108] M. Nastran et al. 'Liquid phase exfoliation of graphene using ammonia as an easy-to-remove additive in low-boiling organic-water co-solvent suspensions'. In: *Communications Chemistry* 8.1 (May 2025), p. 161. ISSN: 2399-3669. DOI: 10.1038/s42004-025-01517-y.

[109] P. R. Wallace. 'The Band Theory of Graphite'. In: *Phys. Rev.* 71 (9 May 1947), pp. 622–634. DOI: 10.1103/PhysRev.71.622.

[110] H. Boehm, R. Setton and E. Stumpp. 'Nomenclature and terminology of graphite intercalation compounds'. In: *Carbon* 24.2 (1986), pp. 241–245. ISSN: 0008-6223. DOI: https://doi.org/10.1016/0008-6223(86)90126-0.

[111] K. S. Novoselov et al. 'Electric Field Effect in Atomically Thin Carbon Films'. In: *Science* 306.5696 (Oct. 2004), pp. 666–669. ISSN: 1095-9203. DOI: 10.1126/science.1102896.

[112] A. K. Geim and I. V. Grigorieva. 'Van der Waals heterostructures'. In: *Nature* 499.7459 (July 2013), pp. 419–425. ISSN: 1476-4687. DOI: 10.1038/nature12385.

[113] A. K. Geim. 'Graphene: Status and Prospects'. In: *Science* 324.5934 (2009), pp. 1530–1534. DOI: 10.1126/science.1158877.

[114] B. M. Kessler et al. 'Tunable Superconducting Phase Transition in Metal-Decorated Graphene Sheets'. In: *Phys. Rev. Lett.* 104 (4 Jan. 2010), p. 047001. DOI: 10.1103/PhysRevLett.104.047001.

[115] K. C. Rahnejat et al. 'Charge density waves in the graphene sheets of the superconductor CaC6'. In: *Nature Communications* 2.1 (Nov. 2011), p. 558. ISSN: 2041-1723. DOI: 10.1038/ncomms1574.

[116] O. V. Kibis et al. 'Magnetoelectronic properties of graphene dressed by a high-frequency field'. In: *Phys. Rev. B* 93 (11 Mar. 2016), p. 115420. DOI: 10.1103/PhysRevB.93.115420.

[117] F. Wu, A. H. MacDonald and I. Martin. 'Theory of Phonon-Mediated Superconductivity in Twisted Bilayer Graphene'. In: *Phys. Rev. Lett.* 121 (25 Dec. 2018), p. 257001. DOI: 10.1103/PhysRevLett.121.257001.

[118] L. Wang, Z. Sofer and M. Pumera. 'Will Any Crap We Put into Graphene Increase Its Electrocatalytic Effect?' In: *ACS Nano* 14.1 (2020). PMID: 31934742, pp. 21–25. DOI: 10.1021/acsnano.9b00184.

[119] P. Joensen, R. Frindt and S. Morrison. 'Single-layer MoS2'. In: *Materials Research Bulletin* 21.4 (1986), pp. 457–461. ISSN: 0025-5408. DOI: https://doi.org/10.1016/0025-5408(86)90011-5.

[120] G. Z. Magda et al. 'Exfoliation of large-area transition metal chalcogenide single layers'. In: *Scientific Reports* 5.1 (Oct. 2015). ISSN: 2045-2322. DOI: 10.1038/srep14714.

[121] A. Gasbarro et al. 'Accessible and Inexpensive Parameter Testing Platform for Adhesive Removal in Mechanical Exfoliation Procedures'. In: *Electronics* 14.3 (2025). ISSN: 2079-9292. DOI: 10.3390/electronics14030533.

[122] A. Gasbarro, Y.-S. D. Masuda and V. M. Lubecke. 'High-Throughput Evaluation of Mechanical Exfoliation Using Optical Classification of Two-Dimensional Materials'. In: *Micromachines* 16.10 (2025). ISSN: 2072-666X. DOI: 10.3390/mi16101084.

[123] Y. Huang et al. 'Universal mechanical exfoliation of large-area 2D crystals'. In: *Nature Communications* 11.1 (May 2020). ISSN: 2041-1723. DOI: 10.1038/s41467-020-16266-w.

[124] S. E. Panasci et al. 'Gold-Assisted Exfoliation of Large-Area Monolayer Transition Metal Dichalcogenides: From Interface Properties to Device Applications'. In: *Advanced Functional Materials* 35.5 (2025), p. 2414532. DOI: https://doi.org/10.1002/adfm.202414532.

[125] Z. Lin et al. 'High-yield exfoliation of 2D semiconductor monolayers and reassembly of organic/inorganic artificial superlattices'. In: *Chem* 7.7 (July 2021), pp. 1887–1902. ISSN: 2451-9294. DOI: 10.1016/j.chempr.2021.03.022.

[126] P. Chavalekvirat et al. 'Liquid Phase Exfoliation of 2D Materials and Its Electrochemical Applications in the Data-Driven Future'. In: *Precision Chemistry* 2.7 (Mar. 2024), pp. 300–329. ISSN: 2771-9316. DOI: 10.1021/prechem.3c00119.

[127] W. Tian et al. 'Liquid-phase exfoliation of 2D transition metal dichalcogenide nanosheets in water'. In: *Chemical Engineering Journal* 513 (2025), p. 162587. ISSN: 1385-8947. DOI: https://doi.org/10.1016/j.cej.2025.162587.

[128] Q. H. Wang et al. 'Electronics and optoelectronics of two-dimensional transition metal dichalcogenides'. In: *Nature Nanotechnology* 7.11 (Nov. 2012), pp. 699–712. ISSN: 1748-3395. DOI: 10.1038/nnano.2012.193.

[129] M. Chhowalla et al. 'The chemistry of two-dimensional layered transition metal dichalcogenide nanosheets'. In: *Nature Chemistry* 5.4 (Mar. 2013), pp. 263–275. ISSN: 1755-4349. DOI: 10.1038/nchem.1589.

[130] J. Wilson and A. Yoffe. 'The transition metal dichalcogenides discussion and interpretation of the observed optical, electrical and structural properties'. In: *Advances in Physics* 18.73 (1969), pp. 193–335. DOI: 10.1080/00018736900101307.

[131] S. Manzeli et al. '2D transition metal dichalcogenides'. In: *Nature Reviews Materials* 2.8 (June 2017). ISSN: 2058-8437. DOI: 10.1038/natrevmats.2017.33.

[132] X. Qian et al. 'Quantum spin Hall effect in two-dimensional transition metal dichalcogenides'. In: *Science* 346.6215 (2014), pp. 1344–1347. DOI: 10.1126/science.1256815.

[133] A. N. Enyashin et al. 'New Route for Stabilization of 1T-WS2 and MoS2 Phases'. In: *The Journal of Physical Chemistry C* 115.50 (Nov. 2011), pp. 24586–24591. ISSN: 1932-7455. DOI: 10.1021/jp2076325.

[134] K.-A. N. Duerloo, Y. Li and E. J. Reed. 'Structural phase transitions in two-dimensional Mo- and W-dichalcogenide monolayers'. In: *Nature Communications* 5.1 (July 2014). ISSN: 2041-1723. DOI: 10.1038/ncomms5214.

[135] K. F. Mak et al. 'Atomically Thin MoS_2: A New Direct-Gap Semiconductor'. In: *Phys. Rev. Lett.* 105 (13 Sept. 2010), p. 136805. DOI: 10.1103/PhysRevLett.105.136805.

[136] A. Splendiani et al. 'Emerging Photoluminescence in Monolayer MoS2'. In: *Nano Letters* 10.4 (2010). PMID: 20229981, pp. 1271–1275. DOI: 10.1021/nl903868w.

[137] A. Ramasubramaniam. 'Large excitonic effects in monolayers of molybdenum and tungsten dichalcogenides'. In: *Phys. Rev. B* 86 (11 Sept. 2012), p. 115409. DOI: 10.1103/PhysRevB.86.115409.

[138] A. Kormányos et al. 'k · p theory for two-dimensional transition metal dichalcogenide semiconductors'. In: *2D Materials* 2.2 (Apr. 2015), p. 022001. DOI: 10.1088/2053-1583/2/2/022001.

[139] P.-C. Yeh et al. 'Layer-dependent electronic structure of an atomically heavy two-dimensional dichalcogenide'. In: *Phys. Rev. B* 91 (4 Jan. 2015), p. 041407. DOI: 10.1103/PhysRevB.91.041407.

[140] S. K. Pandey, R. Das and P. Mahadevan. 'Layer-Dependent Electronic Structure Changes in Transition Metal Dichalcogenides: The Microscopic Origin'. In: *ACS Omega* 5.25 (2020). PMID: 32637790, pp. 15169–15176. DOI: 10.1021/acsomega.0c01138.

[141] Z. Y. Zhu, Y. C. Cheng and U. Schwingenschlögl. 'Giant spin-orbit-induced spin splitting in two-dimensional transition-metal dichalcogenide semiconductors'. In: *Phys. Rev. B* 84 (15 Oct. 2011), p. 153402. DOI: 10.1103/PhysRevB.84.153402.

[142] K. Ko śmider, J. W. González and J. Fernández-Rossier. 'Large spin splitting in the conduction band of transition metal dichalcogenide monolayers'. In: *Phys. Rev. B* 88 (24 Dec. 2013), p. 245436. DOI: 10.1103/PhysRevB.88.245436.

[143] D. Xiao et al. 'Coupled Spin and Valley Physics in Monolayers of MoS_2 and Other Group-VI Dichalcogenides'. In: *Phys. Rev. Lett.* 108 (19 May 2012), p. 196802. DOI: 10.1103/PhysRevLett.108.196802.

[144] A. Kormányos et al. 'Monolayer MoS_2: Trigonal warping, the Γ valley, and spin-orbit coupling effects'. In: *Phys. Rev. B* 88 (4 July 2013), p. 045416. DOI: 10.1103/PhysRevB.88.045416.

[145] M. Rösner, S. Haas and T. O. Wehling. 'Phase diagram of electron-doped dichalcogenides'. In: *Phys. Rev. B* 90 (24 Dec. 2014), p. 245105. DOI: 10.1103/PhysRevB.90.245105.

[146] M. Rösner et al. 'Two-Dimensional Heterojunctions from Nonlocal Manipulations of the Interactions'. In: *Nano Letters* 16.4 (2016). PMID: 26918626, pp. 2322–2327. DOI: 10.1021/acs.nanolett.5b05009.

[147] T. Sohier et al. 'Enhanced Electron-Phonon Interaction in Multivalley Materials'. In: *Phys. Rev. X* 9 (3 Aug. 2019), p. 031019. DOI: 10.1103/PhysRevX.9.031019.

[148] A. F. Kusmartseva et al. 'Pressure Induced Superconductivity in Pristine $1T-TiSe_2$'. In: *Phys. Rev. Lett.* 103 (23 Nov. 2009), p. 236401. DOI: 10.1103/PhysRevLett.103.236401.

[149] A. Newaz et al. 'Electrical control of optical properties of monolayer MoS2'. In: *Solid State Communications* 155 (2013), pp. 49–52. ISSN: 0038-1098. DOI: https://doi.org/10.1016/j.ssc.2012.11.010.

[150] C. Gong et al. 'Band alignment of two-dimensional transition metal dichalcogenides: Application in tunnel field effect transistors'. In: *Applied Physics Letters* 103.5 (Aug. 2013), p. 053513. ISSN: 0003-6951. DOI: 10.1063/1.4817409.

[151] K. He et al. 'Experimental Demonstration of Continuous Electronic Structure Tuning via Strain in Atomically Thin MoS2'. In: *Nano Letters* 13.6 (2013). PMID: 23675872, pp. 2931–2936. DOI: 10.1021/nl4013166.

[152] S. Aeschlimann et al. 'Direct evidence for efficient ultrafast charge separation in epitaxial WS 2 /graphene heterostructures'. In: *Science Advances* 6.20 (May 2020). ISSN: 2375-2548. DOI: 10.1126/sciadv.aay0761.

[153] J. Kang et al. 'Band offsets and heterostructures of two-dimensional semiconductors'. In: *Applied Physics Letters* 102.1 (Jan. 2013), p. 012111. ISSN: 0003-6951. DOI: 10.1063/1.4774090.

[154] H. Yuan et al. 'Evolution of the Valley Position in Bulk Transition-Metal Chalcogenides and Their Monolayer Limit'. In: *Nano Letters* 16.8 (2016). PMID: 27357620, pp. 4738–4745. DOI: 10.1021/acs.nanolett.5b05107.

[155] M. M. Fogler, L. V. Butov and K. S. Novoselov. 'High-temperature superfluidity with indirect excitons in van der Waals heterostructures'. In: *Nature Communications* 5.1 (July 2014). ISSN: 2041-1723. DOI: 10.1038/ncomms5555.

[156] P. Rivera et al. 'Observation of long-lived interlayer excitons in monolayer MoSe2–WSe2 heterostructures'. In: *Nature Communications* 6.1 (Feb. 2015). ISSN: 2041-1723. DOI: 10.1038/ncomms7242.

[157] J. T. Ye et al. 'Superconducting Dome in a Gate-Tuned Band Insulator'. In: *Science* 338.6111 (Nov. 2012), pp. 1193–1196. ISSN: 1095-9203. DOI: 10.1126/science.1228006.

[158] Y. Saito et al. 'Superconductivity protected by spin–valley locking in ion-gated MoS2'. In: *Nature Physics* 12.2 (Dec. 2015), pp. 144–149. ISSN: 1745-2481. DOI: 10.1038/nphys3580.

[159] J. M. Lu et al. 'Evidence for two-dimensional Ising superconductivity in gated MoS_2'. In: *Science* 350.6266 (2015), pp. 1353–1357. DOI: 10.1126/science.aab2277.

[160] K. F. Mak et al. 'Tightly bound trions in monolayer MoS2'. In: *Nature Materials* 12.3 (Dec. 2012), pp. 207–211. ISSN: 1476-4660. DOI: 10.1038/nmat3505.

[161] R. Kumar et al. 'Substitutional doping of 2D transition metal dichalcogenides for device applications: Current status, challenges and prospects'. In: *Materials Science and Engineering: R: Reports* 163 (2025), p. 100946. ISSN: 0927-796X. DOI: https://doi.org/10.1016/j.mser.2025.100946.

[162] Z. Han et al. 'Recent Progress in Tungsten Diselenide Field-Effect Transistors: Materials, Fabrication, and Applications'. In: *Chemistry of Materials* 38.1 (2026), pp. 87–116. DOI: 10.1021/acs.chemmater.5c02909.

[163] A. Ali et al. 'Interplay between charge-density-waves, disorder, and superconductivity in transition metal dichalcogenides'. In: *Results in Physics* 70 (2025), p. 108154. ISSN: 2211-3797. DOI: https://doi.org/10.1016/j.rinp.2025.108154.

[164] Y. Xia et al. 'Superconductivity in twisted bilayer WSe2'. In: *Nature* 637.8047 (Oct. 2024), pp. 833–838. ISSN: 1476-4687. DOI: 10.1038/s41586-024-08116-2.

[165] M. H. Naik and M. Jain. 'Ultraflatbands and Shear Solitons in Moiré Patterns of Twisted Bilayer Transition Metal Dichalcogenides'. In: *Phys. Rev. Lett.* 121 (26 Dec. 2018), p. 266401. DOI: 10.1103/PhysRevLett.121.266401.

[166] E. C. Regan et al. 'Mott and generalized Wigner crystal states in WSe2/WS2 moiré superlattices'. In: *Nature* 579.7799 (Mar. 2020), pp. 359–363. ISSN: 1476-4687. DOI: 10.1038/s41586-020-2092-4.

[167] Y. Guo et al. 'Superconductivity in 5.0° twisted bilayer WSe2'. In: *Nature* 637.8047 (Jan. 2025), pp. 839–845. ISSN: 1476-4687. DOI: 10.1038/s41586-024-08381-1.

[168] S. Kim et al. 'Theory of correlated insulators and superconductor at $\nu = 1$ in twisted WSe2'. In: *Nature Communications* 16.1 (Feb. 2025). ISSN: 2041-1723. DOI: 10.1038/s41467-025-56816-8.

[169] D. Chen et al. 'Excitonic insulator in a heterojunction moiré superlattice'. In: *Nature Physics* 18.10 (Aug. 2022), pp. 1171–1176. ISSN: 1745-2481. DOI: 10.1038/s41567-022-01703-y.

[170] K. L. Seyler et al. 'Signatures of moiré-trapped valley excitons in MoSe2/WSe2 heterobilayers'. In: *Nature* 567.7746 (Feb. 2019), pp. 66–70. ISSN: 1476-4687. DOI: 10.1038/s41586-019-0957-1.

[171] Y. Choi et al. 'Electronic correlations in twisted bilayer graphene near the magic angle'. In: *Nature Physics* 15.11 (Aug. 2019), pp. 1174–1180. ISSN: 1745-2481. DOI: 10.1038/s41567-019-0606-5.

[172] C. Jin et al. 'Observation of moiré excitons in WSe2/WS2 heterostructure superlattices'. In: *Nature* 567.7746 (Feb. 2019), pp. 76–80. ISSN: 1476-4687. DOI: 10.1038/s41586-019-0976-y.

[173] A. Weston et al. 'Atomic reconstruction in twisted bilayers of transition metal dichalcogenides'. In: *Nature Nanotechnology* 15.7 (July 2020), pp. 592–597. ISSN: 1748-3395. DOI: 10.1038/s41565-020-0682-9.

[174] P. Garcia-Goiricelaya et al. 'Long-living carriers in a strong electron–phonon interacting two-dimensional doped semiconductor'. In: *Communications Physics* 2.1 (July 2019), p. 81. ISSN: 2399-3650. DOI: 10.1038/s42005-019-0182-0.

[175] N. S. Wingreen, K. W. Jacobsen and J. W. Wilkins. 'Resonant Tunneling with Electron-Phonon Interaction: An Exactly Solvable Model'. In: *Phys. Rev. Lett.* 61 (12 Sept. 1988), pp. 1396–1399. DOI: 10.1103/PhysRevLett.61.1396.

[176] K. A. Cochrane et al. 'Spin-dependent vibronic response of a carbon radical ion in two-dimensional WS2'. In: *Nature Communications* 12.1 (Dec. 2021), p. 7287. ISSN: 2041-1723. DOI: 10.1038/s41467-021-27585-x.

[177] M. Hohenadler, M. Aichhorn and W. von der Linden. 'Single-particle spectral function of the Holstein-Hubbard bipolaron'. In: *Phys. Rev. B* 71 (1 Jan. 2005), p. 014302. DOI: 10.1103/PhysRevB.71.014302.

[178] M. Capone, P. Carta and S. Ciuchi. 'Dynamical mean field theory of polarons and bipolarons in the half-filled Holstein model'. In: *Phys. Rev. B* 74 (4 July 2006), p. 045106. DOI: 10.1103/PhysRevB.74.045106.

[179] E. V. L. de Mello and J. Ranninger. 'Dynamical properties of small polarons'. In: *Phys. Rev. B* 55 (22 June 1997), pp. 14872–14885. DOI: 10.1103/PhysRevB.55.14872.

[180] J. Ranninger. 'Spectral properties of small-polaron systems'. In: *Phys. Rev. B* 48 (17 Nov. 1993), pp. 13166–13169. DOI: 10.1103/PhysRevB.48.13166.

[181] M. Hohenadler, M. Aichhorn and W. von der Linden. 'Spectral function of electron-phonon models by cluster perturbation theory'. In: *Phys. Rev. B* 68 (18 Nov. 2003), p. 184304. DOI: 10.1103/PhysRevB.68.184304.

[182] M. Hohenadler et al. 'Photoemission spectra of many-polaron systems'. In: *Phys. Rev. B* 71 (24 June 2005), p. 245111. DOI: 10.1103/PhysRevB.71.245111.

[183] M. Hohenadler et al. 'Many-polaron problem by cluster perturbation theory'. In: *Physica B: Condensed Matter* 378-380 (2006). Proceedings of the International Conference on Strongly Correlated Electron Systems, pp. 64–65. ISSN: 0921-4526. DOI: 10.1016/j.physb.2006.01.026.

[184] A. Schobert et al. 'Ab initio electron-lattice downfolding: Potential energy landscapes, anharmonicity, and molecular dynamics in charge density wave materials'. In: *SciPost Physics* 16.2 (Feb. 2024). ISSN: 2542-4653. DOI: 10.21468/scipostphys.16.2.046.

[185] W. H. Sio and F. Giustino. 'Polarons in two-dimensional atomic crystals'. In: *Nature Physics* 19.5 (May 2023), pp. 629–636. ISSN: 1745-2481. DOI: 10.1038/s41567-023-01953-4.

[186] J. P. Perdew, K. Burke and M. Ernzerhof. 'Generalized Gradient Approximation Made Simple'. In: *Phys. Rev. Lett.* 77 (18 Oct. 1996), pp. 3865–3868. DOI: 10.1103/PhysRevLett.77.3865.

[187] E. R. Margine and F. Giustino. 'Anisotropic Migdal-Eliashberg theory using Wannier functions'. In: *Physical Review B* 87.2 (Jan. 2013), p. 024505. ISSN: 1550-235X. DOI: 10.1103/physrevb.87.024505.

[188] R. P. Feynman. *The Pleasure of Finding Things Out: The Best Short Works of Richard Feynman*. Original foreword by Freeman Dyson. USA: Perseus Books, 1999. ISBN: 0-7382-0108-1. URL: https://en.wikipedia.org/wiki/The_Pleasure_of_Finding_Things_Out.

[189] M. N. Disiena et al. 'Effects of Mo Doping on the Superconducting Properties of NbSe2'. In: *ACS Applied Electronic Materials* 7.20 (2025), pp. 9526–9533. DOI: 10.1021/acsaelm.5c01715.

[190] M. Rösner et al. 'Wannier function approach to realistic Coulomb interactions in layered materials and heterostructures'. In: *Phys. Rev. B* 92 (8 Aug. 2015), p. 085102. DOI: 10.1103/PhysRevB.92.085102.

[191] W. Shi et al. 'Superconductivity Series in Transition Metal Dichalcogenides by Ionic Gating'. In: *Scientific Reports* 5.1 (Aug. 2015). ISSN: 2045-2322. DOI: 10.1038/srep12534.

[192] E. Piatti et al. 'Multi-Valley Superconductivity in Ion-Gated MoS2 Layers'. In: *Nano Letters* 18.8 (2018). PMID: 29949374, pp. 4821–4830. DOI: 10.1021/acs.nanolett.8b01390.

[193] W. Guo et al. 'Nonvolatile n-Type Doping and Metallic State in Multilayer-MoS2 Induced by Hydrogenation Using Ionic-Liquid Gating'. In: *Nano Letters* 22.22 (2022). PMID: 36342413, pp. 8957–8965. DOI: 10.1021/acs.nanolett.2c03159.

[194] Y. J. Zhang, J. T. Ye and Y. Iwasa. 'Field-induced superconductivity in MoS2'. In: *MRS Proceedings* 1549 (2013), pp. 79–84. DOI: 10.1557/opl.2013.709.

[195] F. Qin et al. 'Electric-field Control of Electronic States in WS_2 Nanodevices by Electrolyte Gating'. In: *Journal of Visualized Experiments* 134 (Apr. 2018). ISSN: 1940-087X. DOI: 10.3791/56862.

[196] C. H. Lui et al. 'Observation of interlayer phonon modes in van der Waals heterostructures'. In: *Phys. Rev. B* 91 (16 Apr. 2015), p. 165403. DOI: 10.1103/PhysRevB.91.165403.

[197] D. Costanzo et al. 'Gate-induced superconductivity in atomically thin MoS2 crystals'. In: *Nature Nanotechnology* 11.4 (Apr. 2016), pp. 339–344. ISSN: 1748-3395. DOI: 10.1038/nnano.2015.314.

[198] K.-X. Xu et al. 'Superconductivity in monolayer YCI and its strain modulation: A first-principles prediction'. In: *Computational Materials Science* 258 (2025), p. 113986. ISSN: 0927-0256. DOI: https://doi.org/10.1016/j.commatsci.2025.113986.

[199] F. A. Rasmussen and K. S. Thygesen. 'Computational 2D Materials Database: Electronic Structure of Transition-Metal Dichalcogenides and Oxides'. In: *The Journal of Physical Chemistry C* 119.23 (2015), pp. 13169–13183. DOI: 10.1021/acs.jpcc.5b02950.

[200] Z. Li et al. 'Electron-Phonon Coupling from Ab Initio Linear-Response Theory within the *GW* Method: Correlation-Enhanced Interactions and Superconductivity in $Ba_{1-x}K_xBiO_3$'. In: *Phys. Rev. Lett.* 122 (18 May 2019), p. 186402. DOI: 10.1103/PhysRevLett.122.186402.

[201] Z. Li et al. 'Electron-phonon coupling from GW perturbation theory: Practical workflow combining BerkeleyGW, ABINIT, and EPW'. In: *Computer Physics Communications* 295 (2024), p. 109003. ISSN: 0010-4655. DOI: https://doi.org/10.1016/j.cpc.2023.109003.

[202] J. Berges et al. *elphmod: Python modules for electron-phonon models*. Version v0.32. Nov. 2025. DOI: 10.5281/zenodo.17702034.

[203] A. Marini et al. 'Yambo: an ab initio tool for excited state calculations'. In: *Computer Physics Communications* 180.8 (2009), pp. 1392–1403.

[204] S. Carr et al. 'Twistronics: Manipulating the electronic properties of two-dimensional layered structures through their twist angle'. In: *Phys. Rev. B* 95 (7 Feb. 2017), p. 075420. DOI: 10.1103/PhysRevB.95.075420.

[205] R. Bistritzer and A. H. MacDonald. 'Moiré bands in twisted double-layer graphene'. In: *Proceedings of the National Academy of Sciences* 108.30 (2011), pp. 12233–12237. DOI: 10.1073/pnas.1108174108.

[206] Y. Cao et al. 'Unconventional superconductivity in magic-angle graphene superlattices'. In: *Nature* 556.7699 (Mar. 2018), pp. 43–50. ISSN: 1476-4687. DOI: 10.1038/nature26160.

[207] J. Á. Silva-Guillén, P. San-Jose and R. Roldán. 'Electronic Band Structure of Transition Metal Dichalcogenides from Ab Initio and Slater–Koster Tight-Binding Model'. In: *Applied Sciences* 6.10 (2016). ISSN: 2076-3417. DOI: 10.3390/app6100284.

[208] Z. Peng et al. 'Modified tight-binding model for strain effects in monolayer transition metal dichalcogenides'. In: *Phys. Rev. B* 109 (24 June 2024), p. 245412. DOI: 10.1103/PhysRevB.109.245412.

[209] S. Fang et al. 'Ab initio tight-binding Hamiltonian for transition metal dichalcogenides'. In: *Phys. Rev. B* 92 (20 Nov. 2015), p. 205108. DOI: 10.1103/PhysRevB.92.205108.

[210] S. Fang et al. 'Electronic structure theory of strained two-dimensional materials with hexagonal symmetry'. In: *Phys. Rev. B* 98 (7 Aug. 2018), p. 075106. DOI: 10.1103/PhysRevB.98.075106.

[211] F. Wu et al. 'Topological Insulators in Twisted Transition Metal Dichalcogenide Homobilayers'. In: *Phys. Rev. Lett.* 122 (8 Feb. 2019), p. 086402. DOI: 10.1103/PhysRevLett.122.086402.

[212] J. Zang et al. 'Hartree-Fock study of the moiré Hubbard model for twisted bilayer transition metal dichalcogenides'. In: *Phys. Rev. B* 104 (7 Aug. 2021), p. 075150. DOI: 10.1103/PhysRevB.104.075150.

[213] V. Vitale et al. 'Flat band properties of twisted transition metal dichalcogenide homo- and heterobilayers of MoS2, MoSe2, WS2 and WSe2'. In: *2D Materials* 8.4 (Aug. 2021), p. 045010. DOI: 10.1088/2053-1583/ac15d9.

[214] V. Crépel and A. Millis. 'Bridging the small and large in twisted transition metal dichalcogenide homobilayers: A tight binding model capturing orbital interference and topology across a wide range of twist angles'. In: *Phys. Rev. Res.* 6 (3 Aug. 2024), p. 033127. DOI: 10.1103/PhysRevResearch.6.033127.

[215] A. Dunbrack and J. Cano. 'Intrinsically multilayer moiré heterostructures'. In: *Phys. Rev. B* 107 (23 June 2023), p. 235425. DOI: 10.1103/PhysRevB.107.235425.

[216] M. Oudich et al. 'Engineered moiré photonic and phononic superlattices'. In: *Nature Materials* 23.9 (Sept. 2024), pp. 1169–1178. ISSN: 1476-4660. DOI: 10.1038/s41563-024-01950-9.

[217] S. Shallcross et al. 'Electronic structure of turbostratic graphene'. In: *Phys. Rev. B* 81 (16 Apr. 2010), p. 165105. DOI: 10.1103/PhysRevB.81.165105.

[218] S. Carr et al. 'Relaxation and domain formation in incommensurate two-dimensional heterostructures'. In: *Phys. Rev. B* 98 (22 Dec. 2018), p. 224102. DOI: 10.1103/PhysRevB.98.224102.

[219] I. Maity et al. 'Reconstruction of moiré lattices in twisted transition metal dichalcogenide bilayers'. In: *Phys. Rev. B* 103 (12 Mar. 2021), p. L121102. DOI: 10.1103/PhysRevB.103.L121102.

[220] H. Li et al. 'Imaging moiré flat bands in three-dimensional reconstructed WSe2/WS2 superlattices'. In: *Nature Materials* 20.7 (July 2021), pp. 945–950. ISSN: 1476-4660. DOI: 10.1038/s41563-021-00923-6.

[221] C. E. M. Nielsen et al. 'Accurate force-field methodology capturing atomic reconstructions in transition metal dichalcogenide moiré system'. In: *Phys. Rev. B* 108 (4 July 2023), p. 045402. DOI: 10.1103/PhysRevB.108.045402.

[222] M. H. Naik et al. 'Origin and evolution of ultraflat bands in twisted bilayer transition metal dichalcogenides: Realization of triangular quantum dots'. In: *Phys. Rev. B* 102 (7 Aug. 2020), p. 075413. DOI: 10.1103/PhysRevB.102.075413.

[223] M. Angeli and A. H. MacDonald. 'Γ valley transition metal dichalcogenide moiré bands'. In: *Proceedings of the National Academy of Sciences* 118.10 (Mar. 2021). ISSN: 1091-6490. DOI: 10.1073/pnas.2021826118.

[224] M. Spethmann, C. Honerkamp and D. M. Kennes. 'Magnetic ordering tendencies in hexagonal-boron-nitride–bilayer-graphene moiré structures'. In: *Phys. Rev. B* 104 (8 Aug. 2021), p. 085147. DOI: 10.1103/PhysRevB.104.085147.

[225] Z. Tong et al. 'Temperature-dependent infrared optical properties of 3C-, 4H- and 6H-SiC'. In: *Physica B: Condensed Matter* 537 (2018), pp. 194–201. ISSN: 0921-4526. DOI: https://doi.org/10.1016/j.physb.2018.02.023.

[226] T. Balster et al. 'Strong dispersion of the surface optical phonon of silicon carbide in the near vicinity of the surface Brillouin zone center'. In: *Surface Science* 600.14 (2006), pp. 2886–2893. ISSN: 0039-6028. DOI: https://doi.org/10.1016/j.susc.2006.05.031.

[227] R. Mankowsky, M. Först and A. Cavalleri. 'Non-equilibrium control of complex solids by nonlinear phononics'. In: *Reports on Progress in Physics* 79.6 (May 2016), p. 064503. DOI: 10.1088/0034-4885/79/6/064503.

[228] D. Nicoletti and A. Cavalleri. 'Nonlinear light–matter interaction at terahertz frequencies'. In: *Adv. Opt. Photon.* 8.3 (Sept. 2016), pp. 401–464. DOI: 10.1364/AOP.8.000401.

[229] D. N. Basov et al. 'Polariton panorama'. In: *Nanophotonics* 10.1 (2021), pp. 549–577. DOI: doi:10.1515/nanoph-2020-0449.

[230] S. Y. Zhou et al. 'Substrate-induced bandgap opening in epitaxial graphene'. In: *Nature Materials* 6.10 (Sept. 2007), pp. 770–775. ISSN: 1476-4660. DOI: 10.1038/nmat2003.

[231] K. L. Enisherlova et al. 'Effect of SiC substrate properties on structural perfection and electrical parameters of AlGaN/GaN layers'. In: *Modern Electronic Materials* 3.1 (2017), pp. 50–56. ISSN: 2452-1779. DOI: https://doi.org/10.1016/j.moem.2017.03.001.

[232] N. A. Anderson et al. 'Intercalated rare-earth metals under graphene on SiC'. In: *Journal of Magnetism and Magnetic Materials* 474 (2019), pp. 666–670. ISSN: 0304-8853. DOI: https://doi.org/10.1016/j.jmmm.2018.11.007.

[233] S. Chen et al. 'Targeted Dy intercalation under graphene/SiC for tuning its electronic band structure'. In: *Phys. Rev. B* 107 (4 Jan. 2023), p. 045408. DOI: 10.1103/PhysRevB.107.045408.

[234] K. Idczak and E. Wachowicz. 'Influence of intercalated Gd atoms on graphene-4H-SiC(0001) properties'. In: *Applied Surface Science* 609 (2023), p. 155365. ISSN: 0169-4332. DOI: https://doi.org/10.1016/j.apsusc.2022.155365.

[235] U. Starke et al. 'Novel Reconstruction Mechanism for Dangling-Bond Minimization: Combined Method Surface Structure Determination of SiC(111)- (3×3)'. In: *Phys. Rev. Lett.* 80 (4 Jan. 1998), pp. 758–761. DOI: 10.1103/PhysRevLett.80.758.

[236] J. Schardt et al. 'Crystallography of the (3×3) surface reconstruction of $3C-$SiC(111), $4H-$SiC(0001), and $6H-$SiC(0001) surfaces retrieved by low-energy electron diffraction'. In: *Phys. Rev. B* 62 (15 Oct. 2000), pp. 10335–10344. DOI: 10.1103/PhysRevB.62.10335.

[237] I. Gierz et al. 'Phonon-Pump Extreme-Ultraviolet-Photoemission Probe in Graphene: Anomalous Heating of Dirac Carriers by Lattice Deformation'. In: *Phys. Rev. Lett.* 114 (12 Mar. 2015), p. 125503. DOI: 10.1103/PhysRevLett.114.125503.

[238] E. Pomarico et al. 'Enhanced electron-phonon coupling in graphene with periodically distorted lattice'. In: *Phys. Rev. B* 95 (2 Jan. 2017), p. 024304. DOI: 10.1103/PhysRevB.95.024304.

[239] D. Wegkamp and J. Stähler. 'Ultrafast dynamics during the photoinduced phase transition in VO2'. In: *Progress in Surface Science* 90.4 (2015), pp. 464–502. ISSN: 0079-6816. DOI: https://doi.org/10.1016/j.progsurf.2015.10.001.

[240] Y. Li et al. 'Manipulation of surface phonon polaritons in SiC nanorods'. In: *Science Bulletin* 65.10 (2020), pp. 820–826. ISSN: 2095-9273. DOI: https://doi.org/10.1016/j.scib.2020.02.026.

[241] A. Mancini et al. 'Near-Field Retrieval of the Surface Phonon Polariton Dispersion in Free-Standing Silicon Carbide Thin Films'. In: *ACS Photonics* 9.11 (2022), pp. 3696–3704. DOI: 10.1021/acsphotonics.2c01270.

[242] C. R. Gubbin, S. De Liberato and T. G. Folland. 'Surface phonon polaritons for infrared optoelectronics'. In: *Journal of Applied Physics* 131.3 (Jan. 2022), p. 030901. ISSN: 0021-8979. DOI: 10.1063/5.0064234.

[243] S. M. V. Esfidani, M. J. Tadjer and T. G. Folland. 'Lifetime and Molecular Coupling in Surface Phonon Polariton Resonators'. In: *ACS Omega* 9.19 (2024), pp. 21136–21143. DOI: 10.1021/acsomega.4c01009.

[244] Q. Tan et al. 'Enhanced coherence from correlated states in WSe2/MoS2 moiré heterobilayer'. In: *Nature Communications* 16.1 (May 2025). ISSN: 2041-1723. DOI: 10.1038/s41467-025-57391-8.

[245] Y. Li et al. 'Evidence of strong and mode-selective electron–phonon coupling in the topological superconductor candidate 2M-WS2'. In: *Nature Communications* 15.1 (July 2024). ISSN: 2041-1723. DOI: 10.1038/s41467-024-50590-9.

[246] V. Wang et al. 'Effect of direct interlayer coupling on the moiré potentials in twisted WSe2/MoSe2 heterobilayers'. In: *Physica B: Condensed Matter* 699 (2025), p. 416873. ISSN: 0921-4526. DOI: https://doi.org/10.1016/j.physb.2024.416873.

[247] P. Froese, T. Neupert and G. Wagner. 'Topological excitons in moiré $MoTe_2/WSe_2$ heterobilayers'. In: *Phys. Rev. Res.* 7 (2 Apr. 2025), p. 023047. DOI: 10.1103/PhysRevResearch.7.023047.

Listings

List of Figures

List of Tables

Eigenständigkeitserklärung

Hiermit versichere ich an Eides statt, die vorliegende Dissertationsschrift selbst verfasst und keine anderen als die angegebenen Hilfsmittel und Quellen benutzt zu haben. Sofern im Zuge der Erstellung der vorliegenden Dissertationsschrift generative Künstliche Intelligenz (gKI) basierte elektronische Hilfsmittel verwendet wurden, versichere ich, dass meine eigene Leistung im Vordergrund stand und dass eine vollständige Dokumentation aller verwendeten Hilfsmittel gemäß der Guten wissenschaftlichen Praxis vorliegt. Ich trage die Verantwortung für eventuell durch die gKI generierte fehlerhafte oder verzerrte Inhalte, fehlerhafte Referenzen, Verstöße gegen das Datenschutz- und Urheberrecht oder Plagiate.

Hamburg, den 27. Januar 2026 **Michael Winter**